

**Please cite the Published Version**

Slate, Anthony Joseph (2019) Optimisation of a Pseudomonas aeruginosa microbial fuel cell coupled with additive manufacturing of graphene electrodes to enhance power outputs. Doctoral thesis (PhD), Manchester Metropolitan University.

**Downloaded from:** <https://e-space.mmu.ac.uk/625454/>

**Usage rights:**  [Creative Commons: Attribution-Noncommercial-No Derivative Works 4.0](https://creativecommons.org/licenses/by-nc-nd/4.0/)

**Enquiries:**

If you have questions about this document, contact [openresearch@mmu.ac.uk](mailto:openresearch@mmu.ac.uk). Please include the URL of the record in e-space. If you believe that your, or a third party's rights have been compromised through this document please see our Take Down policy (available from <https://www.mmu.ac.uk/library/using-the-library/policies-and-guidelines>)

**Optimisation of a *Pseudomonas aeruginosa*  
microbial fuel cell coupled with additive  
manufacturing of graphene electrodes to  
enhance power outputs**

**Anthony Joseph Slate**

Department of Natural Sciences

Manchester Metropolitan University

A thesis submitted in partial fulfilment of the requirements of  
the Manchester Metropolitan University for the degree of  
Doctor of Philosophy

**2019**

## DECLARATION

This is to certify that the material contained in this thesis has been produced by the author and has not been accepted in substance for any other degree and is not currently submitted in candidature for any other academic award.

**Signed:**



Anthony J. Slate

**Submission Date:** 24/10/2019

**Post *viva voce* Submission date:** 31/1/2020

**Final Word Count:** 55,202

# Table of Contents

Abstract.....	X
Acknowledgments.....	XII
List of Tables.....	XIV
List of Figures .....	XV
Abbreviations .....	XXI
Chapter 1 – Introduction to Microbial Fuel Cells (MFCs).....	1
1.1 Renewable Energy.....	2
1.2 Overview of Microbial Fuel cells .....	4
1.2.1 History of MFCs .....	4
1.2.2 Fundamental Bioelectricity Generation in MFCs .....	5
1.2.2.1 Biofilm Formation .....	8
1.2.3 Structural Configurations .....	8
1.2.4 Limiting Factors .....	12
1.2.5 Optimisation of MFC Power Outputs.....	15
1.3 Electrode Materials .....	16
1.3.1 Electrode Topography .....	16
1.3.2 Carbon Based Electrodes .....	17
1.3.2.1 Graphene.....	18
1.3.3 Surface Hydrophobicity.....	20
1.4 Mechanisms of Electron Transfer .....	21
1.4.1 Direct electron transfer <i>via</i> Nanowires.....	22
1.4.2 Direct electron transfer <i>via</i> redox-active proteins .....	26
1.4.3 Indirect electron transfer <i>via</i> electron shuttles .....	27
1.4.3.1 <i>Pseudomonas aeruginosa</i> .....	29

1.5 Mixed community microbial fuel cells .....	33
1.6 Aim and Objectives .....	34
1.6.1 Academic Aim.....	34
1.6.2 Objectives.....	34
Chapter 2 – Exploring the electrochemical performance of graphite and graphene paste electrodes comprised of varying lateral flake sizes .....	35
2.1 Introduction .....	36
2.1.1 Carbon Based Paste Electrodes.....	36
2.1.2 Graphene.....	36
2.1.3 Edge and Basal Plane Theory .....	37
2.1.4 Current Issue with Graphene Electrochemical Research.....	37
2.1.5 Aim .....	38
2.2 Methods .....	39
2.2.1 Electrochemical Analysis of the Graphite and Graphene Paste Electrodes .....	39
2.2.2 Physiochemical Characterisation .....	40
2.2.3 Fabrication of the Graphite and Graphene Paste Electrodes .....	40
2.2.4 Determination of the Heterogeneous Electron Transfer Rate Kinetics ( $k^0$ ) .....	41
2.2.5 Determination of the Electrochemical Effective Area .....	42
2.2.6 Determination of the Edge to Basal Plane ratio .....	43
2.2.7 Density Functional Theory (DFT) Computation .....	44
2.3 Results .....	45
2.3.1 Structural Characterisation .....	45
2.3.2 Electrochemical Analysis.....	47
2.3.2.1 Hexaammineruthenium(III) Chloride Redox Probe .....	47
2.3.2.2 Potassium Ferrocyanide(II) Redox Probe.....	50
2.3.3 Edge to Basal Plane Ratio.....	54

2.3.4 Density Functional Theory (DFT).....	56
2.4 Discussion.....	58
2.4.1 Graphite Paste Electrodes.....	58
2.4.2 Graphene Paste Electrodes.....	60
2.4.3 Electrostatic Potential Maps of Graphene.....	61
2.5 Conclusion.....	62
Chapter 3 – Fabrication and Characterisation of the Three-Dimensional Printed Graphene Electrodes.....	63
3.1 Introduction.....	64
3.1.1 Three Dimensional Printing.....	64
3.1.2 Determination of the Electroactive Area of 3D-Printed Electrodes.....	65
3.1.3 Surface Characterisation.....	66
3.1.4 Aim.....	67
3.2 Methods.....	68
3.2.1 Fabrication of 3D-Printed Electrodes.....	68
3.2.1.1 Electrode Polishing.....	68
3.2.2 Electrode Characterisation.....	68
3.2.3 Electrochemical Analysis of the 3D-Printed Electrodes.....	69
3.2.4 Determination of the Heterogeneous Electron Transfer Rate Kinetics ( $k^0$ ).....	69
3.2.5 Determination of the Electrochemical Effective Area ( $A_{\text{eff}}$ ).....	69
3.2.6 Electrodeposition of MoO <sub>2</sub> on 3D-Printed BM Electrodes.....	70
3.2.6.1 Multifractal Analysis.....	70
3.2.7 Optical Profilometry.....	72
3.2.8 Physicochemistry.....	72
3.2.9 Statistical Analysis.....	73
3.3 Results.....	74

3.3.1 Electrochemical Analysis .....	74
3.3.2 Electrode Characterisation.....	76
3.3.3 Determination of the Electroactive Area <i>via</i> Molybdenum Dioxide Nanowire Formation.....	78
3.3.3.1 Determination of the deposition potential.....	79
3.3.3.2 Raman spectroscopy .....	80
3.3.3.3 Scanning Electron Microscopy (SEM) .....	83
3.3.3.4 Electrochemical Effect on Surface Areas .....	85
3.3.3.5 Multifractal Analysis (MFA).....	88
3.3.4 Surface Analysis: Optical Profilometry.....	90
3.3.5 Surface Analysis: Physicochemistry .....	93
3.4 Discussion.....	96
3.4.1 Electrochemical Analysis .....	96
3.4.2 Topographical Characterisation .....	96
3.4.3 Determination of the Electroactive Area <i>via</i> Molybdenum Dioxide Nanowire Formation.....	97
3.4.3.1 Electrode Characterisation.....	98
3.4.3.2 Electrochemical Effect on Surface Areas .....	99
3.4.3.3 Multifractal Analysis.....	99
3.4.4 Surface Analysis.....	101
3.4.4.1 Optical Profilometry.....	101
3.4.4.2 Physicochemistry .....	102
3.5 Conclusion .....	104
Chapter 4 – <i>Pseudomonas aeruginosa</i> Selection and Optimisation.....	105
4.1 Introduction .....	106
4.1.1 Exoelectrogenic Properties of <i>P. aeruginosa</i> .....	106

4.1.2 Pyocyanin .....	106
4.1.3 Nanowires .....	107
4.1.4 Cell Surface Hydrophobicity .....	108
4.1.5 Biofilm Effect on Power Outputs .....	109
4.1.6 Anaerobic Survival and Proliferation of <i>P. aeruginosa</i> .....	110
4.1.7 Aim .....	113
4.2 Methods .....	114
4.2.1 Growth Media Preparation and Bacterial Preparation.....	114
4.2.1.1 Agar and Growth Media Preparation .....	114
4.2.1.2 Preparation of Bacterial Cells.....	114
4.2.2 Preliminary Strain Selection .....	115
4.2.2.1 Pyocyanin Production – Chloroform Extraction Assay .....	115
4.2.2.2 Biofilm Quantification – Crystal Violet Biofilm Assay .....	115
4.2.2.3 Motility Assay .....	116
4.2.2.4 Microbial Adhesion To Hydrocarbons (MATH) Assay .....	117
4.2.2.5 Scanning Electron Microscopy (SEM) .....	118
4.2.3 <i>Pseudomonas aeruginosa</i> strain ATCC 9027 Optimisation.....	119
4.2.3.1 Growth Kinetics .....	119
4.2.3.1.1 Optical Density .....	120
4.2.3.1.2 Bacterial Quantification – CFU mL <sup>-1</sup> <i>via</i> Miles and Misra.....	120
4.2.3.1.3 Pyocyanin Quantification: Liquid Chromatography - Mass Spectroscopy (LC-MS) .....	120
4.2.3.1.3.1 Sample preparation for LC-MS .....	120
4.2.3.1.3.2 LC-MS Analysis.....	121
4.2.3.1.3.3 File Conversion .....	122
4.2.3.1.3.4 Quality Assurance .....	122
4.2.3.1.3.5 Data Analysis.....	123
4.2.3.2 Biofilm Quantification – Crystal Violet Biofilm Assay – MFC Conditions...124	

4.2.3.3 Nitrogen Biolog Assay .....	125
4.2.4 Statistical Analysis .....	125
4.3 Results .....	126
4.3.1 Preliminary Strain Selection .....	126
4.3.1.1 Pyocyanin Production – Chloroform Extraction Assay .....	126
4.3.1.2 Biofilm Quantification – Crystal Violet Biofilm Assay .....	127
4.3.1.3 Motility Assay .....	131
4.3.2.4 Microbial Adhesion To Hydrocarbons (MATH) Assay .....	132
4.3.2 <i>Pseudomonas aeruginosa</i> strain ATCC 9027 Optimisation.....	141
4.3.2.1 Bacterial Growth Dynamics.....	141
4.3.2.1.1 Optical Density .....	141
4.3.2.1.2 Bacterial Viability.....	142
4.3.2.1.3 Pyocyanin Quantification – LC-MS .....	144
4.3.2.2 Biofilm Quantification – Crystal Violet Biofilm Assay in MFC Conditions..	146
4.3.2.3 Nitrogen Biolog® Assay .....	147
4.4 Discussion.....	149
4.4.1 Preliminary Strain Selection .....	149
4.4.2 <i>Pseudomonas aeruginosa</i> strain ATCC 9027 Optimisation.....	152
4.4.2.1 Growth Dynamics .....	152
4.4.2.2 Biofilm Quantification – Crystal Violet Biofilm Assay in MFC Conditions..	154
4.4.2.3 Nitrogen Biolog® Assays.....	155
4.5 Conclusion .....	157
Chapter 5 – <i>Pseudomonas aeruginosa</i> MFC Coupled with Additive Manufacturing of Graphene-Based Electrodes.....	158
5.1. Introduction .....	159
5.1.1 Additive Manufacturing of MFCs .....	159
5.1.2 Graphene.....	160

5.1.3	<i>Pseudomonas aeruginosa</i> MFC configurations.....	161
5.1.3.1	Biofilm Formation and Role in <i>P. aeruginosa</i> MFCs.....	162
5.1.3.2	Varying Medium Sources to Influence Metabolic Pathways .....	162
5.1.4	Aim .....	163
5.2	Methods .....	164
5.2.1	Bacterial Cell Preparation .....	164
5.2.2	MFC Configuration .....	164
5.2.2.1	MFC Construction .....	164
5.2.2.2	Measurement and Analysis.....	166
5.2.2.3	Arduino Code .....	167
5.2.2.4	Bacterial Enumeration .....	168
5.2.3	Scanning Electron Microscopy .....	168
5.2.4	Confocal Microscopy .....	169
5.2.5	Statistical Analysis .....	169
5.3	Results .....	170
5.3.1	MFC Cell Potential.....	170
5.3.2	Bacterial Quantification From MFC – Growth kinetics .....	172
5.3.3	MFC Current and Current Density .....	173
5.3.4	MFC Power and Power Density.....	177
5.3.5	Bacterial Visualisation <i>via</i> Microscopy.....	182
5.4	Discussion.....	186
5.4.1	MFC Performance Analysis .....	186
5.4.1.1	Electrodes used in MFC Configurations .....	186
5.4.1.2	<i>Pseudomonas aeruginosa</i> viability in MFC configurations .....	187
5.4.1.3	Power and Current Generation.....	187
5.4.1.4	Varying Media Sources to Influence Metabolic Pathways .....	189

5.4.2 <i>Pseudomonas aeruginosa</i> Visualisation.....	191
5.5 Conclusion .....	194
Chapter 6 - Conclusion and Future Work.....	195
6.1 Conclusion .....	196
6.2 Key Findings.....	200
6.3 Future Work .....	201
6.3.1 Electrode Characterisation and Optimisation.....	201
6.3.2 Bacterial Strain Selection and Optimisation .....	201
6.3.3 MFC Configuration Optimisation .....	202
6.3.4 RNA Sequencing of MFC Samples .....	203
6.4 Publications .....	204
Chapter 7 – References.....	206

## Abstract

Due to the ever-increasing concern of climate change, research into alternative renewable energy generation is a priority. Microbial fuel cells (MFCs) offer one potential avenue to be explored as a partial solution towards combating the over-reliance on fossil fuel based electricity generation. Limitations such as low power generation, expensive electrode materials and the inability to scale up MFCs to industrially-relevant capacities have slowed MFC development. However, new electrode materials (*e.g.* graphene) coupled with a more thorough understanding of the mechanisms in which exoelectrogenic bacteria mediate electron transfer have the potential to dramatically increase MFC power outputs.

The primary aim of this thesis was to optimise MFC power outputs by incorporating graphene in 3D-Printed electrodes. The MFC literature was reviewed in Chapter One. Graphene electrodes were optimised for electrochemical performance by varying individual lateral flake size of carbon paste electrodes (Chapter Two), a reduction in the individual lateral flake size of graphite and graphene electrodes enhanced electrochemical activity up to a specific size (*ca.* 2  $\mu\text{m}$ ). Graphene flakes smaller than this threshold exhibited no further improvement in electrochemical activity.

A commercial filament was 3D-Printed to fabricate electrodes, 3D-Printed BM (Black Magic), which comprised of 8 wt.% graphene. These electrodes were evaluated for electrochemical performance, chemical composition (Raman spectroscopy) and surface properties (optical profilometry and physicochemistry). This included a novel quantification technique, which utilised the electrodeposition of molybdenum dioxide ( $\text{MoO}_2$ ) nanowires coupled with multifractal analysis, to deduce the electroactive areas of the electrodes (Chapter Three). The most exoelectrogenic *Pseudomonas aeruginosa* strain was selected using several key parameters for use within an MFC application (Chapter Four). *Pseudomonas aeruginosa* strain ATCC 9027 was selected, based on growth kinetic assays (cell viability), biofilm formation, pyocyanin production (*via* liquid chromatography-mass spectrometry) and hydrophobicity status, in conditions that were representative of the batch-fed MFC configuration (120 h; 37 °C; anaerobic; static). Alternative anaerobic growth conditions were explored, but there was no significant difference between *P. aeruginosa* cell proliferation in glucose or LB media and interestingly, no accumulation of pyocyanin was evident.

Chapter Five combined the previously described 3D-Printed BM electrodes with bacterial selection and growth conditions in a MFC configuration. MFC cell potential was determined at 0 h, 24 h, 48 h, 72 h, 96 h and 120 h and power, power density, current and current density were calculated via Ohm's law. Bacterial viability was determined for each time-period. The 3D-Printed BM electrodes demonstrated conductivity similar to that of the carbon cloth electrodes (the current benchmark in MFCs) in the presence of *P. aeruginosa*, in both anaerobic LB and glucose based media over a 120 h incubation period. The use of 3D-Printed BM electrodes had no significant detrimental effect on *P. aeruginosa* viability, but dramatically enhanced biofilm production. To visualise *P. aeruginosa* cells on the surface of each electrode and the cationic exchange membrane (CEM), confocal microscopy and scanning electron microscopy was conducted. Chapter Six provided a conclusion to this thesis, summarising the optimisation methods and MFC power outputs obtained. Overall, this study found no significant difference in power outputs from the 3D-Printed BM electrode and the carbon cloth electrode when tested in the same media with *P. aeruginosa*. Furthermore, the potential for future work is also detailed which could progress and translate this MFC research into industrially-relevant and applied areas.

## Acknowledgments

I would like to express the ultimate gratitude towards my supervisors (Dr. Dale Brownson, Professor Kathryn Whitehead and Professor Craig Banks) for enabling me to conduct this body of research. More specifically, I would like to thank Professor Whitehead for her continued and ongoing support, both academically and personally.

I would like to extend my appreciation to both the Microbiology at Interfaces and the Banks research groups. Without the guidance and support from members of both groups, this thesis would not be possible. I would like to express a special thank you to the Microbiology technicians at Manchester Metropolitan University. The advice and support offered, particularly by Dr. Paul Benson-White, Miss. Lindsay Smith and Ms. Gill Collier has been invaluable throughout my PhD studies.

The density functional theory (DFT) calculations reported throughout this thesis were performed by Dr. Ahmed S. Abo Dena (Future University in Egypt). Transmission electron microscopy (TEM) was conducted by Prof. Graham C. Smith (University of Chester). Multifractal analysis (MFA) motifs and  $f(\alpha)$  curves were generated by Dr. Stephen Lynch (Manchester Metropolitan University). I would like to thank, Mr. Niall Hickey and Mr. Lee Harman for their advice with the LC-MS experimentation and analysis, Mr. Daniel Wilson (University of Manchester) for designing and manufacturing the custom circuit board used in the microbial fuel cell (MFC) experiments, Dr. Mohamed El Mohtadi for confocal microscopy advice and Dr. Jonathan Butler for experimental advice.

I am forever grateful to my family for their love, support and selfless sacrifices over the course of my life; I would not have reached this stage of academia or have completed this thesis without your determination to make me succeed. Any accolades gained by myself are also yours.

Throughout my studies, I have gained many special friends and the memories made will be cherished forever. If it were not for the camaraderie between Mr. Niall Hickey, Dr. Jonathan Butler and myself, this journey would not have been as enjoyable.

Finally, I would like to thank Mr. Mark Pittendrigh for his compassionate, caring nature and logical approach, this has allowed me to flourish and improve, both, in a personal and professional sense.

This thesis marks the beginning of a new chapter for myself, but without those mentioned above, this would be but a dream. It is unto the people mentioned above, as only proper, I dedicate this thesis.

## List of Tables

Table 1.1. Possible mechanisms by which to improve the power output. ....	16
Table 2.1. Scanning electron microscope-energy-dispersive X-ray microanalysis (SEM-EDX) analysis of graphite and graphene flakes showing average atomic percentage ( $n = 3$ ). ....	47
Table 2.2. Comparison of the electrochemical behaviour of the four graphitic electrodes against, 1 mM hexaammineruthenium(III) chloride and 1 mM potassium ferrocyanide(II) redox probes (with supporting 0.1 M KCl electrolyte). The redox probes were characterised prior to use with an EPPG electrode and $k^0$ values of $3.33 \times 10^{-3}$ and $1.80 \times 10^{-3}$ were recorded for hexaammineruthenium(III) chloride and potassium ferrocyanide(II), respectively ( $n = 3$ ). ....	53
Table 2.3. Comparison of the electrochemical behaviour of the five graphene electrodes against, 1 mM hexaammineruthenium(III) chloride and 1 mM potassium ferrocyanide(II) redox probes (with supporting 0.1 M KCl electrolyte). The redox probes were characterised prior to use with an EPPG electrode and $k^0$ values of $3.33 \times 10^{-3}$ and $1.80 \times 10^{-3}$ were recorded for hexaammineruthenium(III) chloride and potassium ferrocyanide(II), respectively ( $n = 3$ ). ....	54
Table 2.4. Calculated edge to basal plane ratios for the graphite and graphene paste electrodes. Redox probe: 1 mM Hexaammineruthenium(III) chloride with supporting 0.1 M KCl electrolyte ( $n = 3$ ). ....	55
Table 3.1 Comparison of the electrochemical behaviour of 3D-Printed graphene electrodes, both, polished and unpolished and the filament (prior to printing) against, 1 mM hexaammineruthenium(III) chloride (with supporting 0.1 M KCl electrolyte) ( $n = 3$ ). ....	75
Table 3.2. Electrochemically acquired areas and MFA percentage coverage of one isolated side of the 3D-Printed BM electrodes following MoO <sub>2</sub> deposition, against 1 mM hexaammineruthenium(III) chloride with 0.1 M KCl. The reported $k^0$ value for the control 3D-Printed BM electrode was $1.08 \times 10^{-3}$ ( $\pm 0.000033$ ) cm s <sup>-1</sup> and a $\Delta E_p$ at 100 mV s <sup>-1</sup> of 199.73 ( $\pm 1.68$ ) mV. The 3D-Printed BM electrode exposed to MoO <sub>2</sub> deposition for 300 seconds gave a $k^0$ value of $4.90 \times 10^{-4}$ ( $\pm 0.00014$ ) cm s <sup>-1</sup> and a $\Delta E_p$ at 100 mV s <sup>-1</sup> of 327.71 ( $\pm 13.72$ ) mV ( $n = 3$ ). ....	86
Table 3.3. Physicochemistry values recorded <i>via</i> contact angle measurements of the 3D-Printed BM electrodes and control (3D-Printed PLA) electrode ( $n = 5$ ). ....	95
Table 4.1. LC-MS parameters per sample. ....	122
Table 4.2. Statistical analysis (two-way ANOVAs) comparing the <i>P. aeruginosa</i> strain ATCC 9027, aerobic and anaerobic MATH assay results, over the different time-points. Asterisks denote significance, * $P \leq 0.05$ , ** $P \leq 0.01$ , *** $P \leq 0.001$ and **** $P \leq 0.0001$ . ....	136
Table 4.3. Statistical analysis (two-way ANOVAs) comparing the <i>P. aeruginosa</i> strain PAO1, aerobic and anaerobic MATH assay results, over the different time-points. Asterisks denote significance, * $P \leq 0.05$ , ** $P \leq 0.01$ and **** $P \leq 0.0001$ . ....	140

# List of Figures

Figure 1.1. A) Average power outputs of a range of fuel technologies, including both traditional energy sources (i.e. coal and natural gas) and alternative/renewable energy sources. B) The average efficiency range of traditional and alternative/renewable fuel sources. Data obtained from (Janicek <i>et al.</i> , 2014; Sharaf and Orhan, 2014; Shoener <i>et al.</i> , 2014; Sun <i>et al.</i> , 2016b; Ter Heijne <i>et al.</i> , 2011).....	3
Figure 1.2. Schematic of a typically employed two-chamber microbial fuel cell highlighting the various electrochemical and electro-microbiological processes. Figure adapted from (Du <i>et al.</i> , 2007). .....	9
Figure 1.3. A number of ways in which the performance of MFC technologies can deteriorate. Examples here include biofouling (electrode blockage), inactivation of catalysts and excessive growth of bacterial biofilms leading to the production of non-conductive debris. Figure adapted from Sun <i>et al.</i> , 2016b.	14
Figure 1.4. Scanning Electron Micrograph (SEM) showing the abundant coverage of an <i>E. coli</i> biofilm adhered to the surface of a carbon-paste graphite electrode. Figure reproduced with permission from (Slate <i>et al.</i> , 2019b). .....	18
Figure 1.5. The three known methods of electron transfer demonstrated by exoelectrogenic bacteria, including; direct electron transfer – conductive pili, denoted within the literature as nanowires; redox-active proteins; and indirect electron transfer by electron shuttles. Figure adapted from Kumar <i>et al.</i> (2012). .....	22
Figure 1.6. A) Scanning electron microscopy (SEM) image showing the difference in morphology of flagella and pili on the surface of <i>E. coli</i> . B) Transmission electron microscopy (TEM) showing <i>G. sulfurreducens</i> strain GUP, expressing abundant pili. Section B, adapted from Tan <i>et al.</i> (2016). .....	24
Figure 1.7. A range of known exogenous and endogenous redox mediators which are capable of mediating electron transfer. ....	28
Figure 2.1. Structural characterisation of the graphite lateral flakes <i>via</i> SEM, A) kish graphite, B) flake graphite, C) high crystalline natural graphite, D) nanostructured graphite - 250. Note, the necessary difference in magnification to report the variation in lateral flake size. ....	45
Figure 2.2. Structural characterisation of the graphene lateral flakes <i>via</i> TEM, A) A0-1, B) A0-2, C) A0-3, D) A0-4 and E) C1. Note, the scale bar in each image was 2 $\mu\text{m}$ . ....	46
Figure 2.3. Cyclic voltammetric profiles recorded using the graphite paste electrodes. Redox probe: 1 mM Hexaammineruthenium(III) chloride in 1 M KCl. Scan rate: 100 $\text{mV s}^{-1}$ ( $n = 3$ ). .....	48
Figure 2.4. Cyclic voltammetric profiles of the graphene paste electrodes. Redox probe: 1 mM Hexaammineruthenium(III) chloride in 1 M KCl. Scan rate: 100 $\text{mV s}^{-1}$ ( $n = 3$ ). .....	49
Figure 2.5. Cyclic voltammetric profiles recorded of the graphite paste electrodes. Redox probe: 1 mM potassium ferrocyanide(II) in 1 M KCl. Scan rate: 100 $\text{mV s}^{-1}$ ( $n = 3$ ). .....	51
Figure 2.6. Cyclic voltammetric profiles recorded of the graphene paste electrodes. Redox probe: 1 mM potassium ferrocyanide(II) in 1 M KCl. Scan rate: 100 $\text{mV s}^{-1}$ ( $n = 3$ ). .....	52
Figure 2.7. DFT calculations on graphene flakes of different lateral flake size sizes (a) $2 \times 3$ , b) $3 \times 5$ and c) $6 \times 11$ carbon atoms); (a-c) optimized geometry, (d-f) highest occupied molecular orbital (HOMO), (g-i)	

lowest unoccupied molecular orbital (LUMO) and (j-l) Electrostatic potential maps of 2×3, 3×5 and 6×11 (ring × row) flakes, respectively (Slate <i>et al.</i> , 2018a).....	57
Figure 3.1. Cyclic voltammetric profiles recorded of the 3D-Printed graphene electrodes, both, polished and unpolished and the filament (prior to printing). Redox probe: 1 mM hexaammineruthenium(III) chloride in 1 M KCl. Scan rate: 100 mV s <sup>-1</sup> . .....	75
Figure 3.2. SEM image depicting the surface morphology of the unmodified 3D-Printed BM electrode at 100 × magnification. ....	76
Figure 3.3. SEM images depicting the surface topography of the following electrodes at 2.00 K × magnification, A) BM - polished, B) BM - unpolished, C) PLA - polished and D) PLA - unpolished. ....	77
Figure 3.4. Raman spectra of the 3D-Printed BM electrode. The D band was the defect band in sp <sup>2</sup> hybridised carbon whilst the G band was the first-order Raman band of all sp <sup>2</sup> hybridised carbon. Representative of <i>n</i> = 3. ....	78
Figure 3.5. Cyclic voltammogram recorded in 1 mM Na <sub>2</sub> MoO <sub>4</sub> (in supporting 1 M NaCl and 1 M NH <sub>4</sub> Cl, adjusted to pH 8.5). The deposition (reduction peak) and stripping (oxidation peak) of MoO <sub>2</sub> was observed against the 3D-Printed BM electrodes. Scan rate: 5 mV s <sup>-1</sup> (vs. SCE). Representative of <i>n</i> = 6. ....	79
Figure 3.6. Raman spectra of the eight MoO <sub>2</sub> deposition time-points against the 3D-Printed BM electrodes. A) Control (black), B) 20 s (blue), C) 40 s (green), D) 60 s (grey), E) 120 s (yellow), F) 180 s (orange), G) 240 s (red) and H) 300 s (purple). Representative of <i>n</i> = 3.....	81
Figure 3.7. Raman spectra (focussing on the 0 cm <sup>-1</sup> to 1000 cm <sup>-1</sup> region) of the eight MoO <sub>2</sub> deposition time-points against the 3D-Printed BM electrodes. A) Control (black), B) 20 s (blue), C) 40 s (green), D) 60 s (grey), E) 120 s (yellow), F) 180 s (orange), G) 240 s (red) and H) 300 s (purple). Representative of <i>n</i> = 3. ....	82
Figure 3.8. SEM of the surface of the 3D-Printed BM electrodes showing the deposited MoO <sub>2</sub> A), Control, B) 20 s, C) 40 s, D) 60 s, E) 120 s, F) 180 s, G) 240 s and H) 300 s. Representative of <i>n</i> = 3.....	84
Figure 3.9. Cyclic voltammetric profiles the control (solid line) and 180 s (dashed line) MoO <sub>2</sub> deposition time of the 3D-Printed BM electrodes. Redox probe: 1 mM hexaammineruthenium(III) chloride / 1 M KCl. Scan rate: 100 mVs <sup>-1</sup> . ....	87
Figure 3.10. A) Theory of <i>f</i> ( $\alpha$ ) curves for MFA B) <i>f</i> ( $\alpha$ ) curves of a selection of MoO <sub>2</sub> time-points selected for this study (control, 20 s, 60 s, 120 s, 240 s, 300 s) C) MoO <sub>2</sub> Area cover (deducted from the control background (%)) D) MoO <sub>2</sub> Density E) MoO <sub>2</sub> dispersion F) MoO <sub>2</sub> clustering ( <i>n</i> = 3).....	89
Figure 3.11. Average surface roughness ( <i>S<sub>a</sub></i> ) of both sides of the 3D-Printed BM electrodes and the 3D-Printed PLA control ( <i>n</i> = 9). Asterisks denote statistical significance, * ( <i>P</i> ≤ 0.05), ** ( <i>P</i> ≤ 0.01), *** ( <i>P</i> ≤ 0.001) and **** ( <i>P</i> ≤ 0.0001). ....	90
Figure 3.12. Maximum peak height ( <i>S<sub>p</sub></i> ) of both sides of the 3D-Printed BM electrodes and the 3D-Printed PLA control ( <i>n</i> = 9). Asterisks denote statistical significance, * ( <i>P</i> ≤ 0.05). ....	91
Figure 3.13. Maximum valley depth ( <i>S<sub>v</sub></i> ) of both sides of the 3D-Printed BM electrodes and the 3D-Printed PLA control ( <i>n</i> = 9). Asterisks denote statistical significance, ** ( <i>P</i> ≤ 0.01). ....	92

Figure 3.14. Peak-to-valley ratios ( $S_{pv}$ ) of both sides of the 3D-Printed BM electrodes and the 3D-Printed PLA control ( $n = 9$ ). Asterisks denote statistical significance, ** ( $P \leq 0.01$ ). .....	92
Figure 3.15. Percentage surface analysis of both sides of the 3D-Printed BM electrodes and the 3D-Printed PLA control ( $n = 9$ ). Where error bars are not visible they are of similar or smaller size compared to the symbol.....	93
Figure 4.1. Chemical structure of Pyocyanin.....	107
Figure 4.2. Anaerobic denitrification process, including denitrification gene expression and regulatory network in <i>P. aeruginosa</i> . This process is catalysed by the following metalloenzymes, nitrate reductase (NAR), nitrite reductase (NIR), NO reductase (NOR) and N <sub>2</sub> O reductase (N <sub>2</sub> OR). Figure adapted from Kuroki <i>et al.</i> (2014).....	112
Figure 4.3. Pyocyanin references mass were determined from the 5 ppb and 50 ppb standard controls by plotting base peak intensity against retention time (min). The mass to charge (m/z) peak for pyocyanin was confirmed in both the 5 and 50 ppb reference samples as 211.086. This value was then used to quantify pyocyanin from the <i>P. aeruginosa</i> strain ATCC 9027 growth kinetic studies. Representative of $n = 3$ .....	124
Figure 4.4. Pyocyanin quantification of five <i>P. aeruginosa</i> strains (at OD $1 \pm 0.1$ (OD <sub>600 nm</sub> )) over four time-points (24 h, 48 h, 7 d and 14 d) (incubation conditions: 37 °C; aerobic; aggregation (200 rpm)). Statistical testing indicates significant difference between 48 h and 7 day incubation periods ( $P \leq 0.05$ ) and when comparing 48 h and 14 days pyocyanin production ( $P \leq 0.0001$ ) ( $n = 3$ ). .....	127
Figure 4.5. Biofilm quantification as determined by CVBA against <i>P. aeruginosa</i> strain ATCC 9027 minus the broth controls (incubation conditions: 37 °C; aerobic; static) ( $n = 3$ ). Significance denoted by **** $P \leq 0.0001$ . .....	128
Figure 4.6. Biofilm quantification as determined by CVBA against <i>P. aeruginosa</i> strain PAO1 minus the broth controls (incubation conditions: 37 °C; aerobic; static) ( $n = 3$ ). Significance denoted by ** $P \leq 0.01$ , *** $P \leq 0.001$ **** $P \leq 0.0001$ .....	129
Figure 4.7. Biofilm quantification as determined by CVBA against <i>P. aeruginosa</i> strain MRI minus the broth controls (incubation conditions: 37 °C; aerobic; static) ( $n = 3$ ). No statistical significance was observed ( $P > 0.05$ ). .....	130
Figure 4.8. SEM images depicting bacterial adhesion/retention of <i>P. aeruginosa</i> strain ATCC 9027 following a 24 h incubation period (37 °C; aerobic; static), with the following electrodes (15.00 K × magnification). A) BM - polished, B) BM - unpolished, C) PLA - polished and D) PLA - unpolished. ....	131
Figure 4.9. Motility assay of three <i>P. aeruginosa</i> strains under aerobic or anaerobic conditions over 48 h (incubation conditions: 0.4 % LB agar; 37 °C; static) ( $n = 3$ ). Asterisks denote significance, * $P \leq 0.05$ , ** $P \leq 0.01$ , **** $P \leq 0.0001$ .....	132
Figure 4.10. MATH Assays of aerobic and anaerobic <i>P. aeruginosa</i> strain ATCC 9027 demonstrated adhesion to polar (chloroform and ethyl acetate) and non-polar solvents (hexadecane and decane) following, A) 24 h, B) 72 h and C) 120 h incubation (37 °C; static) ( $n = 3$ ). Asterisks denote significance, * $P \leq 0.05$ , ** $P \leq 0.01$ , *** $P \leq 0.001$ and **** $P \leq 0.0001$ .....	135

- Figure 4.11. MATH Assay of aerobic and anaerobic *P. aeruginosa* strain PAO1 demonstrated adhesion to polar (chloroform and ethyl acetate) and non-polar solvents (hexadecane and decane) following, A) 24 h, B) 72 h and C) 120 h incubation (37 °C; static) ( $n = 3$ ). Asterisks denote significance,  $*P \leq 0.05$ ,  $**P \leq 0.01$  and  $***P \leq 0.0001$ ..... 139
- Figure 4.12. Optical density recorded by sampling *P. aeruginosa* strain ATCC 9027 over 120 h, two media types, glucose-based and LB broth were used (incubation conditions; 37 °C; static). Starting cultures were either aerobic-to-anaerobic or fully anaerobic prior to inoculation ( $n = 3$ ). Where error bars are not visible they are of similar or smaller size compared to the symbol. For the significance testing, the red line indicated LB media in different starting conditions, the black line denoted glucose-based medium in different starting conditions, whilst, the grey dotted line indicated glucose-based against LB medium (anaerobic) and the grey solid line compared glucose-based broth against LB broth (aerobic-to-anaerobic). Asterisks denote significance,  $*P \leq 0.05$ ,  $**P \leq 0.01$ ,  $***P \leq 0.001$  and  $****P \leq 0.0001$ . ..... 142
- Figure 4.13. Growth kinetics were recorded by sampling *P. aeruginosa* strain ATCC 9027 over 120 h and conducting bacterial viability calculations, using two media types, glucose-based and LB broth (incubation conditions; 37 °C; static). Starting cultures were preconditioned as either aerobic-to-anaerobic or anaerobic prior to inoculation ( $n = 3$ ). Where error bars are not visible they are of similar or smaller size compared to the symbol. For the significance analysis, the red line denoted LB medium in different starting conditions, the black line denoted glucose-based medium in different starting conditions, whilst, the grey dotted line indicated glucose-based broth against LB broth (anaerobic) and the grey solid line compared glucose-based broth against LB broth (aerobic-to-anaerobic). Asterisks denote significance,  $*P \leq 0.05$  and  $****P \leq 0.0001$ . ..... 144
- Figure 4.14. Pyocyanin quantification *via* LC-MS from *P. aeruginosa* strain ATCC 9027 over 120 h; utilising two media types, glucose-based and LB broth (incubation conditions; 37 °C; static). Starting cultures were either aerobic-to-anaerobic or anaerobic prior to inoculation ( $n = 3$ ). Where error bars are not visible they are of similar or smaller size compared to the symbol. For significance analysis, a red line represents LB medium in different starting conditions, whilst, a solid grey line compares glucose-based broth against LB broth (aerobic-to-anaerobic). Asterisks denote significance,  $*P \leq 0.05$  and  $***P \leq 0.001$ . ..... 145
- Figure 4.15. Biofilm quantification was determined using CVBA following *P. aeruginosa* strain ATCC 9027 incubation over 120 h in LB broth (deducting the sterile broth controls). Conditions replicated those selected for MFC experimentation (incubation conditions: static, LB broth, 37 °C, anaerobic) ( $n = 3$ ). Asterisks denote significance,  $**P \leq 0.01$ ,  $***P \leq 0.001$  and  $****P \leq 0.0001$ . ..... 146
- Figure 4.16. *Pseudomonas aeruginosa* strain ATCC 9027 growth after incubation for 24 h (37 °C, aerobic conditions) in the presence of varying nitrogen sources (standardised carbon source, sodium succinate) ( $n = 3$ ). Where error bars are not visible they are of similar or smaller size of the symbol. Asterisks denote significance,  $**P \leq 0.01$ ,  $***P \leq 0.001$  and  $****P \leq 0.0001$ . ..... 147

Figure 4.17. *Pseudomonas aeruginosa* strain ATCC 9027 growth after incubation for 24 h (37 °C, anaerobic conditions) in the presence of varying nitrogen sources (standardised carbon source, sodium succinate) ( $n = 3$ ). Asterisks denote significance,  $*P \leq 0.05$ ,  $**P \leq 0.01$ ,  $***P \leq 0.001$  and  $****P \leq 0.0001$ . ..... 148

Figure 5.1. The two-chambered, classical H-shaped MFC utilised in this study.  $K_3Fe(CN)_6$ ; Potassium hexacyanoferrate (III), KCl; Potassium chloride; CEM, Cationic Exchange Membrane, Polytetrafluoroethylene; PTFE..... 165

Figure 5.2. Custom made circuit board that was connected to an Arduino UNO board, in order to switch between open and closed (an external 10 k $\Omega$  resistor) circuit voltage every 30 min of the 120 h incubation period..... 166

Figure 5.3. Cell potential (V) measured from MFCs, which utilised three electrode types, 3D-Printed BM (8 wt.% graphene content), 3D-Printed PLA and carbon cloth with *P. aeruginosa* strain ATCC 9027 incubated in two types of media, LB and glucose-based broth ( $n = 3$ ). Where error bars are not visible they are of similar or smaller size compared to the symbol. For statistical analysis, only results between the 3D-Printed BM and carbon cloth electrodes were analysed, the black solid line denoted the different electrodes in glucose-based medium, the black dotted line denoted 3D-Printed BM in glucose-based broth against carbon cloth in LB broth, whilst, the red dotted line denoted 3D-Printed BM in LB broth against carbon cloth in glucose-based medium. Asterisks denote significance,  $*P \leq 0.05$ ,  $**P \leq 0.01$  and  $***P \leq 0.0001$ ..... 171

Figure 5.4. Growth kinetics of anaerobic *P. aeruginosa* strain ATCC 9027 during the MFC experiments (120 h) were determined in two media types, LB and glucose-based broth, *via* bacterial viability calculations. This was conducted in the presence of three electrode types, 3D-Printed BM (8 wt.% graphene content), 3D-Printed PLA and carbon cloth ( $n = 3$ ). Where error bars are not visible they are of similar or smaller size compared to the symbol. No statistical difference ( $*P > 0.05$ ) was observed between the bacterial growth kinetics and the MFC electrode or media type. .... 173

Figure 5.5. Current ( $\mu A$ ) calculated from the MFCs, which utilised three electrode types, 3D-Printed BM (8 wt.% graphene content), 3D-Printed PLA and carbon cloth utilising two types of media, LB and glucose-based broth ( $n = 3$ ). Where error bars are not visible they are of similar or smaller size compared to the symbol. For statistical analysis, only results between the 3D-Printed BM and carbon cloth electrodes were analysed, the grey solid line denoted the carbon cloth electrode in different media types (glucose-based and LB broth). Asterisks denote significance,  $**P \leq 0.01$ . ..... 175

Figure 5.6. Current density ( $\mu A m^{-2}$ ) calculated from the MFCs, which utilised three electrode types, 3D-Printed BM (8 wt.% graphene content), 3D-Printed PLA and carbon cloth utilising two types of media, LB and glucose-based broth ( $n = 3$ ). Where error bars are not visible they are of similar or smaller size compared to the symbol. For the statistical analysis, only results between the 3D-Printed BM and carbon cloth electrodes were analysed, the grey solid line denoted the carbon cloth electrode in different media types (glucose-based and LB broth). Asterisks denote significance,  $**P \leq 0.01$ ..... 177

Figure 5.7. Power ( $\mu W$ ) calculated from the MFCs, which utilised three electrode types, 3D-Printed BM (8 wt.% graphene content), 3D-Printed PLA and carbon cloth utilising two types of media, LB and glucose-

based broth ( $n = 3$ ). Where error bars are not visible they are of similar or smaller size compared to the symbol. For statistical analysis, only results between the 3D-Printed BM and carbon cloth electrodes were analysed, the black solid line denoted the different electrodes in glucose-based medium, whilst, the black dotted line denoted 3D-Printed BM in glucose-based against carbon cloth in LB broth. Asterisks denote significance,  $*P \leq 0.05$  and  $**P \leq 0.01$ . ..... 179

Figure 5.8. Power density ( $\mu\text{W m}^{-2}$ ) calculated from the *P. aeruginosa* strain ATCC 9027 MFCs, which utilised three electrode types, 3D-Printed BM (8 wt.% graphene content), 3D-Printed PLA and carbon cloth utilising two types of media, LB and glucose-based broth ( $n = 3$ ). Where error bars are not visible they are of similar or smaller size compared to the symbol. For statistical analysis, only results between the 3D-Printed BM and carbon cloth electrodes were analysed, the black solid line denoted the different electrodes in glucose-based medium, whilst, the black dotted line denoted 3D-Printed BM in glucose-based broth against carbon cloth in LB broth. Asterisks denote significance,  $*P \leq 0.05$  and  $**P \leq 0.01$ . ..... 181

Figure 5.9. Following MFC experiments (120 h incubation), electrodes and CEM were isolated and *P. aeruginosa* strain ATCC 9027 was visualised using SEM (5.00 K  $\times$  magnification). A) 3D-Printed BM anode incubation in LB broth, B) 3D-Printed BM cathode (no bacteria present), C) CEM in LB broth (surface from the anodic compartment visualised), D) 3D-Printed PLA anode incubation in LB broth, E) 3D-Printed BM anode incubation in glucose-based medium and F) CEM in glucose-based broth (surface from the anodic compartment visualised). ..... 183

Figure 5.10. Following 120 h of *P. aeruginosa* strain ATCC 9027 incubation in anaerobic LB medium, bacterial attachment to the surface of the 3D-Printed BM anode was visualised using 0.1 % acridine orange (in 2 % v/v glacial acetic acid) via confocal microscopy. A) Horizontal view B) Cross sectional view. .... 185

# Abbreviations

Description	Identifier
Acrylonitrile-Butadiene-Styrene	ABS
Adenosine Triphosphate	ATP
Applied Voltammetric scan rate	$v$
Average Roughness	$S_a$
Basal Plane Contributions	$C_b^0$
Basal Plane Pyrolytic Graphite	BPPG
Black Magic	BM
Carbon Nanotubes	CNTs
Chemical Oxygen Demand	COD
Clustering	$\Delta f(\alpha)$
Colony Forming Units per mL	CFU mL <sup>-1</sup>
Concentration of the redox probe	C
Contact Angles	$\vartheta$
Crystal Violet Biofilm Assay	CVBA
Density	$D_0$
Density Functional Theory	DFT
Diffusion Coefficient	$D$
Dispersion	$\Delta\alpha$
Edge Plane Contributions	$C_e^0$
Edge Plane Pyrolytic Graphite	EPPG
Electrochemical Effective Area	$A_{eff}$
Electrochemical Real Area	$A_{real}$
Electrostatic Potential Map	ESP
Energy-Dispersive X-ray Microanalysis	EDX
Extracellular Polymeric Substances	EPS
Faraday Constant	$F$
Fraction of Edge Planes on the Electrode Surface	$f_e$
Geometrical (Theoretical) Area Of The Electrode	$A_{Geo}$
Gibbs Free Energy	$\Delta G$
Glassy Carbon Electrode	GCE
Heterogeneous Electron Transfer	HET
Heterogeneous Electron Transfer (HET) Rate Constant	$k^0$
High Crystalline Natural	HCN
High performance liquid chromatography	HPLC

Highest Occupied Molecular Orbital	HOMO
Highest Peak	$S_p$
Highly Ordered Pyrolytic Graphite	HOPG
Hydrogen Evolution Reaction	HER
Interfacial free energy	$\Delta G_{iwi}$
Internal Resistance	$R_{in}$
Interplanar Microcrystalline Size	$L_c$
Intraplanar Microcrystalline Size	$L_a$
Kinetic Parameter	$\psi$
Lewis Acid-Base (AB) Forces	$\gamma_s^{AB}$
Lifshitz-van der Waals Forces	$\gamma_s^{LW}$
Liquid Chromatography - Mass Spectroscopy	LC-MS
Lowest Unoccupied Molecular Orbital	LUMO
Lowest Valley	$S_v$
Luria-Bertani	LB
Microbial Adhesion To Hydrocarbons	MATH
Microbial Fuel Cells	MFCs
Molecular Orbital	MO
Multifractal Analysis	MFA
Multiwall Carbon Nanotubes	MWCNTs
Nanostructured graphite – 250	NSG
Nicotinamide Adenine Dinucleotide	NAD
Nicotinamide Adenine Dinucleotide + Hydrogen	NADH
Nicotinamide Adenine Dinucleotide Phosphate	NADPH
Normalised Energy Recovery	NER
Number of electrons involved in the electrochemical process	$n$
Optical Density	OD
Oxygen Reduction Reaction	ORR
Peak-To-Peak Separation	$\Delta E_p$
Peak-To-Valley Ratio	$S_{pv}$
Phosphate Buffer Solution	PBS
Poly(lactic Acid)	PLA
Proton Exchange Membrane	PEM
Pseudomonas quinolone signal	PQS
Redox Potential	$E_h$
Saturated Calomel Electrode	SCE
Scanning Electron Microscope-Energy-Dispersive X-ray Microanalysis	SEM-EDX
Scanning Electron Microscopy	SEM

Screen Printed Electrode	SPE
Sediment Microbial Fuel Cell	SMFC
Single-Wall Carbon Nanotubes	SWCNTs
Surface Energy	$\gamma_s^{SE}$
Temperature	$T$
Three-Dimensional	3D
Total Specific Capacitance	$C^0$
Transmission Electron Microscopy	TEM
Tricarboxylic Acid Cycle	TCA
Tryptone Soya Agar	TSA
Tryptone Soya Broth	TSB
Two-Dimensional	2D
Universal Gas Constant	$R$

# **Chapter 1 – Introduction to Microbial Fuel Cells (MFCs)**

## 1.1 Renewable Energy

Generation, storage and consumption of energy are topics that are increasingly prevalent within modern research fields and are of global interest/importance. Fossil fuels were used as the energy supply for 85 % of the total global energy consumption during 2014, whilst in 2013, renewable energy sources supplied only 2.7 % of the global energy consumed (Wilcox, 2014). The environmental issues faced due to anthropogenic climate-change are often attributed to this worldwide over-reliance on fossil fuels and consequently have produced a requirement to find feasible alternatives of energy generation, with particular focus on developing renewable energy resources (Brownson *et al.*, 2012b).

Research into alternative renewable energy generation sources is increasing rapidly, with research showing promising results in an abundance of areas including, solar (Granqvist, 2007), wind (Herbert *et al.*, 2007), tidal (Antonio, 2010), geothermal (Lund *et al.*, 2011) and biomass energy generation (Figure 1.1) (Berndes *et al.*, 2003; Panwar *et al.*, 2011). Currently, no individual renewable energy source has the ability to compete with and replace the conventional fossil-fuel based energy generation approach (Figure 1.1). However, combining renewable energy sources such as solar-wind hybrids and/or solar-hydrogen fuel cells may provide alternative routes to clean energy generation (Khare *et al.*, 2016; Yilanci *et al.*, 2009).

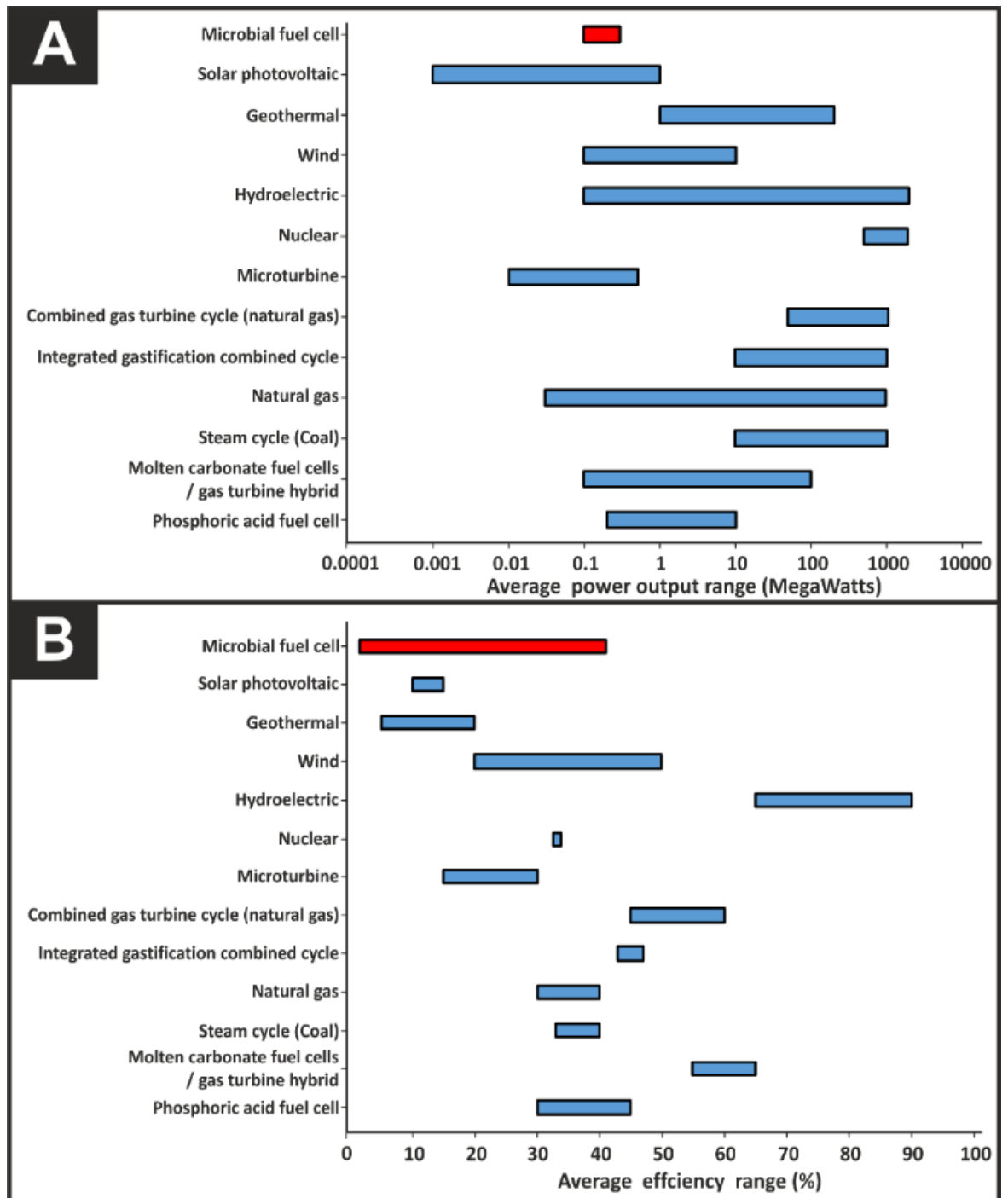


Figure 1.1. A) Average power outputs of a range of fuel technologies, including both traditional energy sources (*i.e.* coal and natural gas) and alternative/renewable energy sources. B) The average efficiency range of traditional and alternative/renewable fuel sources. Data obtained from (Janicek *et al.*, 2014; Sharaf and Orhan, 2014; Shoener *et al.*, 2014; Sun *et al.*, 2016b; Ter Heijne *et al.*, 2011).

## 1.2 Overview of Microbial Fuel cells

One potential alternative energy source is the utilisation of microbial fuel cells (MFCs). Microbial fuel cells follow a similar concept to that of traditional fuel cells. However, they utilise the bio-catalytic capabilities of viable microorganisms. This allows MFCs to use a range of organic fuel sources, by converting the energy stored in the chemical bonds, to generate an electrical current, instead of relying for example, on the use of metal catalysts (Du *et al.*, 2007).

Microorganisms, such as bacteria, can generate electricity by liberating electrons from organic matter, whilst also accomplishing biodegradation and therefore treatment of biodegradable products, such as municipal wastewater (Du *et al.*, 2007; Habermann and Pommer, 1991). It is clear throughout the literature that significant attention has been afforded to MFCs due to their ambient operating conditions (*e.g.* low temperatures) and a variety of biodegradable substrates as the fuel source. This thesis aimed to combine MFC technology with additive manufacturing techniques to fabricate low cost, graphene-based 3D-Printed electrodes, whilst also optimising parameters (such as the growth medium) involved with bacterial proliferation, in order to enhance the performance of MFCs. The introduction to this thesis has previously been published as part of a review in an internationally renowned, peer-reviewed journal (Slate *et al.*, 2019b).

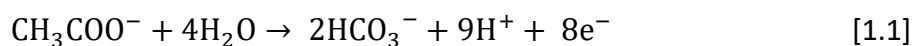
### 1.2.1 History of MFCs

The first recorded occurrence of electrochemical activity between microorganisms and electrodes can be traced back to the early 20th century. This was reported by Potter, who demonstrated electricity production from live cultures of *Escherichia coli* and *Saccharomyces* spp., using platinum macro-electrodes in a battery-type setup with sterile media (Potter, 1911). This was later confirmed by Cohen, in 1931, who reported a voltage of 35 V at a current of 0.2 mA from a stacked bacterial fuel cell system (Cohen, 1931). Although these publications are often referred to as the origin of electromicrobiology, it was not until 1963 when a National Aeronautics and Space Administration (NASA) space program demonstrated the opportunity to recycle and convert human waste into electricity, during space expeditions (Canfield *et al.*, 1963; Guo *et al.*, 2012; Schröder, 2011).

In 1990, pioneering work from Habberman and Pommer reported the first long-term MFC. In this study, the MFC in question was used in continuous service for 5 years (from 1986) using municipal wastewater as the fuel source. Furthermore, this MFC ran continuously for the five year study without malfunction or maintenance (Habermann and Pommer, 1991). This study also for the first time reported indirect electron transfer (a mechanism of electron transfer, which allows specific bacteria to donate electrons) *via* soluble mediators, in this case sulphate/sulphide (Habermann and Pommer, 1991). This study was also the first time that the treatment of domestic wastewater was reported (Habermann and Pommer, 1991; Rabaey and Verstraete, 2005). In 1999, it was demonstrated that mediators were not an essential component within MFC configurations and this allowed MFCs to be developed without the need for expensive mediators (Kim *et al.*, 1999a; Kim *et al.*, 1999b; Nader *et al.*, 2012). Redox mediators are small molecular weight compounds that are oxidised by specific bacterial enzymes and are simultaneously reduced by the substrate continuously resulting in electron transfer (Rabaey, K. & Verstraete, W, 2005; Lovley, 2006b). Following this discovery, there was a significant increase in interest within the field of electromicrobiology research. This field now boasts over a thousand energy generation MFCs reported throughout the literature, with the first commercial prototypes expected in the near future (ElMekawy *et al.*, 2018; Pant *et al.*, 2010b).

### **1.2.2 Fundamental Bioelectricity Generation in MFCs**

The development of an electrical potential, due to bacterial metabolic activity in the anodic compartment (*i.e.* reduction reactions, generating both electrons and protons), and electron acceptor conditions in the cathode (which are often separated by a membrane), results in the generation of bio-electricity in MFCs (Rahimnejad *et al.*, 2015; Rahimnejad *et al.*, 2011). In the anodic compartment, the electrochemically-active microorganisms can attach to, or produce electron shuttles, that can donate electrons to an anode, which are liberated by oxidising organic/inorganic waste (*e.g.* the fuel), thus producing a source of energy (Du *et al.*, 2007). One example of an oxidation reaction that takes place by electrochemically-active bacteria in the anodic compartment, where acetate is the fuel source can be summarised as (Logan *et al.*, 2006):



Electrochemically-active microorganisms capable of donating electrons have been previously defined by Logan as exoelectrogens (Logan and Regan, 2006). Other synonyms used throughout the literature include, anode respiring bacteria (Moon *et al.*, 2004), electrochemically active bacteria (Manish and Banerjee, 2008; Min *et al.*, 2005) and electricigens (Logan, 2004; Parkash, 2016). Microorganisms capable of accepting electrons have been defined as exoelectrotrophs (Kumar *et al.*, 2016; Regan *et al.*, 2015).

In the anode, protons produced *via* the electrochemically-active bacteria diffuse through a half-cell separator (*e.g.* proton exchange membrane (PEM)) into the cathodic compartment. In the cathodic compartment, oxygen is primarily used as the oxidant, due to its abundance and high reduction potential (Rismani-Yazdi *et al.*, 2008; Zhao *et al.*, 2006). However, the oxygen reduction reaction (ORR), remains one of the contributing bottleneck factors which inhibits MFC optimisation (Rismani-Yazdi *et al.*, 2008; Santoro *et al.*, 2017). The application of metal oxidants as electron acceptors in the cathodic compartment of a MFC is one alternative method to avoid the bottleneck issue associated with the ORR. Metal oxidants that have been trailed previously include, copper, cadmium and chromium (Heijne *et al.*, 2010; Li *et al.*, 2015; Nancharaiah *et al.*, 2015; Ntagia *et al.*, 2016; Santoro *et al.*, 2017; Wang *et al.*, 2015a). Once the protons have diffused through the PEM into the cathode they can combine with oxygen present, leading to the generation of water *via* the following ORR, which can be summarised as (Erable *et al.*, 2012; Oh and Logan, 2006):



The majority of MFC configurations are utilised as anaerobic devices (especially in the anodic compartment). This is due to the anaerobic conditions required by bacterial species currently seen as the model microorganisms in regards to electron transfer properties *e.g.* *Geobacter sulfurreducens* (Pant *et al.*, 2010b). However, bacteria capable of electron transfer in aerobic conditions have been demonstrated, with one example being *Escherichia coli* (K12 HB101) (Zhang *et al.*, 2008). To date, examples of fuel sources utilised within MFCs include wastewater, marine sediment soil, freshwater sediment, soil and activated sludge (Niessen *et al.*, 2004; Zhang *et al.*, 2006).

Bacteria in such systems are able to produce electrons by oxidising substrates, which are isolated in the anodic compartment. These electrons flow from the anode to the cathode (positive terminal) *via* an external circuit. This leads to the production of electricity due to the difference in potential coupled to the electron flow (Liu *et al.*, 2004; Logan *et al.*, 2006). Protons that are produced at the anode are able to migrate through the solution and across the PEM (Liu *et al.*, 2005). PEMs are the most frequently used separators in MFCs due to their desirable properties for example, selective permeability to protons, high conductivity to cations, low internal resistance and the ability to undergo long periods of inactivity without producing a detrimental effect on the MFC (Kim *et al.*, 2007a; Kim *et al.*, 2007b; Rowley-Neale *et al.*, 2016b). Once at the cathode, the electrons are able to combine with both protons and oxygen to form water.

Currently, the maximum power densities that microorganisms are theorised to be capable of producing are yet to be achieved. Theoretically, an *E. coli* cell that replicates twice every hour with a volume of  $0.491 \mu\text{m}^3$  has the potential to produce *ca.*  $16,000 \text{ kW m}^{-3}$  (Logan, 2009). A voltage of between 0.3 V and 0.5 V is usually obtained when using energy sources (fuels) such as glucose and acetic acid. However, this is dependent on the energy gain by the bacteria and the loss of energy at the cathode (Logan, 2009). The current produced from a MFC is dependent on the rate of substrate biodegradation. However, the maximum theoretical cell voltage, which is also known as the electromotive force, is dependent on Gibbs free energy ( $\Delta G$ ) which is defined as the thermodynamic quantity equal to the enthalpy change ( $\Delta H$ ) of a system, minus the temperature (T) and entropy change ( $\Delta S$ ) of the overall reaction (Capodaglio *et al.*, 2013).

Thus far, most modern MFC technologies utilise wastewater as the primary fuel source by recovering energy *via* the biodegradation of organic-rich waste (Du *et al.*, 2007). It has been suggested that the ability to produce electricity from wastewater could play a pivotal role in the production of renewable energy. In 2012, it was reported that 5 % of the USA's total energy consumption was used to facilitate water and wastewater treatment facilities (Mustakeem, 2015). For the adequate treatment of wastewater, relevant standards and regulations must be met, thus far the effluent quality of MFC treated wastewater is yet to adhere to such standards (Dong *et al.*, 2015). In light of this, additional steps for example, MFCs integrated with membrane technology and/or conventional treatment technology (*i.e.* sterilisation step post MFC stage) may also be required (Dong *et*

*al.*, 2015; Wang *et al.*, 2015b; Zhang *et al.*, 2009). The potential to incorporate MFCs into wastewater treatment offers a significant advantage over other renewable energy sources. Furthermore, MFCs are less dependent upon geographical location and seasonal change when compared to solar and wind power (Rabaey and Verstraete, 2005). In 2016, Ye *et al.* demonstrated a sediment MFC which was capable of producing power output in a range of temperatures (4 °C - 35 °C) (Ye *et al.*, 2016). Interestingly MFCs have been shown to generate hydrogen from the fermentation of sugar present in wastewater, which in turn can be utilised as a fuel source for other renewable energy sources (Logan, 2004).

### **1.2.2.1 Biofilm Formation**

Bacterial biofilms are formed by communities that are embedded in a self-produced matrix of extracellular polymeric substances (EPS) which are attached to a surface (both inert or living surfaces) (Flemming *et al.*, 2016). It is thought that most bacteria exist in a biofilm state, in order to enhance survival and propagation. In multispecies biofilms the metabolic by-products of one species may support the growth of another, or adhesion of one species may provide ligands to which other species can then adhere (Dunne, 2002; López *et al.*, 2010). Biofilms have been shown to confer greater bacterial resistance to antimicrobial agents (including antibiotics) when compared to planktonic derivatives (Macia *et al.*, 2014). Briefly, biofilm formation consists of reversible and irreversible attachment and adhesion, maturation (this includes biofilm scaffold production due to the secretion of proteins, DNA, and EPS) and finally dispersal (Rabin *et al.*, 2015; Slate *et al.*, 2019b). *Pseudomonas aeruginosa* biofilms have demonstrated conductive properties, due to both direct and indirect electron transfer (Jia *et al.*, 2017).

### **1.2.3 Structural Configurations**

The structural configurations of MFCs vary considerably, ranging from single and two-chamber configurations, with or without the utilisation of membranes such as a PEM (Chae *et al.*, 2009; Liu *et al.*, 2005; Pant *et al.*, 2010a). A typical MFC configuration comprises of two-chambers, an anodic and cathodic chamber, which are connected by a half-cell separator (Figure 1.2). The most common separators include PEMs, salt bridges and ceramics (Oh and Logan, 2006; Ortiz-Martínez *et al.*, 2016; Parkash *et al.*, 2015). Such a

configuration enables generated protons to move freely to the cathode due to the production of a potential gradient, whilst inhibiting the diffusion of oxygen (or the electrode acceptor utilised in the cathode) to the anode, where it could have a potential detrimental effect on the microorganisms present.

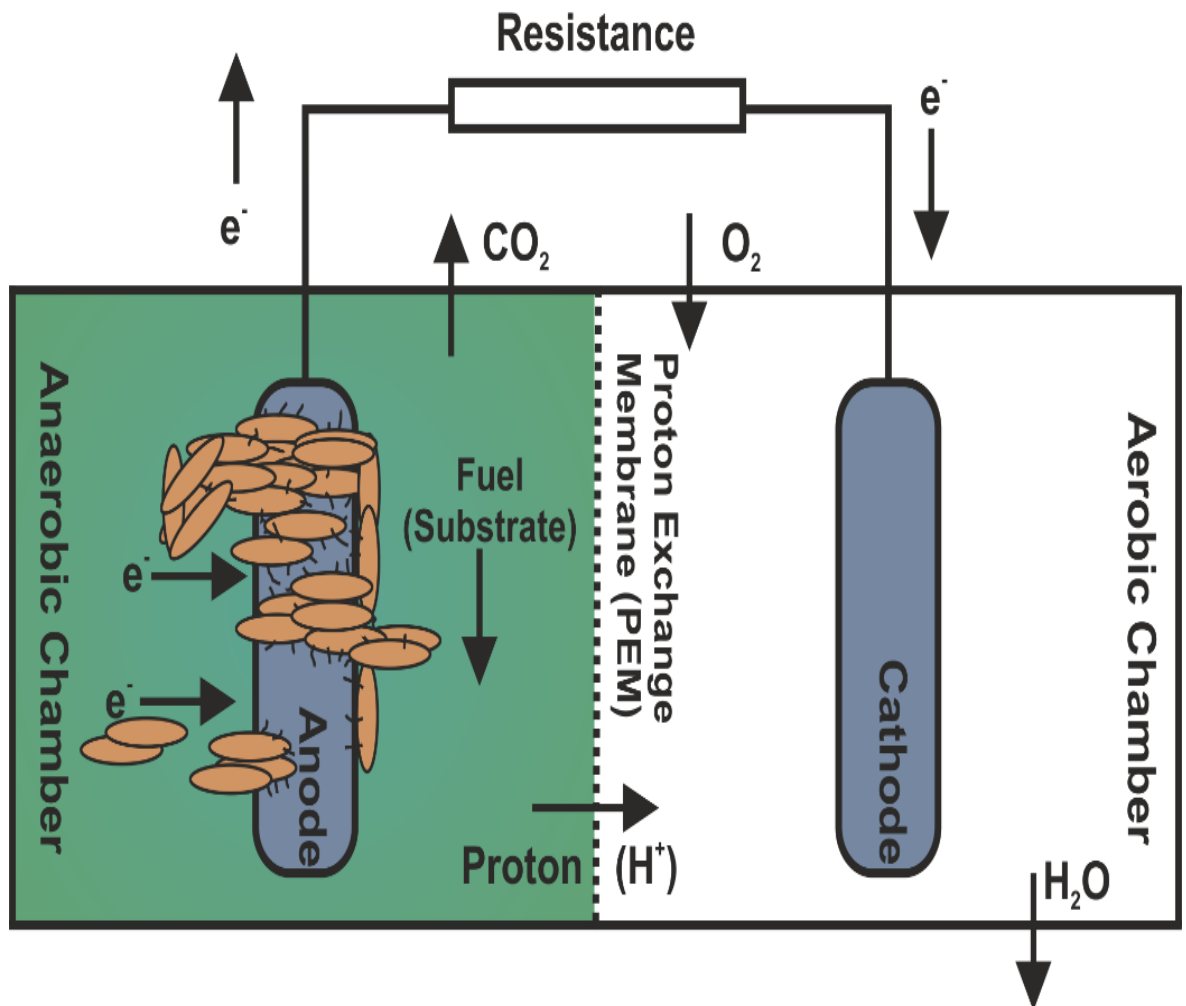


Figure 1.2. Schematic of a typically employed two-chamber microbial fuel cell highlighting the various electrochemical and electro-microbiological processes. Figure adapted from (Du *et al.*, 2007).

The structural design of MFCs and their compartments can vary in order to optimise and enhance power outputs. Two-compartment MFCs are often used in laboratories, typically with a defined medium as the anolyte (*i.e.* glucose/acetate) and run in batch mode (Du *et al.*, 2007). MFC's can also be run in a continuous mode, which is carried out to optimise long term MFC power outputs (Du *et al.*, 2007). Two-compartment MFCs are operated in a multitude of configurations which include, conventional rectangular shaped MFCs (Du *et al.*, 2007; Myung *et al.*, 2018; Wu *et al.*, 2018), cylindrical shaped MFCs

(Ghasemi *et al.*, 2011; Jana *et al.*, 2010; Mohanakrishna *et al.*, 2018; Winfield *et al.*, 2013a), miniature MFCs (Choi and Chae, 2012; Qian and Morse, 2011; Ren *et al.*, 2015), up-flow mode configurations (He *et al.*, 2005; Jayashree *et al.*, 2016) and flat plate MFCs (Kazemi *et al.*, 2015; Min and Logan, 2004).

Miniature MFCs receive a considerable amount of attention in both fundamental and applied studies, due to their intrinsic advantages such as being able to generate electricity at the millilitre to microlitre scale (Qian and Morse, 2011). Mink *et al.*, (2014) utilised a miniaturised MFC with a graphene anode and an air cathode, with a working volume of 25  $\mu\text{L}$ , where human saliva was used as the fuel source (Mink *et al.*, 2014). This configuration produced a maximum current density ( $1190 \text{ A m}^{-3}$ ), which was higher than any previous miniaturised MFC which utilised an air-cathode (Mink *et al.*, 2014). Interestingly, the graphene anode utilised, resulted in a 40 times increase in power when compared to the conventional carbon cloth control (Mink *et al.*, 2014). These findings could potentially result in saliva-powered appliances which utilise MFC technology for both Lab-on-a-Chip and point-of-care diagnostic devices (Mink *et al.*, 2014). Miniature MFCs also have the potential to be optimised as power sources in long-term underwater or littoral autonomous sensors, as the MFCs could scavenge nutrients from the surrounding environment allowing the exoelectrogenic biofilm at the anode to be sustained (Biffinger *et al.*, 2007; Du *et al.*, 2007).

Up-flow mode MFCs have received attention, due to their suitability for application in wastewater treatment and their relative ease in scale-up to industrially-relevant magnitudes (Du *et al.*, 2007). The flat plate MFC was developed by Min and Logan (2014) to replicate traditional parameters found in hydrogen fuel cells, where the electrodes were usually combined in a single strip and separated by a PEM. This configuration allowed the electrodes to be kept in close proximity, thus enhancing proton conduction (Min and Logan, 2004). However, in the case of MFCs, PEMs (with one example being Nafion<sup>®</sup>) are often permeable to oxygen, which can have a detrimental effect on obligate anaerobes if utilised within the anodic compartment (Min and Logan, 2004). This prototype was evaluated in order to see if the design was more beneficial than the risk of oxygen permeation to the anode (Min and Logan, 2004). The results from this configuration demonstrated a maximum power density of  $72 \text{ mW m}^{-2}$  when domestic wastewater was the fuel source.

This resulted in a 2.8 times increase in power output when compared to a single-chambered MFC configuration (Min and Logan, 2004).

Sediment microbial fuel cells (SMFCs) have been explored intensively as an alternative energy generation source from natural sediments, with recent focus in particular on the application of SMFCs within wastewater treatment (Xu *et al.*, 2015). SMFCs generate an electrical current from the organic constituents of sediment *via* bacterial metabolism. SMFCs differ to other MFCs due to their essentially complete anoxic environment ( $< 0.5 \text{ mg/L O}_2$ ) at the anode and their membrane-less structure, where the sediment/water interface acts as the membrane (Dumas *et al.*, 2007; Zabihallahpoor *et al.*, 2015). However, due to their reported limitations such as large internal resistance and issues arising when scaling up, such setups are believed to be unlikely to generate sufficient electricity to compete with other energy sources (Ewing *et al.*, 2014; Xu *et al.*, 2015).

Due to their complex structural designs, two-chambered MFC configurations are difficult to scale up, thus they are often used primarily for laboratory based studies (Du *et al.*, 2007). However, single chambered configurations offer much simpler designs and eliminate the need for a cathodic chamber, as the cathode is often exposed directly to the air (Du *et al.*, 2007). This can greatly reduce the cost of a MFC configuration, due to the lack of cathodic compartment and electron acceptors. Furthermore, passive oxygen transfer does not require air sparging of the catholyte which results in lowered setup costs (Liu and Logan, 2004). In single chambered MFCs, the protons produced (in the anodic compartment) are transferred to the porous air cathode (Liu and Logan, 2004). The first documented single chambered MFC was developed by Park and Zeikus, (2003). This configuration comprised a rubber bunged bottle with an anode inserted into the centre, coupled with a window-mounted cathode, which contained an internal proton-permeable porcelain layer (Park and Zeikus, 2003). When sewage sludge was used as the fuel source, a maximum power density of  $788 \text{ mW m}^{-2}$  was obtained (Park and Zeikus, 2003).

In order to scale up MFC technologies to an industrially-relevant level, it has been demonstrated that a miniaturisation and multiplication approach is a viable route to enhance power outputs, as opposed to merely increasing the size of the reactor (Ieropoulos *et al.*, 2013; Ledezma *et al.*, 2013; Melhuish *et al.*, 2006; Papaharalabos *et al.*, 2013). One approach to scale up MFCs has led to the development of stacked MFCs, which allow multiple, individual MFCs to be connected either in series or parallel, enhancing overall

power outputs (Aelterman *et al.*, 2006). One example of a stacked MFC was demonstrated by Aelterman *et al.* (2006) in this study, six individual continuous MFCs were connected, producing a maximum hourly average of  $258 \text{ W m}^{-3}$  whilst utilising a hexacyanoferrate catholyte and identical graphite granule electrodes (type00514, diameter between 1.5 mm and 5 mm, Le Carbone, Belgium) (Aelterman *et al.*, 2006). One issue that has been identified with stacked MFCs is charge reversal which can result in a reverse in polarity for one or more of the connected cells, resulting in a reduction in power outputs (Oh and Logan, 2007). Voltage reversal is when one (or more) of the stacked cells experiences a more extreme condition when compared to the others. More specifically, this phenomenon may occur when excessive current is drawn from the MFC at a higher rate than its fuel delivery can support (Oh and Logan, 2007). This subsequently results in an increase in the anode potential and therefore voltage reversal (Aelterman *et al.*, 2006; Oh and Logan, 2007). Other conditions that can result in role reversal include, impedance differences, lack of a catalyst, insufficient fuel and lack of oxygen at the cathode (Oh and Logan, 2007). These issues can be overcome by short-circuiting a cell demonstrating voltage reversal. Researchers have previously used diodes connected in parallel to a hydrogen fuel cell, which can automatically short circuit defective cells (Oh and Logan, 2007).

#### **1.2.4 Limiting Factors**

Currently the limiting factors associated with MFCs are reported to be low energy outputs, limited life spans and high-associated costs (most notably due to available electrode materials and PEMs). The key intrinsic factor currently limiting the overall power output of MFC technologies is the electron transfer rate to the anode and the electrochemical properties of the electrode material (Deng *et al.*, 2010a). The PEM has been demonstrated to be the main source of internal resistance ( $R_{in}$ ) (Min *et al.*, 2005; Rahimnejad *et al.*, 2015; Sharma and Li, 2010). Due to the limiting factors, MFCs are unable to attain their theorised power outputs, and currently scale up and implementation of MFC technology into industry is unfeasible. The efficiency and performance of a MFC can be effected by a vast array of factors, which include biofouling (leading to electrode surface blockage and ultimately a reduction in surface area), catalyst inactivation (if applicable) and

excessive biofilm growth, which may lead to the production of non-conductive debris (Figure 1.3) (Sun *et al.*, 2016b).

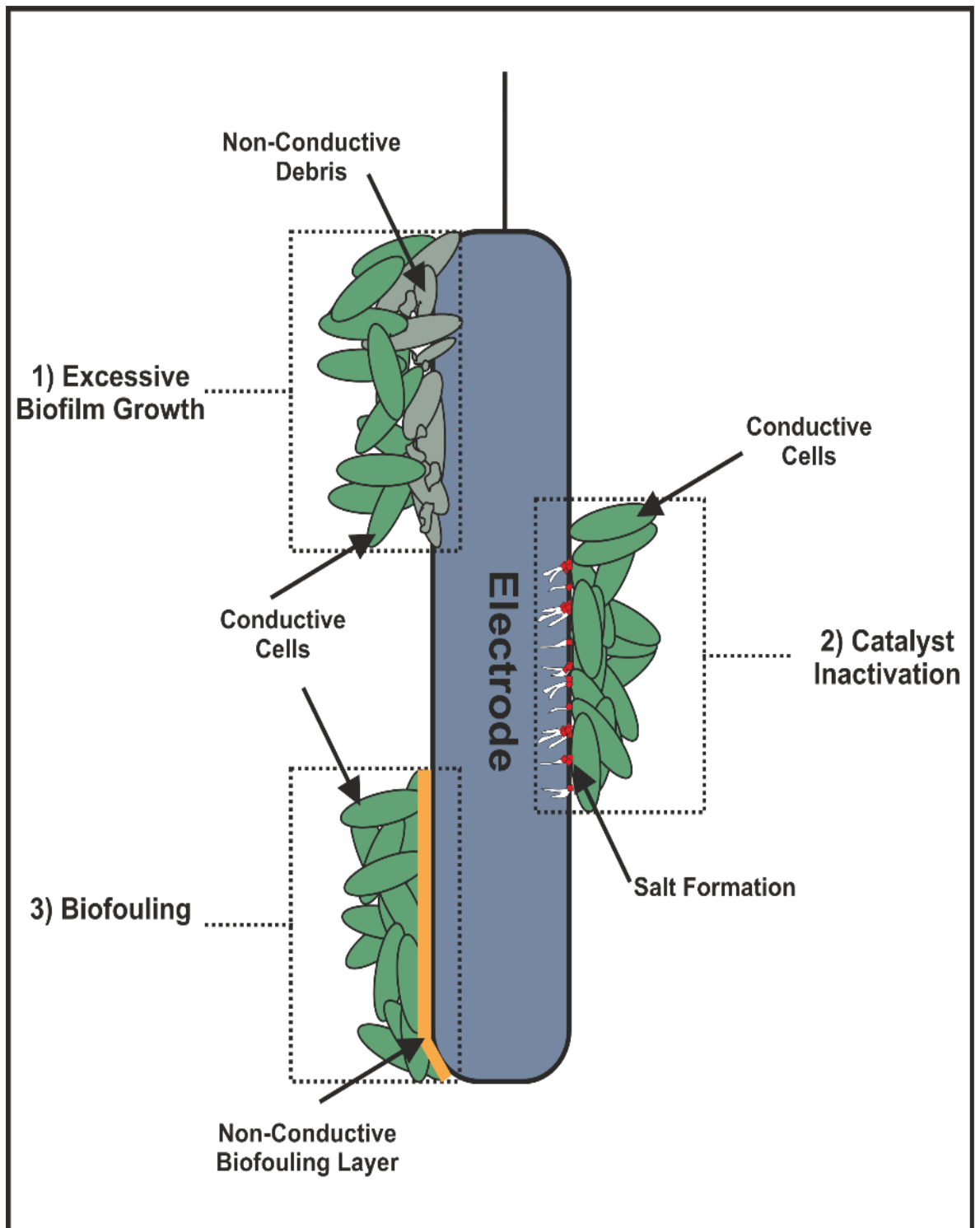


Figure 1.3. A number of ways in which the performance of MFC technologies can deteriorate. Examples here include biofouling (electrode blockage), inactivation of catalysts and excessive growth of bacterial biofilms leading to the production of non-conductive debris. Figure adapted from Sun *et al.*, 2016b.

The production of non-conductive debris such as polymeric substances (and dead cells), can isolate the electrochemically active biofilm from the electrode surface, or with more porous electrodes become entrapped in the 3D architecture, leading to a potential reduction in available surface area and therefore a reduction in power generation (Blanchet *et al.*, 2016; Islam *et al.*, 2016; Sun *et al.*, 2016b). Other factors that may possess a detrimental effect on the efficacy and power outputs of MFCs include the inactivation of electro-catalysts (if present) and the crossover of organic compounds or electron acceptors from the anode to the cathode (and *vice versa*). The latter of which can disrupt biofilm growth due to the flow of internal currents and mixed potentials (Harnisch *et al.*, 2009; Winfield *et al.*, 2013b).

### **1.2.5 Optimisation of MFC Power Outputs**

Before MFCs can be applied to industrially-relevant scenarios, power generation and efficiency of current MFCs must be enhanced. One option to enhance the power generation and efficacy of MFC configurations is the utilisation of biocathodes. Biocathodes, which are microorganisms, can replace traditional (often expensive and exhaustive) catalysts/electron acceptors in the cathodic compartment (He and Angenent, 2006). Aerobic and anaerobic biocathodes have been demonstrated, and the selection of these is of paramount importance depending on the terminal electron acceptor utilised in the cathodic compartment. An example of an aerobic biocathode is *Thiobacillus ferrooxidans*, as this bacterium regenerates ferric ions whilst, an example of an anaerobic biocathode is *Geobacter metallireducens*, which oxidises ammonia and reduces nitrate, leading to denitrification in MFCs (He and Angenent, 2006). Thus it has been suggested that the power output obtained *via* MFC technologies can be improved by a multitude of mechanisms (Table 1.1):

Table 1.1. Possible mechanisms by which to improve the power output.

Mechanism	References
Architectural design of the MFC setup	(Janicek <i>et al.</i> , 2014)
Alternative electrode material selection	(Rinaldi <i>et al.</i> , 2008)
Improvement of the cathode	(Deng <i>et al.</i> , 2010b)
Electrode proximity (reduce ohmic resistance)	(Ahn <i>et al.</i> , 2014)
Solution selection (increased conductivity)	(Lefebvre <i>et al.</i> , 2012)
Substrate addition	(Pant <i>et al.</i> , 2010b)
Enhancement of fuel source	(Kim <i>et al.</i> , 2000; Yang <i>et al.</i> , 2017)
Introduction of a magnetic field	(Yin <i>et al.</i> , 2013; Zhao <i>et al.</i> , 2016)

## 1.3 Electrode Materials

One area that could potentially elevate MFC power outputs to their proposed theoretical outputs is the use of alternative, more effective electrode materials. For a material to be considered effective as an electrode it must have a number of properties, which include, beneficial electrochemical properties (*i.e.* favourable electron transfer), mechanical stability, low cost fabrication and comprise of a large surface area, which in turn gives rise to large current densities. The electrode material is a major constituent of a MFC, determining both the overall cost and performance (Liu *et al.*, 2016). A key area in electrochemical research is to develop alternatives to platinum-based electrodes, due to inadequate supply and cost (Yang, 2009). Furthermore, platinum may not be deemed a suitable electrode material in MFCs due to its reported antimicrobial properties, as platinum produces cisplatin during electrolysis (Rosenberg *et al.*, 1965). In light of this, carbon materials and non-corrosive metals are currently the most widely used base materials for electrodes in MFC configurations (Wei *et al.*, 2011).

### 1.3.1 Electrode Topography

MFC electrodes not only function as conductors, as in traditional fuel cells but the anode material must also act as a viable support for bacterial biofilms and therefore must be biocompatible. Furthermore, a high surface area with a relatively rough surface is thought to enhance bacterial attachment and retention (Wei *et al.*, 2011). Walter *et al.* (2016) demonstrated that increasing the total anodic surface area, within a fixed volume

chamber resulted in an increase in volumetric power density of the MFC (Walter *et al.*, 2016). Ye *et al.* (2012) demonstrated that a relatively rougher surface of glassy carbon plates produced higher power densities. It has been suggested that the utilisation of additive manufacturing (three-dimensional (3D) printing) for the fabrication of electrodes could result in complex architectural designs with high surface areas coupled with beneficial electrochemical properties (Bian *et al.*, 2018).

### 1.3.2 Carbon Based Electrodes

The use of carbon-based electrodes has long been established and this has led to the production of vast amounts of analytical and industrial applications, due to the high heterogeneous electron transfer kinetic rate of carbon (Slate *et al.*, 2018a). As microbial growth on the surface of metal anodes can accelerate the corrosion of metals in aqueous solutions and produce a detrimental antimicrobial effect, carbon-based electrodes are currently the material of choice for application within MFCs (Zhou *et al.*, 2011). A variety of carbon-based electrode materials have been tested within MFC setups and these include graphite rods (Liu *et al.*, 2005), carbon felts (Kim *et al.*, 2002), carbon cloths (Wei *et al.*, 2011) and carbon meshes (Hays *et al.*, 2011).

Carbon cloth has traditionally been the primary electrode material of choice for use within MFCs due to reported high conductivity, stability, wide commercial availability and relatively low cost, in comparison with other carbon-based electrode materials (Liu and Logan, 2004; Liu *et al.*, 2012). Another popular material is graphite, which has exceptional electrochemical properties. In one study, an increase in the surface area of graphite, which was available for microbial colonisation, resulted in an increase in power output (Chaudhuri and Lovley, 2003). A two-chambered MFC was prepared, using a pure culture of *Rhodospirillum rubrum* (anaerobic conditions for the anodic compartment) with added glucose (10 mM) to act as an electron donor (Chaudhuri and Lovley, 2003). Graphite felt electrodes, with an increased surface area, were compared against graphite rods and it was demonstrated that a threefold increase in current was produced (0.57 mA; 620 mV) (Chaudhuri and Lovley, 2003). This study also compared porous graphite foam electrodes against the graphite rods and it was demonstrated that even though the geometric surface area was the same, the porous graphite foam produced a 2.4 fold increase in current (74

$\text{mA m}^{-2}$ ; 445 mV), which was attributed to the higher concentrations of cells able to colonise the graphite foam (Chaudhuri and Lovley, 2003). The biocompatibility of graphite has previously been evaluated; an *E. coli* biofilm demonstrated abundant adherence and biofilm formation in the presence of a carbon-paste graphite electrode (Figure 1.4).

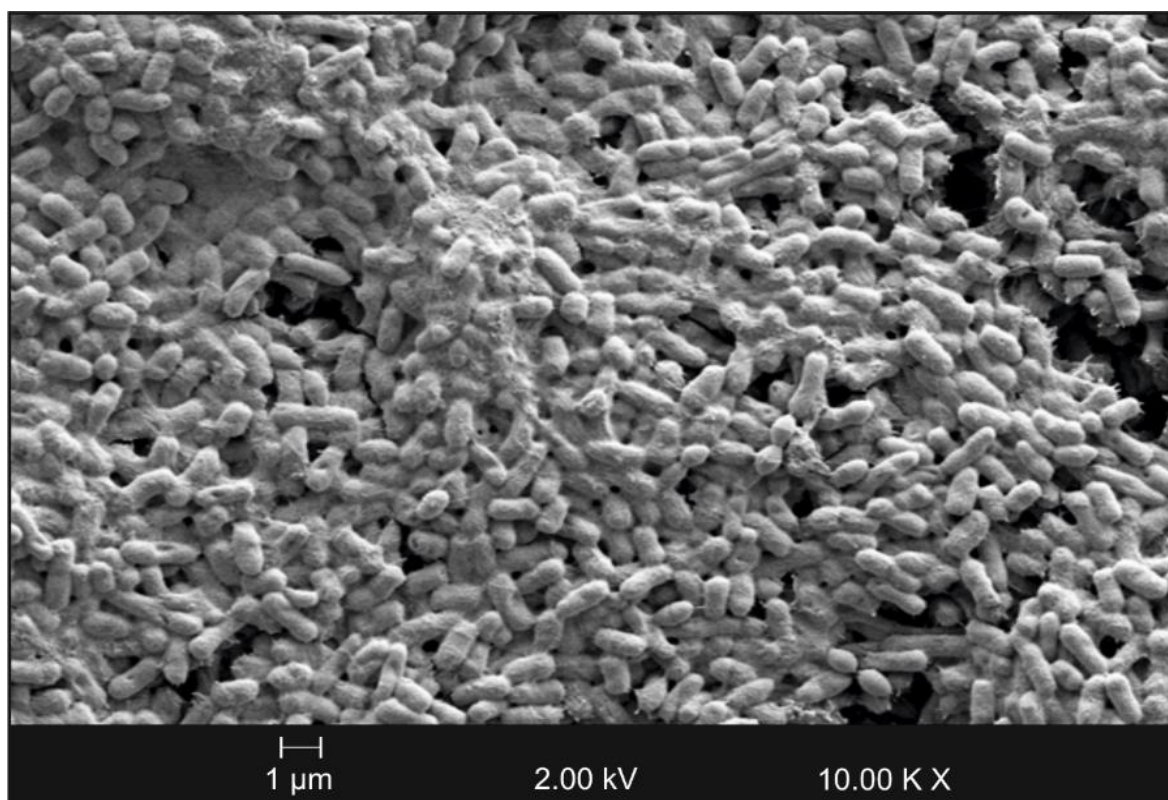


Figure 1.4. Scanning Electron Micrograph (SEM) showing the abundant coverage of an *E. coli* biofilm adhered to the surface of a carbon-paste graphite electrode. Figure reproduced with permission from (Slate *et al.*, 2019b).

### 1.3.2.1 Graphene

Graphene, a two-dimensional (2D) monolayer lattice of  $\text{sp}^2$  hybridised carbon atoms, has attracted diverse and significant interest in both the scientific and technological communities due to its reported unique properties (Brownson *et al.*, 2014). Such properties include its high physical strength (Lee *et al.*, 2008), high electron mobility/conductivity at room temperature ( $2.5 \times 10^5 \text{ cm}^2 \text{ V}^{-1} \text{ s}^{-1}$ ) (Mayorov *et al.*, 2011) and a theoretical surface area estimated at  $2630 \text{ m}^2 \text{ g}^{-1}$  (Stoller *et al.*, 2008). Graphene can sustain extremely high densities of current (reported as one million times higher than copper) (Moser *et al.*, 2007).

Such properties are ideal for efficient and effective electron transfer, making graphene a prime candidate for use as an electrode material within MFCs.

The highest recorded power density produced to date,  $5.61 \text{ W m}^{-2} / 11,220 \text{ W m}^{-3}$ , was achieved using a 3D multilayer graphene macroporous scaffold anode. The power density produced a 3.3 fold increase when compared with its single-layer 2D control counterparts (Ren *et al.*, 2016). Ren *et al.* (2016) also demonstrated the ability to produce highly effective MFCs with advanced 2D nanomaterials, such as graphene as the anode/cathode material. Previously, graphene has been utilised as the anode material within a MFC configuration. When used with a pure culture of *E. coli*, a maximum power density of  $2,668 \text{ mW m}^{-2}$  was achieved (Zhang *et al.*, 2011b). This was 18 and 17 times greater than stainless steel mesh and polytetrafluoroethylene modified electrodes respectively (Zhang *et al.*, 2011b).

Research into graphene, with varying multilayer morphologies (*ca.*  $50 \mu\text{m} - 100 \mu\text{m}$ ) has been conducted. Graphene sheets which have been shown to be more defective (*i.e.* an enhanced edge to basal plane ratio) than pristine graphene, due to the synthesis method (Hummers' synthesis), were compared against crumpled graphene particles that were produced *via* an aerosol-assisted capillary compression process (Luo *et al.*, 2011; Xiao *et al.*, 2012). The varying graphene morphologies were coated onto carbon cloth electrodes (loading rate:  $\sim 5 \text{ mg cm}^{-2}$ ) and the results showed that modification of the graphene sheets to crumpled graphene particles led to an increase in both the surface area and the power density ( $3.6 \text{ W m}^{-3}$ ) (Xiao *et al.*, 2012). This was twice that of the activated carbon modified electrode ( $1.7 \text{ W m}^{-3}$ ) (Xiao *et al.*, 2012). Therefore, it has been postulated that increasing the surface area of graphene-based electrodes would result in increased power outputs in MFCs. A challenge for the advancement of MFCs for industrial and socio-economic end-point applications (*e.g.* wastewater treatment) is the cost and the reliability. Unfortunately, the production of 2D-nanomaterials such as graphene is currently unsustainable for this application. However, it is expected that as more research is invested into the area of nanomaterials, the production costs will decrease significantly (Novoselov *et al.*, 2012).

One approach to enhance the surface area of graphene electrodes is additive manufacturing (also known as 3D-Printing). This fabrication method offers a unique and rapid design of complex structures, which cannot be achieved by other manufacturing routes, potentially allowing for the development and creation of economically viable 3D-

Printed components to be available for use in MFCs (Farahani *et al.*, 2016; Foster *et al.*, 2017; MacDonald and Wicker, 2016).

### 1.3.3 Surface Hydrophobicity

The effect of surface topography on both bacterial adhesion and biofilm formation has been extensively studied (Kargar *et al.*, 2016; Kelleher *et al.*, 2015; Perera-Costa *et al.*, 2014; Yuan *et al.*, 2017). Larger surface areas due to rougher topography can promote bacterial adhesion (Yuan *et al.*, 2017). However, topographic patterns to enhance bacterial adhesion cannot be generalised as the variation in specific bacterial shape and size must also be considered (Yuan *et al.*, 2017). Bacterial attachment is also affected by both long-range forces (*i.e.* hydrophilic interactions, electrostatic interactions and van der Waals forces) and short-range forces such as hydrogen bonding (Ploux *et al.*, 2010).

Surface hydrophobicity is an important, non-specific binding parameter involved in bacterial attachment. An enhanced hydrophobicity has been shown to enhance bacterial attachment to hydrocarbons, leading to an increase in surface attachment (Krasowska and Sigler, 2014; Rosenberg and Kjelleberg, 1986). Furthermore, hydrophobic bacterial cells are thought to adhere more strongly to hydrophobic surfaces, whilst, hydrophilic bacterial cells adhere with greater affinity to more hydrophilic surfaces (Kochkodan *et al.*, 2008). However, microorganisms can switch between hydrophilic and hydrophobic phenotypes in response to environmental conditions and growth phase, which can be beneficial for bacterial attachment and dispersal (Borecka-Melkusova and Bujdakova, 2008; Bujdaková *et al.*, 2013).

It has previously been demonstrated that the anode surface charge and hydrophobicity influences biofilm development, which can affect the performance of bio-electrochemical systems (Guo *et al.*, 2013). In one study, gold anodes in a MFC configuration were modified with self-assembled, hydrophilic ( $-\text{N}(\text{CH}_3)_3^+$ ,  $-\text{OH}$  and  $-\text{COOH}$ ) and hydrophobic ( $-\text{CH}_3$ ) monolayers (Santoro *et al.*, 2015). The hydrophobic monolayer resulted in a decrease in bacterial attachment and anode performance when compared with the hydrophilic monolayers, when an anolyte of 50 % 0.1 M Phosphate Buffered Saline (PBS) with 0.1 M KCl and 50 % activated sludge from a wastewater treatment plant (Santoro *et al.*, 2015). Another study conducted by Chang *et al.* (2016), demonstrated that enhancing

the hydrophilicity of carbon cloth promoted bacterial adhesion and enhanced power outputs. Therefore, the conflicting results suggest that the hydrophobicity of both the electrode materials and bacterial cells should be carefully considered prior to their application within MFC configurations.

## **1.4 Mechanisms of Electron Transfer**

Exoelectrogenic bacterial species have the ability to facilitate electron transfer by two mechanisms, direct and indirect electron transfer (Huang *et al.*, 2011). Direct electron transfer requires a physical connection between the bacterial and the electrode whilst, indirect electron transfer does not require a physical connection; instead this mechanism relies on electron shuttling molecules (Lovley, 2012). Currently, there are three established methods of electron transfer including nanowires, membrane-bound cytochromes and electron mediators, which bacteria use to donate electrons to the anode in MFC configurations (Figure 1.5) (Kumar *et al.*, 2012).

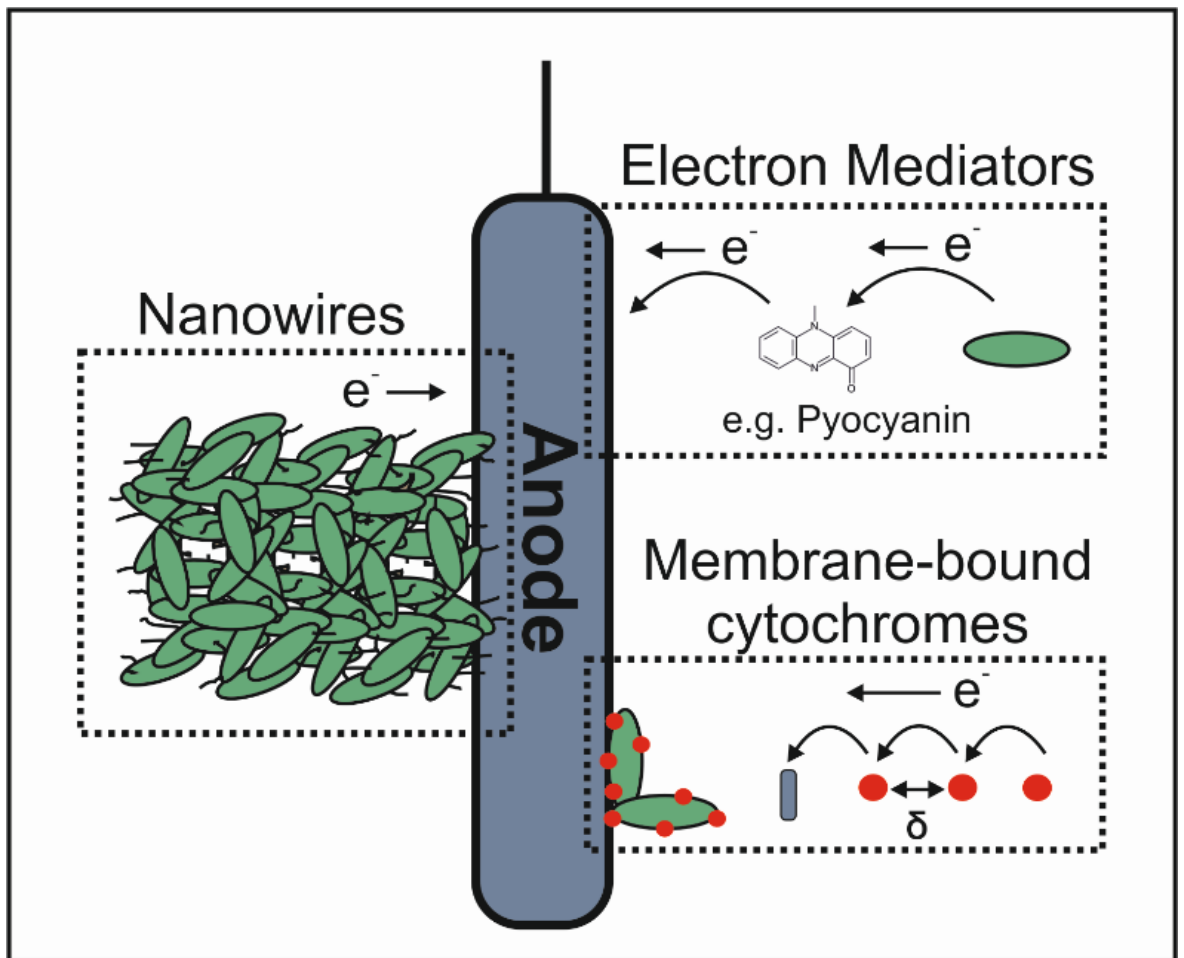


Figure 1.5. The three known methods of electron transfer demonstrated by exoelectrogenic bacteria, including; direct electron transfer – conductive pili, denoted within the literature as nanowires; redox-active proteins; and indirect electron transfer by electron shuttles. Figure adapted from Kumar *et al.* (2012).

### 1.4.1 Direct electron transfer *via* Nanowires

Direct electron transfer requires a physical connection between the bacterial cell and the electrode surface; this is achieved in the form of nanowires and/or redox-active proteins. On the cell surface of specific isolated bacterial species, such as *Shewanella* spp., and *Geobacter* spp., are micrometre long proteinaceous filaments that extend from their outer surface into the extracellular matrix. These appendages which are more commonly known as flagella, are involved in extracellular electron transport processes, and are

referred to as microbial nanowires in regards to MFC studies – due to their long filament-like appearance and conductive attributes (Reguera *et al.*, 2005). Nanowires mediate direct electron transfer, providing an alternative energy source. Nanowires can be both flagella and pili, both of which have distinct properties. Flagella are key structural features of the bacterial cell ultrastructure, which enable cell motility. Flagellin proteins form the flagella filament, which are typically 10 nm – 15 nm in diameter and 2  $\mu\text{m}$  – 15  $\mu\text{m}$  in length (Hobot, 2015). Pili are surface appendages that are involved in bacterial conjugation and surface adhesion, generally between one and ten pili are present on the surface of a bacterial cell (Hobot, 2015). Pili are components of the bacterial ultrastructure and are approximately 0.1  $\mu\text{m}$  – 2  $\mu\text{m}$  in length and 1 nm – 12 nm in diameter (Hobot, 2015). Due to the difference in structure and function the terms micro-nanowires and macro-nanowires were coined for pili and flagella, respectively (Slate *et al.*, 2019b) (Figure 1.6).

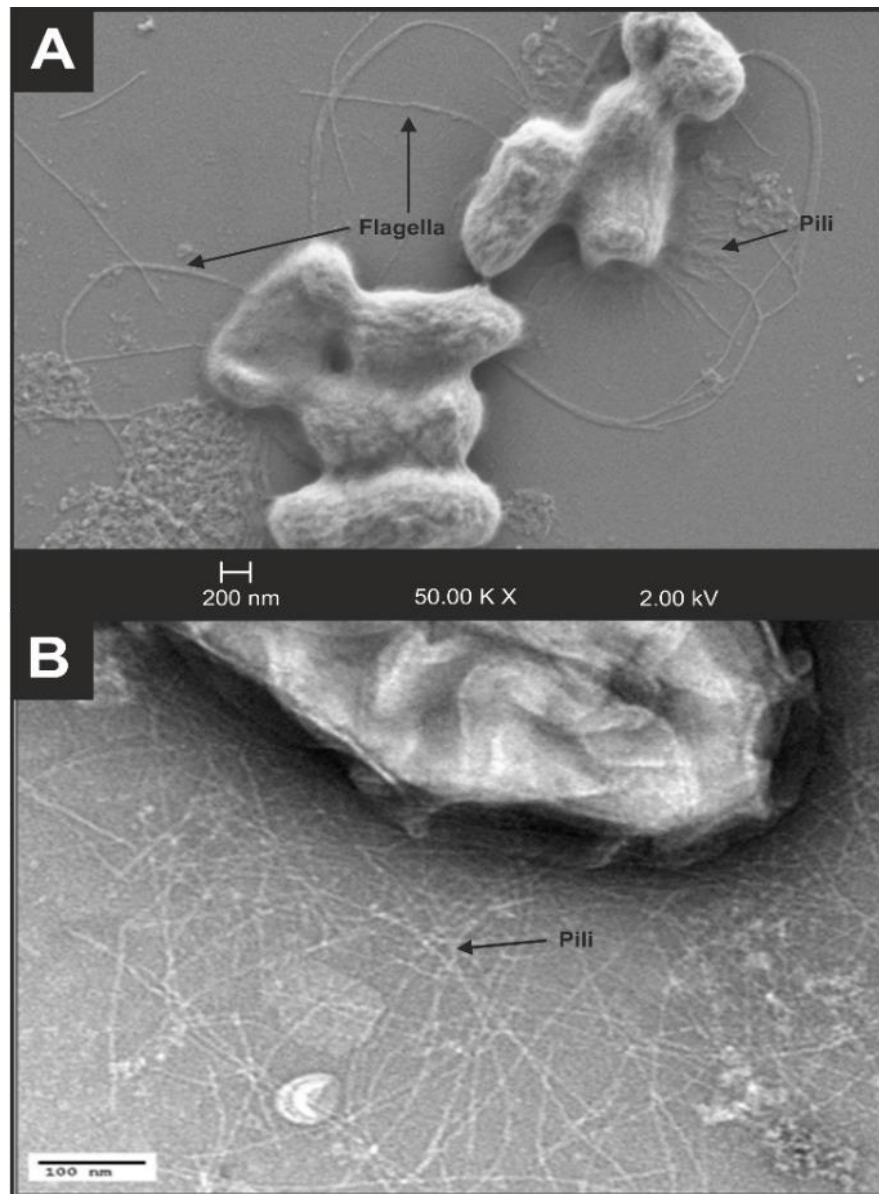


Figure 1.6. A) Scanning electron microscopy (SEM) image showing the difference in morphology of flagella and pili on the surface of *E. coli*. B) Transmission electron microscopy (TEM) showing *G. sulfurreducens* strain GUP, expressing abundant pili. Section B, adapted from Tan *et al.* (2016).

Traditionally, it is thought that the primary role of the flagella of bacteria is to mediate the motility of the cell *via* swarming and swimming mechanisms. One of the roles of Type IV pili is to mediate twitching to enable movement of the bacterial cell across a surface (often in dense aggregates) (Conrad *et al.*, 2011). Furthermore, Type IV pili play vital roles in secretion systems for effectors, microbial adherence and bacterial movement,

establishing contact between the bacterial species and the electrode surface (Shi and Sun, 2002).

In regards to the bacterial species evaluated for electricity generation for potential application in MFC technologies, *G. sulfurreducens* is currently the most comprehensively studied, producing the highest recorded current densities of any known pure culture which uses micro-nanowires (pili) (Badalamenti *et al.*, 2013; Malvankar *et al.*, 2012; Tan *et al.*, 2016).

It is thought that the reduction of iron (and other metal) oxides by *G. sulfurreducens* requires direct contact between the bacteria and the Fe(III) oxides in order to reduce equivalents from the tricarboxylic acid cycle (TCA) / Krebs cycle (Galushko and Schink, 2000). This ability to locate (*via* chemotaxis) and reduce Fe(III) oxides in order to use them as terminal electron acceptors is advantageous in subsurface environments, due to the abundance of Fe(III) oxides (Childers *et al.*, 2002; Methé *et al.*, 2003). *Geobacter sulfurreducens* is able to generate energy in the form of adenosine triphosphate (ATP) due to its ability to reduce metals such as Fe(III), by using metal ion-mediated electron transport mechanisms to oxidise organic compounds to CO<sub>2</sub> (Méthé *et al.*, 2003). Reguera *et al.* (2006a), reported that a wild-type of *G. sulfurreducens* could attach to Fe(III) oxides after 48 hours, as demonstrated by an increase in biomass. However, in the same time period, the *pilA*-deficient strain, which lacked pili formation could not attach to the Fe(III) oxides, which was indicated by a decrease in biomass (Reguera *et al.*, 2006a).

The current density generated by a monolayer of planktonic cells attached to the surface of an electrode is limited by the surface area of the electrode. It is thought that this is due to a lack of available space for the nanowires to adhere, thus leading to a reduction in direct electron transfer (Friman *et al.*, 2013). However, conductive biofilms (which are many layers thick) have the ability to produce much higher power and current densities, due to multiple layers of bacteria contributing to the overall net energy generation (Friman *et al.*, 2013).

The impact of biofilm formation on energy generation has been researched by Friman *et al.* (2013) who reported a current generation (under a constant external resistor of 1 k $\Omega$ ) of 125 mA m<sup>-2</sup> from planktonic cells as opposed to 541 mA m<sup>-2</sup> from an established biofilm, when acetate was used as the substrate with a pure culture of *Cupriavidus basilensis* (Friman *et al.*, 2013). Measurements against *G. sulfurreducens* biofilms have

shown high conductivities, even rivalling those of synthetic conductive polymers, examples of conductive polymers include polyacetylene, polyaniline and polypyrrole (Malvankar *et al.*, 2012). In one study, *G. sulfurreducens*, in multi-layered biofilms with an average height of 40  $\mu\text{m}$  ( $\pm 6 \mu\text{m}$ ), produced a maximum current of 12 mA, while planktonic cells produced a maximum current of 2.5 mA after 4 days of incubation (Reguera *et al.*, 2006a), using a continuous batch method (Lovley and Phillips, 1988). Therefore, exoelectrogenic bacteria with enhanced biofilm formation could result in improved MFC power outputs.

### 1.4.2 Direct electron transfer *via* redox-active proteins

Most studies suggest that the direct contact between the nanowires of the conductive bacterial biofilms and iron oxides are essential for the reduction. However, another mechanism of electron transfer requires redox-active proteins and this facilitates short-range electron transfer (Yue *et al.*, 2006). Smith *et al.* (2014) revealed that the deletion of a gene encoding for PilA, a structural pilin protein, in *G. sulfurreducens* strain KN400 inhibited iron oxide reduction (Smith *et al.*, 2014). One possible explanation for the observed continued iron reduction, even with structurally damaged pili, was due to the presence of *c*-type cytochromes, such as OmcS and OmcE (Nevin *et al.*, 2009). These are commonly known for their primary function in mitochondria, as these molecules play a pivotal role in ATP synthesis (Ow *et al.*, 2008). The *c*-type cytochromes have been isolated in abundance on the surface of *G. sulfurreducens* cells, where OmcS and OmcE were the most commonly isolated. Furthermore, it has been shown that when either *omcS* or *omcE* were deleted, reduction of iron (III) oxides were no longer viable (Mehta *et al.*, 2005). Other studies, including immunolocalization and proteolysis studies have demonstrated that the cytochrome, OmcB is essential for optimal Fe(III) reduction as it is highly expressed during growth upon electrode surfaces and is embedded in the outer membrane of the cell (Leang *et al.*, 2003; Nevin *et al.*, 2009; Qian *et al.*, 2007).

It is hypothesised that bacteria such as *G. sulfurreducens* developed this ability to reduce metal oxides, due to being isolated in harsh environments surrounded by large quantities of insoluble materials. Natural selection and evolution led to the production of effective strategies to overcome the lack of ATP production that is usually achieved by more conventional methods, *i.e.* aerobic respiration (Lovley, 2006a; Lovley, 2011).

### **1.4.3 Indirect electron transfer *via* electron shuttles**

Bacteria can generate electricity due to the production of secondary metabolites, which are able to act as endogenous redox mediators, often referred to as electron shuttles. Electron shuttles are organic molecules with a low molecular weight that have the ability to catalyse both reduction and oxidation reactions, examples include phenazines and quinones (Velasquez-Orta *et al.*, 2010). Bacteria can utilise both exogenous and endogenous shuttle compounds for extracellular electron transfer. For effective electron transfer to take place *via* this mechanism, electron shuttles must be both chemically-stable and not easily biologically degraded (Figure. 1.7) (Velasquez-Orta *et al.*, 2010).

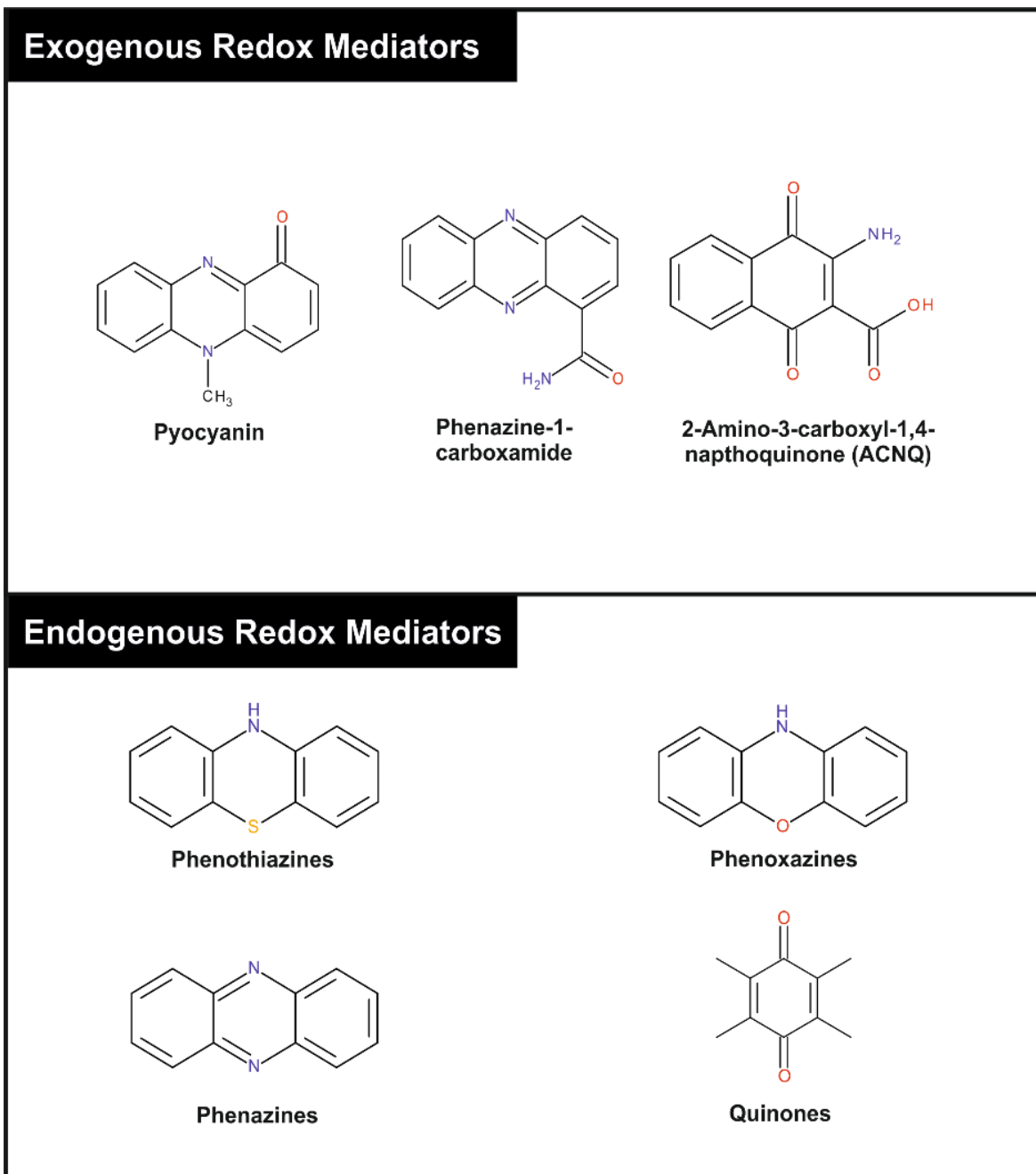


Figure 1.7. A range of known exogenous and endogenous redox mediators which are capable of mediating electron transfer.

Electron shuttles, unlike nanowires, eliminate the need for direct contact between the bacterial cell and the electron acceptor (Reguera *et al.*, 2005). Within the bacterial cells, electrons are first transported to the cell surface *via* a range of metabolic pathways. This is dependent on the conditions and fuel source available and this process involves redox-active proteins and low molecular weight compounds. Subsequently, electrons are

transported to cytochromes or electron shuttles in either the periplasm or the outer-membrane of the bacterial cell (Velasquez-Orta *et al.*, 2010). Soluble electron shuttles can diffuse from the bacterial cell surface into the surrounding media, and electrons can be transferred to suitable external acceptors, with examples including insoluble Fe(III) oxides or the anode of a MFC (Velasquez-Orta *et al.*, 2010). Examples of known, effective electron shuttles include methyl viologen, 2-hydroxy-1,4-naphthoquinone, thionine, methylene blue, humic acids and anthraquinone-2,6-disulfonic acid (Figure 1.7). More common examples of electron shuttles are molecules known as flavins (Bennetto *et al.*, 1983; Newman and Kolter, 2000; Roller, 1984; Sund *et al.*, 2007).

Flavins demonstrate enhanced redox potential efficiency during bio-geochemical iron cycles, which improves electron transfer. Therefore, flavins have the potential to be applied to MFC technologies as these can be used as endogenous electron transfer mediators (Lee *et al.*, 2015). The importance as flavins as electron shuttles has been acknowledged. When a pure culture of *Shewanella oneidensis* was utilised in a MFC, the concentration of flavins was adjusted from 0.2  $\mu\text{M}$  – 0.6  $\mu\text{M}$  to 4.5  $\mu\text{M}$  – 5.5  $\mu\text{M}$ , which resulted in a four-fold peak current increase (Velasquez-Orta *et al.*, 2010).

Flavins are often produced as secondary metabolites in bacteria and one example is riboflavin (also known as vitamin B2), which facilitated electron transfer in *Shewanella oneidensis* biofilms (Marsili *et al.*, 2008). The removal of riboflavin from the biofilms resulted in an electron transfer rate reduction of more than 70 % (Marsili *et al.*, 2008). Pyocyanin is a flavin which mediates electron transfer in MFCs (Qiao *et al.*, 2008). The concentration of pyocyanin in an anodic culture directly correlates to power generation efficiency, due to its ability to transport electrons through the cell membrane (Shen *et al.*, 2014).

#### **1.4.3.1 *Pseudomonas aeruginosa***

*Pseudomonas aeruginosa* is defined as a rod-shaped, Gram-negative, monoflagellated, facultative anaerobic bacterium (Wilson and Dowling, 1998). Common characteristics which can often assist in the preliminary identification of *P. aeruginosa* (before further testing) is its characteristic green pigmentation (due to pyocyanin) and its fruity, grape-like odour which is derived from the production of 2-aminoacetophenone

(Jayaseelan *et al.*, 2014). *Pseudomonas aeruginosa* was first isolated in 1882 by Gerrard and has cell dimensions in the region of  $0.5 \mu\text{m} - 1.0 \mu\text{m} \times 1.5 \mu\text{m} - 5.0 \mu\text{m}$  (Bédard *et al.*, 2016; Forkner, 1961). *Pseudomonas aeruginosa* is an opportunistic pathogen that is responsible for high morbidity and mortality rates, especially in immunocompromised patients, such as those with cystic fibrosis (where it affects 80 % of patients) and major burn injuries (Anvarinejad *et al.*, 2014; Nathwani *et al.*, 2014; Prickett *et al.*, 2016).

*Pseudomonas aeruginosa* produces four phenazine derivatives, pyocyanin, phenazine-1-carboxylic acid, phenazine-1-carboxamide and 1-hydroxyphenazine, all of which have similar electron transfer mediating properties (Boon *et al.*, 2008; Shen *et al.*, 2014; Venkataraman *et al.*, 2010). It has been previously determined that *P. aeruginosa* strains vary their phenazine production rate, due to a range of factors in relation to that of the growth phase (Price-Whelan *et al.*, 2007). Therefore, it is theorised that alterations in growth media conditions could result in increased phenazine production, coupled with a subsequent increase in power outputs when *P. aeruginosa* is applied in MFC configurations and other biotechnological systems (Price-Whelan *et al.*, 2007).

Pyocyanin is produced as a secondary metabolite by *P. aeruginosa*. It is a water-soluble blue-green phenazine compound, responsible for the green pigmentation often associated with infected wounds (El-Fouly *et al.*, 2015). Pyocyanin has multiple essential functions including, a role in antimicrobial activity against a range of microorganisms (including bacteria, fungi and protozoa). It also acts as an electron shuttle and is a key sensing molecule which upregulates the transcription of quorum sensing genes, leading to biofilm formation (Baron and Rowe, 1981; Dietrich *et al.*, 2006; Diggle *et al.*, 2003; Jayaseelan *et al.*, 2014; Kerr *et al.*, 1999; Rabaey *et al.*, 2005; Wang *et al.*, 2010; Watanabe *et al.*, 2009; Williams and Cámara, 2009). Pyocyanin has a standard redox potential of -34 mV, which is high enough to allow electron transfer from organic molecules such as NAD(P)H ( $E_h = -320 \text{ mV}$ ) and glutathione ( $E_h = -240 \text{ mV}$ ) (Friedheim and Michaelis, 1931; Schwarzer *et al.*, 2008). The addition of pyocyanin to non-pyocyanin producing MFC biofilms has shown varying results. Rabaey *et al.* (2005) demonstrated that the addition of pyocyanin to a pure culture of *Enterococcus faecium* (strain KRA3), led to a peak power increase from  $294 \pm 49 \mu\text{W m}^{-2}$  to  $3977 \pm 612 \mu\text{W m}^{-2}$ , a 13-fold increase (Rabaey *et al.*, 2005). However, with *E. coli* strain ATCC 4157 the power output showed a reduction of 50 %, after the addition of pyocyanin ( $117 \pm 16 \mu\text{W m}^{-2}$  to  $50 \pm 53 \mu\text{W m}^{-2}$ ) (Rabaey *et al.*, 2005).

A possible explanation for this could be due to the selective antimicrobial activity of redox-active metabolites, such as pyocyanin (Baron and Rowe, 1981; Kerr *et al.*, 1999).

Pyocyanin production is regulated by the *rhlI/rhlR* quorum-sensing system (Latifi *et al.*, 1995; Mahajan-Miklos *et al.*, 1999). The gene *rhlI* directs the synthesis of *N*-butanoyl-L-homoserine lactone (C4-HSL), which activates *rhlR*, and in turn, the *rhlR*/C4-HSL interaction induces the production of pyocyanin, rhamnolipid, LasA protease, elastase, hydrogen cyanide, siderophores and the cytotoxic lectins PA-I and PA-II (Brint and Ohman, 1995; Diggle *et al.*, 2002; Latifi *et al.*, 1996; Ochsner *et al.*, 1994; Pearson *et al.*, 1995; Winson *et al.*, 1995; Winzer *et al.*, 2000).

The synthesis and production of pyocyanin (and other phenazine derivatives), is highly variable due to culture conditions (*i.e.* nutrient source present) and physiological status (Romano *et al.*, 2015). One example of this is the change in biochemistry, which is observed in the presence and absence of oxygen. In aerobic conditions, *P. aeruginosa* is able to generate energy by catabolism *via* utilisation of the tricarboxylic acid (TCA) cycle. This biochemical pathway is common, and variations of this pathway exist in almost all aerobic living organisms (Krebs and Eggleston, 1945; Krebs and Johnson, 1937; Krebs *et al.*, 1938). Theoretically, since each 6-carbon carbohydrate produces two 3-carbon-pyruvate molecules, the total amount of energy attained from one glucose molecule *via* the TCA cycle is 24 ATP. This is often combined with 8 ATP from glycolysis and 6 ATP molecules from the Pyruvate dehydrogenase complex (PDH complex), producing a total of 38 ATP molecules (Dashty, 2013). Pyruvate has been established as a key intermediate of the TCA cycle in *P. aeruginosa*, and its oxidation to acetyl coenzyme A is essential as a means to oxidising glucose *via* the TCA cycle (Campbell and Stokes, 1951). Glasser *et al.* (2017) demonstrated that pyruvate and  $\alpha$ -ketoglutarate dehydrogenase complexes could directly catalyse phenazine reductions, when utilising pyruvate or  $\alpha$ -ketoglutarate as electron donors (Glasser *et al.*, 2017). This occurs as both complexes transfer electrons to phenazines *via* dihydrolipoamide dehydrogenase (Glasser *et al.*, 2017). Paradoxically, oxygen is also a final electron acceptor, due to its ability to form water *via* the combination of protons and electrons, and thus oxygen can compete with the anode in a MFC configuration (Cheng *et al.*, 2015). This can lead to a reduction in the overall energy output of a MFC configuration, and to avoid this, anaerobic conditions are often utilised.

In anaerobic conditions, a variety of pathways exist to promote the survival of *P. aeruginosa*. In one fermentation pathway, pyruvate is used as the substrate and is converted into acetate, lactate and small amounts of succinate (Eschbach *et al.*, 2004). Pyruvate fermentation allows for the survival of *P. aeruginosa*, but will not sustain anaerobic growth, therefore it can be suggested that this pathway is not viable for long term utilisation (Schobert and Jahn, 2010). This is due to the conversion of pyruvate to acetate, which generates ATP but in addition reduces NAD<sup>+</sup> to NADH. The NADH molecules can then be regenerated (producing NAD<sup>+</sup>) due to lactate dehydrogenase, resulting in the reduction of pyruvate to lactate (Eschbach *et al.*, 2004). Arginine fermentation can also occur, this moderately supports anaerobic growth (Schobert and Jahn, 2010). *Pseudomonas aeruginosa* can respire nitrate and nitrite *via* a process called denitrification. This process requires four reductases, nitrate-, nitrite, NO- and nitrous oxygen reductases, which reduce nitrate to N<sub>2</sub> (Schobert and Jahn, 2010; Schreiber *et al.*, 2006; Zumft, 1997).

In one study, pyocyanin reduction by *P. aeruginosa* in standing liquid cultures was readily observed when all the oxygen in a medium had been consumed (Price-Whelan *et al.*, 2007). Furthermore, in the same study, the addition of pyocyanin to phenazine-null mutants lead to a reduction in intracellular NADH levels, which led to suggestions that pyocyanin reduction facilitated redox-balancing when other electron acceptors are absent (Price-Whelan *et al.*, 2007).

As MFCs have to be conducted under predefined growth conditions such as ambient temperature, atmospheric pressure and neutral or slightly acidic pH, other factors have to be optimised in order to improve power outputs and efficiency (Balat, 2009). An example of an optimisation technique was the addition of sophorolipid (a glycolipid) to *P. aeruginosa* inoculated MFCs. This resulted in an increase in both current and power density of 1.7 times and 2.6 times, respectively (Shen *et al.*, 2014). Upon further investigation, it was shown that the addition of sophorolipid led to a significant improvement in both pyocyanin production and membrane permeability (Haque *et al.*, 2016; Shen *et al.*, 2014). In light of this, further research into indirect electron shuttles is required, in order to develop more effective MFCs with increased power density generation.

## 1.5 Mixed community microbial fuel cells

Currently, most fundamental MFC studies which examine electron transfer methods and the optimisation of biochemical and electrochemical conditions, employ model microorganisms (pure strains) under strictly controlled conditions (Santoro *et al.*, 2017). However, few monoculture strains have the capacity to produce power densities as great as strains that are inoculated in mixed communities. The projected overall industrial application of MFCs is wastewater treatment, due to dual functionalities, allowing for electricity generation and wastewater treatment (*via* the removal of specific contaminants) (Xu *et al.*, 2015). However, the use of pure cultures is not feasible in such environments (Xu *et al.*, 2015). Therefore, in order to progress and optimise this technology to an industrially-relevant level, mixed community biofilms must be employed. Although the use of mixed community biofilms was not the focus of this thesis, enriched anodic biofilms have previously been shown to generate power densities as high as  $6.9 \text{ W m}^{-2}$  (Logan and Regan, 2006). Furthermore, some bacterial species which were isolated in MFC biofilms have shown that the cells do not interact directly with the anode, but through interactions with other bacteria present and contributed indirectly to the net production of electricity. One example of this phenomenon was demonstrated by *Brevibacillus* spp. (strain PTH1), which was found in abundance in a MFC community (Franks and Nevin, 2010). Power production from this bacterium alone was low ( $2 \mu\text{A}$ ) (Boon *et al.*, 2008). However, when co-cultured with *Pseudomonas* spp., (or supernatant from a MFC community containing *Pseudomonas* spp.) there was a marked increase in electricity generation (Franks and Nevin, 2010). Clearly, mixed community biofilms, which can generate electricity by more than one mechanism, will play a role in the optimisation and industrial scale up of MFCs (Li *et al.*, 2016).

MFC technologies have the potential to play a pivotal role in the transition from fossil fuel based technologies to more renewable energy sources. Research into this area is rapidly progressing but there is still more research required in order for MFC technologies to be routinely adopted by industry. MFCs are expected to advance due to the optimisation and tailored development of individual parameters, such as enhanced electrode materials that are more suitable for this application. This, alongside interdisciplinary research into further exoelectrogenic bacteria, their biochemical pathways and the influence of

secondary metabolites that underpin electron transfer mechanisms, could lead to power outputs much closer to that of the theoretical limits whilst, furthering the advancing field of electromicrobiology.

## **1.6 Aim and Objectives**

### **1.6.1 Academic Aim**

To contribute to the fundamental understanding of *P. aeruginosa* electromicrobiology through the incorporation of graphene to 3D-Printed electrodes, and optimisation of the growth medium and biochemical pathways utilised, in order to increase bacterial proliferation and pyocyanin production, resulting in enhanced efficiency and power outputs in MFCs.

### **1.6.2 Objectives**

- Optimisation of graphene electrochemistry due to alteration in lateral flake size of carbon-based paste electrodes.
- Fabrication and characterisation of 3D-Printed graphene electrodes.
- Selection and optimisation of a *P. aeruginosa* strain that demonstrates maximum pyocyanin production and biofilm growth.
- Generate power outputs from a MFC configuration using *P. aeruginosa* and in-house fabricated 3D graphene electrodes.

**Chapter 2 – Exploring the electrochemical performance of graphite and graphene paste electrodes comprised of varying lateral flake sizes**

## 2.1 Introduction

The use of carbon-based electrodes has long been established due to the high heterogeneous electron transfer (HET) kinetics of carbon. Since the discovery of graphene in 2004, there has been a significant increase in research focussed on utilising this and other novel 2D-nanomaterials. Carbon nanomaterials possess many reported beneficial properties, which theoretically make them ideal for electrode materials (Yang *et al.*, 2015a).

### 2.1.1 Carbon Based Paste Electrodes

Carbon-based paste electrodes are utilised widely, due to their advantageous attributes over more traditional electrodes. These attributes include low background currents, large potential domains and their ease of modification and rapid surface regeneration (Banks *et al.*, 2004; Foster *et al.*, 2016; Grewal *et al.*, 2013; Moorcroft *et al.*, 2001). Due to this, graphitic paste electrodes have universal requisition combining both the beneficial properties of carbon-based materials (*i.e.* graphene/graphite) with the significant benefits of paste electrodes.

### 2.1.2 Graphene

The reported unique properties of graphene, which include high electron conductivity/mobility, excellent biocompatibility, potential for functionalization and high theoretical surface area ( $2630 \text{ m}^2 \text{ g}^{-1}$ ) have resulted in numerous fields reporting its beneficial application (Brownson *et al.*, 2012b). Theoretically, such properties are ideal for both effective electron transfer, making graphene a prime candidate for use as an electrode material. There are many optimistic reports throughout the literature detailing the 'outstanding' electrochemical behaviour of graphene (Service, 2009; Shao *et al.*, 2010). In light of this, graphene is utilised in fundamental studies, as the quantum of carbon electrodes (*i.e.* the minimalist structure). Investigations into the electrochemical properties of graphene have aided the exploration, discovery and understanding of carbon electrochemistry (Brownson and Banks, 2014; Brownson *et al.*, 2014; Brownson *et al.*, 2012b; Li *et al.*, 2011b; Valota *et al.*, 2011; Yuan *et al.*, 2013).

### 2.1.3 Edge and Basal Plane Theory

Graphitic surfaces are heterogeneous (anisotropic) and their overall chemical and electrochemical reactivity differs greatly between two distinct structural contributions, which are fundamental to the behaviour of graphene and graphite electrodes alike, namely the edge and basal planes (McCreery, 2008; Neumann *et al.*, 2011). Currently, the accepted understanding throughout the literature, is that the primary origin of heterogeneous electron transfer (HET) kinetics is due to the edge plane like-sites/defects and that the basal planes are effectively inert (Banks *et al.*, 2005; Brownson *et al.*, 2012b; Davies *et al.*, 2005a; McCreery, 2008; Rowley-Neale *et al.*, 2016a). Edge plane sites/defects are the predominant origin for fast electron kinetics in graphitic materials therefore, slow HET rates demonstrated by pristine graphene is likely to be due to the fundamental conformation of graphene (*i.e.* the low edge plane to high basal plane ratio) (Brownson *et al.*, 2014). The ratio of the edge : basal planes found on the electrode surface could play a pivotal role in the electrochemical efficacy (Hu *et al.*, 2016). A key structural feature of graphitic flakes that may have been overlooked thus far is the intraplanar microcrystalline size ( $L_a$ ), *i.e.* the lateral flake size. In relation to graphite and graphene electrodes, there is a notable lack of focus on the electrochemical effect of varying lateral flake sizes. Evidently, variation in the lateral flake size of the graphitic sheet will sequentially alter the relative structural contributions of the edge/basal plane sites and therefore the 'edge to basal plane ratio'. This chapter addresses this important gap in knowledge, the understanding of which will contribute to the fundamental knowledge base of such materials.

### 2.1.4 Current Issue with Graphene Electrochemical Research

A major issue in graphene research, particularly in the field of electrochemistry, is how to electrically 'wire' graphene, in order to explore its unique properties in a manner that is stringent, controlled and reproducible (Brownson *et al.*, 2012a; Figueiredo-Filho *et al.*, 2013a; Figueiredo-Filho *et al.*, 2013b). Thus far, the most common approach is to immobilise the graphene on the surface of a suitable electrode material and average the response exhibited against the graphene domains present. However, this method is not ideal as modifying such surfaces has the potential to leave underlying 'reactive' surfaces exposed, potentially interfering with the reported electrochemical activity. In order to

overcome this issue, researchers have recently turned to fabricating three-dimensional graphene architectures (Foster *et al.*, 2017; Jakus *et al.*, 2015; Li and Shi, 2012; Zhu *et al.*, 2015), or by utilising graphitic paste electrodes which comprise primarily of the electrode material in question (Bo *et al.*, 2011; Figueiredo-Filho *et al.*, 2013b; Gasnier *et al.*, 2013; Huang *et al.*, 2012; Li *et al.*, 2011a; Parvin, 2011). The utilisation of graphitic paste electrodes enables the reproducible electrical wiring of graphitic electrode materials, with varying lateral flake sizes to ensure accurate electrochemical analysis, whilst also maintaining stringent controls and limiting other variable factors.

Throughout this study, the fabrication, physicochemical characterisation and electrochemical analysis of graphite and graphene paste electrodes was reported. Four graphite and five graphene powders with varying lateral flake sizes, ranging from *ca.* 2.0 mm to 0.1  $\mu\text{m}$  were selected and tested, in order to analyse a diverse range and establish if variation in lateral flake size,  $L_a$ , and therefore the edge plane density of the electrode surface, had an effect on the reported electrochemical properties. Density Functional Theory (DFT) provided further support allowing the electronic structure (*i.e.* HOMO-LUMO) to be explored as a function of flake size. This demonstrated that the edge plane like sites/defects comprising the geometric structure of the relatively small graphene flakes resulted in the entire flake becoming effectively, electrochemically active. The study reported throughout this thesis chapter has previously been published in an international, peer-reviewed journal (Slate *et al.*, 2018a).

### **2.1.5 Aim**

The aim of this study was to determine how the lateral flake sizes of graphene and graphite paste electrodes affected electrochemical performance.

## 2.2 Methods

All chemicals (of analytical grade or higher) were used as received from Merck (UK) without further purification. All solutions were prepared with deionised water of resistivity no less than 18.2 M $\Omega$  cm and vigorously degassed, prior to electrochemical measurements being conducted, with high purity, oxygen free nitrogen.

### 2.2.1 Electrochemical Analysis of the Graphite and Graphene Paste Electrodes

The redox probes utilised were as follows (unless stated otherwise): hexaammineruthenium(III) chloride and potassium ferrocyanide(II) which were prepared separately in solution at a concentration of 1 mM with a 0.1 M KCl supporting electrolyte.

Voltammetric measurements were performed using an 'Autolab PGSTAT 101' (Metrohm Autolab, The Netherlands) potentiostat and data generated were collected and controlled using the software, NOVA (Version 2.0). Electrochemical analysis was conducted using a three-electrode system. The working electrode was either a graphene or graphite paste electrode (fabrication details below), with a platinum wire and a saturated calomel electrode (SCE) used as counter/auxiliary and reference electrodes, respectively. Where voltammetric scan rate studies were employed, the following increments were utilised within the specific ranges stated; 5 mV s<sup>-1</sup>, 10 mV s<sup>-1</sup>, 15 mV s<sup>-1</sup>, 25 mV s<sup>-1</sup>, 50 mV s<sup>-1</sup>, 75 mV s<sup>-1</sup>, 100 mV s<sup>-1</sup>, 150 mV s<sup>-1</sup>, 250 mV s<sup>-1</sup> and 500 mV s<sup>-1</sup>.

Both the graphite and graphene powders utilised throughout this study were commercially obtained from 'Graphene Supermarket' (Reading, MA, USA). The graphite powders are as follows: 'Kish graphite', 'Flake graphite', 'High Crystalline Natural (HCN) graphite' and 'Nanostructured graphite – 250 (NSG)'. The graphite flakes were independently measured *via* SEM and TEM image analysis using ImageJ (Version J2, 2009), to determine the average lateral flake size ( $n = 20$ ) which comprised average lateral flake sizes of 1390.0 ( $\pm 147.5$ )  $\mu\text{m}$ , 608.0 ( $\pm 39.8$ )  $\mu\text{m}$ , 12.2 ( $\pm 0.7$ )  $\mu\text{m}$  and 0.5 ( $\pm 0.1$ )  $\mu\text{m}$  for kish graphite, Flake graphite, HCN graphite and Nanostructured graphite-250, respectively. The graphene powders utilised were as follows: 'AO-2', 'AO-3', 'AO-4', 'AO-1' and 'C1', which comprised an average lateral flake size of 9.4 ( $\pm 0.7$ )  $\mu\text{m}$ , 5.0 ( $\pm 0.3$ )  $\mu\text{m}$ , 4.0 ( $\pm 0.3$ )  $\mu\text{m}$ , 2.3

( $\pm 0.5$ )  $\mu\text{m}$  and 1.3 ( $\pm 0.1$ )  $\mu\text{m}$ , respectively. An edge plane pyrolytic graphite (EPPG) electrode was included as a control in order for appropriate comparisons to be made (Figueiredo-Filho *et al.*, 2013b). In order to confirm that the oxidation and reduction peaks recorded throughout this study were solely due to the analytes utilised (redox probes), the electrodes first had cyclic voltammetric profiles recorded in 0.1 M KCl and no oxidation or reduction peaks were reported (Slate *et al.*, 2018a).

### **2.2.2 Physiochemical Characterisation**

Independent physiochemical characterisation of the fabricated graphite and graphene paste electrodes was performed. For scanning electron microscope-energy-dispersive X-ray microanalysis (SEM-EDX), transmission electron microscopy (TEM) and Raman Spectroscopy, the respective powders were used as received from the supplier, without any additional modifications. Scanning electron microscopy (SEM) images and surface element analysis were obtained using a JEOL JSM-5600LV model SEM, which was equipped with an energy-dispersive X-ray microanalysis (EDX) package. Transmission electron microscopy (TEM) images were obtained with a JEOL JEM-2010 (Oxford, Inca Energy TEM 100).

### **2.2.3 Fabrication of the Graphite and Graphene Paste Electrodes**

The paste mixtures were prepared by adding the relevant graphite or graphene powder in question to mineral oil (Nujol) at a 60 : 40 (% weight) composition, the paste was then homogenised by agitation. The paste composition was compressed into a piston-driven polymeric-composite electrode shell, where the polymeric cylindrical shell possessed an inner diameter of 4.5 mm, defining the working electrodes surface area. An electrical contact point was positioned at the rear of the paste electrode. Before experimental use, the paste electrode was prepared by applying pressure in order to force out a small portion of the paste. The paste electrodes 'working surface' was polished against clean, lint-free filter paper (Whatman<sup>®</sup>, Merck, UK) by applying slight pressure and friction, until a visually uniform working area was obtained. The surface was washed briefly (5 s) in 10 mL deionised water prior to electrochemical analysis. The calculated theoretical

area of the graphite and graphene paste electrodes used throughout this study was 0.201 cm<sup>2</sup> whilst the calculated theoretical area of the control EPPG electrode was 0.196 cm<sup>2</sup>.

## 2.2.4 Determination of the Heterogeneous Electron Transfer Rate Kinetics ( $k^0$ )

The Heterogeneous Electron Transfer (HET) rate constant ( $k^0$ ) values for the various paste electrodes were calculated using the Nicholson equation for an electrochemically *quasi*-reversible process as described by Equation [2.1] (Nicholson, 1965):

$$\psi = k^0 [(\pi D n \nu F)/(RT)]^{-1/2} \quad [2.1]$$

Where,  $\psi$  is the kinetic parameter,  $D$  is the diffusion coefficient of the electroactive species,  $n$  is the number of electrons involved in the electrochemical process,  $F$  is the Faraday constant,  $\nu$  the applied voltammetric scan rate,  $R$  the universal gas constant, and  $T$  is the temperature. The kinetic parameter,  $\psi$ , is tabulated as a function of peak-to-peak separation ( $\Delta E_p$ ) at a set temperature (298 K) for a one-step, one-electron process. The function of  $\psi$  ( $\Delta E_p$ ), which fits Nicholson's data, for practical usage (rather than producing a working curve) is given by (Cumba *et al.*, 2016; Metters *et al.*, 2013):

$$\psi = (-0.6288 + 0.0021X)/(1 - 0.017X) \quad [2.2]$$

where  $X = \Delta E_p$  is used to determine  $\psi$  as a function of  $\Delta E_p$  from the experimentally obtained voltammetry. From this,  $\psi$  against  $[(\pi D n \nu F)/(RT)]^{-1/2}$  can be plotted, allowing the  $k^0$  to be readily determined *via* the gradient. In cases where the  $\Delta E_p$  values exceed 212 mV, the following equation should be implemented (Lavagnini *et al.*, 2004):

$$k^0 = [2.18 (\alpha D n \nu F / RT)^{1/2}] \exp \left[ - \left( \frac{\alpha^2 n F}{RT} \right) \times \Delta E_p \right] \quad [2.3]$$

where, the constants are the same as described in equation [2.1] however,  $\alpha$  was the transfer coefficient which was assumed to correspond to the value of 0.5 (Guidelli *et*

*al.*, 2014). The  $k^0$  values were calculated assuming diffusion coefficients of  $9.10 \times 10^{-6} \text{ cm}^2 \text{ s}^{-1}$  and  $7.60 \times 10^{-6} \text{ cm}^2 \text{ s}^{-1}$  for hexaammineruthenium(III) chloride and potassium ferrocyanide(II), respectively (Banks *et al.*, 2004; Foster *et al.*, 2016; Grewal *et al.*, 2013; Moorcroft *et al.*, 2001).

Throughout this study, both an inner- and outer- sphere probe were used. Outer-sphere redox mediators, such as hexaammineruthenium(III) chloride, are commonly described as surface insensitive. Therefore, the oxygen to carbon ratio on the surface of the electrode, in addition to any specific surface characteristics in regards to surface sites/groups (*i.e.* ligands), should not have a profound influence on the  $k^0$  values obtained (Brownson *et al.*, 2012b). In these cases, the observed electrochemical response was dependent only upon the electronic structure of the electrode material *e.g.* electronic density of states (DoS). However, inner-sphere redox mediators, such as potassium ferrocyanide(II), are deemed surface sensitive since the  $k^0$  was strongly influenced by the state of the electrode surface, for example the presence of functional groups. This refers to a plethora of factors including surface chemistry and the electrode microstructure. Inner-sphere redox probes may be highly dependent on the presence or the absence of specific oxygenated species, leading to either a detrimental or beneficial electrochemical effect (Brownson *et al.*, 2012b). Therefore when evaluating an electrode for electrochemical performance, it was important to assess the electrode with both an outer-sphere and inner-sphere redox mediator.

## 2.2.5 Determination of the Electrochemical Effective Area

The electrochemical effective area ( $A_{eff}$ ) of the graphite and graphene paste electrodes was deduced using the Randles–Ševčík equation at room temperature, for an electrochemically *quasi*-reversible process by rearranging the described Equation [2.4] (Blanco *et al.*, 2016):

$$I_p = 2.65 \times 10^5 n^{3/2} D^{1/2} v^{1/2} C A_{eff} \quad [2.4]$$

where, the constants were the same as described in equation [2.3] and, C was the concentration of the redox probe. Following the calculation of  $A_{eff}$ , the electrochemical real area ( $A_{real}$ ) was determined *via* equation [2.5] (García-Miranda Ferrari *et al.*, 2018):

$$\text{Electrochemical Real Area, } A_{real} (\%) = \left( \frac{A_{eff}}{A_{Geo}} \right) \times 100 \quad [2.5]$$

where,  $A_{Geo}$  was the geometrical (theoretical) area of the electrode. To effectively calculate the  $A_{eff}$ , a true outer-sphere redox probe should be utilised to obtain an accurate representation of the area, therefore, hexaammineruthenium(III) chloride was exclusively utilised for this purpose (García-Miranda Ferrari *et al.*, 2018).

## 2.2.6 Determination of the Edge to Basal Plane ratio

The ‘edge to basal plane ratio’ of the graphene and graphite paste electrodes was calculated *via* the total specific capacitance ( $C^0$ ). Cyclic voltammetry was performed using 0.1 mM hexaammineruthenium(III) chloride (with 0.1 M KCl), at incremental scan rates of 100  $\text{mV s}^{-1}$ , 200  $\text{mV s}^{-1}$  and 500  $\text{mV s}^{-1}$ . The voltammetric window selected was in a non-faradaic region (between 0.2 V – 0.3 V – with capacitance values taken at 0.255 V (vs. SCE)).

A non-faradaic region was selected to ensure the anodic and cathodic current densities were associated with charging of the electrical double layer. The difference between the anodic and cathodic current density at 0.255 V versus the corresponding scan rate was plotted, so that the linear regression indicated the double layer capacitance value. Using the equation [2.6], the capacitance ( $C^0$ ) for each scan rate was calculated (Rowley-Neale *et al.*, 2017; Shin *et al.*, 2015):

$$C^0 = \left( \frac{\text{Anodic capacitance} - \text{Cathodic capacitance}}{2} \right) \quad [2.6]$$

Following this equation, the  $C^0$  values were plotted against the corresponding scan rate which resulted in a slope that was representative of the total specific capacitance for each electrode (reported as in  $\mu\text{F cm}^{-2}$ ). The ‘edge to basal plane ratio’ was calculated using the following equation [2.7] (Smith *et al.*, 2015):

$$C^0 = C_e^0 f_e + C_b^0(1 - f_e) \quad [2.7]$$

where,  $C^0$  was the total specific capacitance (as calculated above from equation [2.6]), which was the weighted average of the edge and basal plane contributions.  $C_e^0$  (70) and  $C_b^0$  (1) were the specific capacitance values for the edge and basal plane surfaces (theoretical calculations), respectively, whilst,  $f_e$  was the fraction of edge plane on the surface of the electrode (Smith *et al.*, 2015).

### 2.2.7 Density Functional Theory (DFT) Computation

The Gaussian 09W package software was used for all DFT calculations, including both molecular geometry optimisation and molecular orbital (MO) calculations. For geometry optimisation and MO calculations the Beck's three-parameter hybrid (B3LYP) method was utilised (Ortiz *et al.*, 2009). This method (B3LYP) was selected as it had been suggested that it produced results more accurate than semi-empirical and the pure Hartree-Fock level of theory (Hassan and Abo Dena, 2014). This method represented a combination of Beck's three parameters with the correlation functional of Lee, Yang and Parr (Lee *et al.*, 1988). The basis set 6-31G was selected for all calculations, as it was deemed more suitable for calculations carried out on large molecules (> 100 atoms) (Ditchfield, 1974; Ditchfield, 1971; Dobbs and Hehre, 1986; Dobbs and Hehre, 1987a; Dobbs and Hehre, 1987b). Results derived from the calculations were visualised with the aid of GaussView 05 package software (Dennington, 2009). Electron distribution in regards to the highest occupied molecular orbital (HOMO) and lowest unoccupied molecular orbital (LUMO) were also visualised to predict possible electron transfer processes; electrostatic potential maps were visualised to further investigate the distribution of electronic charges.

## 2.3 Results

### 2.3.1 Structural Characterisation

In order to independently characterise the average lateral flake size of the carbonaceous flakes, SEM and TEM were performed and the size was measured using image processing software, ImageJ ( $n = 20$ ) (Schneider *et al.*, 2012). Scanning electron microscopy (SEM) of the graphite flakes (Figure 2.1) demonstrated that the graphite powders comprised of large interplanar microcrystalline sizes,  $L_c$ , indicating the presence of multi-layer graphite. The intraplanar microcrystalline size,  $L_a$  (lateral flake size), varied significantly across the samples, with the following ranges exhibited: 1389  $\mu\text{m}$  ( $\pm 147.5 \mu\text{m}$ ) for kish graphite; 608.0  $\mu\text{m}$  ( $\pm 39.8 \mu\text{m}$ ) for flake graphite; 12.2  $\mu\text{m}$  ( $\pm 0.7 \mu\text{m}$ ) for HCN graphite; and 0.5  $\mu\text{m}$  ( $\pm 0.1 \mu\text{m}$ ) for nanostructured graphite ( $n = 20$ ).

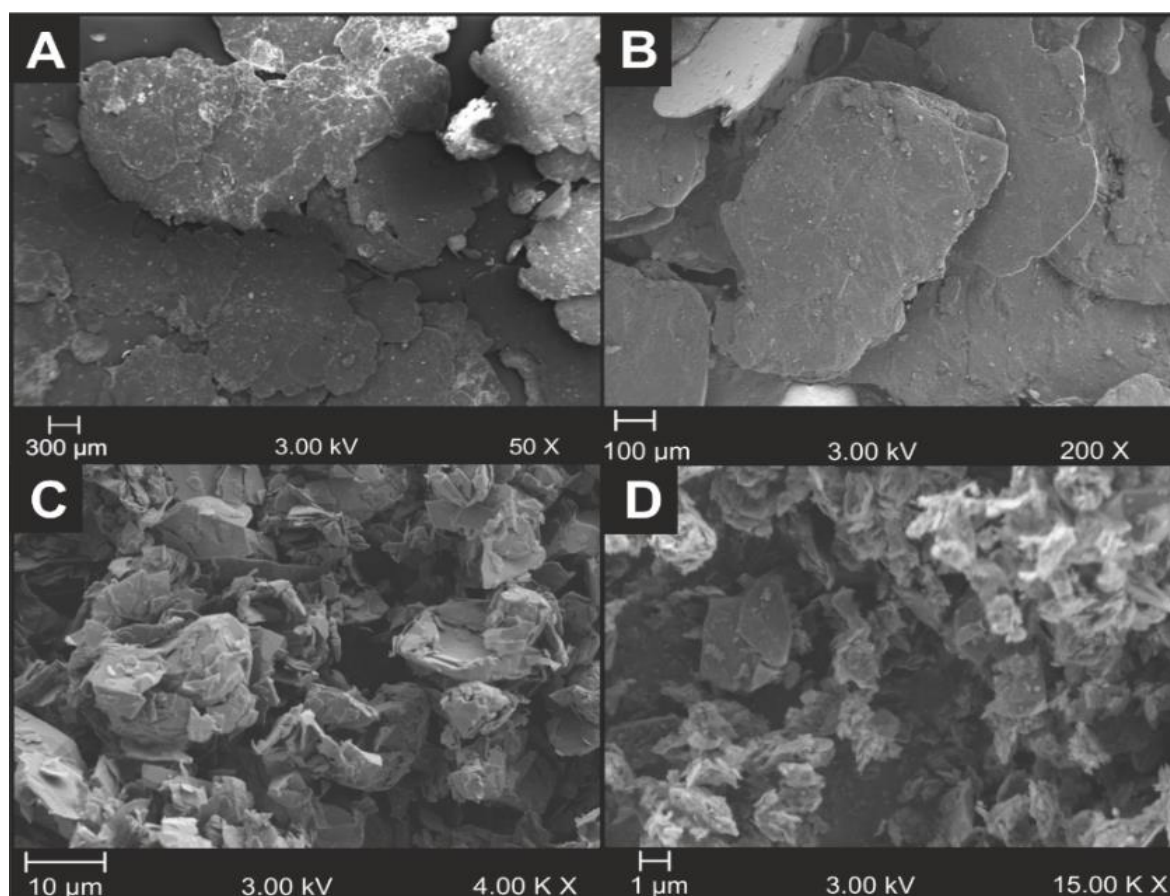


Figure 2.1. Structural characterisation of the graphite lateral flakes *via* SEM, A) kish graphite, B) flake graphite, C) high crystalline natural graphite, D) nanostructured graphite - 250. Note, the necessary difference in magnification to report the variation in lateral flake size.

The graphene flakes utilised throughout this study were also individually characterised. Transmission electron microscopy (TEM) images of the five graphene powders demonstrated the lateral flake sizes (Figure 2.2). It was evident that the graphene consisted of a mixture of single- and *quasi*- layer graphene (Brownson *et al.*, 2014; Brownson *et al.*, 2013; Brownson *et al.*, 2012b). The intraplanar microcrystalline size,  $L_a$  (lateral flake size), exhibited the following sizes: 2.3  $\mu\text{m}$  ( $\pm 0.5 \mu\text{m}$ ) for AO-1; 9.4  $\mu\text{m}$  ( $\pm 0.7 \mu\text{m}$ ) for AO-2; 5.0  $\mu\text{m}$  ( $\pm 0.3 \mu\text{m}$ ) for AO-3; 4.0  $\mu\text{m}$  ( $\pm 0.3 \mu\text{m}$ ) for AO-4; and 1.3  $\mu\text{m}$  ( $\pm 0.1 \mu\text{m}$ ) for C1 ( $n = 3$ ).

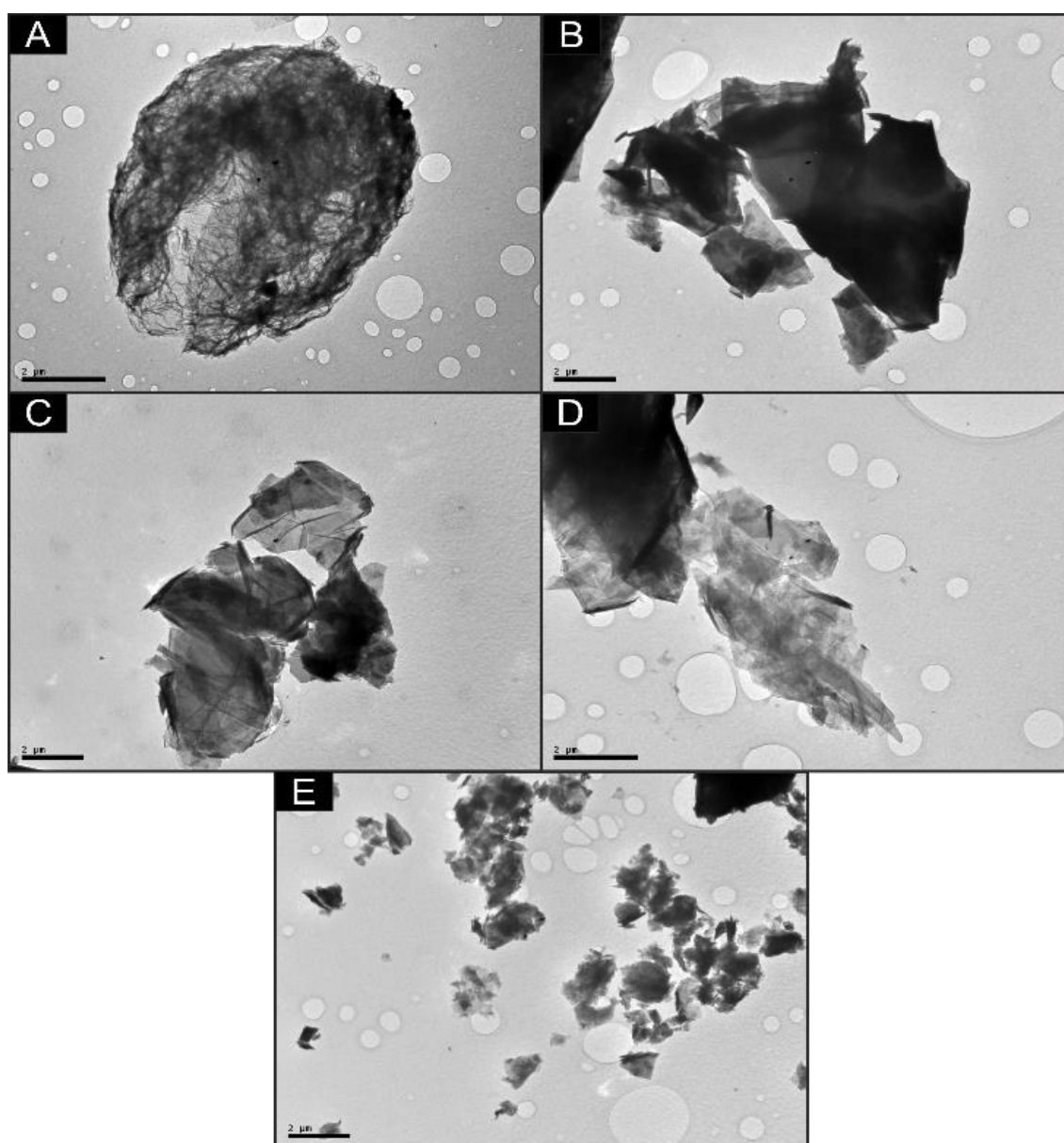


Figure 2.2. Structural characterisation of the graphene lateral flakes *via* TEM, A) A0-1, B) A0-2, C) A0-3, D) A0-4 and E) C1. Note, the scale bar in each image was 2  $\mu\text{m}$ .

Scanning electron microscope-energy-dispersive X-ray microanalysis of the carbon flakes showed their elemental composition (Table 2.1). As expected, all the samples consisted mostly of carbon (> 88.0 % carbon content) with oxygenated species present. The presence of oxygenated species can lead to increased sensitivity towards structural alterations on the electrode surface, whilst utilising inner-sphere probes such as potassium(II) ferrocyanide (Brownson *et al.*, 2012b). The other elements observed in trace amounts could have been present in the procured products as part of the manufacturing process, or incorporated from the surrounding environment during electrode fabrication.

Table 2.1. Scanning electron microscope-energy-dispersive X-ray microanalysis (SEM-EDX) analysis of graphite and graphene flakes showing average atomic percentage ( $n = 3$ ).

Elemental composition	Average Atomic Percentage (%)								
	Graphene Flakes					Graphite Flakes			
	AO-1	AO-2	AO-3	AO-4	C1	Kish	Flake	HCN	NSG
Carbon	91.33	96.75	95.50	96.20	96.43	96.25	88.23	96.85	96.20
Oxygen	4.56	3.01	4.27	3.18	3.03	3.45	10.62	2.88	3.56
Silicon	0.63	0.24	0.23	0.08	0.25	0.25	0.81	0.20	0.18
Sodium				0.26					
Sulphur	1.02				0.19				
Potassium	2.32								
Aluminium				0.11	0.27	0.07	0.34	0.06	0.14
Calcium				0.50					
Magnesium								0.05	0.04

## 2.3.2 Electrochemical Analysis

### 2.3.2.1 Hexaammineruthenium(III) Chloride Redox Probe

The graphite comprised paste electrodes were tested against the hexaammineruthenium(III) chloride redox probe (Table 2.3; Figure 2.3). Nanostructured graphite – 250 produced the shortest  $\Delta E_p$  at  $100 \text{ mV s}^{-1}$  at 78.1 mV, followed by the EPPG

control at 80.57 mV, this was followed by HCN graphite, 85.6 mV, flake graphite, 118.3 mV and finally kish graphite, which produced the largest peak-to-peak separation of 141.0 mV. The average  $k^0$  values obtained (Table 2.2), demonstrated that nanostructured graphite – 250 produced the fastest rate of electron transfer –  $3.48 \times 10^{-3} \text{ cm s}^{-1}$ , compared to Kish graphite (which comprised the largest average lateral flake size tested in this study), which produced the slowest rate of electron transfer –  $1.69 \times 10^{-3} \text{ cm s}^{-1}$ . Cyclic voltammetric profiles of the graphite paste electrodes and the EPPG control recorded with 1 mM hexaammineruthenium(III) chloride in 1 M KCl at a scan rate of  $100 \text{ mV s}^{-1}$ , demonstrated that a smaller lateral flake size resulted in the fastest electron transfer, as nanostructured graphite exhibited the greatest response (Figure 2.3).

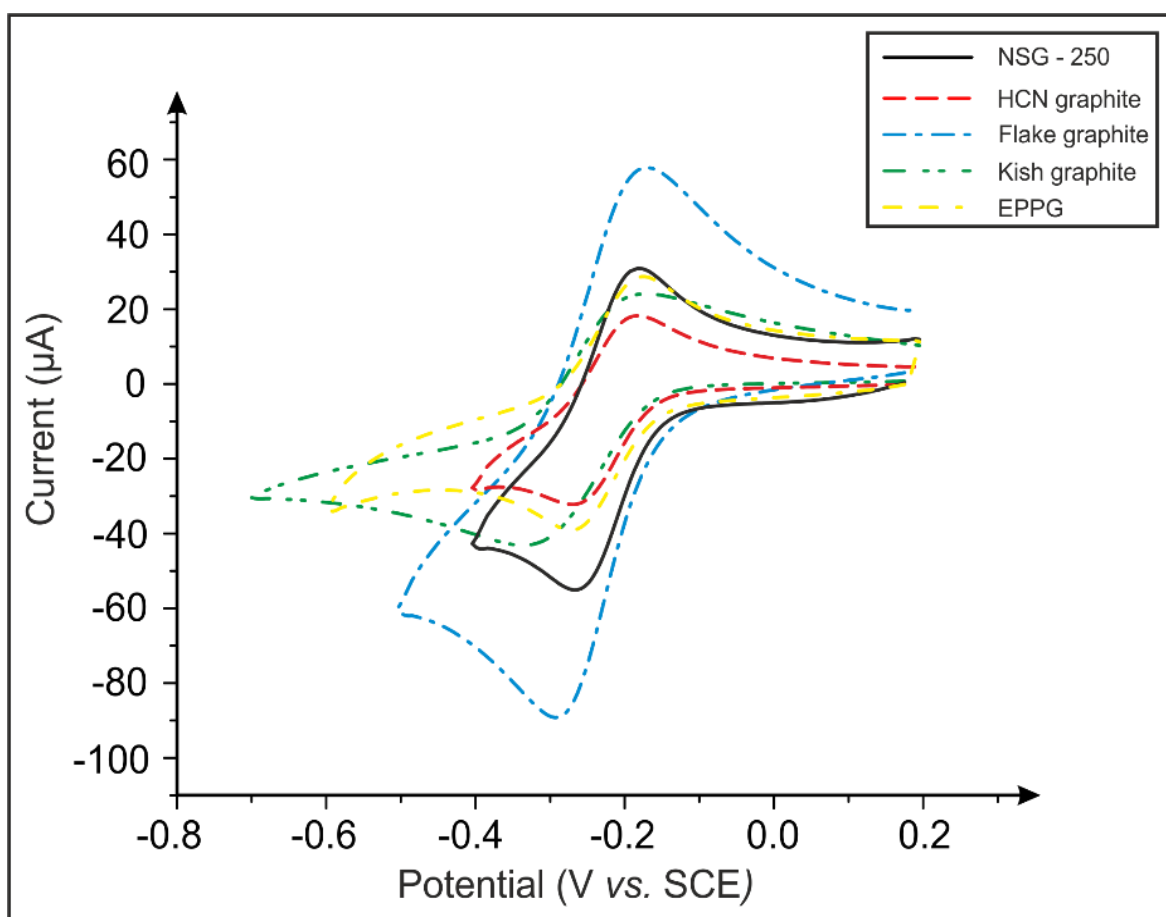


Figure 2.3. Cyclic voltammetric profiles recorded using the graphite paste electrodes. Redox probe: 1 mM Hexaammineruthenium(III) chloride in 1 M KCl. Scan rate:  $100 \text{ mV s}^{-1}$  ( $n = 3$ ).

The graphene electrodes were also tested against the hexaammineruthenium(III) chloride redox probe (Table 2.4; Figure 2.4). C1 demonstrated the shortest  $\Delta E_p$  at  $100 \text{ mV}$

$s^{-1}$  – 64.5 mV, followed by AO-2 – 65.5 mV, AO-4 – 73.02 mV, AO-3 – 85.6 mV and finally, AO-1 – 93.2 mV. Heterogenous electron transfer (HET) rate calculations revealed that C1 also produced the fastest rate of electron transfer  $5.45 \times 10^{-3} \text{ cm s}^{-1}$ , followed by AO-2 –  $4.38 \times 10^{-3} \text{ cm s}^{-1}$ , AO-4 –  $2.99 \times 10^{-3} \text{ cm s}^{-1}$ , AO-3 –  $2.75 \times 10^{-3} \text{ cm s}^{-1}$ , and finally, AO-1 –  $2.37 \times 10^{-3} \text{ cm s}^{-1}$ . However, when compared to the graphite paste electrodes, the difference between the overall significant impact (or improvement observed) in regards to rates of electron transfer and the variation in flake size was minimal, possibly due to the electrodes approaching the electrochemical reversible limit.

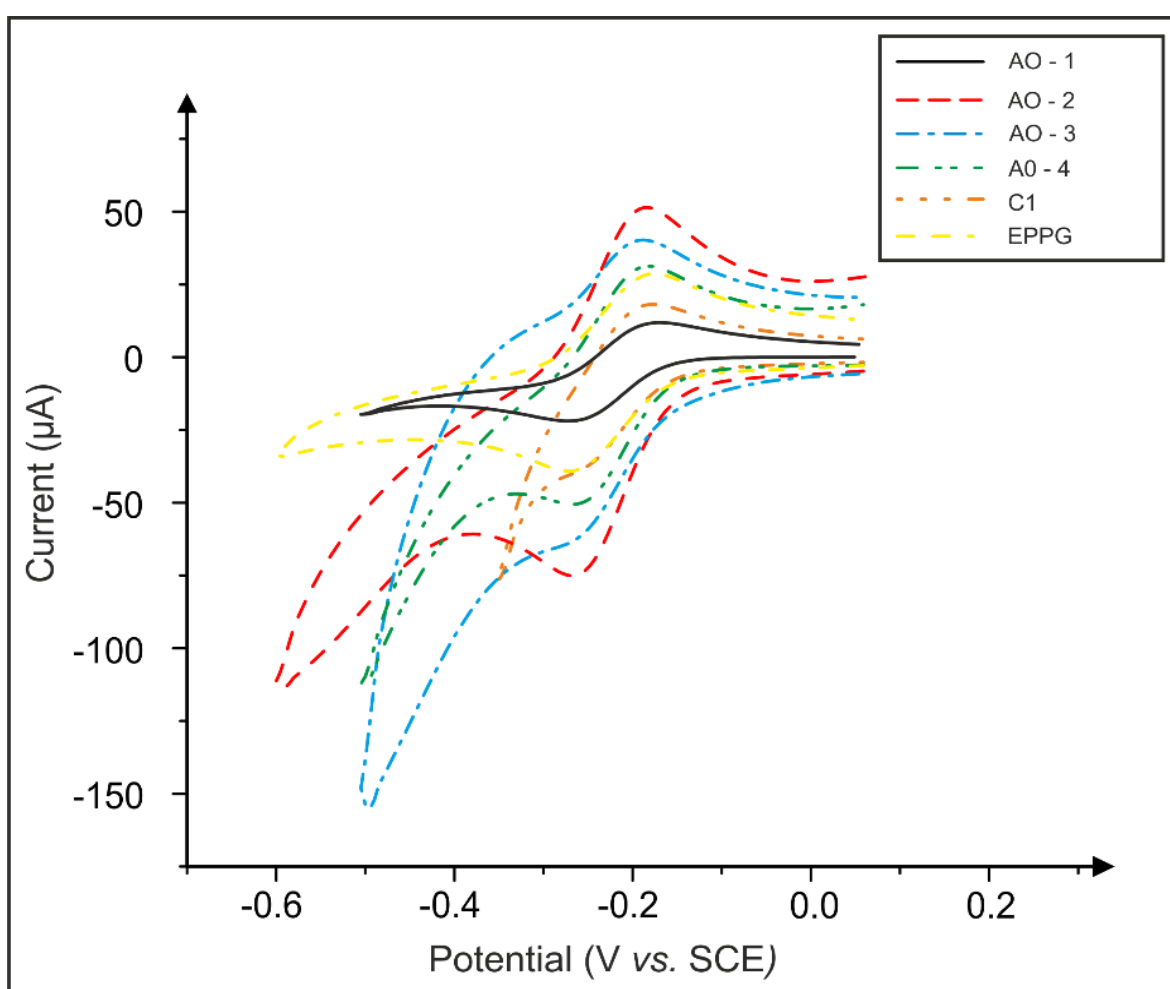


Figure 2.4. Cyclic voltammetric profiles of the graphene paste electrodes. Redox probe: 1 mM Hexaammineruthenium(III) chloride in 1 M KCl. Scan rate:  $100 \text{ mV s}^{-1}$  ( $n = 3$ ).

### 2.3.2.2 Potassium Ferrocyanide(II) Redox Probe

Potassium ferrocyanide(II) was selected for utilisation throughout this study, due to its status as an inner-sphere probe. Typical cyclic voltammetry profiles were recorded using the graphite electrodes tested (Table 2.3; Figure 2.5), HCN graphite produced the shortest  $\Delta E_p$  at  $100 \text{ mV s}^{-1}$  - 105.8 mV, followed by the EPPG electrode – 133.4 mV, followed by Flake graphite – 143.5 mV and then Nanostructured graphite 250 - 151.1 mV. Kish graphite produced the largest peak-to-peak separation of 833.4 mV. The calculated HET rate kinetic ( $k^0$ ) values showed that flake graphite was the most efficient at electron transfer against this specific redox probe producing a  $k^0$  of  $1.93 \times 10^{-3} \text{ cm s}^{-1}$ . This was followed by HCN graphite producing the second fastest electron transfer rate ( $1.79 \times 10^{-3} \text{ cm s}^{-1}$ ), whilst nanostructured graphite-250 produced a  $k^0$  of  $1.71 \times 10^{-3} \text{ cm s}^{-1}$ . Kish graphite produced the slowest average  $k^0$  value,  $6.04 \times 10^{-5} \text{ cm s}^{-1}$ , whilst comprising the largest average lateral flake size ( $1,389.00 \text{ }\mu\text{m}$  ( $\pm 147.5 \text{ }\mu\text{m}$ )) employed throughout this study.

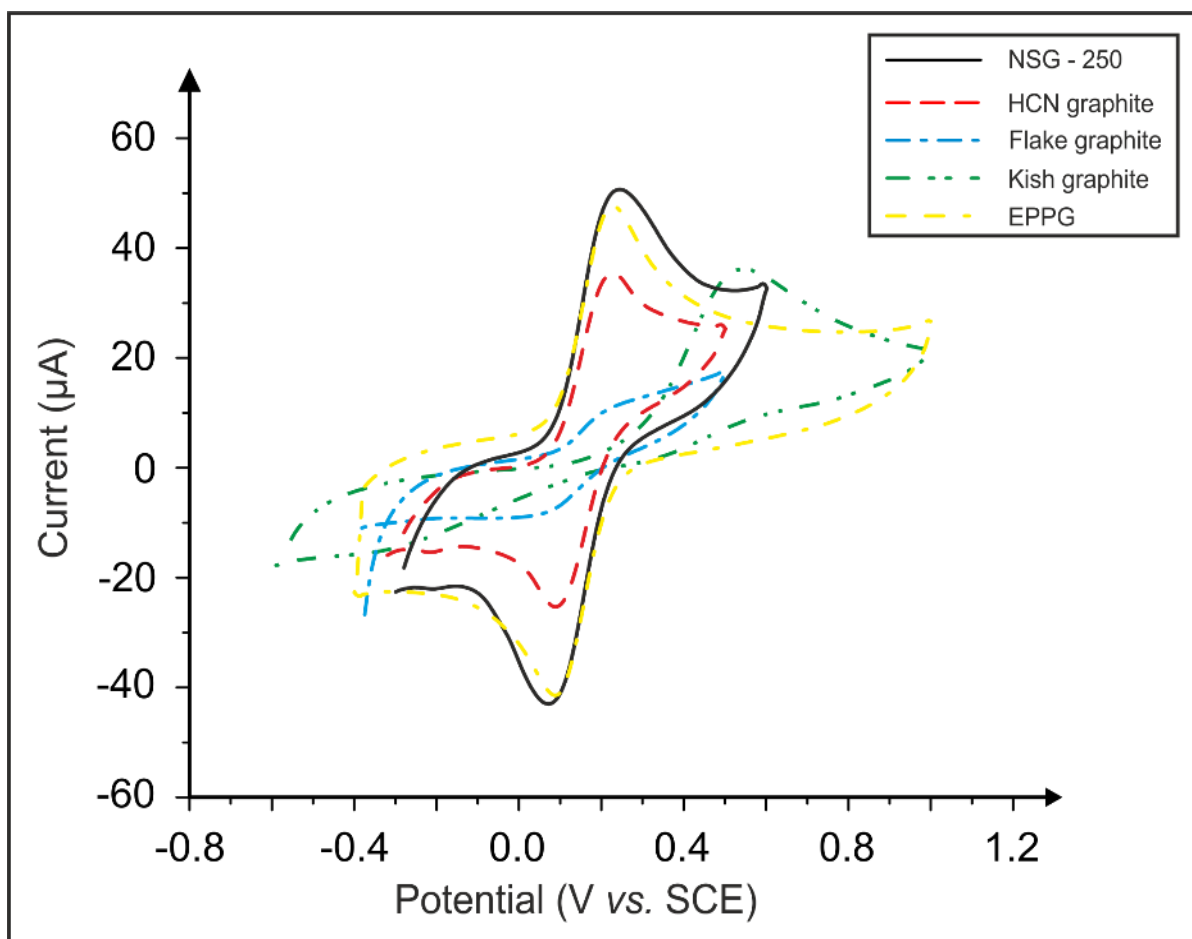


Figure 2.5. Cyclic voltammetric profiles recorded of the graphite paste electrodes. Redox probe: 1 mM potassium ferrocyanide(II) in 1 M KCl. Scan rate:  $100 \text{ mV s}^{-1}$  ( $n = 3$ ).

The graphene paste electrodes were also tested against potassium ferrocyanide(II) (Table 2.4; Figure 2.6), C1 produced the shortest  $\Delta E_p$  at  $100 \text{ mV s}^{-1}$  - 98.2 mV, whilst AO-2 produced a  $\Delta E_p$  of 176.2 mV. Heterogenous electron transfer rate calculations revealed that C1 produced the fastest rate of electron transfer ( $2.71 \times 10^{-3} \text{ cm s}^{-1}$ ) whilst AO-3 produced the least efficient HET rate ( $7.65 \times 10^{-4} \text{ cm s}^{-1}$ ). These results suggest that in the case of the graphene paste-electrodes utilised, there was no correlation between a decrease in lateral flake size and an increase in electrochemical activity.

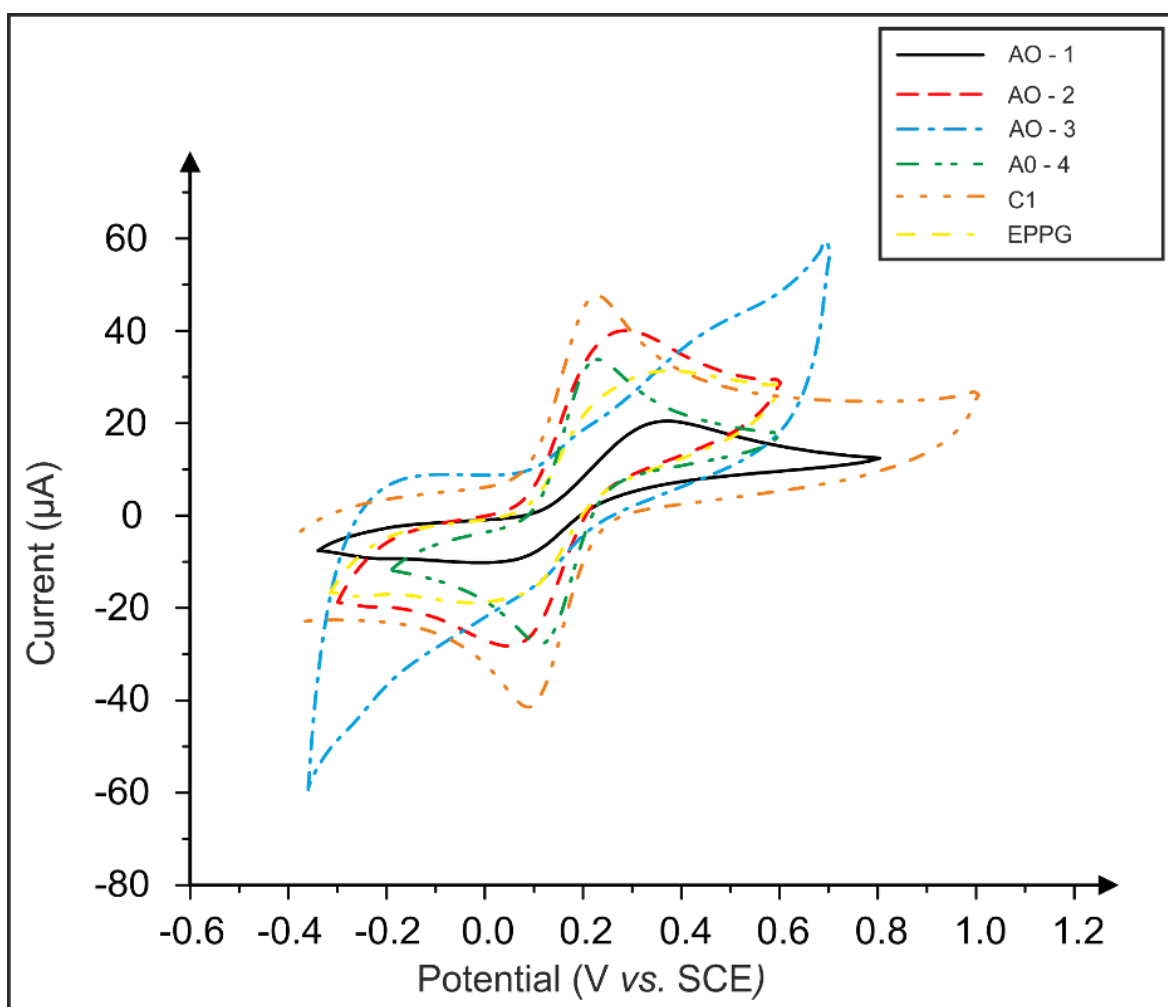


Figure 2.6. Cyclic voltammetric profiles recorded of the graphene paste electrodes. Redox probe: 1 mM potassium ferrocyanide(II) in 1 M KCl. Scan rate:  $100 \text{ mV s}^{-1}$  ( $n = 3$ ).

Table 2.2. Comparison of the electrochemical behaviour of the four graphitic electrodes against, 1 mM hexaammineruthenium(III) chloride and 1 mM potassium ferrocyanide(II) redox probes (with supporting 0.1 M KCl electrolyte). The redox probes were characterised prior to use with an EPPG electrode and  $k^0$  values of  $3.33 \times 10^{-3}$  and  $1.80 \times 10^{-3}$  were recorded for hexaammineruthenium(III) chloride and potassium ferrocyanide(II), respectively ( $n = 3$ ).

Graphite material utilised	Average Lateral Flake Size ( $n = 20$ ) ( $\mu\text{m}$ )	$k^0$ ( $\text{cm s}^{-1}$ )	$A_{\text{eff}}$ ( $\text{cm}^2$ )	$A_{\text{real}}$ (%)	$\Delta E_p$ (mV) at $100 \text{ mV s}^{-1}$
<b>Hexaammineruthenium(III) chloride / 0.1 M KCl</b>					
Kish graphite	1389.90 ( $\pm 147.5$ )	$1.69 \times 10^{-3}$	0.169	84.1	141.0 ( $\pm 2.8$ )
Flake graphite	608.0 ( $\pm 39.8$ )	$2.05 \times 10^{-3}$	0.208	103.5	118.3 ( $\pm 3.6$ )
HCN graphite	12.2 ( $\pm 0.7$ )	$3.35 \times 10^{-3}$	0.147	73.1	85.6 ( $\pm 7.1$ )
Nanostructure graphite – 250	0.5 ( $\pm 0.1$ )	$3.48 \times 10^{-3}$	0.150	74.6	78.1 ( $\pm 3.6$ )
<b>Potassium ferrocyanide(II) / 0.1 M KCl</b>					
Kish graphite	1389.9 ( $\pm 147.5$ )	$6.04 \times 10^{-5}$	-	-	833.4 ( $\pm 1.1$ )
Flake graphite	608.0 ( $\pm 39.8$ )	$1.93 \times 10^{-3}$	-	-	143.5 ( $\pm 35.0$ )
HCN graphite	12.2 ( $\pm 0.7$ )	$1.79 \times 10^{-3}$	-	-	105.8 ( $\pm 7.1$ )
Nanostructure graphite – 250	0.5 ( $\pm 0.1$ )	$1.71 \times 10^{-3}$	-	-	151.1 ( $\pm 7.1$ )

Table 2.3. Comparison of the electrochemical behaviour of the five graphene electrodes against, 1 mM hexaammineruthenium(III) chloride and 1 mM potassium ferrocyanide(II) redox probes (with supporting 0.1 M KCl electrolyte). The redox probes were characterised prior to use with an EPPG electrode and  $k^0$  values of  $3.33 \times 10^{-3}$  and  $1.80 \times 10^{-3}$  were recorded for hexaammineruthenium(III) chloride and potassium ferrocyanide(II), respectively ( $n = 3$ ).

Graphene material utilised	Average Lateral Flake Size ( $n = 20$ ) ( $\mu\text{m}$ )	$k^0$ ( $\text{cm s}^{-1}$ )	$A_{\text{eff}}$ ( $\text{cm}^2$ )	$A_{\text{real}}$ (%)	$\Delta E_p$ (mV) at $100 \text{ mV s}^{-1}$
<b>Hexaammineruthenium(III) chloride / 0.1 M KCl</b>					
AO-1	9.4 ( $\pm 0.7$ )	$2.37 \times 10^{-3}$	0.083	41.2	93.2 ( $\pm 3.6$ )
AO-3	5.0 ( $\pm 0.3$ )	$2.75 \times 10^{-3}$	0.190	94.5	85.6 ( $\pm 14.3$ )
AO-4	4.0 ( $\pm 0.3$ )	$2.99 \times 10^{-3}$	0.162	80.6	73.0 ( $\pm 2.00$ )
AO-2	2.3 ( $\pm 0.5$ )	$4.38 \times 10^{-3}$	0.225	111.9	65.5 ( $\pm 3.6$ )
C1	1.3 ( $\pm 0.1$ )	$5.45 \times 10^{-3}$	0.115	57.2	64.5 ( $\pm 3.6$ )
<b>Potassium ferrocyanide(II) / 0.1 M KCl</b>					
AO-1	9.4 ( $\pm 0.7$ )	$4.40 \times 10^{-4}$	-	-	299.6 ( $\pm 14.4$ )
AO-3	5.0 ( $\pm 0.3$ )	$7.65 \times 10^{-4}$	-	-	332.3 ( $\pm 24.7$ )
AO-4	4.0 ( $\pm 0.3$ )	$1.15 \times 10^{-3}$	-	-	209.0 ( $\pm 18.5$ )
AO-2	2.3 ( $\pm 0.5$ )	$1.23 \times 10^{-3}$	-	-	176.2 ( $\pm 0.1$ )
C1	1.3 ( $\pm 0.1$ )	$2.71 \times 10^{-3}$	-	-	98.2 ( $\pm 2.1$ )

### 2.3.3 Edge to Basal Plane Ratio

In order to establish if the edge planes present in the graphite and graphene electrodes were responsible for the electrochemical activity demonstrated, the edge to basal plane ratio was calculated *via* equations 2.6 and 2.7 (Table 2.5).

Results from the graphite electrodes demonstrated that nanostructured graphite – 250 with the smallest average lateral flake size ( $0.5 \mu\text{m} (\pm 0.1 \mu\text{m})$ ) comprised the greatest edge plane percentage 27.99 % (basal – 72.01 %). Flake graphite with the second largest average lateral flake size ( $608.0 \mu\text{m} (\pm 39.8 \mu\text{m})$ ) comprised the least amount of edge planes at a ratio of 0.02 % : 99.98 % (edge : basal plane ratio). In the case of the graphite electrodes, an increase in the edge plane ratio had a direct correlation towards  $k^0$  values obtained (Table 2.5).

Table 2.4. Calculated edge to basal plane ratios for the graphite and graphene paste electrodes. Redox probe: 1 mM Hexaammineruthenium(III) chloride with supporting 0.1 M KCl electrolyte ( $n = 3$ ).

Material utilised	Average Lateral Flake Size ( $n = 20$ ) ( $\mu\text{m}$ )	Total specific capacitance ( $\mu\text{F cm}^2$ )	Edge plane (%)	Basal plane (%)	$k^0$ ( $\text{cm s}^{-1}$ )
<b>Graphite paste electrodes</b>					
Kish	1389.9 ( $\pm 147.5$ )	0.20	1.06	98.94	$1.69 \times 10^{-3}$
Flake	608.0 ( $\pm 39.8$ )	0.99	0.02	99.98	$2.05 \times 10^{-3}$
High crystalline natural graphite	12.2 ( $\pm 0.7$ )	0.23	1.11	98.89	$3.35 \times 10^{-3}$
Nanostructured graphite - 250	0.5 ( $\pm 0.1$ )	20.31	27.99	72.01	$3.48 \times 10^{-3}$
<b>Graphene paste electrodes</b>					
AO-1	9.4 ( $\pm 0.7$ )	1.48	0.70	99.30	$2.37 \times 10^{-3}$
AO-3	5.0 ( $\pm 0.3$ )	3.33	3.38	96.62	$2.75 \times 10^{-3}$
AO-4	4.0 ( $\pm 0.3$ )	15.86	21.53	78.47	$2.99 \times 10^{-3}$
AO-2	2.3 ( $\pm 0.5$ )	11.64	15.42	84.58	$4.38 \times 10^{-3}$
C1	1.3 ( $\pm 0.1$ )	33.57	47.20	52.80	$5.45 \times 10^{-3}$

Against the graphene paste electrodes, AO-1 which was the least effective in terms of HET rate ( $2.37 \times 10^{-3} \text{ cm s}^{-1}$ ) comprised the lowest edge plane percentage (0.70 %). The electrode with the smallest average lateral flake size (C1;  $1.3 (\pm 0.1) \mu\text{m}$ ), produced an edge plane percentage of 47.20 % and a  $k^0$  value of  $5.45 \times 10^{-3} \text{ cm s}^{-1}$ . This further implied that for the graphene electrodes tested, as the lateral flake size reached a critical point (*ca.*  $< 2 \mu\text{m}$ ) the edge to basal plane ratio became less significant, possibly due to the entire geometric structure of the flakes becoming electrochemically active.

### **2.3.4 Density Functional Theory (DFT)**

To provide further evidence of this phenomenon, DFT simulations were performed on a sample set of smaller graphene lateral flake sizes ( $2 \times 3$ ,  $3 \times 5$  and  $6 \times 11$  carbon atoms). Electrostatic potential maps (ESP) of the graphene models were then generated (Figure 2.7). In regards to the smaller graphene lateral flakes ( $2 \times 3$  and  $3 \times 5$ ), electron transfer occurred in the central region of the flakes, in comparison to the larger flake set ( $6 \times 11$ ), where the outer regions of the flakes (*i.e.* edge planes) demonstrated a lower electrostatic potential.

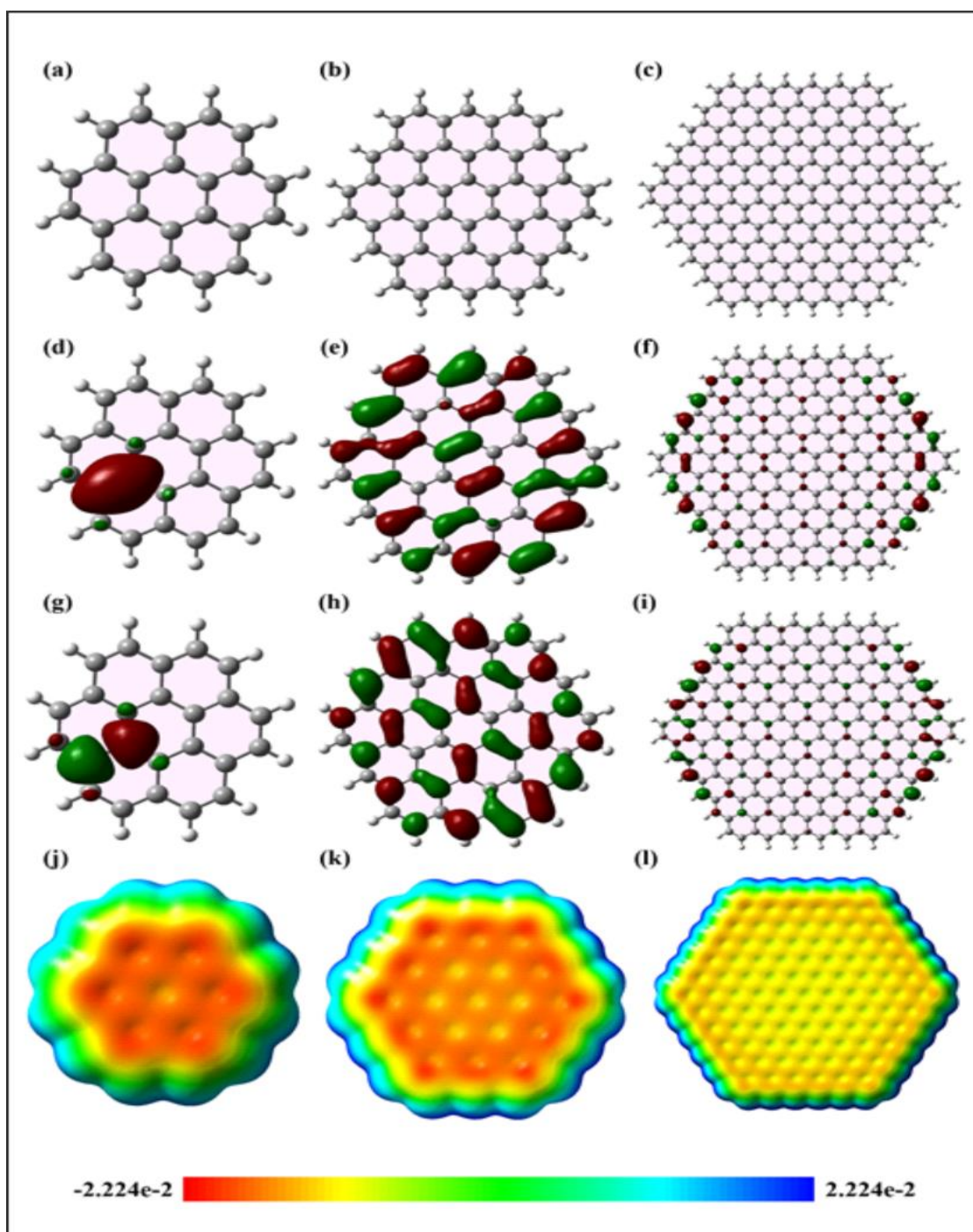


Figure 2.7. DFT calculations on graphene flakes of different lateral flake size sizes (a)  $2 \times 3$ , b)  $3 \times 5$  and c)  $6 \times 11$  carbon atoms); (a-c) optimized geometry, (d-f) highest occupied molecular orbital (HOMO), (g-i) lowest unoccupied molecular orbital (LUMO) and (j-l) Electrostatic potential maps of  $2 \times 3$ ,  $3 \times 5$  and  $6 \times 11$  (ring  $\times$  row) flakes, respectively (Slate *et al.*, 2018a).

## 2.4 Discussion

Most fundamental studies explore the electrochemical properties of graphitic electrodes by focusing primarily either on the orientation of highly ordered pyrolytic graphite (HOPG) or more recently in the case of graphene electrodes, through the comparison of the number of graphene layers present, *i.e.* single- vs. *quasi*- vs. multi- layers (Brownson *et al.*, 2014; Brownson *et al.*, 2013; Brownson *et al.*, 2012b; McCreery, 2008). However, a key structural attribute of carbonaceous electrode materials is their lateral flake size (*i.e.* intraplanar microcrystalline size ( $L_a$ )). Graphite surfaces consist of a heterogeneous structure and throughout the field of electrochemistry the current consensus is that the variation in overall electrochemical reactivity is due to the presence of two distinct structural contributions, namely the edge and basal planes (McCreery, 2008; Neumann *et al.*, 2011). These structural contributions are fundamental to the behaviour elicited by both graphite and graphene electrodes (McCreery, 2008; Neumann *et al.*, 2011).

This study addressed the void in knowledge, in regards to the electrochemical contribution of the edge to basal plane ratio, which was not reported throughout the literature prior to this research (Slate *et al.*, 2018a). More specifically, the variation in the lateral flake size of graphite and graphene powders and consequently the fabricated paste electrodes, and how this altered the edge plane density on the surface of the electrodes, was investigated by determining the difference in HET kinetics (Slate *et al.*, 2018a).

### 2.4.1 Graphite Paste Electrodes

Throughout this study, a reduction in lateral flake size of the graphite paste electrodes demonstrated a marked increase in HET rates and a reduction in the peak-to-peak separation ( $\Delta E_p$ ). When tested against the outer-sphere redox probe, hexaammineruthenium(III) chloride, kish graphite which comprised the largest average lateral flake size (1389.9  $\mu\text{m}$  ( $\pm 147.5 \mu\text{m}$ )) produced the slowest, least favourable HET rate ( $1.69 \times 10^{-3} \text{ cm s}^{-1}$ ) and the largest peak-to-peak separation at 100  $\text{mV s}^{-1}$  (141.0 ( $\pm 2.8$ )  $\text{mV}$ ). This was compared with nanostructured graphite – 250 which comprised the smallest average lateral flake size (0.5  $\mu\text{m}$  ( $\pm 0.1 \mu\text{m}$ )) and produced the fastest, most favourable HET rate ( $3.48 \times 10^{-3} \text{ cm s}^{-1}$ ) and the shortest peak-to-peak separation at 100  $\text{mV s}^{-1}$  (78.1 ( $\pm 3.6$ )  $\text{mV}$ ). Calculation of the percentage edge/basal plane ratio also revealed that

nanostructured graphite – 250 comprised the highest edge plane percentage (27.99 %) of the graphite paste electrodes.

The results from this thesis demonstrated that a reduction in average lateral flake size resulted in an increase in the number of edge plane like sites/defects, which in turn resulted in a faster, more efficient HET rate and a shorter  $\Delta E_p$ , which indicated enhanced electrochemical activity. Ultimately, the variations in the graphite lateral flake sizes may lead to a difference in the comprising edge to basal plane ratio observed. The results in this thesis are in agreement with a study by Banks *et al.* (2005), where the surface geometry of graphitic flakes was a pivotal factor in the electrochemical response recorded. This study demonstrated that the electrode kinetics of EPPG electrodes were at least three orders of magnitude faster, and therefore more effective, when directly compared against basal plane pyrolytic graphite (BPPG) electrodes (Banks *et al.*, 2005).

When tested against the inner-sphere redox probe, potassium ferrocyanide(II), Kish graphite produced the slowest HET rate ( $6.04 \times 10^{-5} \text{ cm s}^{-1}$ ) and the largest peak-to-peak separation at  $100 \text{ mV s}^{-1}$  ( $833.4 (\pm 1.1) \text{ mV}$ ). Flake graphite produced the fastest HET rate ( $1.93 \times 10^{-3} \text{ cm s}^{-1}$ ), whilst, HCN graphite produced the shortest  $\Delta E_p$  at  $100 \text{ mV s}^{-1}$  ( $105.8 (\pm 7.1) \text{ mV}$ ). This demonstrated that the graphite material comprising the largest lateral flake size produced the most unfavourable electrochemical response. However, no overall significant trend was observed during electrochemical analysis of the graphite paste electrodes against the inner-sphere redox-probe, potassium ferrocyanide(II). This inconsistency when compared to the results obtained against the hexaammineruthenium(III) chloride redox probe could be due to the inner-sphere status of potassium ferrocyanide(II). Inner-sphere redox probes are able to penetrate the inner Helmholtz plane, leading to direct contact between the redox probe and the electrode surface, potentially introducing oxygenated species and ligands (Tanimoto and Ichimura, 2013). Oxygenated species and ligands can have a detrimental or beneficial effect on electron transfer and therefore the rate constant of the reaction between inner-sphere redox probes and electrode. This process is highly dependent upon the physical structure of the electrode surface (Tanimoto and Ichimura, 2013). Scanning electron microscope-energy-dispersive X-ray microanalysis demonstrated that throughout this study all the electrodes contained oxygen (average of 4.28 %), and therefore results obtained against potassium ferrocyanide(II) could be skewed due to increased sensitivity leading to

convoluted results if the surface state is not accurately characterised. Furthermore, the confirmed presence of trace elements could also have a beneficial or detrimental effect on electrode activity.

## 2.4.2 Graphene Paste Electrodes

Results obtained from varying the size of graphene paste electrodes indicated that a reduction in the average lateral flake size gave rise to a more effective electrochemical response. However, the overall significant impact towards electrochemical response was minimal when compared to the graphite electrodes. This was possibly due to electrodes becoming close to the electrochemical reversible limit of the redox probe studied ( $\sim 57.0$  mV) (Elgrishi *et al.*, 2018; García-Miranda Ferrari *et al.*, 2018). When tested against the outer-sphere redox probe, hexaammineruthenium(III) chloride, AO-1 with the largest average lateral flake size ( $9.4 \mu\text{m} (\pm 0.7 \mu\text{m})$ ) elicited the slowest HET rate ( $2.37 \times 10^{-3} \text{ cm s}^{-1}$ ) and the largest  $\Delta E_p$  at  $100 \text{ mV s}^{-1}$  ( $93.2 \text{ mV} (\pm 3.6 \text{ mV})$ ). Whilst C1, with the smallest average lateral flake size ( $1.3 \mu\text{m} (\pm 0.1 \mu\text{m})$ ), produced the fastest HET rate ( $5.45 \times 10^{-3} \text{ cm s}^{-1}$ ) and the shortest  $\Delta E_p$  at  $100 \text{ mV s}^{-1}$  ( $64.5 \text{ mV} (\pm 3.6 \text{ mV})$ ). The recorded edge to basal plane value provided further evidence towards the importance of a reduction in lateral flake size in relation to an improved electrochemical response, AO-1 with the largest average lateral flake size comprised the lowest edge plane percentage (0.70 %) compared to C1 which comprised the highest edge plane percentage (47.20 %).

When tested against the inner-sphere redox probe, potassium ferrocyanide(II), the same trend was seen with C1, which comprised the smallest average lateral flake size ( $1.3 \mu\text{m} (\pm 0.1 \mu\text{m})$ ) and produced the fastest HET rate ( $2.71 \times 10^{-3} \text{ cm s}^{-1}$ ) with the shortest  $\Delta E_p$  at  $100 \text{ mV s}^{-1}$  ( $98.2 (\pm 2.1) \text{ mV}$ ). AO-1 comprising the largest average lateral flake size ( $9.4 \mu\text{m} (\pm 0.7 \mu\text{m})$ ) produced the slowest HET rate ( $4.40 \times 10^{-4} \text{ cm s}^{-1}$ ), whilst AO-3 comprising an average lateral flake size ( $5.0 \mu\text{m} (\pm 0.3 \mu\text{m})$ ) produced the largest  $\Delta E_p$  of  $100 \text{ mV s}^{-1}$  ( $332.3 \text{ mV} (\pm 24.7 \text{ mV})$ ). However, the results against the potassium ferrocyanide(II) redox probe could potentially be convoluted due to its status as an inner-sphere probe and therefore its interactions with surface and functional groups on the electrode (Tanimoto and Ichimura, 2013).

### 2.4.3 Electrostatic Potential Maps of Graphene

Atomic charges can be calculated in order to predict the electronic properties and reactivity of molecules (Dena and Hassan, 2016). Gaussian software can predict the electrostatic potential energy distribution on the entirety of a molecule *via* the atomic charges of the molecule, to build up an electrostatic potential map (ESP). The electrostatic potential energy is maximum where the colour of the ESP was blue, which indicated a high relative positive charge. A red colour on the ESP indicated the minimum electrostatic potential energy (high relative negative charge), as ESPs are related to molecule electron density, electron concentration on the molecular structure can be determined (Mansour *et al.*, 2013). The ESPs obtained from this study were simulated using graphene sheets (with varying lateral flake sizes) and the level of theory used in geometry optimisation was (B3LYP/6-31G\*\*) to investigate the influence of lateral flake size on the electronic density and its effect on recorded HET rates. The selected model sizes used throughout this study were in agreement with previous literature concerning graphene material modelling (Brownson *et al.*, 2011).

The ESPs of the graphene flakes ( $2 \times 3$ ,  $3 \times 5$  and  $6 \times 11$  (ring  $\times$  row)) demonstrated that an orange colour was concentrated in the central region of the flakes with a reduction in lateral flake size (Figure 2.7). This indicated that the central carbon atoms of the smaller graphene flakes studied  $2 \times 3$  and  $3 \times 5$  possessed high electron clouds. However, in the case of the larger graphene flake ( $6 \times 11$ ), the electron cloud (*i.e.* low electrostatic potential) was directed toward the edge plane regions located around the periphery of the flake. This provided further evidence for the HET rates and  $\Delta E_p$  values reported previously in this study as the electron-transfer process occurred in the central regions of the smaller graphene flakes (*i.e.* a larger area) as opposed to just the edges as demonstrated in the larger graphite flakes. These results were in agreement with previously published literature (Ji *et al.*, 2006; Kampouris and Banks, 2010; Yuan *et al.*, 2013).

## 2.5 Conclusion

This study is the first to report the correlation between structural composition and electrochemical reactivity of graphite and graphene paste electrodes. This phenomenon has been determined by varying the lateral flake size. The findings were attributed to the comprising 'edge to basal plane ratio' of the various flake sizes. When using an outer-sphere probe, a reduction in lateral flake size resulted in an enhanced number of edge planes present on the electrode surface, this resulted in an improvement in electrochemical response. Therefore, it was inferred that this improvement in electrochemical activity was directly related to the lateral flake size of graphite-based electrodes. Interestingly, the results obtained from the study of graphene electrodes (which comprised the smallest range of lateral flake sizes) demonstrated that the same trend was observed until a distinct point, after which the number of edge planes available to contribute towards the HET became such that no further enhanced electrochemical activity was observed. This was likely due to the process becoming close to the reversible limit. An inner-sphere probe (potassium ferrocyanide) was also combined with the graphite and graphene paste electrodes and similar underlying trends were observed. However, these trends were less apparent, due to the possible interactions between the redox probe and favourable surface groups. The above results were further supported by DFT calculations, which elicited a similar trend using simulations of graphene with varying lateral flake size.

This study highlights lateral flake size as an important factor when selecting possible carbonaceous electrode materials with favourable electrochemical responses, such as an increased HET rate. The insights given in this study suggest that novel materials (*i.e.* 2D-nanomaterials) selected for development as potential electrode materials should have a higher edge plane density, leading to an enhanced electrochemical effect. Future research should focus on optimising the flake sizes in carbonaceous electrode materials for potential application in energy storage materials and electrochemical sensors.

# **Chapter 3 – Fabrication and Characterisation of the Three-Dimensional Printed Graphene Electrodes**

## 3.1 Introduction

Additive manufacturing, also known more commonly as three dimensional (3D) printing provides a unique platform for both the rapid design and fabrication of complex geometries and infinite architectural designs. Such structures cannot be created utilising more traditional manufacturing routes (Peltola *et al.*, 2008).

### 3.1.1 Three Dimensional Printing

Much interest has been afforded to the creation of low-cost 3D-Printed components in a plethora of applications, including biomedical devices such as, scaffolds for bone tissue engineering, airway splints and biodegradable polymers for drug delivery (Bracci *et al.*, 2013; Butscher *et al.*, 2011; Lu and Chen, 2004). Due to such properties, 3D-Printed electrochemical systems have been increasingly reported throughout the literature. Applications thus far include electrode and electronic component fabrication (Foster *et al.*, 2017; Javey *et al.*, 2007; Zhao *et al.*, 2014).

The incorporation of 2D nanomaterials (*i.e.* graphene) (Hou *et al.*, 2011; Novoselov *et al.*, 2004) and other carbon nanomaterials (Eatemadi *et al.*, 2014; Georgakilas *et al.*, 2015; Jariwala *et al.*, 2013) have resulted in electrodes with superior electrochemical and physical properties, when compared against equivalent systems, containing macroscopic counterparts. In 2015, Wei *et al.* (2015) successfully fabricated graphene-based conductive filaments which consisted of polylactic acid (PLA) and acrylonitrile-butadiene-styrene (ABS) where graphene loadings of up to 5.6 % were incorporated and conductive filaments were 3D-Printed for the first time (Wei *et al.*, 2015). Furthermore, graphene-based PLA filaments have been fabricated with varying architectures as macroelectrodes and applied as both, solid-state capacitors and freestanding anodes within Li-ion batteries (Foster *et al.*, 2017).

The commercial filament containing graphene/polylactic acid (Black Magic (New York, USA)) which is utilised throughout this thesis has previously demonstrated beneficial electrochemical sensing activity (Manzanares Palenzuela *et al.*, 2018). It was reported that following a developed activation method in which dimethylformamide was used to partially remove the insulating polymer, detection for sensing both picric acid and ascorbic acid increased by almost two magnitudes (Manzanares Palenzuela *et al.*, 2018). This filament

has also been 3D-Printed previously to act as base electrode materials, which was sputter coated with gold for use as solid-state supercapacitors (Foo *et al.*, 2018).

### **3.1.2 Determination of the Electroactive Area of 3D-Printed Electrodes**

3D-Printing offers a distinct advantage over traditional fabrication methods, as infinite architectural designs, with large surface areas can be explored (Foster *et al.*, 2017). However, current characterisation methods are exclusively applicable to 2D electrodes. Due to this, there are no appropriate standardised methods for accurate determination of the surface area and quantification of the electrochemically active regions of 3D-Printed architectures.

Nucleation and growth of MoO<sub>2</sub> nanowires on the surface of carbonaceous electrodes may be one method to accurately quantify the electrochemically active regions present. This method, which is also known as “step edge decoration” (Rowley-Neale *et al.*, 2016a), has previously been developed by Davies *et al.* (2005b) and Walter *et al.* (2003) and resulted in the electrochemical deposition of molybdenum oxides (both MoO<sub>2</sub> and MoO<sub>3</sub>, but generally MoO<sub>2</sub>) onto the electrochemically active regions of electrodes. This method has also been used to decorate the surface of highly ordered pyrolytic graphite (HOPG) electrodes, where it was revealed that molybdenum oxide was preferentially deposited on the edge planes (Rowley-Neale *et al.*, 2016a). Davies *et al.* (2005) used cyclic voltammetry to demonstrate that complete blockage of available edge plane surfaces on a basal plane pyrolytic graphite (BPPG) electrode, resulted in a near complete reduction in electrochemical response (Davies *et al.*, 2005b). Furthermore, removal of the MoO<sub>2</sub> nanowires by HCl treatment resulted in a restoration of electrochemical activity, this is almost certainly due to re-exposure of the edge planes present (Davies *et al.*, 2005b). This technique has also been performed on two dimensional graphene-like and graphite screen printed electrodes (SPEs) and demonstrated MoO<sub>2</sub> deposition was specific to the electroactive regions present (Rowley-Neale *et al.*, 2016a).

In this chapter, this novel quantification technique of electrodeposition of MoO<sub>2</sub> nanowires was applied to 3D-Printed electrodes to determine the electrochemical area. Multifractal analysis (MFA) was also conducted to quantify the physical MoO<sub>2</sub> coverage,

allowing the electrochemical active area to be more accurately determined and characterised.

### 3.1.3 Surface Characterisation

The topography of a surface (in this instance an electrode surface) plays a key role in mediating bacterial attachment and retention (Whitehead and Verran, 2006). Factors affecting bacterial attachment include, surface roughness (at the macroscale, microscale and nanoscale level), physicochemical properties and environmental conditions (Crawford *et al.*, 2012). Despite intensive research into bacterial attachment processes, the mechanisms of attachment and the under-pinning surface properties which are involved remain largely unclear (Cheng *et al.*, 2019). The main parameter often associated with bacterial attachment and adhesion is surface roughness (Crawford *et al.*, 2012). It is suggested that a rougher surface topography results in enhanced bacterial attachment and is more beneficial for biofilm formation (Katsikogianni and Missirlis, 2004; Teughels *et al.*, 2006). The average size of a bacterial cell length ranges from 0.2 – 2.0  $\mu\text{m}$  for cocci, and 1.5 – 5.0  $\mu\text{m}$  for rod shaped bacteria, therefore topographical features in this region of size will undoubtedly result in increased bacterial attachment (Bédard *et al.*, 2016; Tortora *et al.*, 2004).

The physicochemical properties of a surface including wettability, hydrophobicity, interfacial surface free energy, Van der Waals forces, Lewis acid-base interactions and electrostatic interactions all play a role in bacterial attachment to the surface (Chavant *et al.*, 2002; van Loosdrecht *et al.*, 1989; Wilson-Nieuwenhuis *et al.*, 2017). High surface hydrophobicity enables bacteria to attach to hydrocarbon droplets present, surface attachment is then achieved due to a transition from the aqueous solution to the organic, hydrocarbon phase (Krasowska and Sigler, 2014). It is known that hydrophobic bacterial cells attach more strongly to hydrophobic surfaces (Kochkodan *et al.*, 2008; Yuan *et al.*, 2017), however, microorganisms can adapt in response to changes in the environment and growth phases and therefore switch between hydrophobic and hydrophilic phenotypes (Borecka-Melkusova and Bujdakova, 2008). This will affect their attachment to a surface and subsequent biofilm formation. To demonstrate this, the electrode surfaces employed in this study were characterised using optical profilometry (roughness) and sessile drop

goniometry, in order to obtain the various components of surface energy of wetting parameters. These investigations will result in greater insights into the surface parameters affecting bacterial attachment and to determine the potential for optimisation in order to enhance biofilm growth in a MFC configuration.

### **3.1.4 Aim**

The aim of this study was to characterise 3D-Printed BM electrodes for both electrochemical activity and surface properties, in order to better understand the parameters that affect bacterial attachment and adhesion, whilst, providing a novel method to determine the electroactive regions of the fabricated 3D-Printed electrodes.

## 3.2 Methods

### 3.2.1 Fabrication of 3D-Printed Electrodes

The 3D-printed designs utilised in this study were fabricated using a MakerBot Replicator + (MakerBot Industries, USA) with a direct drive extruder, at a temperature of 210 °C, using a commercially procured filament, Black Magic (Black Magic 3D, USA).

This Graphene/PLA composite has a calculated conductivity of 2.13 S/cm (Foster *et al.*, 2017). The 3D-Printed designs were drawn *via* the software, Fusion 360 (Autodesk, USA), to create a circular disc electrode architecture with a diameter of 6.0 mm and a thickness of 1.0 mm. The electrodes were 3D-Printed with a connecting strip, allowing simple connection of the electrode to the electrochemical system *via* a crocodile clip (Galdino *et al.*, 2015). These 3D-Printed electrodes had a theoretical surface area of 7.5 cm<sup>2</sup>.

#### 3.2.1.1 Electrode Polishing

Electrodes were polished using polishing pads (Type: PSU-M, Kermet, UK) which were sprayed with diamond spray (Kermet, UK), with 1.00 µm and 0.25 µm particle sizes, respectively. The 1.00 µm diamond spray was applied to the polishing pads, and the electrodes were polished against the polishing pads until deemed smooth (*i.e.* uniform tension of the polished electrodes was achieved when relative hand pressure applied). This was carried out for both sides of the electrode before transferring the electrodes to the 0.25 µm diamond spray polishing pad, where the same procedure was carried out. Following polishing, the 3D-printed electrodes were rinsed with 10 mL sterile distilled water and dried at room temperature for 2 h. Unpolished electrodes were also rinsed with 10 mL sterile distilled water and dried at room temperature for 2 h prior to use ( $n = 3$ ).

### 3.2.2 Electrode Characterisation

Scanning electron microscopy (SEM) images were obtained as described in Section 2.2.2. Raman Spectroscopy was conducted using a 'Renishaw InVia' spectrometer, which was equipped with a confocal microscope (× 50 objective) and an argon laser (excitation wavelength of 514.3 nm). To prevent potential heating effects, measurements were

performed using a low laser power level (0.8 mW) ( $n = 3$ ) (Randviir *et al.*, 2014; Rowley-Neale *et al.*, 2015).

### 3.2.3 Electrochemical Analysis of the 3D-Printed Electrodes

All chemicals (of analytical grade or higher) were used as received from Sigma-Aldrich (UK) without any further purification. All solutions were prepared with deionised water of resistivity no less than 18.2 M $\Omega$  cm and were vigorously degassed for 30 min with high-purity, oxygen-free nitrogen prior to electrochemical measurements. This degassing stage was important, as it removed any trace oxygen, which if present could confound the data acquired due to oxygen reduction reactions (ORR) occurring (Rowley-Neale *et al.*, 2015).

Electrochemical measurements were conducted using an 'Autolab PGSTAT 101' (Metrohm Autolab, The Netherlands) potentiostat. The data generated was collected and analysed using the software, NOVA (Version 2.0). All measurements were conducted using a typical three-electrode system. The working electrodes utilised throughout this study were 3D-Printed Black Magic (BM) electrodes, using a platinum wire and a saturated calomel electrode (SCE) as counter/auxiliary and reference electrodes, respectively.

### 3.2.4 Determination of the Heterogeneous Electron Transfer Rate Kinetics ( $k^0$ )

The Heterogeneous Electron Transfer (HET) rates were calculated as per Section 2.2.4, in line with previously reported literature, in order to deduce the transfer rate kinetics ( $k^0$ ) (Banks *et al.*, 2015; Brownson *et al.*, 2015; Lavagnini *et al.*, 2004; Nicholson, 1965). The  $k^0$  values were calculated assuming the diffusion coefficient of  $9.10 \times 10^{-6}$  cm<sup>2</sup> s<sup>-1</sup> for hexaammineruthenium(III) chloride (Banks *et al.*, 2004; Brownson *et al.*, 2014).

### 3.2.5 Determination of the Electrochemical Effective Area ( $A_{eff}$ )

The electrochemical effective area ( $A_{eff}$ ) of the 3D-Printed BM electrodes were calculated using the Randles-Ševčík equation, at room temperature, for an

electrochemically *quasi*-reversible process employing the described equation [3.1] (García-Miranda Ferrari *et al.*, 2018):

$$I_{p_{quasi}} = \pm 0.436nFA_{eff}C\sqrt{\frac{nFDv}{RT}} \quad [3.1]$$

The constants were the same as described in Section 2.2.4 and 2.2.5. The electrochemical real area ( $A_{real}$ ) was determined as per Section 2.2.5 (García-Miranda Ferrari *et al.*, 2018; Slate *et al.*, 2018a).

### 3.2.6 Electrodeposition of MoO<sub>2</sub> on 3D-Printed BM Electrodes

A solution containing 1 mM sodium molybdate (NaMoO<sub>4</sub>), 1 M sodium chloride (NaCl) and 1 M ammonium chloride (NH<sub>4</sub>Cl) was prepared and adjusted to a pH of 8.5 with ammonium hydroxide (NH<sub>4</sub>OH). Cyclic voltammetry was performed within the potential range of + 0.5 V to – 1.2 V at a scan rate of 5 mV s<sup>-1</sup> (vs. SCE) (Walter *et al.*, 2003). On the cathodic sweep, MoO<sub>2</sub> deposition manifested as a reduction peak at *ca.* - 0.9 V to - 1.0 V. The average half peak potential of the reduction peak (- 0.805 V (vs. SCE)) was taken as the deposition value for use throughout this study ( $n = 6$ ).

Subsequently, this potential was held during chronoamperometry for varying time-points, namely, 20 s, 40 s, 60 s, 120 s, 180 s, 240 s and 300 s in order to achieve the deposition of MoO<sub>2</sub> nanowires on the 3D-Printed BM electrodes. Following chronoamperometry, the electrodes were rinsed gently by gradually pipetting 1 mL of deionised water, in order to remove excess salt residues. At each time-point, MoO<sub>2</sub> deposition was carried out in triplicate with three independent electrodes ( $n = 3$ ).

#### 3.2.6.1 Multifractal Analysis

Datasets were constructed using MATLAB®, from a set of motifs generated from SEM images (Moreira *et al.*, 2017), and both theoretical and physical  $f(\alpha)$  spectra were compared. Using an iterative program, datasets of 512 × 512 pixels were computed by overlapping the given motifs on top of one another, thus, after one iteration a 4 × 4 matrix was formed, a second iteration led to an 8 × 8 matrix, through until completion. Datasets

were converted to greyscale images *via* the MathWorks Image Processing Toolbox<sup>®</sup>. In this scale a value of zero would give a black pixel whilst a value of one would give a white pixel (Moreira *et al.*, 2017; Wickens *et al.*, 2014). It is important to note that the theoretical  $f(\alpha)$  spectra exist for,  $-\infty \leq q \leq \infty$ . However, in physical applications the  $q$  values are usually restricted by physical constraints thus, the numerical  $f(\alpha)$  spectra were computed for,  $-10 \leq q \leq 10$ , in all cases and dataset boxes of size,  $\varepsilon = 4, 8, 16, 32, 64, 128$  and  $256$  were used in the computation (Wickens *et al.*, 2014). From this, the  $f(\alpha)$  curves were generated and this enabled relative density, dispersion and clustering of the MoO<sub>2</sub> nanowires to be computed. The maximum value of the  $f(\alpha)$  curve (when  $q = 0$ ):

$$D_0 = f(\alpha_0) \quad [3.2]$$

gives a numerical value for the density of MoO<sub>2</sub> upon the surface of the electrodes, whilst dispersion is measured by [3.3]:

$$\Delta\alpha = \alpha_{-10} - \alpha_{10} \quad [3.3]$$

Further, clustering can be established *via* the symmetry/antisymmetry of the generated  $f(\alpha)$  curves (Wickens *et al.*, 2014) using the formula [3.4]:

$$\Delta f(\alpha) = f(\alpha_{10}) - f(\alpha_{-10}) \quad [3.4]$$

A positive value of  $\Delta f(\alpha)$  indicated clustering of MoO<sub>2</sub>, whilst a negative value of  $\Delta f(\alpha)$  indicated clustering of gaps. Independently of the  $f(\alpha)$  curves, analysis of the images was also conducted to determine maximum area and the total MoO<sub>2</sub> percentage coverage (Wickens *et al.*, 2014). The previously obtained SEM images (all at 15.00 K X) were analysed using MFA. Firstly, grey-scale images were converted to a binary format using image processing and MFA was carried out and the resultant computed curves were plotted.

### 3.2.7 Optical Profilometry

The topography of the surfaces was measured using optical profilometry (Slate *et al.*, 2019c). Surface roughness was quantitatively defined through the measurement of average roughness ( $S_a$ ), highest peak ( $S_p$ ), lowest valley ( $S_v$ ) and the peak-to-valley ratio ( $S_{pv}$ ) values using a Zometrics, Zegage 3D optical profiler (Zygo, USA) at  $\times 50$  magnification. The image analysis software used was Zemaps (version 1.14.38) ( $n = 9$ ).

### 3.2.8 Physicochemistry

To evaluate the physicochemistry of the 3D-Printed electrodes, 3D-Printed BM and 3D-Printed PLA (control), contact angles ( $\theta$ ) were measured. Contact angles were obtained using HPLC grade water (BDH, UK), ethylene glycol and diodomethane (Alfa Aesar, USA), using a drop size of 5  $\mu\text{m}$ , and were measured using a MobileDrop goniometer (Krüss GMBH, Germany). Both the advanced and the receding contact angles were determined, with five measurements being conducted on five separate samples with each chemical, in order to ensure no cross-contamination between solvents ( $n = 5$ ).

In order to calculate physicochemical properties, equations from Van Oss (1995) were used. The interfacial free energy of interaction between molecules ( $i$ ) immersed in water ( $w$ ) can be expressed as  $\Delta G_{iwi}$  [3.5]:

$$\Delta G_{iwi} = -2\gamma_{iw} \quad [3.5]$$

Subsequently, the surface free energy of either a liquid or a solid ( $\gamma_i$ ), is the sum of its polar, acid-base interactions ( $\gamma_i^{AB}$ ) and the apolar Lifshitz-van der Waals forces ( $\gamma_i^{LW}$ ) [3.6] (Slate *et al.*, 2018c; Van Oss *et al.*, 1988; Wilson-Nieuwenhuis *et al.*, 2017):

$$\gamma_i = \gamma_i^{LW} + \gamma_i^{AB} \quad [3.6]$$

Where the individual acid-base interaction ( $\gamma_i^{AB}$ ), comprises of two parameters, the electron donor ( $\gamma_i^-$ ) and acceptor ( $\gamma_i^+$ ) components, which can be calculated as [3.7] (Slate *et al.*, 2018c; Van Oss *et al.*, 1988; Wilson-Nieuwenhuis *et al.*, 2017):

$$\gamma_i^{AB} = 2\sqrt{\gamma_i^+ \gamma_i^-} \quad [3.7]$$

Measuring contact angles ( $\theta$ ) of three different liquids (two polar and one non-polar) in combination with Young's equation [3.8], the  $\gamma_i^{LW}$ ,  $\gamma_i^+$  and  $\gamma_i^-$  can be determined [3.8] (Slate *et al.*, 2018c; Van Oss *et al.*, 1988; Wilson-Nieuwenhuis *et al.*, 2017):

$$(1 + \cos\theta) + \gamma_l = 2 \left( \sqrt{\gamma_s^{LW} \gamma_l^{LW}} + \sqrt{\gamma_s^+ \gamma_l^-} + \sqrt{\gamma_s^- \gamma_l^+} \right) \quad [3.8]$$

Where, the subscripts, s and l, denote the surface energies attributed to the solid and liquid, respectively.

### 3.2.9 Statistical Analysis

Datasets were collected and analysed using Microsoft Excel (2016). Graphs were generated using Graphpad Prism (version 8). The standard error of the mean (SEM) was represented using error bars. For statistical analysis,  $P$  values were calculated at the 95% confidence level by two-way ANOVAs as determined using Graphpad Prism (version 8). In all cases,  $P < 0.05$  was considered statistically significant. Asterisks denote significance, \* $P \leq 0.05$ , \*\* $P \leq 0.01$ , \*\*\* $P \leq 0.001$  and \*\*\*\* $P \leq 0.0001$ .

## 3.3 Results

### 3.3.1 Electrochemical Analysis

The 3D-Printed BM electrodes were tested against 1 mM hexaammineruthenium(III) chloride redox probe (in 0.1 M KCl supporting electrolyte) (Table 3.1; Figure 3.1). The unpolished 3D-Printed BM electrode produced the fastest and most efficient HET rate producing a  $k^0$  of  $1.35 \times 10^{-3} \text{ cm s}^{-1}$  compared to the polished 3D-Printed BM electrode,  $1.48 \times 10^{-3} \text{ cm s}^{-1}$ , and the BM filament (prior to 3D-Printing),  $2.14 \times 10^{-3} \text{ cm s}^{-1}$ . The unpolished 3D-Printed BM electrode and the polished 3D-Printed BM electrode produced similar  $A_{real}$  values, 8.55 % and 8.77 %, respectively compared to the BM filament 2.11 %.

When comparing the  $\Delta E_p$  (mV) at  $100 \text{ mV s}^{-1}$ , the Black Magic (8 wt.% graphene) filament produced the shortest peak-to-peak separation ( $135.96 (\pm 7.1) \text{ mV}$ ) followed by the polished 3D-Printed BM electrode,  $151.07 (\pm 12.88) \text{ mV}$ , and then the unpolished 3D-Printed BM electrode ( $179.60 (\pm 8.6) \text{ mV}$ ). A consistent surface area value of  $7.5 \text{ cm}^2$  was used to ensure the results obtained were comparable.

Table 3.1 Comparison of the electrochemical behaviour of 3D-Printed graphene electrodes, both, polished and unpolished and the filament (prior to printing) against, 1 mM hexaammineruthenium(III) chloride (with supporting 0.1 M KCl electrolyte) ( $n = 3$ ).

Electrode Material	$k^0$ (cm s <sup>-1</sup> )	$A_{eff}$ (cm <sup>2</sup> )	$A_{real}$ (%)	$\Delta E_p$ (mV) at 100 mV s <sup>-1</sup>
<b>Hexaammineruthenium(III) chloride / 0.1 M KCl</b>				
3D-Printed Graphene (BM) – Polished	$1.48 \times 10^{-3}$	0.66	8.77	151.07 ( $\pm 12.88$ )
3D-Printed Graphene (BM) – Unpolished	$1.35 \times 10^{-3}$	0.64	8.55	179.60 ( $\pm 8.6$ )
Graphene (BM) Filament	$2.14 \times 10^{-3}$	0.16	2.11	135.96 ( $\pm 7.1$ )

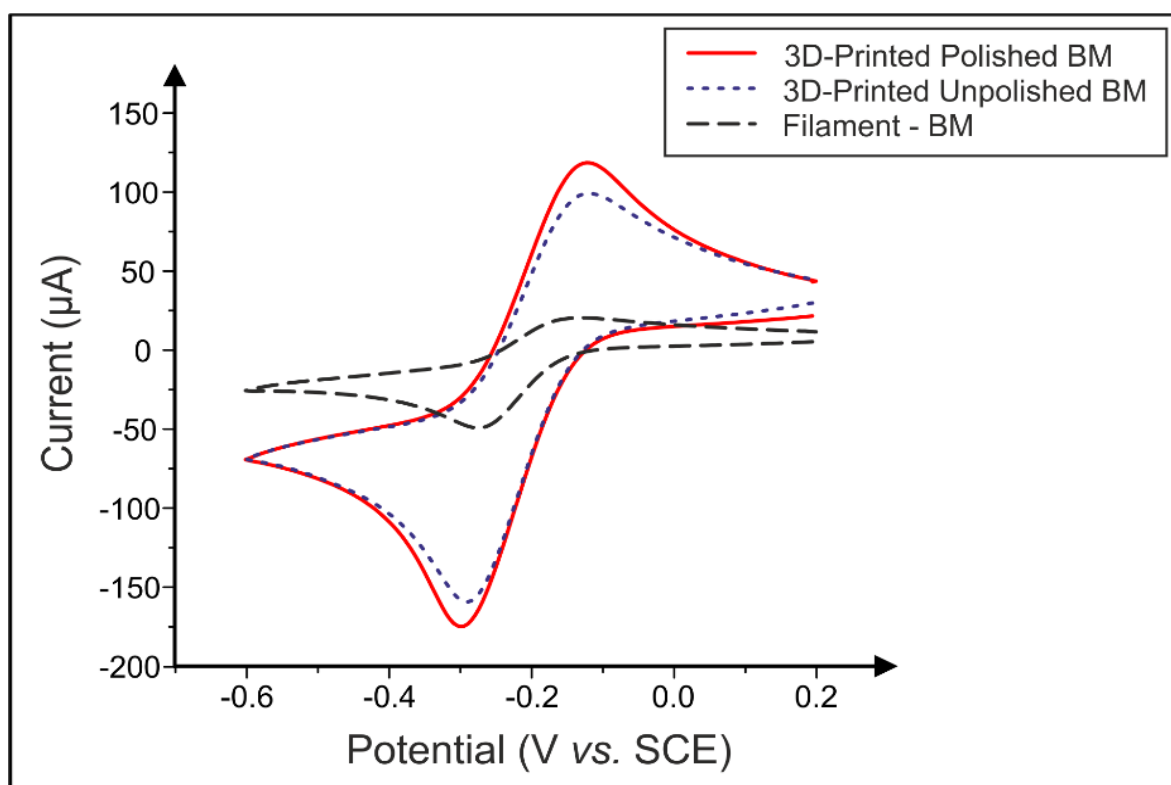


Figure 3.1. Cyclic voltammetric profiles recorded of the 3D-Printed graphene electrodes, both, polished and unpolished and the filament (prior to printing). Redox probe: 1 mM hexaammineruthenium(III) chloride in 1 M KCl. Scan rate: 100 mV s<sup>-1</sup>.

### 3.3.2 Electrode Characterisation

The surface morphology of the 3D-Printed BM electrodes was examined using SEM (Figure 3.2 and 3.3). At a relatively lower magnification (100 ×) the surface topography of the unmodified 3D-Printed BM electrodes was observed, this revealed a highly heterogenous topography due to the striations created during the manufacturing process (Figure 3.2).

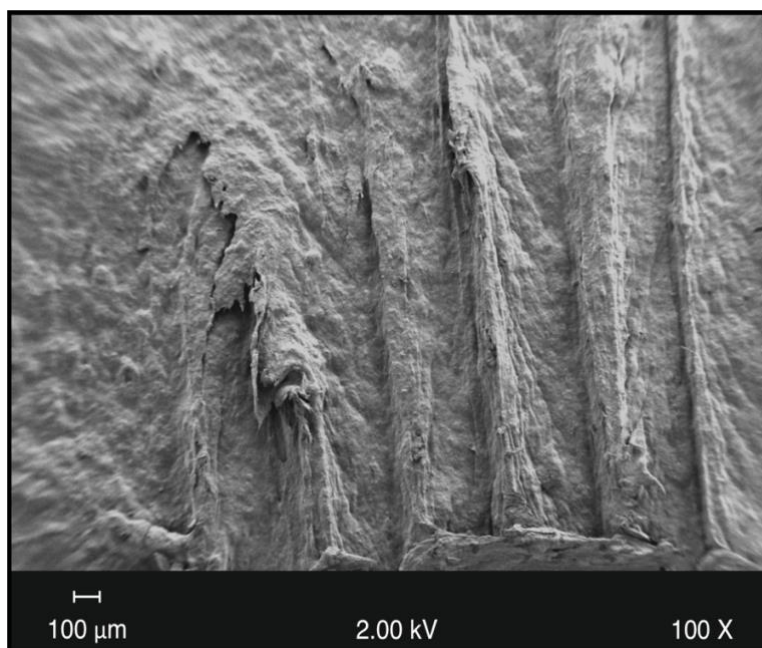


Figure 3.2. SEM image depicting the surface morphology of the unmodified 3D-Printed BM electrode at 100 × magnification.

To produce a more uniform topography and to determine the effect this had on electrochemical activity, the 3D-Printed BM electrodes were polished. The polished 3D-Printed BM electrodes resulted in a more uniform surface topography (Figure 3.3.A) when compared to the unpolished 3D-Printed BM electrodes, and in the selected SEM image a pit of *ca.* 50 μm was evident (Figure 3.3.B). Further, polished and unpolished controls of 3D-Printed PLA (graphene deficient) were also included (Figure 3.3.C and Figure 3.3.D respectively). Again, a smoother surface was observed after the polishing procedure (Figure 3.3.C).

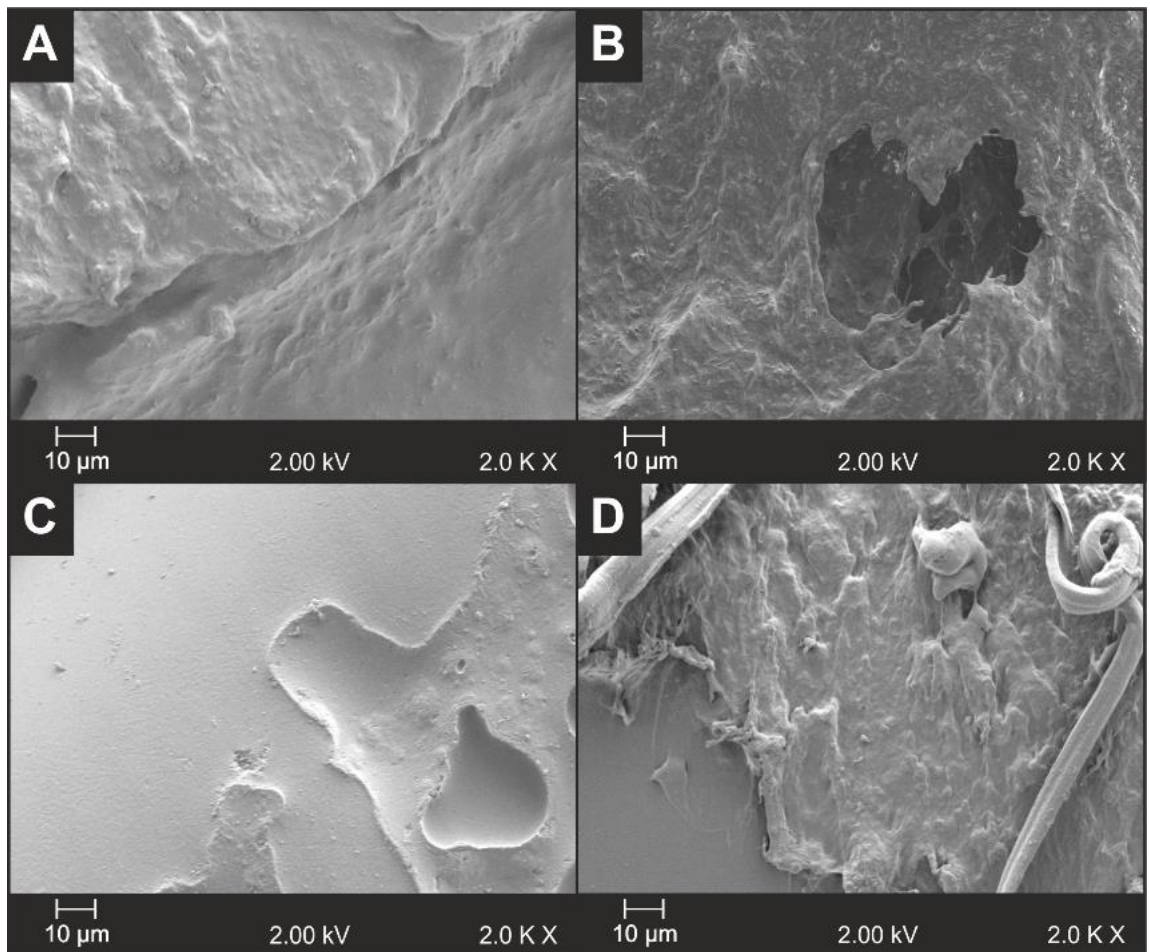


Figure 3.3. SEM images depicting the surface topography of the following electrodes at 2.00 K × magnification, A) BM - polished, B) BM - unpolished, C) PLA - polished and D) PLA - unpolished.

Raman spectroscopy was performed to gain insight into the nature of carbon bonding on the 3D-Printed BM electrode samples (Figure 3.4). The Raman spectra of the 3D-Printed BM electrodes featured the characteristic carbonaceous peaks, commonly referred to as the G and 2D ( $G'$ ) bands at *ca.*  $1580\text{ cm}^{-1}$  and  $2690\text{ cm}^{-1}$  respectively (Ferrari, 2007; Graf *et al.*, 2007; Kondratowicz *et al.*, 2015; Wang *et al.*, 2008; Yoon *et al.*, 2009). The graphene content of the 3D-Printed BM electrodes comprised of multi-layer graphene sheets, determined from the highly symmetrical 2D ( $G'$ ) band peak. Furthermore, there was a distinct lack of a characteristic shoulder on the 2D ( $G'$ ) band, which was observed in graphitic materials (Ferrari, 2007; Reich and Thomsen, 2004). Finally, the large D band was indicative of a high number of edge plane-like sites (Casiraghi *et al.*, 2009).

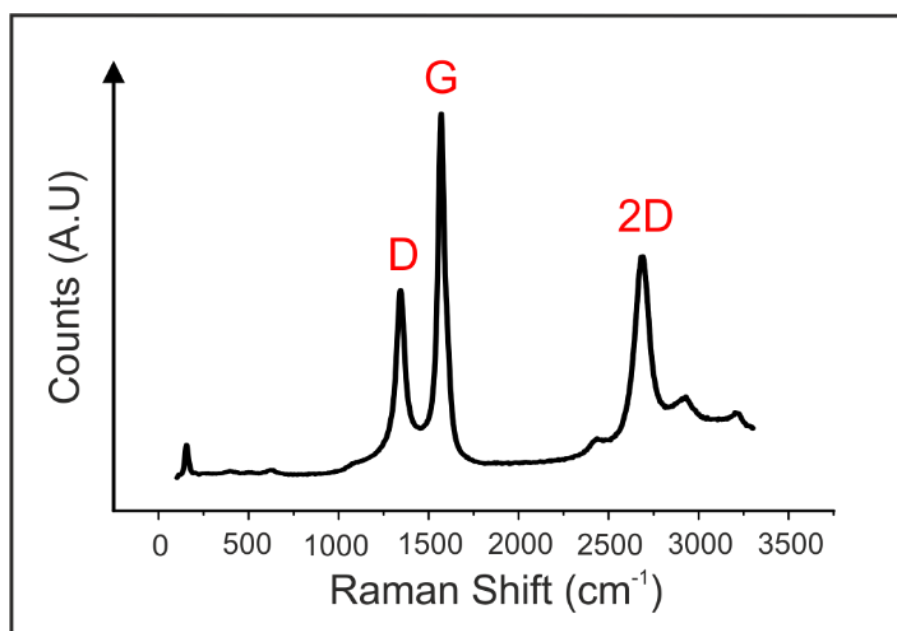


Figure 3.4. Raman spectra of the 3D-Printed BM electrode. The D band was the defect band in  $sp^2$  hybridised carbon whilst the G band was the first-order Raman band of all  $sp^2$  hybridised carbon. Representative of  $n = 3$ .

### 3.3.3 Determination of the Electroactive Area *via* Molybdenum Dioxide Nanowire Formation

Due to the lack of effective methods currently proposed throughout the literature to determine the electrochemically active areas of 3D/porous electrodes, the deposition

and formation of MoO<sub>2</sub> nanowires upon the 3D-Printed BM electrodes was performed for the first time. The 3D-Printed electrodes were fabricated as per Section 3.2.1 Fabrication of 3D-Printed Electrodes.

### 3.3.3.1 Determination of the deposition potential

Cyclic voltammetry was used to determine an effective deposition potential value for the MoO<sub>2</sub> to deposit upon the electrochemically active areas of the 3D-Printed BM electrodes. An average half reduction peak potential was determined at  $-0.805 (\pm 0.0022)$  V ( $n = 6$ ) (Figure 3.5). This value ( $-0.805$  V) was used as the deposition potential value during the chronoamperometry studies, leading to the formation of MoO<sub>2</sub> nanowires. The nanowire formation was studied at varying time-points; 0 s, 20 s, 40 s, 60 s, 120 s, 180 s, 240 s and 300 s.

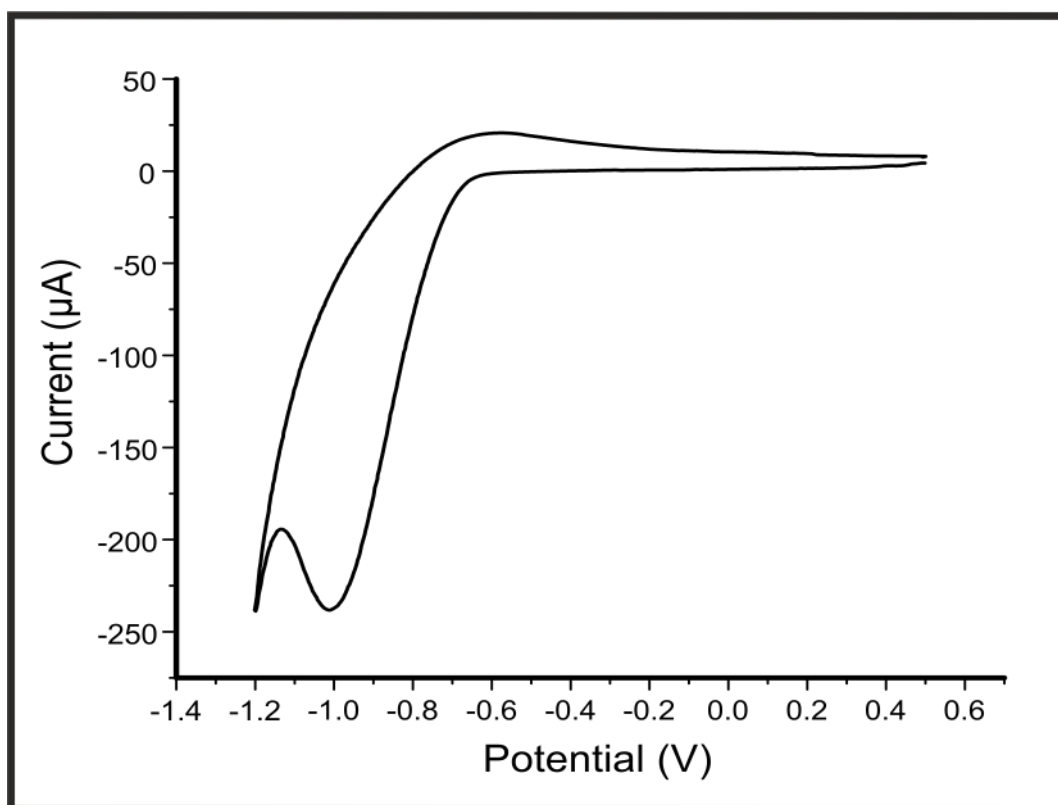


Figure 3.5. Cyclic voltammogram recorded in 1 mM Na<sub>2</sub>MoO<sub>4</sub> (in supporting 1 M NaCl and 1 M NH<sub>4</sub>Cl, adjusted to pH 8.5). The deposition (reduction peak) and stripping (oxidation peak) of MoO<sub>2</sub> was observed against the 3D-Printed BM electrodes. Scan rate: 5 mV s<sup>-1</sup> (vs. SCE). Representative of  $n = 6$ .

### 3.3.3.2 Raman spectroscopy

To validate the successful deposition of the MoO<sub>2</sub> on the 3D-Printed BM electrodes, Raman spectroscopy was used at the eight varying deposition times (Figure 3.6). Each of the Raman spectra obtained revealed the characteristic carbonaceous peaks, commonly referred to a G and 2D (G') bands. Full width half maximum (FWHM) analysis of the 2D bands, revealed the control 3D-Printed BM electrode demonstrated a Raman shift of 86.55 cm<sup>-1</sup> ( $\pm 0.98$  cm<sup>-1</sup>). The FWHM of the 2D bands of the 3D-Printed BM electrodes subjected to MoO<sub>2</sub> deposition, produced Raman Shift values in the range of 72.80 cm<sup>-1</sup> ( $\pm 1.07$  cm<sup>-1</sup>) after 300 s MoO<sub>2</sub> deposition and 103.96 cm<sup>-1</sup> ( $\pm 2.83$  cm<sup>-1</sup>) after 180 s MoO<sub>2</sub> deposition. Therefore, the presence of multi-layered graphene was confirmed.

Subsequently, the 0 cm<sup>-1</sup> to 1000 cm<sup>-1</sup> range of the spectra was studied in depth, due to the diversity in both the presence and intensity of peaks reported in this region (Figure 3.7). The MoO<sub>2</sub> coated 3D-Printed BM electrodes of deposition times, 20 s, 40 s and 60 s had three distinct peaks at *ca.* 404 cm<sup>-1</sup>, 510 cm<sup>-1</sup> and 630 cm<sup>-1</sup>, respectively; these peaks were also evident in the control 3D-Printed BM electrode (Figure 3.7.A) and were therefore assumed to be from the manufacturing/printing process. The 3D-printed BM electrodes, which were electro-deposited with MoO<sub>2</sub> for 120 s, 180 s and 240 s, displayed a distinct peak at *ca.* 281 cm<sup>-1</sup>. The 3D-Printed BM electrode that was exposed to MoO<sub>2</sub> deposition over 300 s exhibited different Raman spectra, compared to the other time-points analysed, with two new peaks that were specific to this time-point, observed at *ca.* 860 cm<sup>-1</sup> and 960 cm<sup>-1</sup>, providing further evidence of MoO<sub>2</sub> on the surface of the electrode (Zhou *et al.*, 2016a).

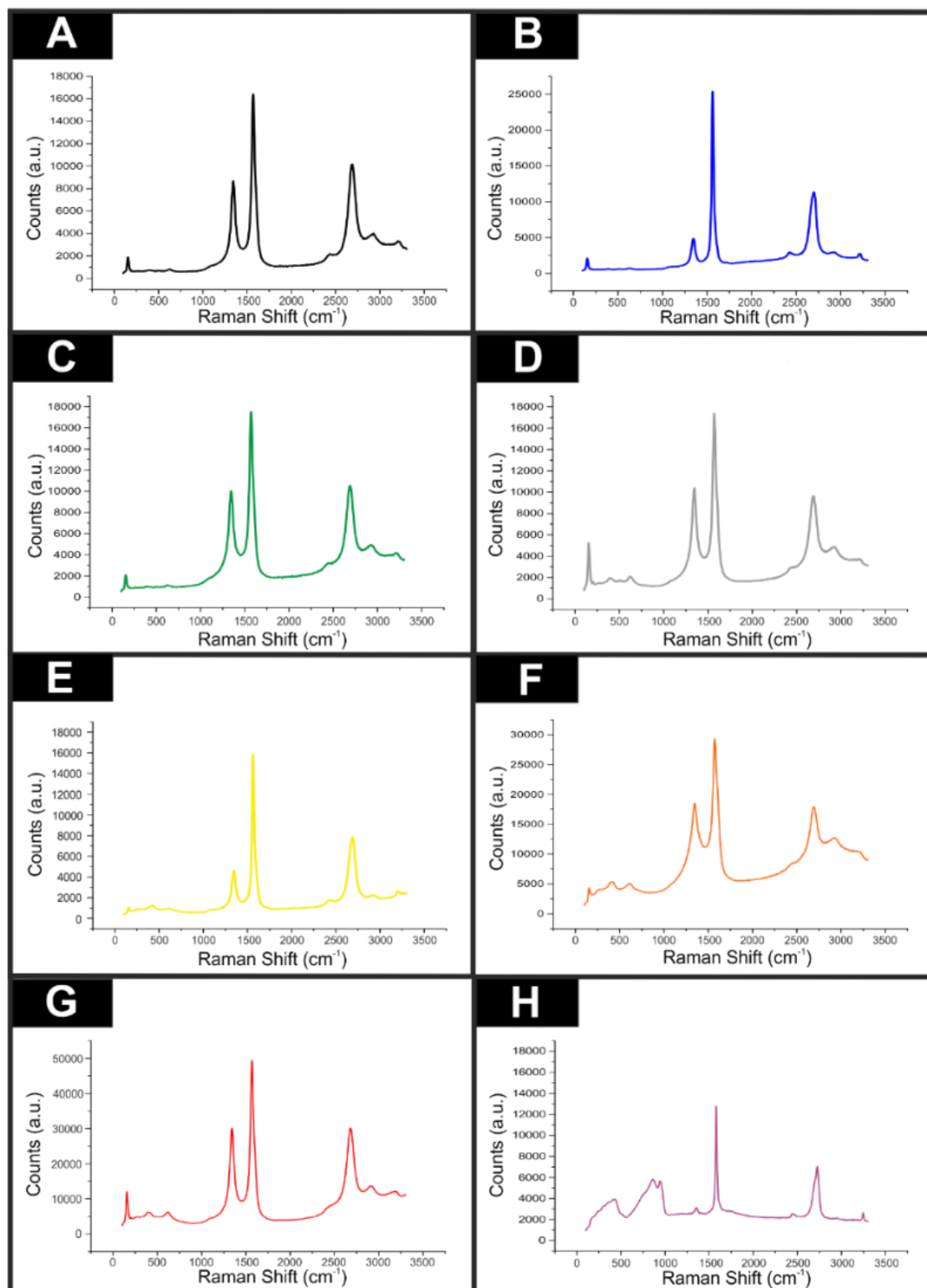


Figure 3.6. Raman spectra of the eight MoO<sub>2</sub> deposition time-points against the 3D-Printed BM electrodes. A) Control (black), B) 20 s (blue), C) 40 s (green), D) 60 s (grey), E) 120 s (yellow), F) 180 s (orange), G) 240 s (red) and H) 300 s (purple). Representative of  $n = 3$ .

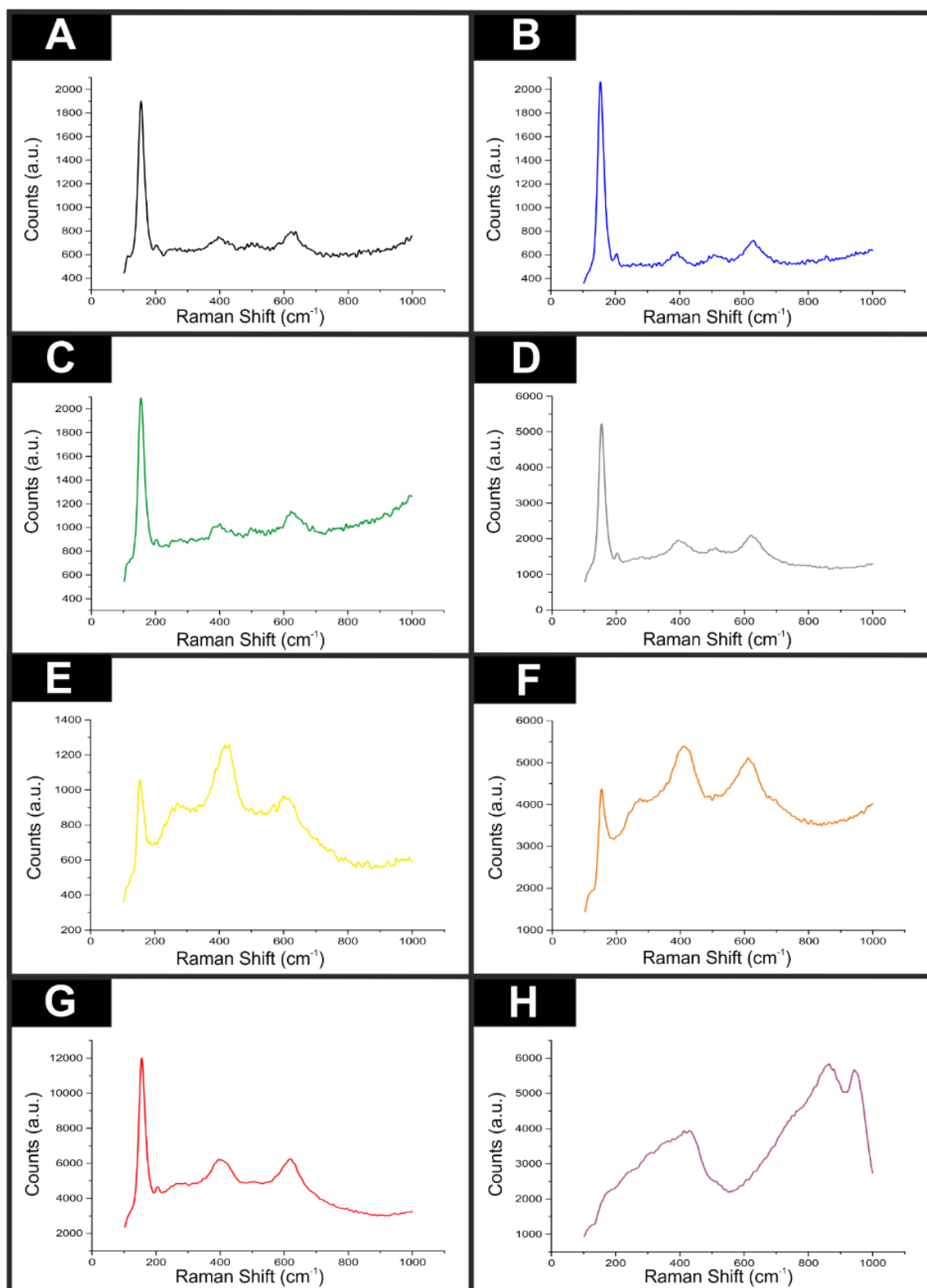


Figure 3.7. Raman spectra (focussing on the 0  $\text{cm}^{-1}$  to 1000  $\text{cm}^{-1}$  region) of the eight  $\text{MoO}_2$  deposition time-points against the 3D-Printed BM electrodes. A) Control (black), B) 20 s (blue), C) 40 s (green), D) 60 s (grey), E) 120 s (yellow), F) 180 s (orange), G) 240 s (red) and H) 300 s (purple). Representative of  $n = 3$ .

### 3.3.3.3 Scanning Electron Microscopy (SEM)

Scanning electron microscopy was conducted to visualise the MoO<sub>2</sub> deposition on the 3D-Printed BM electrodes (Figure 3.8). The electrodes coated with MoO<sub>2</sub> for 20 s, 40 s and 60 s demonstrated no variation from the control electrode. However, electrodes electrodeposited with MoO<sub>2</sub> for 120 s, 180 s, 240 s and 300 s, demonstrated the formation of MoO<sub>2</sub> nanowires. More specifically, after MoO<sub>2</sub> deposition of 240 s, the formation of filamentous MoO<sub>2</sub> nanowires was observed, particularly, along the edge plane like-sites/defects. The nucleation of MoO<sub>2</sub> increased in a time-dependent manner, as an increase in deposition time resulted in enhanced MoO<sub>2</sub> nucleation on the electrode surface. The electrode coated with MoO<sub>2</sub> for the maximum amount of time (300 s) resulted in a thick nucleation along the edge planes of the electrodes. Furthermore, for both the 240 s and 300 s time-points, MoO<sub>2</sub> nanowires > 2 μm in length were observed (Figure 3.8). These results demonstrate that an increase in MoO<sub>2</sub> deposition time resulted in an increased nucleation rate on the electroactive regions of the electrodes.

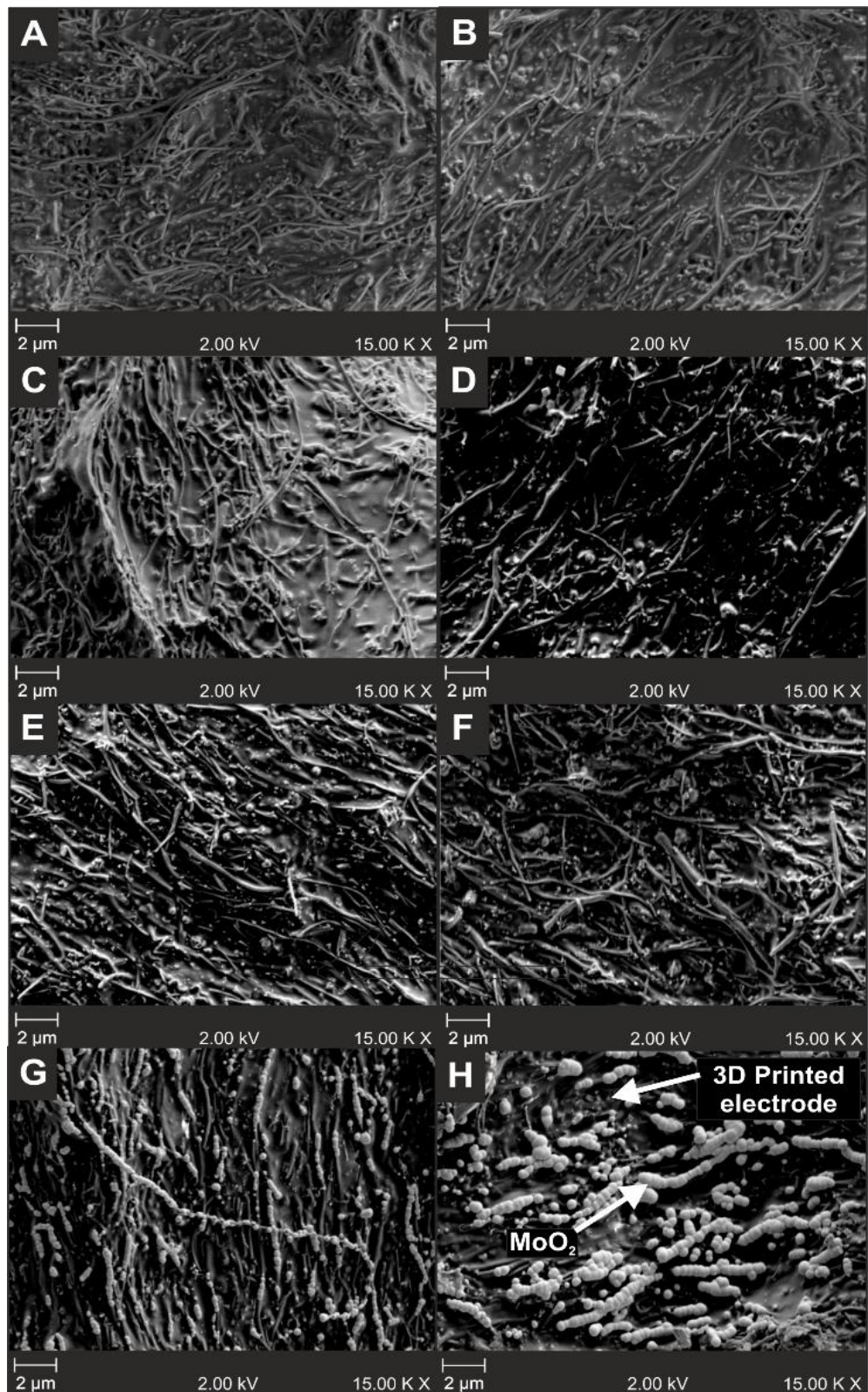


Figure 3.8. SEM of the surface of the 3D-Printed BM electrodes showing the deposited MoO<sub>2</sub> A), Control, B) 20 s, C) 40 s, D) 60 s, E) 120 s, F) 180 s, G) 240 s and H) 300 s. Representative of  $n = 3$ .

### 3.3.3.4 Electrochemical Effect on Surface Areas

The electrochemical behaviour of the 3D-Printed BM electrodes with the eight varying MoO<sub>2</sub> deposition time-points were characterised by cyclic voltammetry against 1 mM Hexaammineruthenium(III) chloride (with 0.1 M KCl). An example of the voltammograms obtained showed an increase in the  $\Delta E_p$  of the electrode coated for 180 s compared to the control, indicating a detrimental effect upon electron transfer properties (Figure 3.9). From this, the active surface, which contributed towards the electrochemical activity was determined (Table 3.2). The results for the electrochemical effective area ( $A_{eff}$ ) revealed no overall trend with the control electrode giving an area of 0.47 cm<sup>2</sup>, whilst the lowest area determined was by the electrode deposited with MoO<sub>2</sub> for 240 s (0.24 cm<sup>2</sup>), the highest area was observed in both the 40 s and 180 s electrodes (0.53 cm<sup>2</sup>). The electrochemical real area ( $A_{real}$ ) results also revealed no overall trend with the electrode deposited with MoO<sub>2</sub> for 240 s producing the lowest area (7.88 %) whilst, the electrode deposited for 40 s produced the largest active area (19.36 %). Due to the lack of trends revealed in this data, which exhibited no clear correlation with the SEM acquired images, MFA was conducted to provide further analysis for MoO<sub>2</sub> percentage surface coverage.

Table 3.2. Electrochemically acquired areas and MFA percentage coverage of one isolated side of the 3D-Printed BM electrodes following MoO<sub>2</sub> deposition, against 1 mM hexaammineruthenium(III) chloride with 0.1 M KCl. The reported  $k^0$  value for the control 3D-Printed BM electrode was  $1.08 \times 10^{-3} (\pm 0.000033)$  cm s<sup>-1</sup> and a  $\Delta E_p$  at 100 mV s<sup>-1</sup> of 199.73 ( $\pm 1.68$ ) mV. The 3D-Printed BM electrode exposed to MoO<sub>2</sub> deposition for 300 seconds gave a  $k^0$  value of  $4.90 \times 10^{-4} (\pm 0.00014)$  cm s<sup>-1</sup> and a  $\Delta E_p$  at 100 mV s<sup>-1</sup> of 327.71 ( $\pm 13.72$ ) mV ( $n = 3$ ).

Electrode Type (MoO <sub>2</sub> deposition time)	Electrochemically derived surface areas		MFA derived surface area
	$A_{eff}$ (cm <sup>2</sup> )	$A_{real}$ (%)	MoO <sub>2</sub> Surface Coverage (%)
Control	0.47 ( $\pm 0.008$ )	16.41	N/A
20 Seconds	0.33 ( $\pm 0.013$ )	10.97	-0.04 ( $\pm 0.40$ )
40 Seconds	0.53 ( $\pm 0.008$ )	19.36	4.07 ( $\pm 2.61$ )
60 Seconds	0.42 ( $\pm 0.004$ )	14.66	2.52 ( $\pm 1.05$ )
120 Seconds	0.46 ( $\pm 0.003$ )	16.58	8.37 ( $\pm 0.99$ )
180 Seconds	0.53 ( $\pm 0.008$ )	18.59	19.34 ( $\pm 3.20$ )
240 Seconds	0.24 ( $\pm 0.011$ )	7.88	13.07 ( $\pm 2.17$ )
300 Seconds	0.50 ( $\pm 0.019$ )	18.94	20.14 ( $\pm 5.82$ )

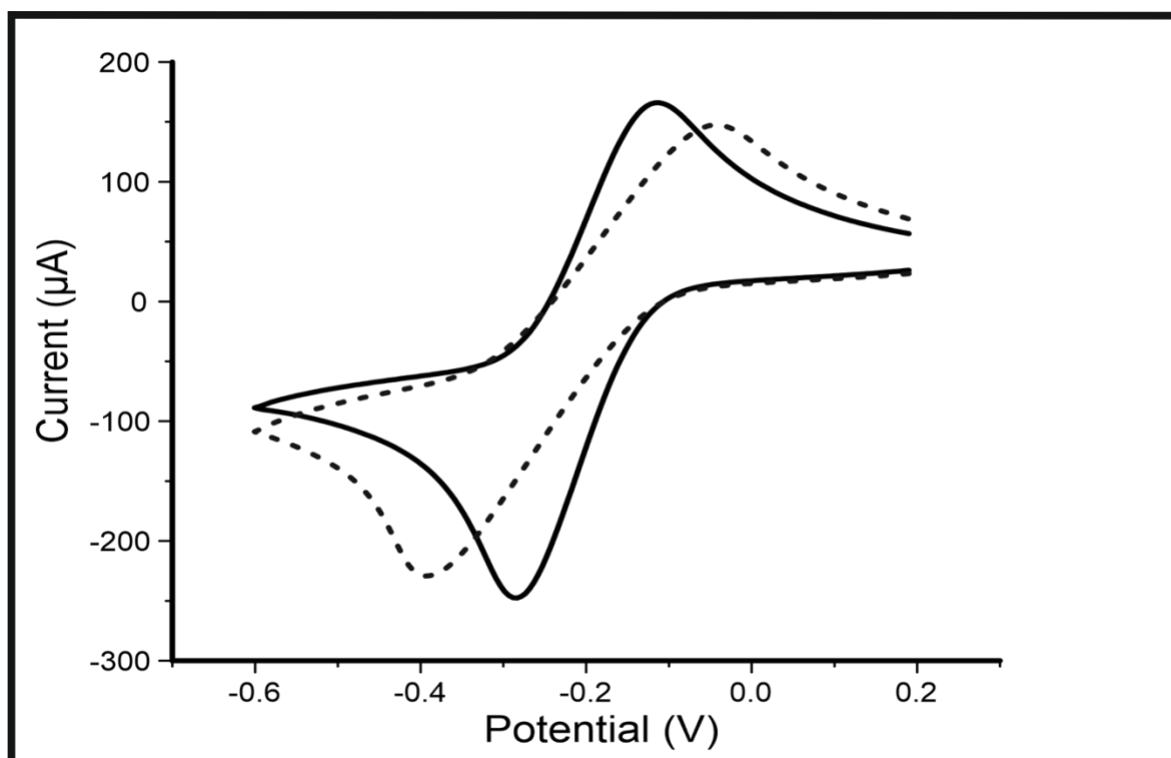


Figure 3.9. Cyclic voltammetric profiles the control (solid line) and 180 s (dashed line) MoO<sub>2</sub> deposition time of the 3D-Printed BM electrodes. Redox probe: 1 mM hexaammineruthenium(III) chloride / 1 M KCl. Scan rate: 100 mVs<sup>-1</sup>.

### 3.3.3.5 Multifractal Analysis (MFA)

Firstly, grey scale SEM images (at 15.00 K X) were converted to binary images. Image analysis and MFA was performed to produce  $f(\alpha)$  curves (Figure 3.10.A), which were used to calculate MoO<sub>2</sub> density, dispersion and clustering (Figure 3.10.B). The area percentage coverage of MoO<sub>2</sub> was also calculated and revealed that the 3D-Printed BM electrode coated for 20 s had the lowest coverage of MoO<sub>2</sub> (Table 3.2). The electrodes coated from 120 s onwards revealed an increase in percentage area coverage in a linear fashion (excluding the 180 s deposition time-point – 19.34 %). The 3D-Printed BM electrode coated for 120 s produced an area coverage of (8.37 %), whilst the 240 s and 300 s deposition time-points demonstrated MoO<sub>2</sub> area coverage of 13.07 % and 20.14 % respectively (Figure 3.10.C). This confirmed a time-dependent process, with a greater coverage of MoO<sub>2</sub> exhibited after greater periods of MoO<sub>2</sub> deposition. The  $f(\alpha)$  curves (Figure 3.10.B) demonstrated that the electrode coated with MoO<sub>2</sub> for 20 s produced the lowest density (Figure 3.10.D),  $D_0 = 1.45$ , whilst the 3D-Printed BM electrode coated with MoO<sub>2</sub> for 300 s produced the greatest density,  $D_0 = 1.75$ .

Dispersion can be related to the heterogeneity (a more heterogeneous value is indicative of enhanced dispersion). In this study, the distribution of the MoO<sub>2</sub> nanowires was calculated (Figure 3.9.E). Dispersion of the MoO<sub>2</sub> was highest for the electrode coated with MoO<sub>2</sub> for 20 s,  $\Delta\alpha = 1.17$ , and lowest for the 3D-Printed BM electrode coated with MoO<sub>2</sub> for 300 s,  $\Delta\alpha = 0.69$ , this indicates that an increase in MoO<sub>2</sub> deposition resulted in enhanced distribution, resulting in a more homogenous MoO<sub>2</sub> deposition on the electrode surface. Clustering ( $\Delta f(\alpha)$ ) of the MoO<sub>2</sub> was determined as per equation [3.4]. Excluding the control electrode with no MoO<sub>2</sub> deposition, the electrode that was exposed to MoO<sub>2</sub> for 20 s had the highest clustering value (Figure 3.10.F). An  $\Delta f(\alpha) > 1$  indicates a cluster of gaps (in this case the bare electrode) and therefore more space between the MoO<sub>2</sub> on the surface of the electrode (Tetlow *et al.*, 2017; Wickens *et al.*, 2014). An increase in deposition time resulted in the clustering value becoming more negative, the first negative value was reported at 180 s (-0.055) and the most negative value was observed after 300 s of MoO<sub>2</sub> deposition. Therefore, as the deposition times of MoO<sub>2</sub> increased, the deposition of MoO<sub>2</sub> became more sporadic but overall remained clustered around the electroactive regions of the electrodes.

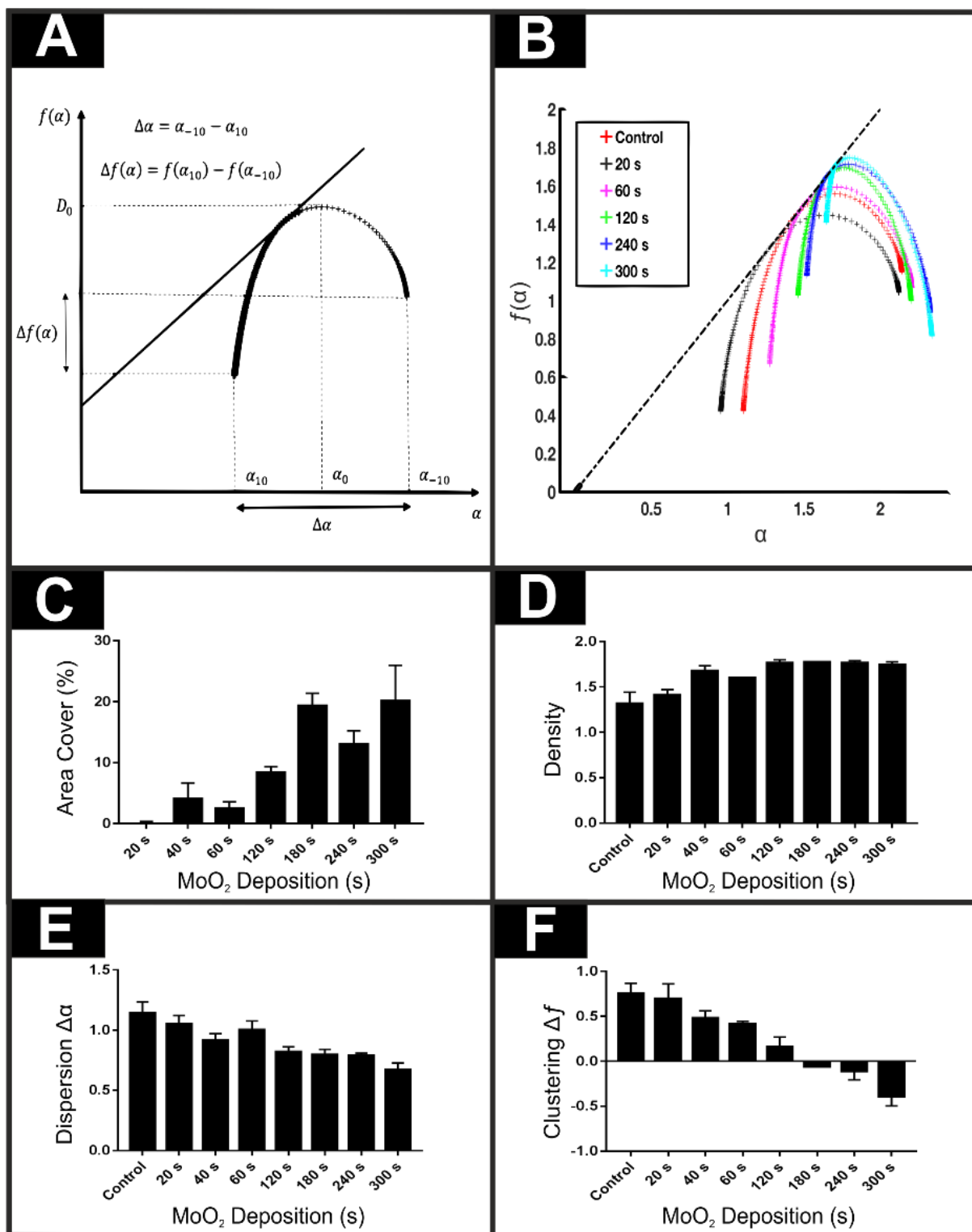


Figure 3.10. A) Theory of  $f(\alpha)$  curves for MFA B)  $f(\alpha)$  curves of a selection of MoO<sub>2</sub> time-points selected for this study (control, 20 s, 60 s, 120 s, 240 s, 300 s) C) MoO<sub>2</sub> Area cover (deducted from the control background (%)) D) MoO<sub>2</sub> Density E) MoO<sub>2</sub> dispersion F) MoO<sub>2</sub> clustering ( $n = 3$ ).

### 3.3.4 Surface Analysis: Optical Profilometry

Optical profilometry was conducted to determine the topographical features of the 3D-Printed BM electrodes. Average surface roughness (Figure 3.11) of the electrodes revealed a difference in topography when comparing the top and the underside of the electrodes. The topside of the surface produced an average roughness of  $4.40\ \mu\text{m}$  compared to the underside of the same electrode ( $2.65\ \mu\text{m}$ ). Both sides of the 3D-Printed BM electrode exhibited a significantly greater surface roughness than their respective 3D-Printed PLA control (containing no graphene).

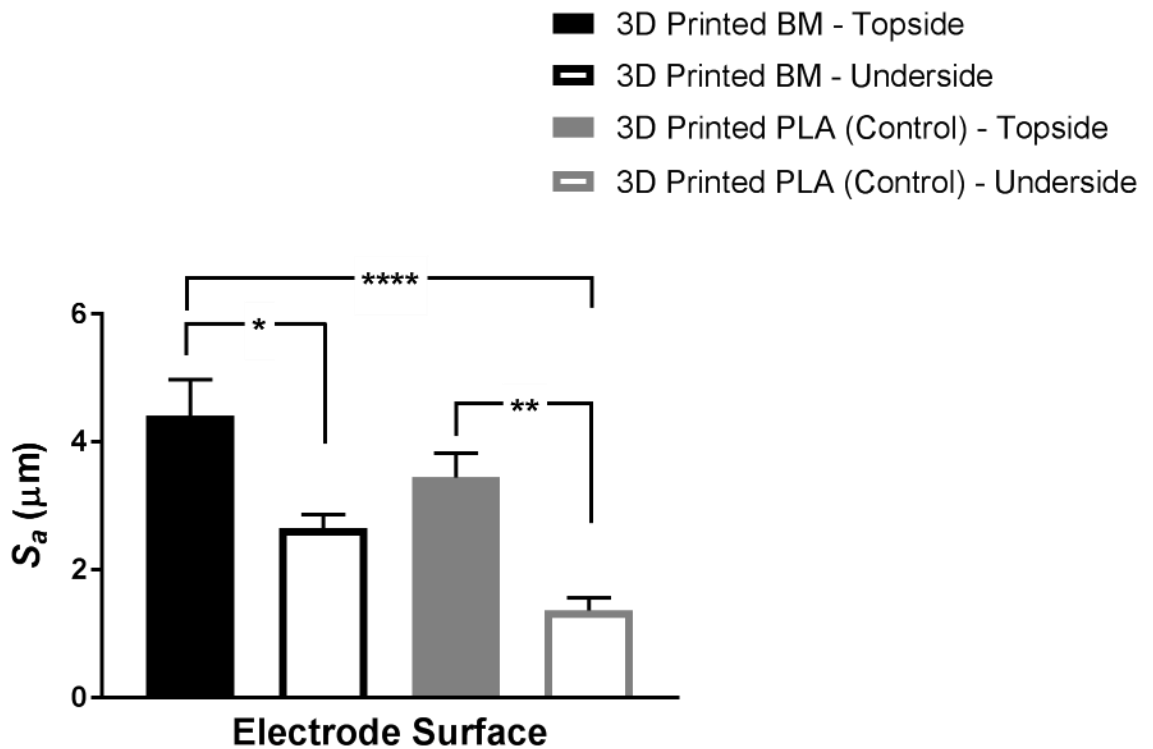


Figure 3.11. Average surface roughness ( $S_a$ ) of both sides of the 3D-Printed BM electrodes and the 3D-Printed PLA control ( $n = 9$ ). Asterisks denote statistical significance, \* ( $P \leq 0.05$ ), \*\* ( $P \leq 0.01$ ), \*\*\* ( $P \leq 0.001$ ) and \*\*\*\* ( $P \leq 0.0001$ ).

The maximum peak height ( $S_p$ ) and maximum valley depth ( $S_v$ ) were also determined. The underside of the 3D-Printed BM electrode had the greatest maximum peak height ( $15.77\ \mu\text{m}$ ) compared with the topside of the 3D-Printed BM electrode ( $13.86\ \mu\text{m}$ ) and both these peaks from either side of the 3D-Printed BM electrode, were greater

than their corresponding PLA controls (Figure 3.12). The topside of the 3D-Printed BM electrode showed the maximum valley depth (21.12  $\mu\text{m}$ ) followed by the underside of the 3D-Printed BM electrode (8.52  $\mu\text{m}$ ) (Figure 3.13). The 3D-Printed BM electrode exhibited deeper valleys than the PLA control. This variation in electrode surface topography between the two electrodes and both sides of the electrodes was further evidenced when comparing the peak-to-valley ratio ( $S_{pv}$ ) (Figure 3.14). The topside of the 3D-Printed BM electrodes possessed the greatest peak-to-valley ratio (34.95  $\mu\text{m}$ ), whilst, the underside of the 3D-Printed PLA control exhibited the smallest peak-to-valley ratio (11.98  $\mu\text{m}$ ). Only samples that had > 90 % of the surface analysed were included in this study to enhance accuracy and reliability (Figure 3.15). The results obtained from optical profilometry demonstrated high levels of variation both between each side of the same electrode and between the material used to fabricate the electrode. However, these results were indicative of the electrodes produced throughout this study ( $n = 9$ ).

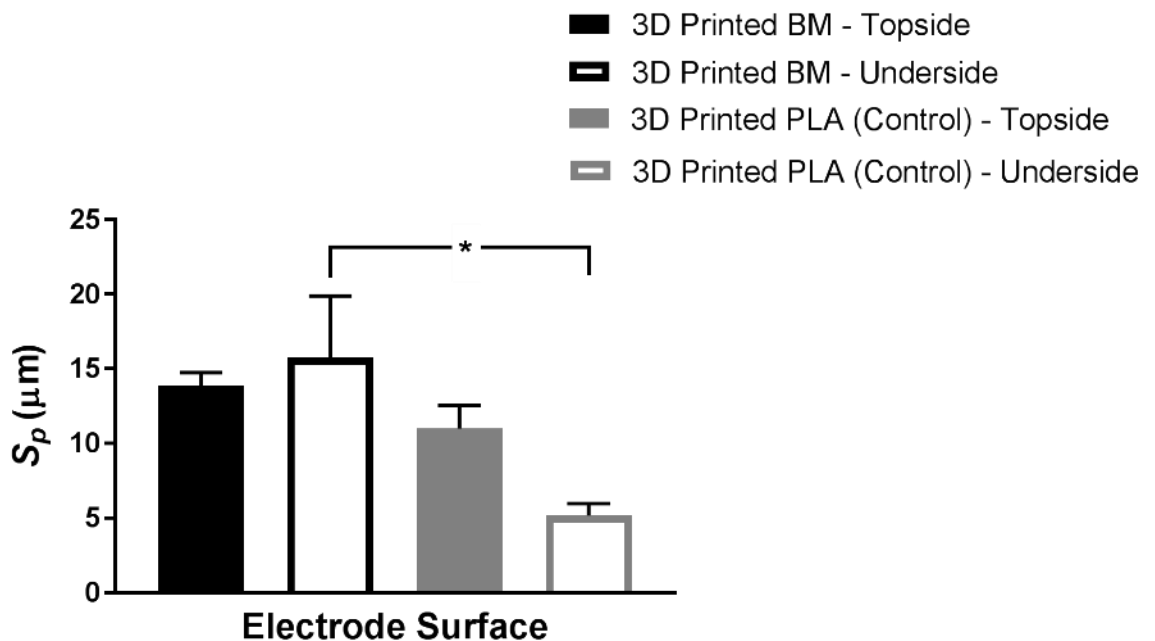


Figure 3.12. Maximum peak height ( $S_p$ ) of both sides of the 3D-Printed BM electrodes and the 3D-Printed PLA control ( $n = 9$ ). Asterisks denote statistical significance, \* ( $P \leq 0.05$ ).

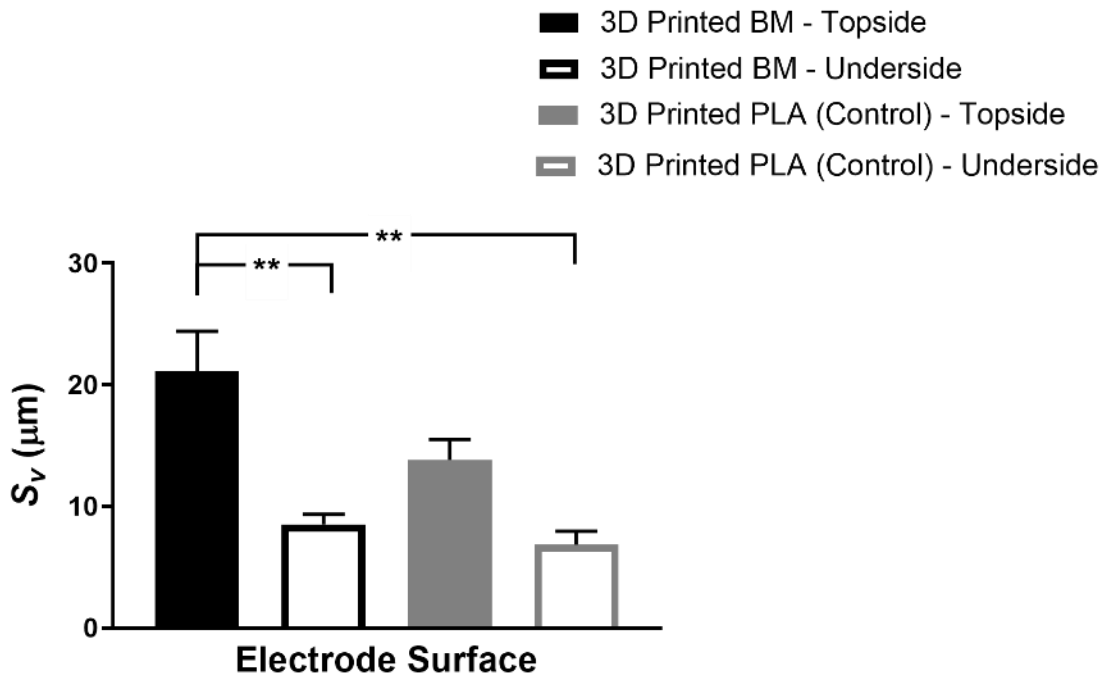


Figure 3.13. Maximum valley depth ( $S_v$ ) of both sides of the 3D-Printed BM electrodes and the 3D-Printed PLA control ( $n = 9$ ). Asterisks denote statistical significance, \*\* ( $P \leq 0.01$ ).

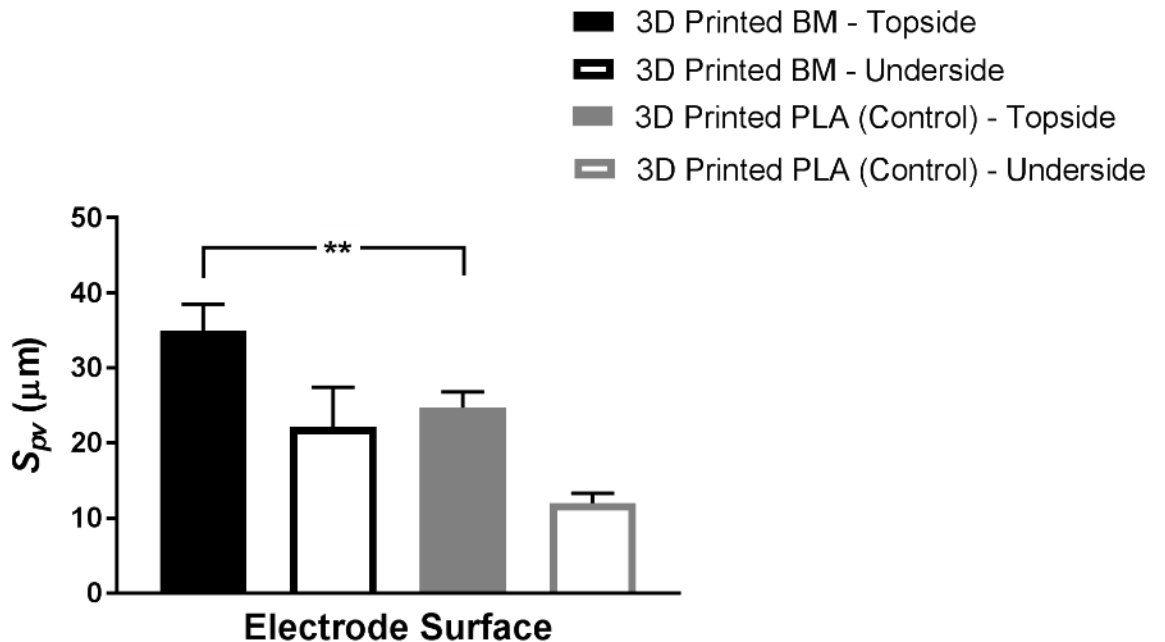


Figure 3.14. Peak-to-valley ratios ( $S_{pv}$ ) of both sides of the 3D-Printed BM electrodes and the 3D-Printed PLA control ( $n = 9$ ). Asterisks denote statistical significance, \*\* ( $P \leq 0.01$ ).

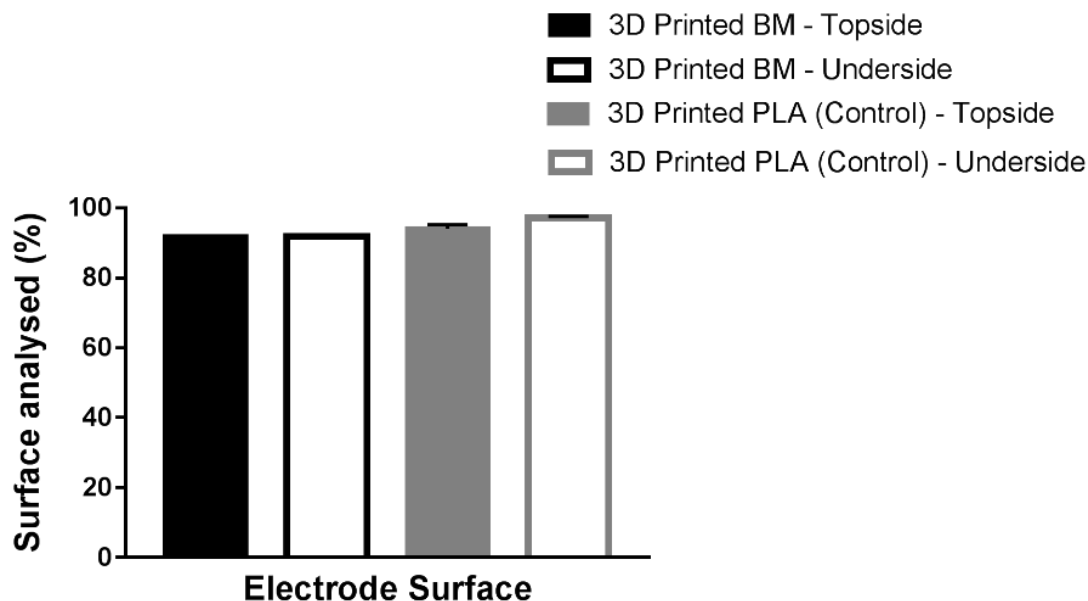


Figure 3.15. Percentage surface analysis of both sides of the 3D-Printed BM electrodes and the 3D-Printed PLA control ( $n = 9$ ). Where error bars are not visible they are of similar or smaller size compared to the symbol.

### 3.3.5 Surface Analysis: Physicochemistry

The hydrophobicity of the electrodes, total surface energy ( $\gamma_s$ ), Lifshitz van der Waals forces ( $\gamma_{sLW}$ ), Acid-Base interactions ( $\gamma_{sAB}$ ), electron accepting interactions ( $\gamma_{s+}$ ) and electron donating interactions ( $\gamma_{s-}$ ) were calculated following contact angle measurements (Table 3.3). Due to the variability in roughness of either side of the same electrode, experiments were conducted on both sides. The interfacial free energy of interaction between molecules,  $\Delta G_{iwi}$  was determined to quantify hydrophobicity. Both sides of the PLA control and the underside of the 3D-Printed BM electrode produced negative values. These surfaces were therefore hydrophobic, with the underside of the 3D-Printed BM electrode being the most hydrophobic surface ( $-26.40 \text{ mJ m}^{-2}$ ). The topside of the same electrode produced the most hydrophilic response ( $11.05 \text{ mJ m}^{-2}$ ). Surface free energy was evaluated ( $\gamma_s$ ), with the top side of the 3D-Printed BM electrode showing the greatest surface energy ( $48.06 \text{ mJ m}^{-2}$ ), whilst the topside of the PLA control showed the least surface energy ( $36.58 \text{ mJ m}^{-2}$ ). The underside of the 3D-Printed BM electrode produced the highest Lifshitz van der Waals forces ( $\gamma_{sLW}$ ),  $38.37 \text{ mJ m}^{-2}$ . The Acid-Base interactions ( $\gamma_{sAB}$ )

revealed that the topside of the 3D-Printed BM electrode produced a significantly higher Acid-Base value ( $16.32 \text{ mJ m}^{-2}$ ), whilst the underside of the electrode produced the lowest Acid-Base value ( $1.72 \text{ mJ m}^{-2}$ ). The electron accepting ( $\gamma_{s+}$ ) values showed that the topside of the 3D-Printed BM was the most electron accepting surface ( $1.88 \text{ mJ m}^{-2}$ ), whilst the opposite (under) side had the lowest electron accepting preference ( $0.08 \text{ mJ m}^{-2}$ ). This same trend was seen with the electron donating ( $\gamma_{s-}$ ) values, with the topside of the 3D-Printed BM electrode showing the greatest electron donating preference ( $36.49 \text{ mJ m}^{-2}$ ), whilst the underside produced the lowest electron donating preference ( $0.08 \text{ mJ m}^{-2}$ ).

In summary, these results indicated that the 3D-Printed BM electrode featured the greatest variance with the underside being the most hydrophobic, non-polar surface and the topside the most hydrophilic polar surface. All electrodes had a greater affinity as electron donors.

Table 3.3. Physicochemistry values recorded *via* contact angle measurements of the 3D-Printed BM electrodes and control (3D-Printed PLA) electrode ( $n = 5$ ).

Surface Tested	Physicochemistry Parameters Recorded ( $\text{mJ m}^{-2}$ )					
	$\Delta G_{iwi}$	$\gamma_s$	$\gamma_s^{LW}$	$\gamma_s^{AB}$	$\gamma_s^+$	$\gamma_s^-$
PLA – topside	-18.37 ( $\pm 5.45$ )	36.58 ( $\pm 1.77$ )	31.86 ( $\pm 1.30$ )	4.72 ( $\pm 1.24$ )	0.43 ( $\pm 0.17$ )	17.36 ( $\pm 2.40$ )
PLA – underside	-7.80 ( $\pm 2.81$ )	42.81 ( $\pm 1.47$ )	36.52 ( $\pm 0.68$ )	6.29 ( $\pm 0.96$ )	0.46 ( $\pm 0.14$ )	23.36 ( $\pm 1.43$ )
3D-Printed BM - topside	11.05 ( $\pm 5.44$ )	48.06 ( $\pm 3.82$ )	31.74 ( $\pm 1.11$ )	16.32 ( $\pm 3.10$ )	1.88 ( $\pm 0.46$ )	36.49 ( $\pm 4.67$ )
3D-Printed BM - underside	-26.40 ( $\pm 3.19$ )	40.09 ( $\pm 1.59$ )	38.37 ( $\pm 1.23$ )	1.72 ( $\pm 0.69$ )	0.08 ( $\pm 0.06$ )	15.53 ( $\pm 1.10$ )

## 3.4 Discussion

### 3.4.1 Electrochemical Analysis

The electrochemical activity of the 3D-Printed BM electrodes were examined under three conditions, namely, the filament prior to printing, polished and unpolished 3D-Printed electrodes. This was conducted to assess the best method for future MFC studies, which included bacterial growth optimisation. The unpolished 3D-Printed BM electrode produced the fastest  $K^0$  ( $1.35 \times 10^{-3} \text{ cm s}^{-1}$ ) compared with the polished 3D-Printed BM electrode ( $1.48 \times 10^{-3} \text{ cm s}^{-1}$ ) and the original filament (prior to printing),  $2.14 \times 10^{-3} \text{ cm s}^{-1}$ . The BM filament produced the shortest  $\Delta E_p$  at  $100 \text{ mV s}^{-1}$ ,  $151.07 \text{ mV}$ , indicating this electrode was the most reversible (and therefore most efficient) in the presence of a redox probe. The electrochemical area indicated that the 3D-Printed BM electrodes, both polished and unpolished, produced greater surface areas than the BM filament (prior to 3D-Printing), this could explain why the BM filament produced the shortest peak-to-peak separation, due to the graphene in the 3D-Printed electrodes being more evenly distributed (Foster *et al.*, 2017). Due to the similar results obtained for both the polished and unpolished 3D-Printed BM electrodes, coupled with the reduction in post-print modification (Foster *et al.*, 2017), the unpolished 3D-Printed BM electrodes were selected for further study.

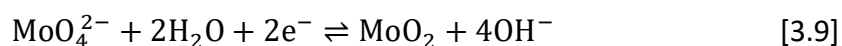
### 3.4.2 Topographical Characterisation

Characterisation of the 3D-Printed BM electrodes was performed using a range of techniques. Scanning electron microscopy of the 3D-Printed BM electrodes revealed a difference in surface topography which was a direct result of the electrodes post-print modifications (*i.e.* the polishing step). As expected, the unpolished electrode revealed a rougher surface topography. This feature could potentially enhance the attachment and retention of the bacteria to the electrodes, due to the presence of pits and grooves at a microscale level, which could subsequently enhance the power output of applications such as MFCs (Dantas *et al.*, 2016; Liu *et al.*, 2017). Raman spectroscopy of the 3D-Printed BM electrode revealed characteristic carbon spectra (Ferrari, 2007; Ferrari and Robertson, 2000). The electrodes were composed of multi-layered graphene, which was determined

due to the presence of a highly symmetrical 2D ( $G'$ ) peak (Ferrari *et al.*, 2006). Multi-layered graphene (also known as *quasi*-graphene) exhibits enhanced HET kinetics than monolayer graphene, due to the increased coverage of edge planes (the predominate origin of fast electron kinetics from graphitic electrodes) (Brownson *et al.*, 2014).

### 3.4.3 Determination of the Electroactive Area *via* Molybdenum Dioxide Nanowire Formation

Electro-deposition of  $\text{MoO}_2$  on electrodes was performed to determine the electroactive area of the 3D-Printed BM electrodes. Cyclic voltammetry was used to establish an effective deposition potential. Subsequently, the selected potential (-0.805 V) was held during chronoamperometry studies for varying time-points, namely, 0 s, 20 s, 40 s, 60 s, 120 s, 180 s, 240 s and 300 s allowing for an optimised coating of the 3D-Printed BM electrodes with  $\text{MoO}_2$ . The deposition of the  $\text{MoO}_2$  on the surface of the 3D-Printed electrode BM, was due to the reduction of  $\text{Mo}^{6+}$  to  $\text{Mo}^{4+}$  at -0.805 V, this occurred *via* the following equation [3.9] (Rowley-Neale *et al.*, 2016a; Walter *et al.*, 2003):



At the appropriate potential -0.805 ( $\pm 0.002$ ) V (*vs.* SCE), the production and nucleation of  $\text{MoO}_2$  nanowires was observed after 120 s, 180 s, 240 s and 300 s deposition time. The anodic sweep of the voltammogram demonstrated the inverse reaction. This was presented as an oxidation peak which related to the oxidation of  $\text{MoO}_2$  on the surface of the electrode to  $\text{MoO}_4^{2-}$ , which was then re-dissolved in the solution. The oxidation peak in this case was smaller than that of the reduction peak. This indicates that the  $\text{MoO}_2$  could potentially be entrapped within the porous architecture (as observed in the SEM images) of the 3D-Printed BM electrodes. Walter *et al.* (2003) demonstrated that  $\text{MoO}_2$  nanowire formation was specific to the electroactive sites of highly orientated pyrolytic (HOPG) electrodes by optimising stringent parameters (*i.e.* deposition potential and time), which revealed at -0.7 V (*vs.* SCE), the  $\text{MoO}_2$  formation was exclusive to the edge planes (Walter *et al.*, 2003). However, at -1.25 V (*vs.* SCE)  $\text{MoO}_2$  nucleation dramatically increased on the basal planes (Walter *et al.*, 2003). This study indicated that for  $\text{MoO}_2$  nucleation to be

specific to the electro-active regions of the electrode surface, parameters such as the deposition time and potential should be evaluated for the electrode material in question. In line with the previous literature, an average half-reduction peak potential (-0.805 V) was selected for this study, in order to control the rate of MoO<sub>2</sub> nucleation which was then evaluated by varying the deposition time.

### 3.4.3.1 Electrode Characterisation

Raman spectroscopy was utilised to validate the deposition of the MoO<sub>2</sub> on the surface of the electrodes over the eight selected time-points. All of the Raman spectra revealed characteristic carbonaceous peaks, routinely referred to as the G and 2D (G') bands (Baranov *et al.*, 1987; Ferrari, 2007; Graf *et al.*, 2007; Kondratowicz *et al.*, 2015; Wang *et al.*, 2008; Yoon *et al.*, 2009). Full width at half maximum (FWHM) analysis of the 2D bands confirmed the presence graphene. The FWHM values of the 2D band for monolayer graphene and *quasi-layer* graphene correspond to 28 cm<sup>-1</sup> and 58 cm<sup>-1</sup> respectively (Kim *et al.*, 2012; Lin *et al.*, 2015). This was also in agreement with Foster *et al.*, (2017) who utilised the same 3D-Printed BM electrode material and reported a FWHM value of 94 cm<sup>-1</sup>. It can be deduced that this was due to agglomeration of the graphene in the PLA filament (Foster *et al.*, 2017). Zhou *et al.* (2016) used Raman spectroscopy to confirm the fabrication of MoO<sub>2</sub> nanoparticles, with the Raman spectra indicating peaks at 287 cm<sup>-1</sup>, 341 cm<sup>-1</sup>, 606 cm<sup>-1</sup>, 819 cm<sup>-1</sup> and 987 cm<sup>-1</sup> (Zhou *et al.*, 2016a). The peaks in the Raman spectra, which confirmed the presence of MoO<sub>2</sub> in the present study, were in agreement with previous literature.

Scanning electron microscopy was conducted and a time dependent deposition process of the MoO<sub>2</sub> on the surface of the electrodes was observed. The electrodes coated for 20 s, 40 s and 60 s showed no variation from the control, whilst the electrodes coated for 240 s and 300 s resulted in a thick nucleation of MoO<sub>2</sub> upon the electroactive areas. The optimisation of specific parameters can alter the sensitivity and rate of deposition upon an electrode surface. In one study where screen printed electrodes (SPEs) were used, MoO<sub>2</sub> deposition was controlled by varying the deposition potential in chronoamperometry studies (Rowley-Neale *et al.*, 2015). This demonstrated that as the MoO<sub>2</sub> deposition time increased, the specific nucleation along the electrochemical active sites also increased.

### 3.4.3.2 Electrochemical Effect on Surface Areas

The electrochemically-derived areas in this study did not produce a coherent trend as expected. This may be due to the porous nature and large variability in surface topography of the 3D-Printed BM electrodes. It has been stated that due to the 3D-fabrication process, it is a challenge to control the microscopic and macroscopic topographies of 3D graphene-based structures (Yang *et al.*, 2015c). Due to this, MFA analysis was found to be an effective alternative method for determination and quantification of the electrochemically active areas of the 3D-Printed BM electrodes.

### 3.4.3.3 Multifractal Analysis

Multifractal analysis (MFA) was conducted to produce  $f(\alpha)$  curves, derived from the SEM images of the electrode surfaces after the eight MoO<sub>2</sub> deposition times. From the  $f(\alpha)$  curves, percentage coverage, density, dispersion and clustering data was determined. MFA analysis revealed that as the deposition time of MoO<sub>2</sub> increased, density results showed that the 3D-Printed BM electrode coated for 20 s produced the lowest density,  $D_0 = 1.45$  whilst the 300 s electrode produced the highest density  $D_0 = 1.75$ . As expected, dispersion (and therefore heterogeneity) of the MoO<sub>2</sub> was the greatest on the electrode coated for 20 s, this was due to the smaller concentration of MoO<sub>2</sub> present. As  $\Delta f(\alpha) < 1$  indicates a greater degree of clustering of the MoO<sub>2</sub> (Tetlow *et al.*, 2017; Wickens *et al.*, 2014). This indicated that as the MoO<sub>2</sub> deposition time increased, the clustering value became more negative, which resulted in a more targeted deposition on the electrochemically active sites.

The percentage surface coverage of the MoO<sub>2</sub> was found to be a time dependent processes, the 3D-Printed BM electrode coated for 20 s had the lowest coverage of MoO<sub>2</sub>, whilst the 3D-Printed electrode coated for the maximum amount of time tested in this study (300 s) demonstrated the greatest percentage coverage. Unlike the electrochemically derived areas, the area calculated *via* MFA determined the electro-active regions of the electrodes by quantifying only the deposited MoO<sub>2</sub>. Multifractal analysis relies heavily on the estimation of fractional features, and in the current study, the fractional features in this study were the MoO<sub>2</sub> depositions (Lopes and Betrouni, 2009).

Multifractal analysis has been utilised in a plethora of biological and chemical applications, such as bacterial quantification and cell dispersion (Wickens *et al.*, 2014), disease diagnosis (Lopes and Betrouni, 2009) and to evaluate the sensitivity of catalytic reactions in relation to their structure (Gutfraind *et al.*, 1991). Furthermore, MFA has been used to characterise surface topographies, such as, amplitude and spatial distribution of Cu-Ni nanoparticles in hydrogenated amorphous carbon surfaces (Țălu *et al.*, 2015). The present study was the first example where MFA was performed to quantify the electro-active regions of an electrode surface *via* MoO<sub>2</sub> nucleation.

### 3.4.4 Surface Analysis

To characterise the surface topography of both sides of the 3D-Printed electrodes, optical profilometry and physicochemistry studies were conducted. These results demonstrated which surface of the electrode may promote enhanced bacterial adherence due to a variety of parameters including, surface roughness and hydrophobicity (Slate *et al.*, 2019c; Wilson-Nieuwenhuis *et al.*, 2017).

#### 3.4.4.1 Optical Profilometry

Understanding the topography of surfaces (in this case the 3D-Printed BM electrodes), is a vital parameter to be considered when investigating bacterial attachment (Perera-Costa *et al.*, 2014; Whitehead and Verran, 2006). The size and shape of morphological features on the surface can directly influence bacterial attachment, with cells aligning in such a way that maximises surface contact (Hsu *et al.*, 2013). Current research indicates that an increased surface topography results in an increase in bacterial attachment and this may also facilitate biofilm formation (Katsikogianni and Missirlis, 2004; Teughels *et al.*, 2006).

Optical profilometry was used to characterise the surface roughness of the electrodes in this study. Both sides of the 3D-Printed BM and PLA (graphene deficient) electrodes were evaluated and  $S_a$  (average surface roughness),  $S_p$  (max peak height),  $S_v$  (max valley depth) and  $S_{pv}$  (max height of the surface) values were recorded. The  $S_a$  values revealed that that the topside of the 3D-Printed electrodes (both the BM and the PLA control) resulted in a greater surface roughness than the underside of the electrodes. The average surface roughness ( $S_a$ ) of the 3D-Printed BM electrodes topside was 4.40  $\mu\text{m}$  and for the underside it was 2.65  $\mu\text{m}$ . *Pseudomonas aeruginosa* has cell dimensions in the region of 0.5  $\mu\text{m}$  - 1.0  $\mu\text{m}$  (diameter) and 1.5  $\mu\text{m}$  - 5.0  $\mu\text{m}$  (length) (Bédard *et al.*, 2016). The exhibited difference in surface roughness of the 3D-Printed BM electrodes could have an effect on bacterial attachment and adhesion (Bédard *et al.*, 2016; Tellefsen *et al.*, 2016; Yoda *et al.*, 2014).

The optical profilometry results demonstrated that the additive manufacturing process did not yield homogeneous surfaces, as the observed smoother underside of the electrodes may be due to the surface/scaffold-electrode interface during printing (Serra *et*

*al.*, 2014). The underside of the 3D-Printed BM electrode demonstrated the max peak height ( $S_p$ ), whilst, the topside of the same electrode displayed the max valley depth ( $S_v$ ) and the max height of the surface ( $S_{pv}$ ). Thus, the 3D-Printed BM electrode produced a rougher surface topography than its PLA control. Furthermore, the surface topography of both sides (*i.e.* topside and underside) of the same electrode also varied. In one study, optical profilometry was used to determine the surface roughness of a 3D-Printed PLA surface where the surface roughness ranged from 2.46  $\mu\text{m}$  and 22.48  $\mu\text{m}$  (Akande, 2015). These values are comparable to the average surface roughness values obtained throughout this chapter.

#### 3.4.4.2 Physicochemistry

Another set of important parameters to be considered when investigating bacterial attachment is the physicochemistry of the surfaces. Due to the complex nature of processes involved in surface physicochemistry, bacterial attachment mechanisms are poorly understood (Wang *et al.*, 2015c). Hydrophobic interactions (measured as interfacial surface free energy -  $\Delta G_{iwi}$ ) can mediate the thermodynamic forces that occur between bacterial cells, substratum surfaces and liquid suspending medium (Araújo *et al.*, 2009; Van Oss, 1989). Hydrophobic interactions consist of both long-range Lifshitz-van der Waals forces ( $\gamma_{sLW}$ ) and short-range Lewis acid-base (AB) forces ( $\gamma_{sAB}$ ) (Yang *et al.*, 2015b). Electrostatic interactions can also impact the attachment of bacteria to a surface (Dotto *et al.*, 2015; Wang *et al.*, 2015c).

Interfacial surface free energy, ( $\Delta G_{iwi}$ ) results revealed that the underside of the 3D-Printed BM electrodes and both sides of the PLA control were hydrophobic, with the underside of the 3D-Printed BM electrode being the most hydrophobic. Conversely, the topside of the 3D-Printed BM electrode was the most hydrophilic. Therefore, it was clear that both sides of the 3D-Printed BM electrode have a degree of variation and this could be due to the manufacturing process. The topside of the 3D-Printed BM electrode resulted in the greatest surface free energy ( $\gamma_s$ ), a significantly greater Acid-Base interaction ( $\gamma_{sAB}$ ) and the highest electron accepting ( $\gamma_{s+}$ ) and electron donating ( $\gamma_{s-}$ ) values. This showed that the topside of this electrode was the most polar, indicating a greater presence of functional groups, for example carboxylic acid and hydroxyl groups (Baran and Erbil, 2019). This is

particularly important, as these functional groups are known to bind with bacteria and therefore enhance attachment (Kinnari *et al.*, 2010). However, the underside of the 3D-Printed BM electrodes produced the greatest Lifshitz van der Waals forces ( $\gamma_{sLW}$ ), indicating an increased affinity for long-range interactions (Lundqvist *et al.*, 1995). The higher base energies ( $\gamma_{s-}$ ) indicated that all electrodes utilised in this study were preferential to donating electrons as opposed to accepting electrons, whilst the introduction of graphene to the top side of the 3D-Printed BM electrode doubled both the electron donating and accepting properties when compared to the top side of the 3D-Printed PLA control. This could potentially enhance bacterial attachment and electron donating ability, resulting in an enhanced power output in future MFC studies (refer to Chapter Five).

### 3.5 Conclusion

The 3D-Printed BM electrodes (incorporating graphene) were fabricated and characterised *via* SEM and Raman spectroscopy. The fabricated electrodes were electrochemically evaluated to determine if topographical modification (by polishing) enhanced electrode performance. Electrochemical analysis *via* cyclic voltammetry revealed little difference in electrode response when comparing polished and non-polished electrodes. The electrodeposition of MoO<sub>2</sub> nanowires was applied to determine the electro-active sites on the 3D-Printed electrodes. The deposition of MoO<sub>2</sub> was investigated using MFA. Finally, the surface characteristics were investigated using optical profilometry to determine surface roughness, which revealed that each side of the 3D-Printed BM electrode consisted of a varying topography, due to the fabrication process. Physicochemistry analysis revealed that whilst the underside of the 3D-Printed BM was hydrophobic, the topside of the 3D-Printed BM electrode was hydrophilic. Furthermore, the topside of the 3D-Printed BM electrode was the most polar and this indicated an increased presence of functional groups, which could be beneficial for bacterial attachment. When comparing the topside of the PLA control to the topside of the 3D-Printed BM electrode, the presence of graphene doubled both the electron donating and accepting properties of the electrode. The increased surface roughness observed by the 3D-Printed BM electrodes, coupled with the enhanced electron donating and accepting properties could be beneficial for bacterial attachment and power output when utilised in a MFC.

# **Chapter 4 – *Pseudomonas aeruginosa* Selection and Optimisation**

## 4.1 Introduction

### 4.1.1 Exoelectrogenic Properties of *P. aeruginosa*

*Pseudomonas aeruginosa* has previously been shown to exhibit exoelectrogenic properties and thus this bacteria has been utilised in a number of MFC configurations (Ali *et al.*, 2017; Price-Whelan *et al.*, 2007; Shen *et al.*, 2014). Power outputs of *P. aeruginosa* strains in MFCs can vary depending on a range of factors, including phenazine (e.g. pyocyanin) production, flagella efficiency and biofilm formation (Ali *et al.*, 2017; Rabaey *et al.*, 2005). Bacterial cell surface hydrophobicity plays a crucial role in surface attachment and detachment (Krasowska and Sigler, 2014). Therefore, pyocyanin production, flagella efficiency, biofilm formation and bacterial cell surface hydrophobicity, were used as the criteria to select an optimal exoelectrogenic *P. aeruginosa* strain. Pyocyanin is responsible for the characteristic green phenotype of *P. aeruginosa* strains, therefore, strains with increased pyocyanin production demonstrate an enhanced green pigmentation (Gellatly and Hancock, 2013). In light of this, strains which demonstrated a green phenotypic appearance after 24 h growth on solid media were selected for initial experimentation.

### 4.1.2 Pyocyanin

The exoelectrogenic attributes of *P. aeruginosa* are due to the production of soluble redox mediators, such as phenazines (Bosire and Rosenbaum, 2017). Phenazines exhibit electron transfer mediating properties by acting as electron shuttles, transferring liberated electrons to the anode in a MFC (Rabaey *et al.*, 2005). Examples of phenazines include pyocyanin, phenazine-1-carboxylic acid, phenazine-1-carboxamide and 1-hydroxyphenazine (Boon *et al.*, 2008; Shen *et al.*, 2014; Venkataraman *et al.*, 2010). Pyocyanin is a predominant phenazine secreted by *P. aeruginosa* and is the most well characterised natural phenazine (Allen *et al.*, 2005; Price-Whelan *et al.*, 2007).

Pyocyanin is a blue-green pigmented, redox-active secondary metabolite (other synonyms include, Pyocyanine, 5-Methyl-1(5H)-phenazinone, Pyocyanine, Sanazin and Sanasin), and the chemical formula for pyocyanin is  $C_{13}H_{10}N_2O$  (Figure 4.1) (Lau *et al.*, 2004).

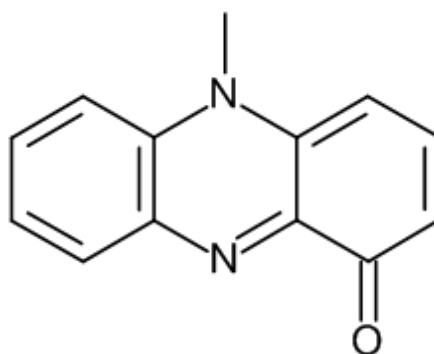


Figure 4.1. Chemical structure of Pyocyanin.

Pyocyanin plays a crucial role in *P. aeruginosa* metabolism, in cases when the natural electron acceptor, such as oxygen, is insufficient or absent (Bosire and Rosenbaum, 2017). Pyocyanin maintains a cellular redox balance by oxidising NADH and under anaerobic conditions this may enable *P. aeruginosa* survival (Wang *et al.*, 2010). In MFC applications, the concentration of pyocyanin in an anodic culture has previously been shown to have a direct correlation to enhanced power generation, due to its ability to transport electrons through the cell membrane (Shen *et al.*, 2014). Furthermore, the addition of pyocyanin produced by *P. aeruginosa* can be utilised by other microorganisms (which may be incapable of pyocyanin production) in MFCs, thus resulting in enhanced current generation (Hernandez *et al.*, 2004; Rabaey *et al.*, 2005). The production rate of pyocyanin by *P. aeruginosa* is affected by a range of factors, including the growth media conditions, physiological status and the growth phase (Price-Whelan *et al.*, 2007; Romano *et al.*, 2015). Therefore, it is theorised that enhancing and maximising pyocyanin production by optimisation of the growth medium (*e.g.* fuel) could enhance power outputs in *P. aeruginosa* MFCs (Price-Whelan *et al.*, 2007).

### 4.1.3 Nanowires

Flagella and pili (also known as bacterial nanowires) have previously shown electron transfer properties; this is another mechanism *via* which *P. aeruginosa* can transfer electrons in a MFC configuration (Malvankar and Lovley, 2014; Maruthupandy *et al.*, 2015; Reguera *et al.*, 2006a). However, the mechanism of electron transfer has yet to be fully

elucidated. Current hypothesised mechanisms include the metallic-like conductivity model and the electron-hopping model (Sure *et al.*, 2016). In the metallic-like conducting model, synthetic organic metals are able to transfer electrons due to overlapping  $\pi$ - $\pi$  orbitals of aromatic rings present. The metallic-like conductivity model postulates that the proteins, which constitute bacterial nanowires, contain several aromatic amino acids, and these aromatic constituents may play a similar role to that of organic metals in regards to electron transfer (Sure *et al.*, 2016). In the electron-hopping model hypothesis, long-range electron transfer takes place through the nanowires *via* an intricate cytochrome network (Strycharz-Glaven *et al.*, 2011; Tender, 2011).

The flagella and type IV pili of *P. aeruginosa* are required for optimal biofilm formation (O'toole and Kolter, 1998). A number of genes are involved in flagella and pili formation and an example of one such gene is *pilT*, which encodes an ATPase (Hassett *et al.*, 2010). However, when this gene is absent an increase in the number of type IV pili are observed (Mukherjee *et al.*, 2013). *Pseudomonas aeruginosa*, *pilT* mutants have the ability to generate substantially higher power outputs than their wild-type counterparts (Shreeram *et al.*, 2016). The flagellum of *P. aeruginosa* is also highly conductive (Maruthupandy *et al.*, 2015). As the flagellum is anchored in the periplasm and outer membrane of the cell, it has been hypothesised that the flagellum can accept electrons from periplasmic and/or outer membrane electron transfer proteins (Maruthupandy *et al.*, 2015). Therefore, more motile *P. aeruginosa* strains are hypothesised to demonstrate enhanced power generation when utilised within a MFC configuration.

#### **4.1.4 Cell Surface Hydrophobicity**

Bacterial cell surface hydrophobicity is known to have a crucial role in cell attachment and detachment (Krasowska and Sigler, 2014). Previous chemical compatibility concepts applied to solution and adhesion theories suggest that more hydrophobic cells adhere more strongly to hydrophobic surfaces, whilst hydrophilic cells attach with greater affinity to hydrophilic surfaces. Several researchers have found this to be true (Giaouris *et al.*, 2009; Kochkodan *et al.*, 2008; Krasowska and Sigler, 2014). However, this effect still remains controversial, being dependent on a number of surface and environmental factors (Verran and Whitehead, 2005; Whitehead and Verran, 2015). Another factor that may

influence bacterial attachment is electrostatic interactions, more specifically the electrical double layer structure (James, 1991). This structure consists of two spatial regions forming a relatively thin layer that is directly adjacent to the bacterial cell. This is termed the Stern layer and consists of cations, due to the relative negative charge of the bacterial cell (Daeschel and McGuire, 1998). The outer layer is more heterogeneous and diffuse in regards to ion content and a decrease in potential is observed the further the layer extends from the bacterial cell (Daeschel and McGuire, 1998). In the presence of a higher electrolyte concentration or in the presence of counter ions, electrostatic interactions are reduced and therefore bacterial cell adhesion will be decreased (Daeschel and McGuire, 1998). Kouzuma *et al.* (2010) demonstrated that cell surface hydrophobicity influenced the adhesiveness of *S. oneidensis* cells to graphite felt anodes, which had a direct influence on current generation of the MFC configuration (Kouzuma *et al.*, 2010). In the previous chapter of this thesis, it was determined that the 3D-Printed BM electrodes consisted of a hydrophilic topside and hydrophobic underside, possibly due to the manufacturing process. Thus, it is important to determine the surface hydrophobicity of *P. aeruginosa* in order to understand how this affects the attachment mechanisms used to attach to the 3D-Printed BM electrodes.

#### **4.1.5 Biofilm Effect on Power Outputs**

The power output from planktonic cells attached to the anode surface is limited by the total surface area of the electrode. Biofilms are able to produce much higher power and current densities due to the increased number of bacteria available for electron generation and transfer (Friman *et al.*, 2013). The composition, morphology, thickness and physical properties of biofilms play a pivotal role in bioelectricity production (Angelaalincy *et al.*, 2018). Enhanced biofilm formation on the anodic surface is directly proportional to power outputs in MFCs (Yuvraj and Aranganathan, 2017). Other studies suggest that the presence of viable bacteria is more influential than an enhanced thickness in biofilm formation (Sun *et al.*, 2016a). Therefore, the underlying substrata and the bacterial strains used may influence energy generation. Thus, a more thorough understanding of this phenomenon is required for meaningful insights into electron transfer optimisation. As such, *P. aeruginosa*

strains were evaluated for their ability to form biofilms, in order to potentially enhance the power outputs in MFC configurations.

#### **4.1.6 Anaerobic Survival and Proliferation of *P. aeruginosa***

*Pseudomonas aeruginosa* is a facultative anaerobe with remarkable metabolic versatility, being able to assimilate a wide range of compounds, which not only allows for survival but also proliferation in low nutrient and anaerobic environments (Arai, 2011). Glucose is not the preferred carbon source for *P. aeruginosa*, and other sources of carbon which include some organic acids (such as succinate) and amino acids are metabolised preferentially before glucose (Rojo, 2010).

Under anaerobic conditions, pyruvate allows for long-term anaerobic survival (not growth) of *P. aeruginosa* by converting pyruvate to lactate, acetate and succinate whilst, arginine sustains moderate anaerobic growth *via* fermentation (Eschbach *et al.*, 2004; Vander Wauven *et al.*, 1984). To metabolise glucose, *P. aeruginosa* uses the Entner-Doudoroff pathway. This pathway converts one glucose molecule into two pyruvate molecules and is coupled to the synthesis of one net ATP molecule and two excess reducing equivalents (nicotinamide adenine dinucleotide phosphate (NAD(P)H)), per pyruvate molecule (Glasser *et al.*, 2014). Pyruvate molecules can be degraded further to produce acetate, producing additional ATP and reducing equivalents (Glasser *et al.*, 2014). To sustain anaerobic glycolysis, oxidants, such as nicotinamide adenine dinucleotide (NAD<sup>+</sup>) and nicotinamide adenine dinucleotide phosphate (NADP<sup>+</sup>), which were metabolised during pyruvate and acetate generation must be regenerated. Thus, it is thought that the redox cycling attributes of phenazines plays a pivotal role in the regeneration of such molecules (Glasser *et al.*, 2014).

Another pathway utilised under anaerobic (and low oxygen) conditions is the denitrification process (Hasset *et al.*, 2002). This pathway supports *P. aeruginosa* growth under anaerobic conditions due to the utilisation of alternative terminal acceptors in the form of nitrogen oxides (Kuroki *et al.*, 2014; Schreiber *et al.*, 2007). The production of energy under anaerobic conditions *via* the denitrification pathway is important for the pathogenesis of *P. aeruginosa* (Kuroki *et al.*, 2014). This process consists of the sequential reduction of nitrate to nitrite, nitrous oxide (NO), nitric oxide (N<sub>2</sub>O) and finally N<sub>2</sub>. This

pathway is catalysed by the metalloenzymes, nitrate reductase (NAR), nitrite reductase (NIR), NO reductase (NOR) and N<sub>2</sub>O reductase (N<sub>2</sub>OR), respectively (Figure 4.2.) (Kuroki *et al.*, 2014). Two transcriptional regulators ANR (anaerobic regulator of arginine deiminase and nitrate reductase) and DNR (dissimilatory nitrate respiration regulator), which belong to the FNR (fumarate and nitrate reductase regulator)/cAMP receptor protein family, hierarchically control the expression of denitrification genes in *P. aeruginosa* (Arai *et al.*, 1995; Arai *et al.*, 1997). Expression of the *dnr* gene is under control of the ANR, which is induced under low oxygen or anaerobic conditions (Arai *et al.*, 1997). In addition to ANR and DNR, integration host factor, the two-component nitrate-sensing regulator NarXL, *rhl* quorum-sensing system and the PQS system are also involved in the regulation of denitrification in *P. aeruginosa* (Schreiber *et al.*, 2007; Toyofuku *et al.*, 2007; Toyofuku *et al.*, 2008; Yoon *et al.*, 2002).

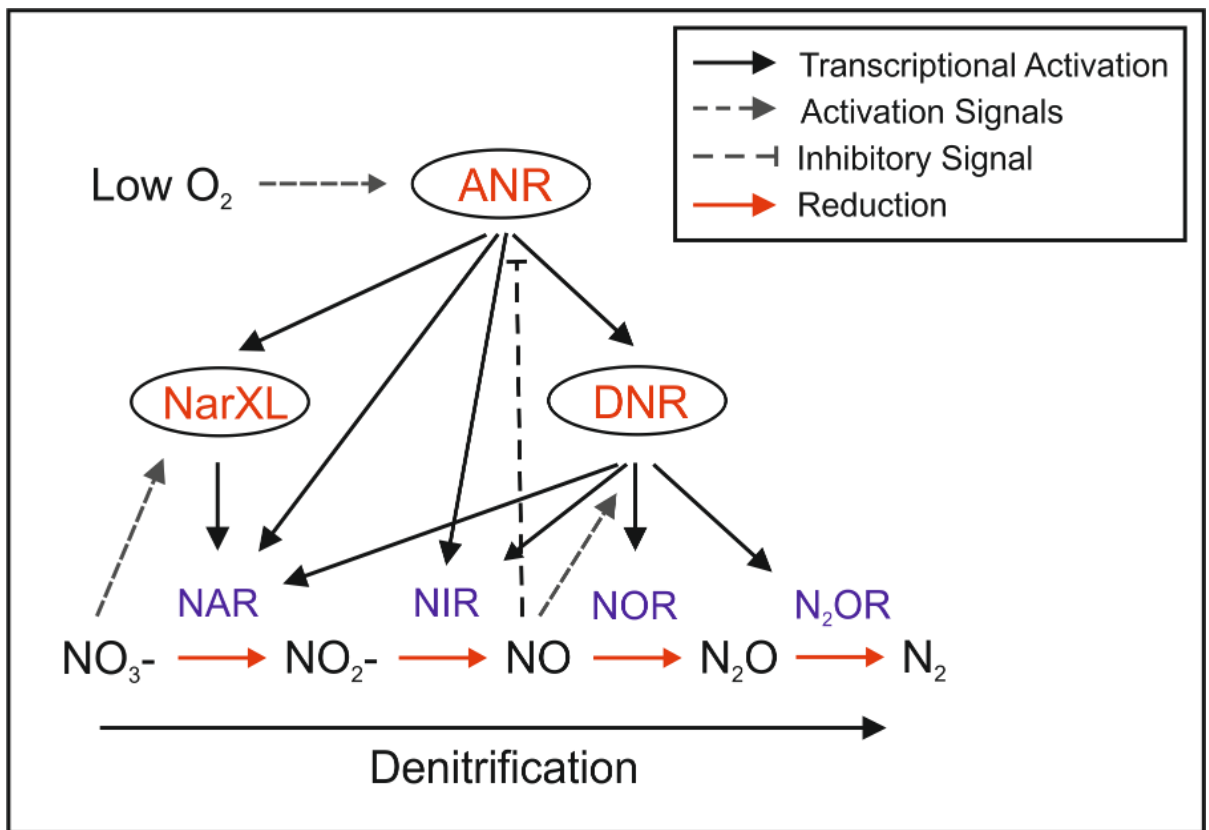


Figure 4.2. Anaerobic denitrification process, including denitrification gene expression and regulatory network in *P. aeruginosa*. This process is catalysed by the following metalloenzymes, nitrate reductase (NAR), nitrite reductase (NIR), NO reductase (NOR) and N<sub>2</sub>O reductase (N<sub>2</sub>OR). Figure adapted from Kuroki *et al.* (2014).

This denitrification process supports electron transfer in MFCs as simultaneous denitrification and electricity generation has previously been reported (Zhou *et al.*, 2016b). Due to the complexity and variation in *P. aeruginosa* metabolism, which is dependent on the carbon/nitrogen source present, this chapter investigated selection and optimisation of the growth media (*i.e* the fuel) used in MFCs, in order to enhance power outputs. Selection of the most beneficial media should result in exoelectrogenic *P. aeruginosa* cells that could potentially remain viable for longer, proliferate at a greater rate and liberate more electrons, which could then be transported to the anode, therefore enhancing the power output in MFC configurations.

In the absence of nitrate or nitrite, arginine serves as a substrate for anaerobic growth as it can be catabolised to yield ornithine and ATP (Vander Wauven *et al.*, 1984;

Eschbach *et al.*, 2004). Without arginine or an alternative electron acceptor, *P. aeruginosa* rapidly becomes energy starved in anaerobic growth medium and the cell numbers decline from  $1 \times 10^9$  to  $5 \times 10^5$  CFU mL<sup>-1</sup> within 16 days (Binnerup and Sørensen, 1993). In the case of the experimental studies conducted here, it is likely that anaerobic growth in LB was supported by arginine fermentation rather than denitrification, as arginine is present at *ca.* 2.8 mM (determined by high performance liquid chromatography) in LB and the medium was not supplemented by nitrate (Sezonov, Joseleau-Petit and D'Ari, 2007).

#### **4.1.7 Aim**

The aim of this study was to screen a range of *P. aeruginosa* strains and select the most optimal strain which expressed the most exoelectrogenic attributes for MFC application. Key parameters included high pyocyanin production, good biofilm formation, enhanced motility and cell surface hydrophobicity. Further optimisation by changes in bacterial growth conditions was performed to determine bacterial growth dynamics coupled with LC-MS studies for the optimisation of pyocyanin production and anaerobic growth. Biofilm formation was assessed on the 3D-Printed electrodes.

## 4.2 Methods

### 4.2.1 Growth Media Preparation and Bacterial Preparation

#### 4.2.1.1 Agar and Growth Media Preparation

Growth media used throughout this study included, Tryptone Soya Agar (TSA) and Broth (TSB) (Oxoid, UK) Luria-Bertani (LB) agar and broth (BD Difco™, USA) and a glucose-based medium that consisted: 10 g glucose, 5 g yeast extract, 6.8 g sodium bicarbonate and 8.5 g sodium phosphate monobasic per litre (Liu *et al.*, 2012). Growth media was prepared as per the manufacturer's instructions.

#### 4.2.1.2 Preparation of Bacterial Cells

The *P. aeruginosa* strains used throughout this study were type strains - PAO1 and ATCC 9027 and the following medical isolates were also selected - *P. aeruginosa* strain Hollings, *P. aeruginosa* strain MRI and *P. aeruginosa* strain Bolton. Prior to the start of the experiment, strains were removed from a -80 °C freezer stock and cultured onto the agar. Inoculated plates were incubated at 37 °C for 24 h. Following incubation, a single colony was isolated from the culture plate, inoculated into 10 mL of the corresponding broth and vortexed for 5 seconds. The inoculated broth was subjected to agitation (200 rpm) and incubated at 37 °C for 24 h, in either aerobic or anaerobic conditions.

Following incubation, the broth was vortexed (5 s) and centrifuged (2,342 *g* for 10 min). Pellets were resuspended and cells were washed with 10 mL of sterile distilled water, followed by centrifugation (2,342 *g* for 10 min). The final pellet was resuspended in 10 mL of broth. To standardise results, a spectrophotometer (Jenway, UK) was used to obtain an optical density (OD) of  $1 \pm 0.1$  (OD<sub>600 nm</sub>) (unless stated otherwise) *via* the adjustment in bacteria/broth concentrations, which equates to  $5.0 \times 10^8$  CFU mL<sup>-1</sup>.

## 4.2.2 Preliminary Strain Selection

### 4.2.2.1 Pyocyanin Production – Chloroform Extraction Assay

In order to quantify pyocyanin production, a range of *P. aeruginosa* strains were selected and prepared as per “Section 4.2.1 Growth Media Preparation and Bacterial Preparation”. This assay quantified pyocyanin production based on the absorbance of pyocyanin at 520 nm, under acidic conditions. Bacterial strains were inoculated into 5 mL of TSB and placed into an orbital shaker (200 rpm) for 24 h, 48 h, 7 d and 14 d at 37 °C.

Aliquots of 6 mL of inoculated broth ( $OD\ 1 \pm 0.1$  ( $OD_{600\text{ nm}}$ )) were transferred to sterile universals and incubated for a further 24 h (200 rpm, 37 °C). Samples were centrifuged for 10 min at 3,059 *g* and 5 mL of the supernatant was extracted and transferred to a sterile glass universal. Samples were vortexed (5 s) and 3 mL of chloroform was added to the supernatant. This was vortexed vigorously (10 times for 2 s) and was centrifuged at 1,721 *g* for 1 min. Upon visual inspection the chloroform was a faint blue colour, indicating pyocyanin isolation. The upper phase (TSB) was discarded, leaving the chloroform phase, to which 1 mL of 0.2 M HCl was added to the chloroform/pyocyanin solution, and a colour change was visualised from faint blue to faint pink/red.

Following the addition of HCl, the samples were vortexed vigorously (30 s) and were left stationary to settle for 10 min. The spectrophotometer (Jenway, UK) was calibrated at 520 nm, with the 0.2 M HCl solution. Once settled, 1 mL of the solution was taken and absorbance was then measured at 520 nm. Pyocyanin production ( $\mu\text{g/mL}$ ) was quantified by the following equation [4.1] (Essar *et al.*, 1990; Ho Sui *et al.*, 2012; Kurachi, 1958):

$$\text{Pyocyanin Quantification } (\mu\text{g/mL}) = \text{Optical Density (OD}_{520}) \times 17.072 \text{ (Extinction Coefficient)} \quad [4.1]$$

This experiment was repeated after 24 h, 48 h, 7 d and 14 d. Experiments were carried out in triplicate ( $n = 3$ ).

### 4.2.2.2 Biofilm Quantification – Crystal Violet Biofilm Assay

In order to quantify biofilm growth on the electrode surface, a Crystal Violet Biofilm Assay (CVBA) was carried out. Bacterial strains selected for this study were *P. aeruginosa*

strains ATCC 9027, PAO1 and MRI due to their high pyocyanin production quantified previously (as per Section 4.2.2.1). Growth media and bacterial strains were prepared as per “Section 4.2.1”. For *P. aeruginosa* biofilm formation, 1 mL of inoculated TSB, with an OD<sub>600 nm</sub> adjusted to  $1.0 \pm 0.1$  was added to a 12-well, flat-bottomed culture plate.

The fabricated 3D-Printed electrodes (Section 3.2.1) both polished and unpolished (Section 3.2.1.1), were sterilised using 70 % ethanol (submerged for 10 min) and individually placed into the wells of a 12 well culture plate, with the inoculated broth and the 12-well plate lid was added and sealed using Parafilm® to prevent evaporation during incubation. The inoculated well plates were incubated for 0 h, 1 h, 1 day, 5 days, 7 days and 14 days.

Following the incubation period, the broth was removed and discarded and the electrodes were dried at room temperature (1 h) in a type two biosafety cabinet (Atlas Clean Air, UK). One millilitre of 0.1 % Crystal Violet was added into each well containing the electrodes and left to stand for 30 min, thus staining the biofilm attached to the electrode surface. Excess Crystal Violet was rinsed from the electrodes with sterile deionised water (1 mL) over the electrode surface (carefully as to not disrupt/damage the attached biofilm) and the electrodes were transferred to a sterile 12 well culture plate. The electrodes were dried at room temperature for 1 h before the addition of 1 mL of 33 % glacial acetic acid into the wells to solubilise the Crystal Violet present.

A spectrophotometer (Jenway, UK) was calibrated against 1 mL 33 % glacial acetic acid at OD<sub>540 nm</sub>. Aliquots of 1 mL solubilised Crystal Violet were transferred into cuvettes for absorbance measurement. The absorbance/turbidity of the solubilised Crystal Violet is directly proportional to the amount of biomass present (Wilson *et al.*, 2017) ( $n = 3$ ).

#### **4.2.2.3 Motility Assay**

Luria Bertani (LB) agar was prepared at 0.4 % (addition of microbiological agar to LB broth (Oxoid, UK)). Cultures of *P. aeruginosa* strains, namely ATCC 9027 and PAO1 and MRI were prepared to an OD of  $1 \pm 0.1$  (OD<sub>600 nm</sub>) after overnight incubation at 37 °C in either aerobic or anaerobic conditions as required. One microlitre of the bacterial culture was point inoculated through the centre of the agar. For anaerobic growth, plates were immediately placed into a 2.5 L Oxoid™ AnaeroJar™ 2.5L (Thermo Scientific, UK) with an

*AnaeroGen*<sup>™</sup> sachet (Thermo Scientific, UK) to generate and maintain anaerobic conditions. Inoculated plates were incubated at 37 °C for 48 h and 72 h. Following the incubation period, the zone of bacterial growth through the agar was measured using calipers (Mitutoyo, UK). The zone of growth correlates directly to the motility attributes of the bacteria present ( $n = 3$ ).

#### 4.2.2.4 Microbial Adhesion To Hydrocarbons (MATH) Assay

Cultures of *P. aeruginosa* strains ATCC 9027 and PAO1, were inoculated and incubated under static, aerobic and anaerobic conditions at 37 °C for 24 h, 72 h and 120 h in LB broth. Due to the low biofilm production of the MRI strain over the first 5 days, characterisation of this strain for MFC application was discontinued. Bacterial cells were harvested by centrifugation (2,342 *g* for 15 min) and the supernatant was discarded and replaced with 5 mL phosphate urea magnesium (PUM) buffer (pH 7.1, K<sub>2</sub>HPO<sub>4</sub>·3H<sub>2</sub>O; 22.2 g/L, KH<sub>2</sub>PO<sub>4</sub>; 7.26 g/L, CH<sub>4</sub>N<sub>2</sub>O; 1.8 g/L, MgSO<sub>4</sub>·7H<sub>2</sub>O; 0.2 g/L) and the samples were centrifuged (2,342 *g* for 15 min). This washing process was repeated three times. Cell suspensions were adjusted to an OD of  $1.0 \pm 0.1$  (OD<sub>400 nm</sub>). Aliquots of 2 mL of the washed bacterial suspension were added to sterile test tubes (15 mm diameter) and 400 µL of the hydrocarbons, chloroform, hexadecane, decane and ethyl acetate (all chemicals were sourced from Merck, UK at a grade no less than 99 %) were added individually to cell samples. The test tubes were vortexed for 30 s and incubated at 37 °C for 30 min. Following incubation, 1 mL of the lower aqueous phase was removed and the absorbance was measured at OD<sub>400 nm</sub>. In order to determine cell surface hydrophobicity, the percent adhesion of the lower phase was calculated using the following equation [4.2] (Rosenberg *et al.*, 1983; Wilson-Nieuwenhuis *et al.*, 2017):

$$\text{Percentage Adhesion (\%)} = \left( \frac{1-A}{A_0} \right) \times 100 \quad [4.2]$$

where,  $A_0$  is the OD before the addition of the hydrocarbon and  $A$  is the OD from the lower aqueous phase, following the addition of the hydrocarbons ( $n = 3$ ).

#### 4.2.2.5 Scanning Electron Microscopy (SEM)

Due to the high pyocyanin and biomass production of *P. aeruginosa* strain ATCC 9027, this was selected for SEM analysis. Overnight bacterial cultures were incubated at 37 °C for 24 h on an orbital shaker (200 rpm). The bacterial culture was adjusted to an OD<sub>600 nm</sub> of 1.0 (± 0.1) and 1 mL was transferred into a 12 well, flat-bottomed culture plate. The fabricated 3D-Printed electrodes (Section 3.2.1) both polished and unpolished (Section 3.2.1.1), were sterilised using 70 % ethanol (submerged for 10 min). Individual 3D-Printed electrodes were added into the inoculated wells and the 12-well plate lid was added and sealed using Parafilm® to prevent evaporation during incubation. The samples were incubated for 24 h at 37 °C (conditions: aerobic, static). Subsequently, the inoculated broth was removed and samples were dried at room temperature for 1 h in a type two biosafety cabinet (Atlas Clean Air, UK). The 3D-Printed electrodes were submerged in 4 % glutaraldehyde for 24 h at 4 °C.

After fixing, the glutaraldehyde was discarded and the samples were washed in 5 mL sterile deionised water and dried at room temperature for 1 h in a class two biohazard cabinet (Atlas Clean Air, UK). The samples were dehydrated using an ethanol (absolute ethanol, Merck, UK) gradient of 10 %, 30 %, 50 %, 70 %, 90 % and 100 %, with the samples submerged in each ethanol concentration for 10 min. Immediately after the ethanol gradient the samples were placed in a desiccator (Silica gel, Merck, UK) for 24 h. Samples were attached to SEM stubs (diameter: 12.5 mm) using carbon tabs (Agar Scientific, UK) and were sputter coated with gold (Polaron, UK) for 30 s (800 V; 5 mA). The samples were visualised *via* SEM.

## 4.2.3 *Pseudomonas aeruginosa* strain ATCC 9027 Optimisation

### 4.2.3.1 Growth Kinetics

In order to determine the most appropriate growth media for use in the MFC configuration, bacterial growth kinetics were determined using *P. aeruginosa* strain ATCC 9027 grown in glucose-based and LB media under both complete anaerobic and aerobic-to-anaerobic starting conditions. Final anaerobic conditions were used throughout in order to replicate future MFC configurations.

Both optical density (OD<sub>540 nm</sub>) of cultures and bacterial viability were measured to evaluate the bacterial growth kinetics. Liquid chromatography-mass spectroscopy (LC-MS) analysis was used to quantify pyocyanin production. This was used to determine if the growth media and/or oxygen presence during initial bacterial growth can lead to an increase in pyocyanin production, thus allowing effective optimisation of the growth conditions for use in MFC applications.

A single colony of *P. aeruginosa* strain ATCC 9027 was inoculated into 10 mL of either glucose-based or LB broth (BD Difco™, USA). Following inoculation, anaerobic conditions were generated by purging media with nitrogen for 30 min. For the aerobic starting cultures, the same procedure was followed but the nitrogen-degassing step was omitted. The cultures were then incubated with agitation (200 rpm) at 37 °C for 18 h.

Following 18 h Incubation, the inoculated broth was centrifuged (1,721 x *g* for 10 min), the supernatant was discarded, and the pellet re-suspended in either glucose-based or LB broth, maintaining anaerobic conditions where required. The starting cultures were transferred to an anaerobic cabinet (Ruskin, Wales) and an OD<sub>540 nm</sub> of 1.0 (± 0.1) was obtained and 1 mL was transferred into 200 mL of either, sterile glucose-based or LB broth, (which was left overnight in the anaerobic cabinet to equilibrate) to start the growth experiment. This produced a starting OD<sub>540 nm</sub> of 0.01. This experiment was conducted in triplicate from three independent starting cultures (*n* = 3).

Aliquots of 6.1 mL were taken independently from the three conical flasks (starting culture volume: 200 mL) at each time-point, namely 0 h, 2 h, 4 h, 6 h, 24 h, 48 h, 72 h, 96 h and 120 h. At each time-point, 1 mL of the suspension was removed for optical density measurements (OD<sub>540 nm</sub>), 100 µL for the viable counting and 5 mL for LC-MS sample

preparation. Appropriate controls (either sterile glucose-based or LB broth) were also prepared in triplicate for analysis.

#### **4.2.3.1.1 Optical Density**

Aliquots of 1 mL were pipetted into cuvettes from the 6.1 mL of broth taken at each time-point. A spectrophotometer (Jenway, UK) was calibrated using an appropriate broth control (either glucose-based or LB depending on the media used) at OD<sub>540nm</sub>. Both samples and their controls were processed in triplicate ( $n = 3$ ).

#### **4.2.3.1.2 Bacterial Quantification – CFU mL<sup>-1</sup> *via* Miles and Misra**

Bacterial viability was determined by Miles and Misra assays (Miles *et al.*, 1938). At each time-point, 100  $\mu$ L of inoculated broth was removed from the growing culture and a serial dilution was performed with sterile water ( $10^{-1}$  to  $10^{-8}$ ). Following vigorous vortexing (5 s), 20  $\mu$ L of each diluted sample was pipetted onto either glucose-based or LB agar (depending on the previous media used). Agar plates were dried at room temperature, before incubation at 37 °C for 18 h. Following incubation, colonies were counted and CFU mL<sup>-1</sup> was calculated using the following equation [4.3]:

$$\text{CFU mL}^{-1} = \text{Number of Colonies} \times \text{Conversion (mL)} \times \text{Dilution Factor} \quad [4.3]$$

#### **4.2.3.1.3 Pyocyanin Quantification: Liquid Chromatography - Mass Spectroscopy (LC-MS)**

##### **4.2.3.1.3.1 Sample preparation for LC-MS**

Aliquots of 5 mL of the suspension were removed from the initial 6.1 mL at each time-point of the growth. Suspensions were centrifuged at 1,721  $\times g$  for 10 min. A volume of 1 mL of the supernatant was added to 300  $\mu$ L of methanol (with 0.1 M formic acid). Samples underwent further centrifugation (10,625  $\times g$  for 20 min) and 400  $\mu$ L of the supernatant was removed and added to 800  $\mu$ L of sterile deionised water. Once the samples were vortexed, 1 mL of the solution was filter sterilised using 0.22  $\mu$ m filters (Millex®, Ireland) and placed into 0.3 mL glass vials (Agilent, USA) for storage at -80 °C.

Pooled quality controls were prepared for LC-MS, which were produced following every six samples from the growth dynamic study. This was performed in order to

accommodate for any drifts in peaks seen during LC-MS. To prepare the pooled quality control, an equal volume was taken from each sample and distributed evenly between each of the quality controls produced.

To quantify the production of the pyocyanin, standards of different pyocyanin concentrations were prepared from High Performance Liquid Chromatography (HPLC) grade pyocyanin (Merck, UK). One millilitre of methanol with 0.1 M formic acid was added to the ampule of pyocyanin. This was vortexed (5 s), giving an initial concentration of 5 parts per million (ppm). For the LC-MS experiments, 5 ppb and 50 ppb concentrations were prepared from the above stock solution. The 5 ppb and 50 ppb were analysed alongside the LC-MS experiments in order to provide a known standard baseline at two different concentrations, thus enabling comparison of pyocyanin production between microbial samples.

#### **4.2.3.1.3.2 LC-MS Analysis**

After preparation, samples were analysed immediately or frozen until use (-80 °C). The LC-MS used was an Agilent LC-MS 6540 UHD Q-TOF (Agilent, USA) with an ACE UltraCore 2.5 µm SuperC18™ 100 mm x 2.1 mm column (Advanced Chromatography Technologies, Scotland). The polar solvent used was LC-MS grade H<sub>2</sub>O with 0.1 % formic acid, whilst, acetonitrile with 0.1 % formic acid was the mobile phase solvent due to its less polar properties than water. The LC-MS analysis was conducted in positive ion mode at 45 °C with a MS range of 100 - 3,000, which was calibrated using four reference masses. A constant flow rate of 0.3 mL/min was maintained within the column for 30 min and 10 µL samples were taken from each pre-prepared sample vial. The following parameters were used per sample (Table 4.1):

Table 4.1. LC-MS parameters per sample.

Time (min)	H <sub>2</sub> O and 0.1 % formic acid (%)	Acetonitrile with 0.1 % formic acid (%)	Flow (mL/min)	Max Pressure (bar)
0	5	95	0.3	350
2	95	5	0.3	350
14	5	95	0.3	350
17	5	95	0.3	350
17.01	95	5	0.3	350
20	95	5	0.3	350

#### 4.2.3.1.3.3 File Conversion

The data generated from the LC-MS was multiple Agilent .D files. All the .D output files from the LC-MS were converted to an open source format (.mzXML) to facilitate further analysis, utilising the open source converter ProteoWizard MSConvert (Chambers *et al.*, 2012). The peak-picking filter was chosen as this uses centroidisation, which facilitated the use of the feature detection algorithm, *centWave* to detect and compare close-by and partially overlapping features (Tautenhahn *et al.*, 2008).

#### 4.2.3.1.3.4 Quality Assurance

To reduce the number of false positives/negatives, quality assurance of raw data files was undertaken prior to further analysis. The average peak intensity of all the sample peaks was calculated alongside the average intensity of the blanks. The percentage contribution of the blanks to the sample intensity of each peak was calculated using the following formula [4.4]:

$$\% \text{ Blank Contribution} = \left( \frac{\text{Average intensity of blanks}}{\text{Average intensity of samples}} \right) \times 100 \quad [4.4]$$

The results were filtered accordingly, with peaks with a percentage blank contribution of > 5 % removed.

#### 4.2.3.1.3.5 Data Analysis

The .mzXML files were imported into MzMine2 for peak detection and analysis (Pluskal *et al.*, 2010). The m/z peak for pyocyanin was confirmed in both the 5 ppm and 50 ppm reference samples as 211.086, which corresponded to the monoisotopic peak of Pyocyanin (210.079) with the addition of [M+H]<sup>+</sup> peak (Figure 4.3) (Kushwaha *et al.*, 2018). This reference mass was selected as the targeted peak to be used with the peak detection function with the corresponding reported retention time. An intensity deviation tolerance of 50 %, noise level of  $1.0 \times 10^3$ , m/z deviation of 5 ppm and retention time deviation of 10 % were selected. The concentration for each sample was determined by using the average calculated response factor for the two standards. The relative response factor was multiplied by 1000 to convert from mg/mL to ppm. This value was divided by the calculated sample dilution factor for LC-MS preparation (which was 0.256) to determine the actual pyocyanin concentration at different time-points, per sample. The response factor was calculated *via* the following equation [4.5]:

$$\text{Response factor (Rf)} = \frac{\text{Peak area of standard}}{\text{Concentration of standard (mg/mL)}} \quad [4.5]$$

This response factor was then used to determine the relative response factor for each sample [4.6]:

$$\text{Relative Response Factor (RRF)} = \frac{\text{Peak area of sample}}{\text{Response factor of standard}} \quad [4.6]$$

Datasets generated were analysed and the pyocyanin present quantified. Graphs were generating using the average sample concentration *via* Graphpad Prism (Version 7.04) and the standard error of the mean was notated using error bars.

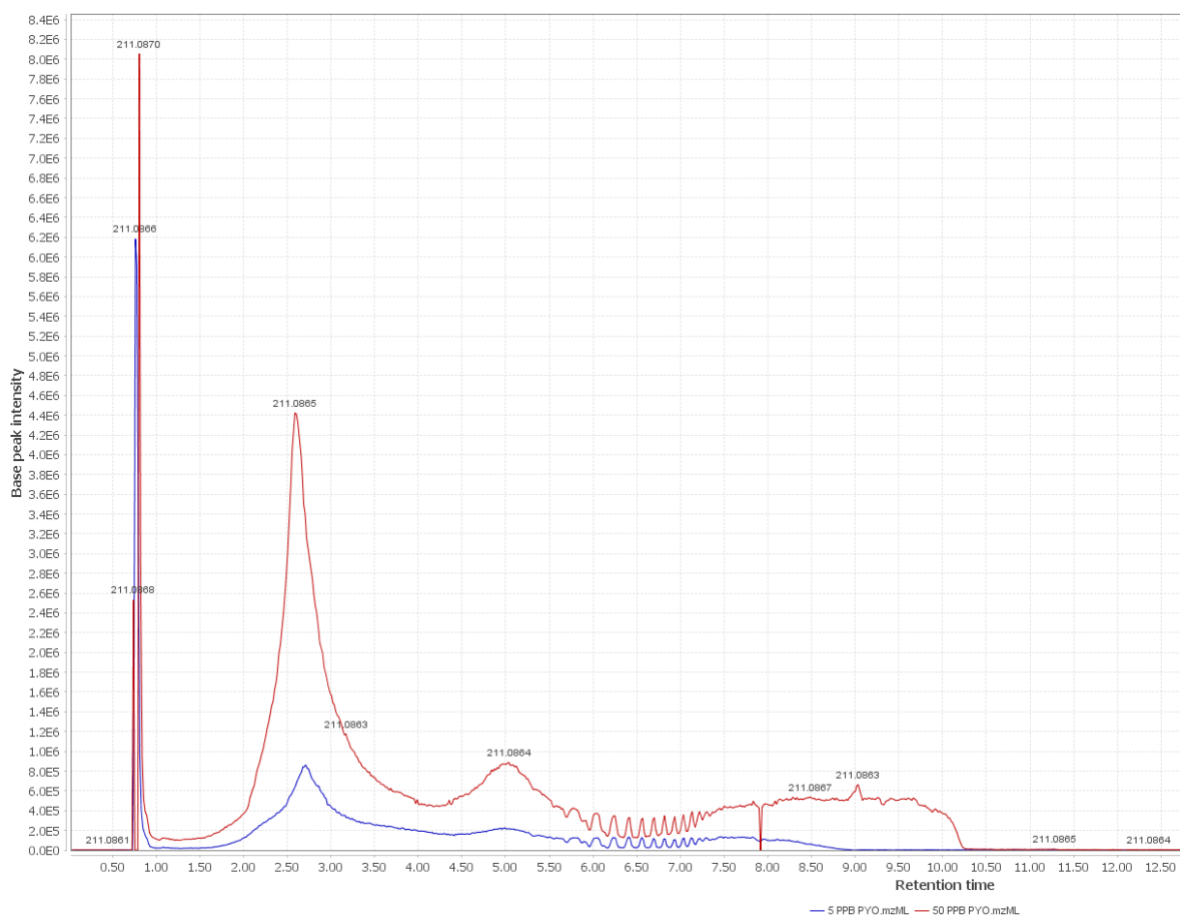


Figure 4.3. Pyocyanin references mass were determined from the 5 ppb and 50 ppb standard controls by plotting base peak intensity against retention time (min). The mass to charge ( $m/z$ ) peak for pyocyanin was confirmed in both the 5 and 50 ppb reference samples as 211.086. This value was then used to quantify pyocyanin from the *P. aeruginosa* strain ATCC 9027 growth kinetic studies. Representative of  $n = 3$ .

#### 4.2.3.2 Biofilm Quantification – Crystal Violet Biofilm Assay – MFC Conditions

*Pseudomonas aeruginosa* strain ATCC 9027 biofilm formation on the 3D-Printed BM electrodes was measured (as per Section 4.2.2.2), under MFC conditions. These conditions consisted of LB broth, incubated at 37 °C under static anaerobic conditions in an anaerobic cabinet (Ruskin, Wales). Biofilm growth was determined at set time-points, namely 0 h, 1 h, 24 h, 48 h, 72 h, 96 h and 120 h. This correlated with the lifespan of the batch MFC configuration later developed (Chapter 5).

#### 4.2.3.3 Nitrogen Biolog Assay

Aliquots of *P. aeruginosa* strain ATCC 9027 was cultured onto LB agar (BD Difco™, USA) and incubated at 37 °C, under aerobic conditions for 24 h. An OD<sub>600 nm</sub> of 0.25 (± 0.05) was prepared in 20 mL saline, this was calibrated against sterile saline. The inoculated solution was centrifuged at 3,059 *g* for 10 min. Following centrifugation, 18 mL of the supernatant was removed and the pellet was re-suspended in 18 mL saline. Two millilitres of this solution was added to 18 mL of saline, giving a final OD<sub>600 nm</sub> of 0.025. Six microliters of Biolog Redox Dye A® was added and the suspension was vortexed thoroughly (10 s). Sodium succinate was used as the carbon source as per the manufacturer's instructions for *P. aeruginosa* (Biolog®, USA). Aliquots of 100 µL, were added into each well of the following Biolog MicroPlates™ (Hayward, CA) with varying nitrogen sources; PM 3B, PM 6, PM 7 and PM 8. The 96-well plates were incubated at 37 °C under static anaerobic or aerobic conditions. Each well contained a different nitrogen source (*i.e.* specific amino acid type or combination of amino acids).

Aerobic and anaerobic conditions were tested. For aerobic conditions, the plates were incubated at 37 °C under aerobic conditions for 24 h, whilst, for anaerobic conditions, the plates were transferred to an anaerobic cabinet (Ruskinn, Wales) and incubated at 37 °C for 24 h. Following incubation, the absorbance of the plates was determined after 10 s of shaking using a Multiskan™ GO Microplate Spectrophotometer (Thermo Fisher Scientific, USA) at OD<sub>590 nm</sub>. The ten most effective nitrogen sources, which were determined from the greatest absorbance readings, were analysed *via* Graphpad Prism (Version 8). Experiments were carried out in triplicate ( $n = 3$ ).

#### 4.2.4 Statistical Analysis

Datasets were collated and analysed using Microsoft Excel (2016). Graphs were generated using Graphpad Prism (version 8). The standard error of the mean (SEM) was denoted *via* error bars. For statistical analysis, *P* values were calculated at the 95% confidence level by two-way ANOVAs, this was determined using Graphpad Prism (version 8). In all cases,  $P < 0.05$  was considered statistically significant. Asterisks denote significance, \* $P \leq 0.05$ , \*\* $P \leq 0.01$ , \*\*\* $P \leq 0.001$  and \*\*\*\* $P \leq 0.0001$ .

## 4.3 Results

### 4.3.1 Preliminary Strain Selection

#### 4.3.1.1 Pyocyanin Production – Chloroform Extraction Assay

Five strains of *P. aeruginosa* were selected and grown over a range of time-points from 0 h to 14 days in order to quantify pyocyanin production (Figure 4.4). The results showed that *P. aeruginosa* strains ATCC 9027, PAO1 and MRI (medical strain) produced the highest quantities of pyocyanin over the set time-points with the maximum pyocyanin production being recorded after two weeks for both PAO1 and ATCC 9027 at  $6.04 \mu\text{g mL}^{-1}$  and  $6.34 \mu\text{g mL}^{-1}$  respectively. Interestingly, the MRI strain produced a maximum pyocyanin at 48 h ( $6.18 \mu\text{g mL}^{-1}$ ) (Figure 4.4). The lowest pyocyanin production was observed for *P. aeruginosa* strain Hollings, where this medical isolate produced a maximum pyocyanin concentration of  $3.57 \mu\text{g mL}^{-1}$  after two weeks incubation. The difference in pyocyanin production between each time-point was non-significant.

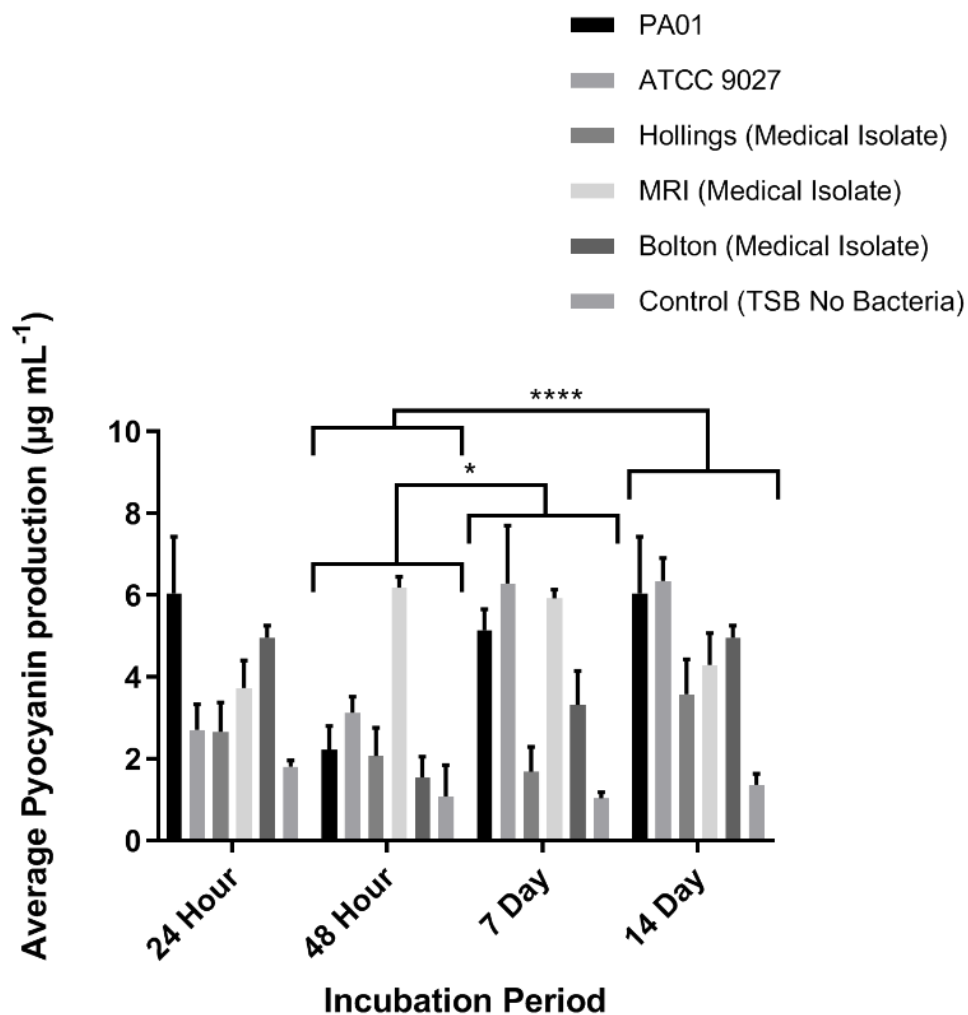


Figure 4.4. Pyocyanin quantification of five *P. aeruginosa* strains (at OD  $1 \pm 0.1$  (OD<sub>600 nm</sub>)) over four time-points (24 h, 48 h, 7 d and 14 d) (incubation conditions: 37 °C; aerobic; aggregation (200 rpm)). Statistical testing indicates significant difference between 48 h and 7 day incubation periods ( $P \leq 0.05$ ) and when comparing 48 h and 14 days pyocyanin production ( $P \leq 0.0001$ ) ( $n = 3$ ).

#### 4.3.1.2 Biofilm Quantification – Crystal Violet Biofilm Assay

Biofilm formation on the electrode surfaces was evaluated using a Crystal Violet Biofilm Assay (CVBA), against three *P. aeruginosa* strains (ATCC 9027, PA01 and MRI) which were shown to produce the highest quantities of pyocyanin. Against strain ATCC 9027 (Figure 4.5), the results were indicative of a linear correlation between the incubation period and biofilm cell accumulation between 0 h to 7 days. However, a decrease in

biomass was observed after 7 days when a reduction in absorbance was recorded when all four electrode types were tested. When the biofilms were grown on the polished the electrodes, there was an effect on bacterial cell attachment and therefore biofilm development, leading to an increase in recorded biomass on both the polished 3D-Printed BM (maximum absorbance 14.02 after 5 d) and Polished 3D-Printed PLA (maximum absorbance 7.68 after 7 d) electrodes (compared with the unpolished samples).

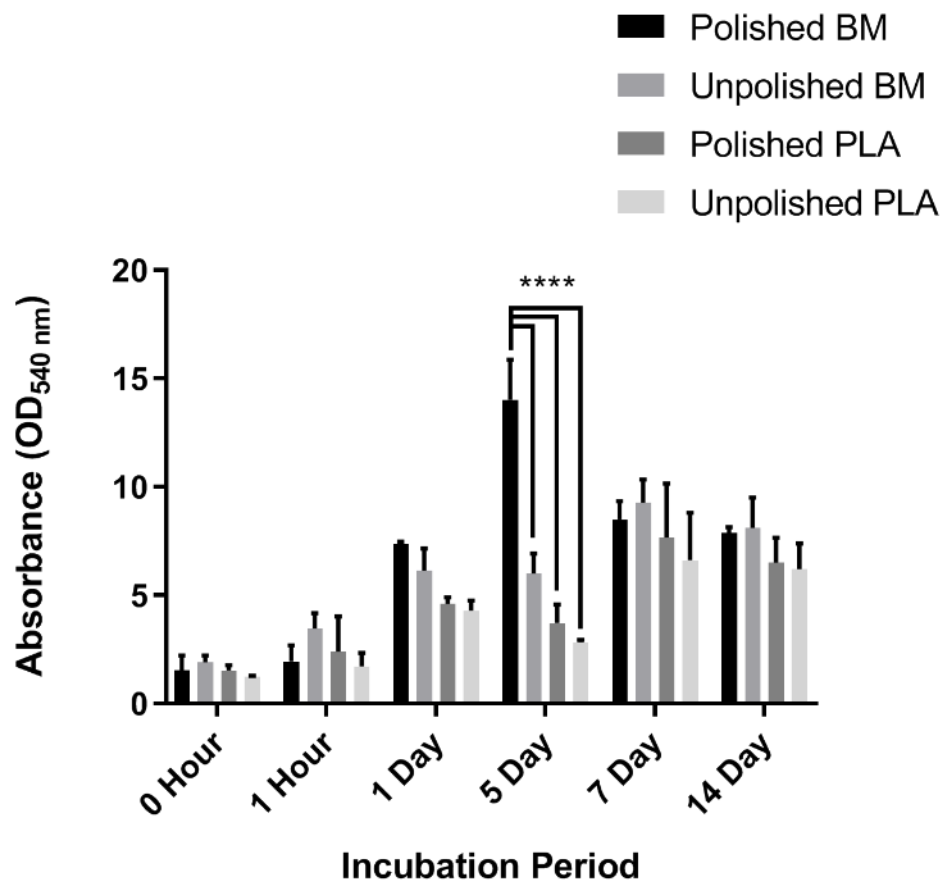


Figure 4.5. Biofilm quantification as determined by CVBA against *P. aeruginosa* strain ATCC 9027 minus the broth controls (incubation conditions: 37 °C; aerobic; static) ( $n = 3$ ). Significance denoted by \*\*\*\*  $P \leq 0.0001$ .

Biofilm quantification was determined using strain PAO1, which showed a similar trend to strain ATCC 9027, with a peak in biomass observed between 5 to 7 days, followed by an eventual decrease in biomass. However, biomass quantification with strain PAO1 was much lower than that of strain ATCC 9027. The highest recorded strain PAO1 biofilm

quantification was observed from the unpolished BM electrode after 7 days of growth, which produced an absorbance value of 7.92 (Figure 4.6).

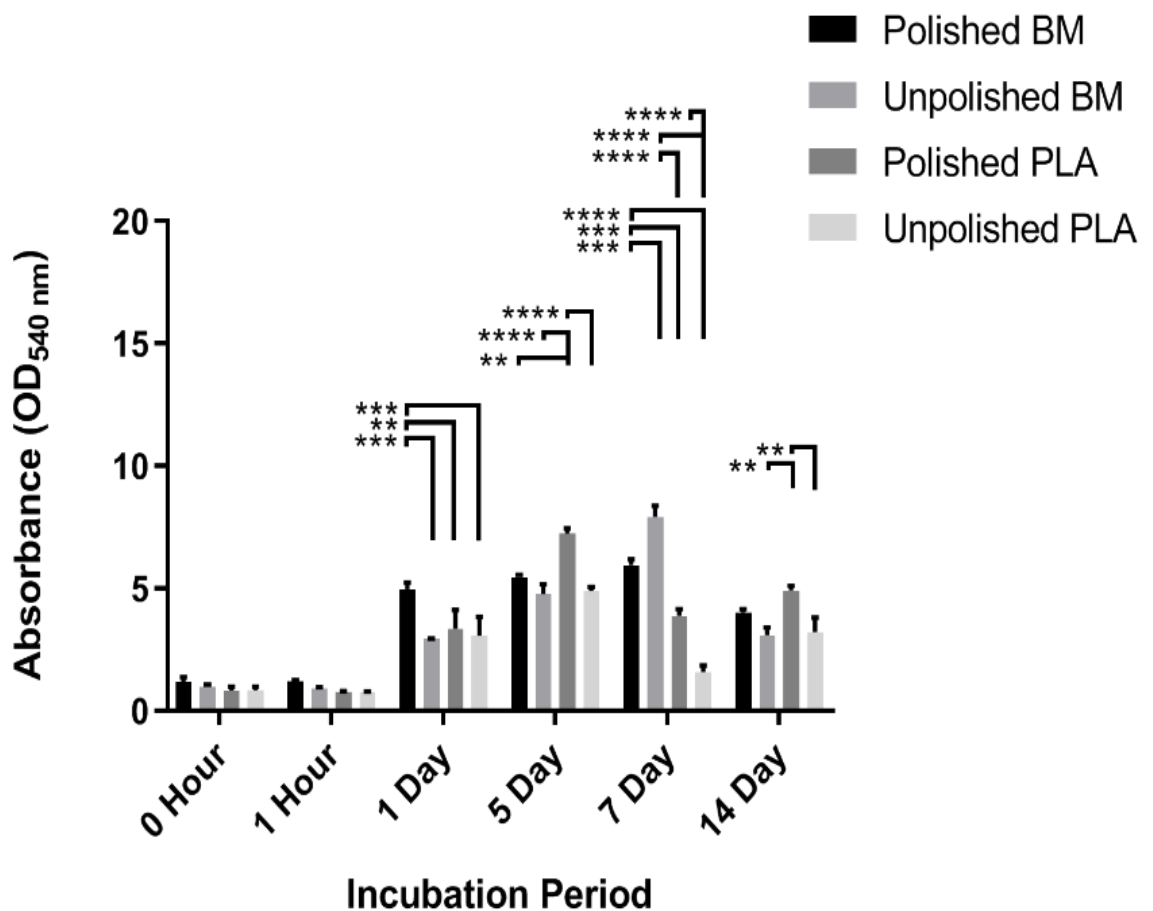


Figure 4.6. Biofilm quantification as determined by CVBA against *P. aeruginosa* strain PAO1 minus the broth controls (incubation conditions: 37 °C; aerobic; static) ( $n = 3$ ). Significance denoted by  $**P \leq 0.01$ ,  $***P \leq 0.001$   $****P \leq 0.0001$ .

When *P. aeruginosa* strain MRI was grown on the electrodes, there was a direct correlation with incubation time and biomass production except for the polished 3D-Printed BM electrodes. The largest quantity of biomass was observed during incubation with the unpolished 3D-Printed BM electrode after 14 days, producing an absorbance value of 12.66. This was comparable to that of the polished 3D-Printed BM electrode which produced an absorbance value of 11.65 (Figure 4.7).

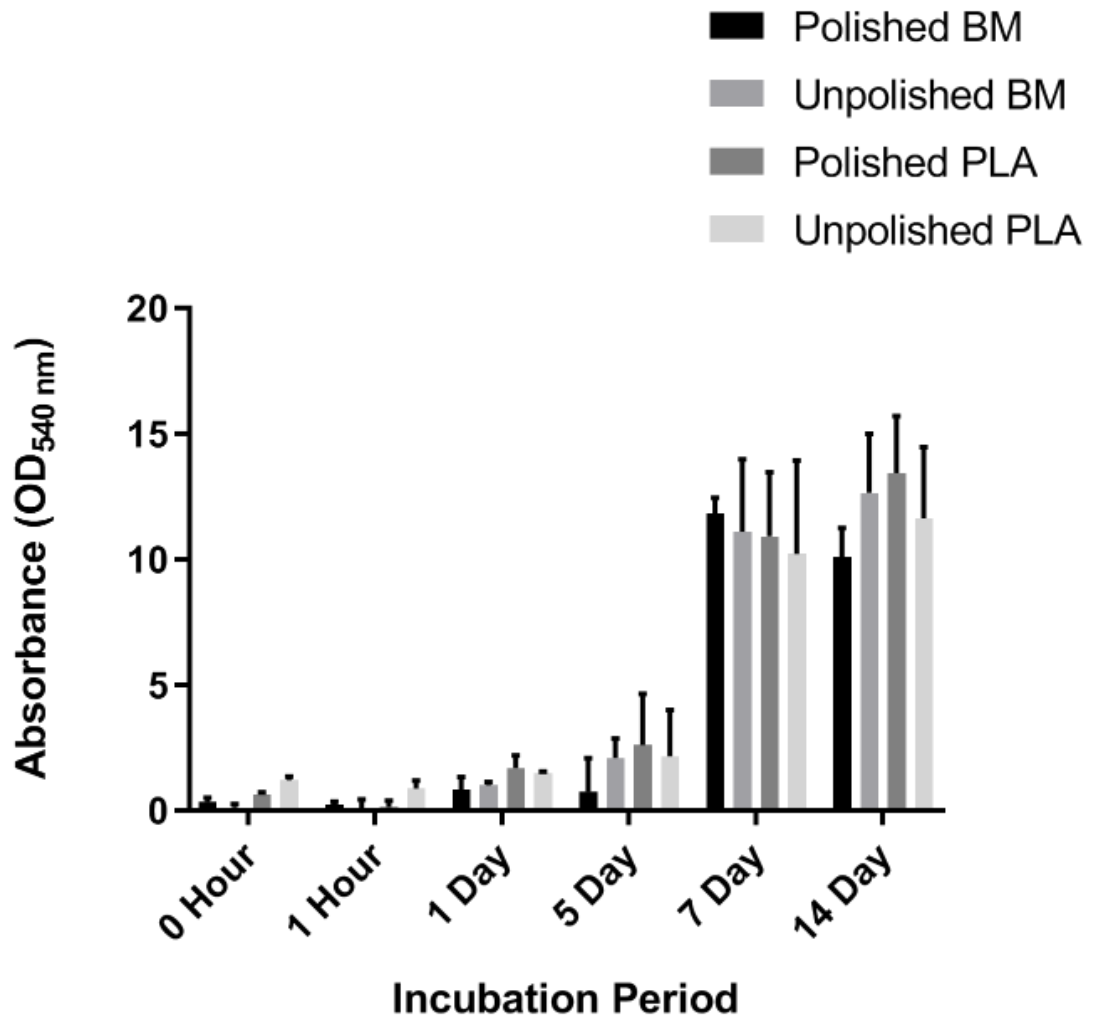


Figure 4.7. Biofilm quantification as determined by CVBA against *P. aeruginosa* strain MRI minus the broth controls (incubation conditions: 37 °C; aerobic; static) ( $n = 3$ ). No statistical significance was observed ( $P > 0.05$ ).

By comparing the three bacterial strains for biofilm production on the electrode surface, *P. aeruginosa* strain ATCC 9027 produced the greatest bacterial growth when incubated with the electrodes for the first 5 days. This can be highlighted in the case of polished 3D-Printed BM electrode, where the 5 day incubation period produced an absorbance value of 14.02 for *P. aeruginosa* strain ATCC 9027, 5.46 for strain PAO1 and 0.84 for the strain MRI. Overall, the polished electrodes promoted bacterial adhesion and biomass production as opposed to the unpolished controls. *Pseudomonas aeruginosa* strain ATCC 9027 demonstrated the most optimal characteristics for application in a MFC configuration, due to high pyocyanin production and superior biomass production.

Subsequently, biofilm morphology was observed by SEM analysis of the polished and unpolished electrode surfaces following 24 h exposure to *P. aeruginosa* strain ATCC 9027 (Figure 4.8).

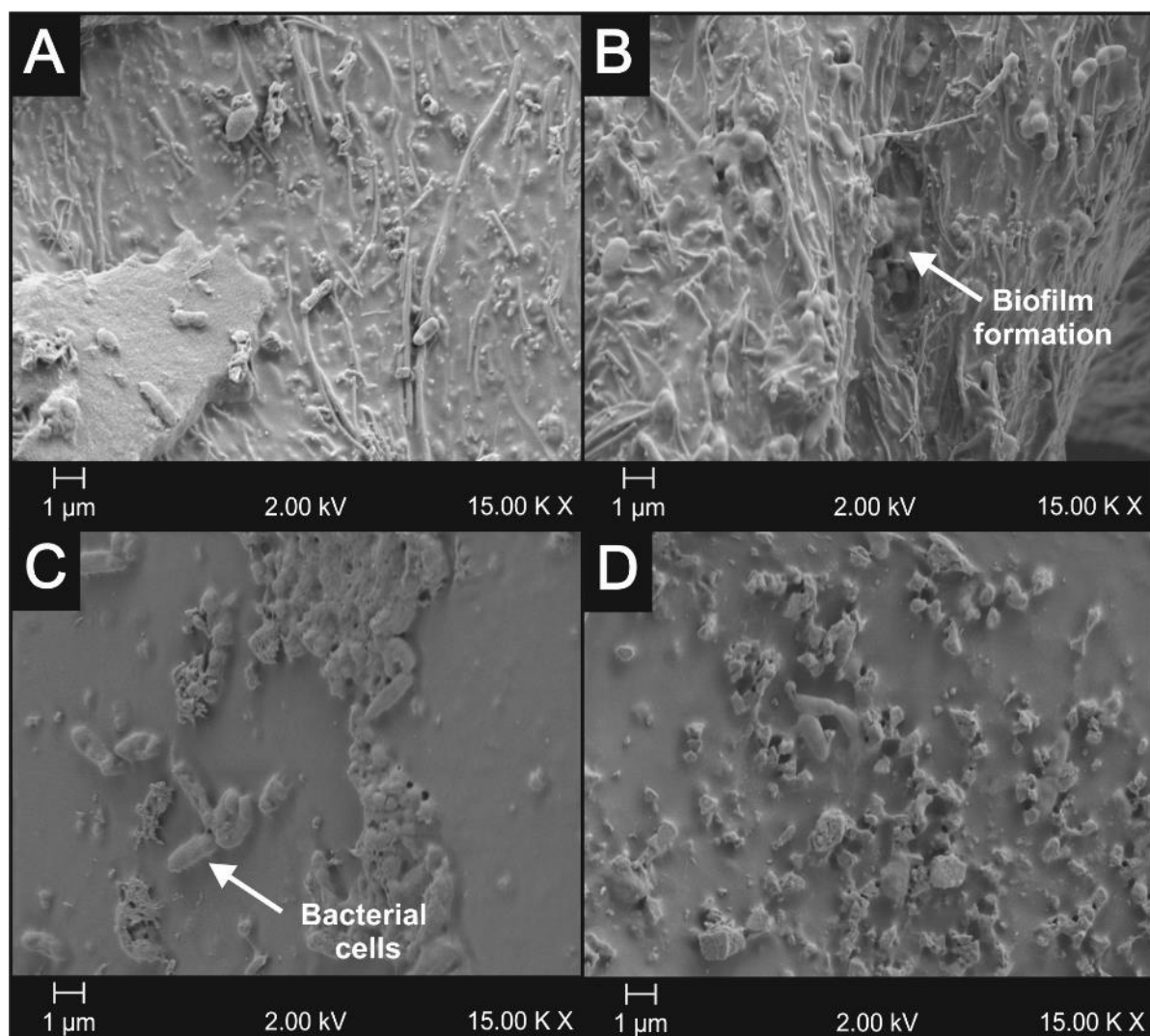


Figure 4.8. SEM images depicting bacterial adhesion/retention of *P. aeruginosa* strain ATCC 9027 following a 24 h incubation period (37 °C; aerobic; static), with the following electrodes (15.00 K × magnification). A) BM - polished, B) BM - unpolished, C) PLA - polished and D) PLA - unpolished.

#### 4.3.1.3 Motility Assay

Due to the known alternative mechanisms of electron transfer (*e.g.* nanowire production), flagella quality was determined by motility assays in order to select the most

appropriate *P. aeruginosa* strain for MFC applications. After 48 h growth in the presence of oxygen no significant difference in motility was observed between all strains tested (Figure 4.9). However, in anaerobic conditions *P. aeruginosa* strain ATCC 9027 produced the greatest motility zone of 5.98 mm, followed by strain MRI with 3.30 mm and finally strain PAO1 with 1.87 mm growth (Figure 4.9). These results further suggested that *P. aeruginosa* strain ATCC 9027 should be pursued further for MFC experiments, due to the anaerobic nature of most MFC configurations.

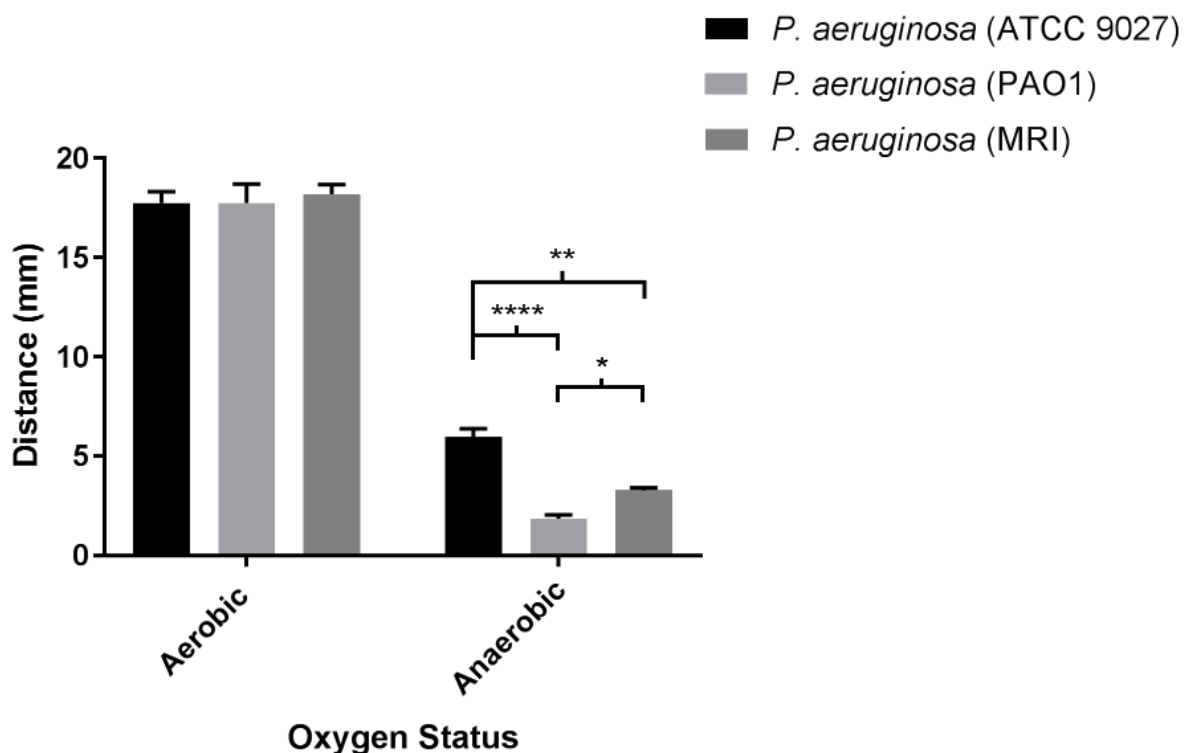


Figure 4.9. Motility assay of three *P. aeruginosa* strains under aerobic or anaerobic conditions over 48 h (incubation conditions: 0.4 % LB agar; 37 °C; static) ( $n = 3$ ). Asterisks denote significance,  $*P \leq 0.05$ ,  $**P \leq 0.01$ ,  $****P \leq 0.0001$ .

#### 4.3.2.4 Microbial Adhesion To Hydrocarbons (MATH) Assay

Microbial Adhesion To Hydrocarbons (MATH) assays were conducted against *P. aeruginosa* strain ATCC 9027 after 24 h, 72 h and 120 h aerobic incubation (37 °C). After 24 h, *P. aeruginosa* strain ATCC 9027 demonstrated greatest adhesion to the polar hydrocarbons, chloroform (35.03 %) and ethyl acetate (33.03 %), which indicated that the bacterial cells had hydrophilic properties. Due to the similar levels of adhesion to the acidic

(chloroform) and basic (ethyl acetate) polar solvents (35.03 % and 38.03 %, respectively) it was demonstrated that after 24 h of aerobic incubation, the cells were both moderate electron acceptors and donors (Figure 4.10.A.). Adhesion values between 10 % and 55 % were deemed moderate in regards to electron accepting and donating properties. *Pseudomonas aeruginosa* strain ATCC 9027 cells were also hydrophilic following 72 h incubation. A greater adhesion to polar hydrocarbons, chloroform (38.63 %) and ethyl acetate (45.13 %) was apparent relative to the non-polar solvents hexadecane (31.1 %) and decane (22.4 %). Furthermore, the increased adhesion to both chloroform and ethyl acetate suggested that *P. aeruginosa* strain ATCC 9027 acted as a moderate electron acceptor and donor. However, greater adhesion to the basic polar hydrocarbon, ethyl acetate (45.13 %), indicated that the bacterial cells had a moderate preference to accept electrons (Figure 4.10.B). Following 120 h incubation, *P. aeruginosa* strain ATCC 9027 showed greater adhesion to polar hydrocarbons, chloroform (53.30 %) and ethyl acetate (34.30 %). This trend demonstrated cell hydrophilicity was similar to that shown at 24 h and 72 h. Again, moderate levels (10 % - 55 %) of adhesion to both the acidic solvent, chloroform and basic solvent, ethyl acetate, suggesting both electron donating and accepting properties. However, as the adhesion to chloroform was greater, a preference for donating electrons dominated (Figure 4.10.C).

MATH assays were repeated against *P. aeruginosa* strain ATCC 9027 after 24 h, 72 h and 120 h under anaerobic conditions. After 24 h of anaerobic growth, a greater binding affinity to the polar hydrocarbons, chloroform (62.47 %) and ethyl acetate (61.83 %), as opposed to the non-polar hydrocarbons, hexadecane (36.07 %) and decane (36.7 %) was observed which indicated that the bacterial cells had hydrophilic properties (Figure 4.10.A). After 72 h of anaerobic incubation, *P. aeruginosa* strain ATCC 9027 cells demonstrated hydrophilic properties. As an increased adhesion affinity to the polar solvents, chloroform (35.9 %) and ethyl acetate (36.2 %) was observed when compared to the non-polar solvents hexadecane (11.33 %) and decane (10.43 %) (Figure 4.10.B). After 120 h, *P. aeruginosa* strain ATCC 9027 demonstrated hydrophilic properties due to a greater adhesion to the polar hydrocarbons. Furthermore, at all incubation periods, the bacterial cells showed similar moderate adhesion to both the acidic and basic polar hydrocarbon indicating strong electron acceptor and donor status. However, electron donation was preferred due to the slight increase in adhesion to chloroform (Figure 4.10). Two-way ANOVAs were

performed to determine the statistical significance of the aerobic and anaerobic *P. aeruginosa* strain ATCC 9027, MATH assay results over the time-points tested (Table 4.2).

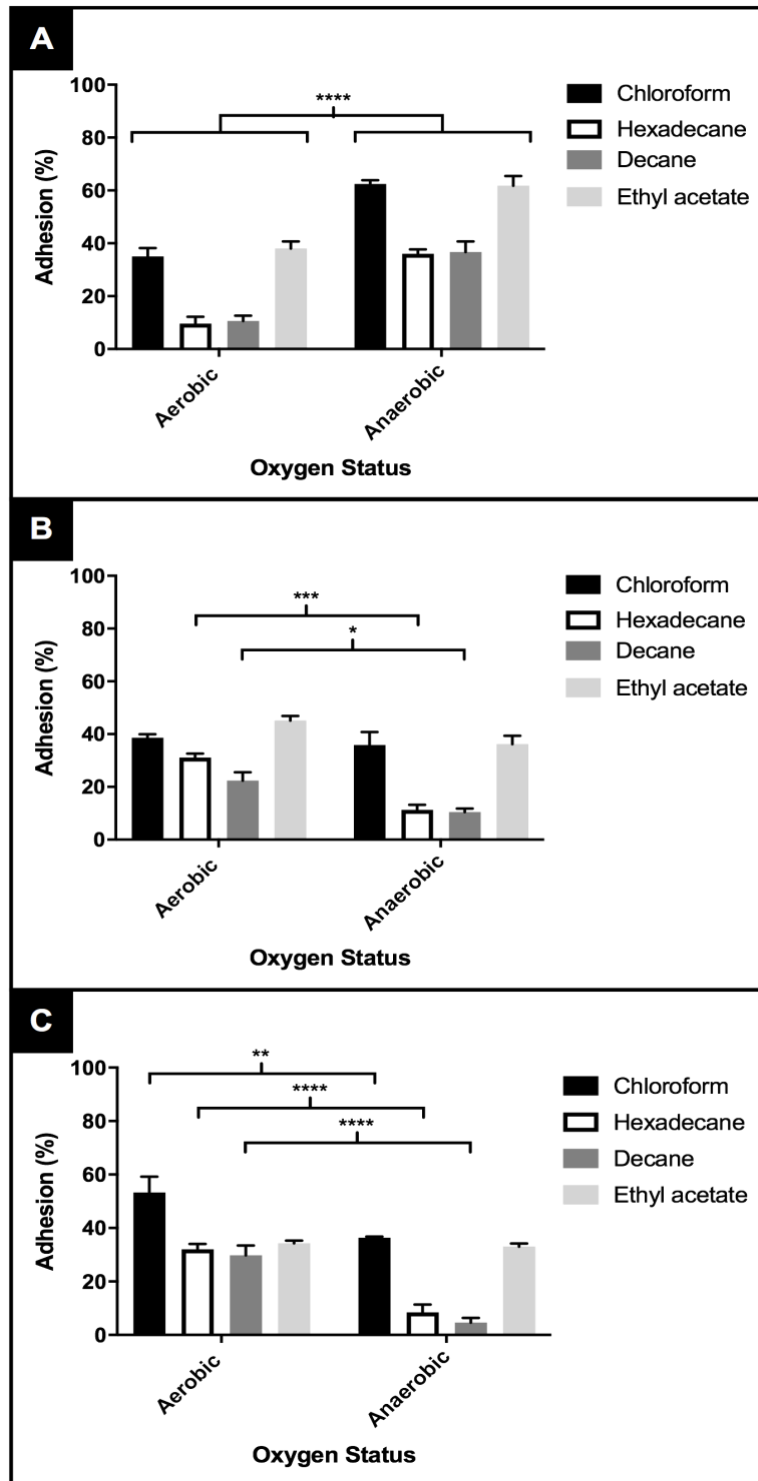


Figure 4.10. MATH Assays of aerobic and anaerobic *P. aeruginosa* strain ATCC 9027 demonstrated adhesion to polar (chloroform and ethyl acetate) and non-polar solvents (hexadecane and decane) following, A) 24 h, B) 72 h and C) 120 h incubation (37 °C; static) ( $n = 3$ ). Asterisks denote significance,  $*P \leq 0.05$ ,  $**P \leq 0.01$ ,  $***P \leq 0.001$  and  $****P \leq 0.0001$ .

Table 4.2. Statistical analysis (two-way ANOVAs) comparing the *P. aeruginosa* strain ATCC 9027, aerobic and anaerobic MATH assay results, over the different time-points. Asterisks denote significance, \* $P \leq 0.05$ , \*\* $P \leq 0.01$ , \*\*\* $P \leq 0.001$  and \*\*\*\* $P \leq 0.0001$ .

Hydrocarbons	Time-points tested (h)	P value	Significance
<b>Aerobic – <i>P. aeruginosa</i> strain ATCC 9027</b>			
Chloroform	24 vs. 72	0.8010	Non-significant
	24 vs. 120	0.0003	***
	72 vs. 120	0.0046	**
Hexadecane	24 vs. 72	<0.0001	****
	24 vs. 120	<0.0001	****
	72 vs. 120	0.9953	Non-significant
Decane	24 vs. 72	0.0285	*
	24 vs. 120	0.0002	***
	72 vs. 120	0.2694	Non-significant
Ethyl acetate	24 vs. 72	0.2995	Non-significant
	24 vs. 120	0.5864	*
	72 vs. 120	0.0046	Non-significant
<b>Anaerobic - <i>P. aeruginosa</i> strain ATCC 9027</b>			
Chloroform	24 vs. 72	<0.0001	****
	24 vs. 120	<0.0001	****
	72 vs. 120	0.9989	Non-significant
Hexadecane	24 vs. 72	<0.0001	****
	24 vs. 120	<0.0001	****
	72 vs. 120	0.8396	Non-significant
Decane	24 vs. 72	<0.0001	****
	24 vs. 120	<0.0001	****
	72 vs. 120	0.3566	Non-significant
Ethyl acetate	24 vs. 72	<0.0001	****
	24 vs. 120	<0.0001	****
	72 vs. 120	0.7962	Non-significant

MATH assays were repeated using *P. aeruginosa* strain PAO1 and were conducted after 24 h, 72 h and 120 h bacterial aerobic incubation (37 °C). After 24 h incubation, a greater adhesion to the polar hydrocarbons, chloroform (44.80 %) and ethyl acetate (45.33 %) was observed, compared to the non-polar solvents, hexadecane (24.50 %) and decane (15.70 %). This indicated that the bacterial cells had hydrophilic properties (Figure 4.11.A). Following 72 h incubation, bacterial cell hydrophilicity was indicated, due to the greater adhesion to the polar hydrocarbons chloroform (35.76 %) and ethyl acetate (38.57 %), compared to the non-polar solvents, hexadecane (2.43 %) and decane (0.40 %) (Figure 4.11.B). After 120 h incubation, bacterial cell hydrophilicity was observed, due to greater adhesion to the polar hydrocarbons, chloroform (40.67 %) and ethyl acetate (47.23 %) compared to the non-polar solvents, hexadecane (12.93 %) and decane (16.57 %). Throughout all incubation periods, similar adhesion values were recorded, for both the acidic polar solvent (chloroform) and basic polar solvent (ethyl acetate). This indicated moderate electron donating and accepting properties. However, a slight preference to accepting electrons was observed, due to greater adhesion towards ethyl acetate (Figure 4.11).

MATH assays were performed under anaerobic conditions, in order to determine if the biochemical pathways responsible for respiration played a role in bacterial cell hydrophobicity (Figure 4.11). After 24 h incubation, bacterial cell hydrophobicity was indicated due to the greater adherence to the polar hydrocarbons, chloroform (62.67 %) and ethyl acetate (57.00 %) compared to the non-polar solvents hexadecane (28.00 %) and decane (38 %). Similar levels of adhesion to both the acidic and basic polar solvent was observed, which indicated high electron donating and accepting properties. Bacterial adhesion towards chloroform was slightly higher, which indicated a preference to donating electrons. Bacterial cell hydrophilicity was indicated following 72 h incubation as a greater adherence to the polar hydrocarbons, chloroform (51.67 %) and ethyl acetate (42.87 %), compared to the non-polar solvents, hexadecane (14.60 %) and decane (14.50 %) was observed (Figure 4.11.B). After 120 h of anaerobic incubation, the same trend was observed as the bacterial cells demonstrated hydrophilic properties. A greater adherence to the polar hydrocarbons, chloroform (33.90 %) and ethyl acetate (39.97 %) compared to the non-polar solvents, hexadecane (3.67 %) and decane (8.33 %) was recorded. Following 72 h and 120 h anaerobic incubation, moderate levels of adhesion towards the acidic and basic polar

solvents was demonstrated, which indicated moderate bacterial electron donating and accepting properties. However, as adhesion to ethyl acetate was slightly higher, a preference to accepting electrons was observed (Figure 4.11). In order to determine the statistical significance of the *P. aeruginosa* strain PAO1 MATH assay results over the time points tested (24 h, 72 h and 120 h), two-way ANOVAs were conducted, for both the aerobic and anaerobic conditions trialled (Table 4.3).

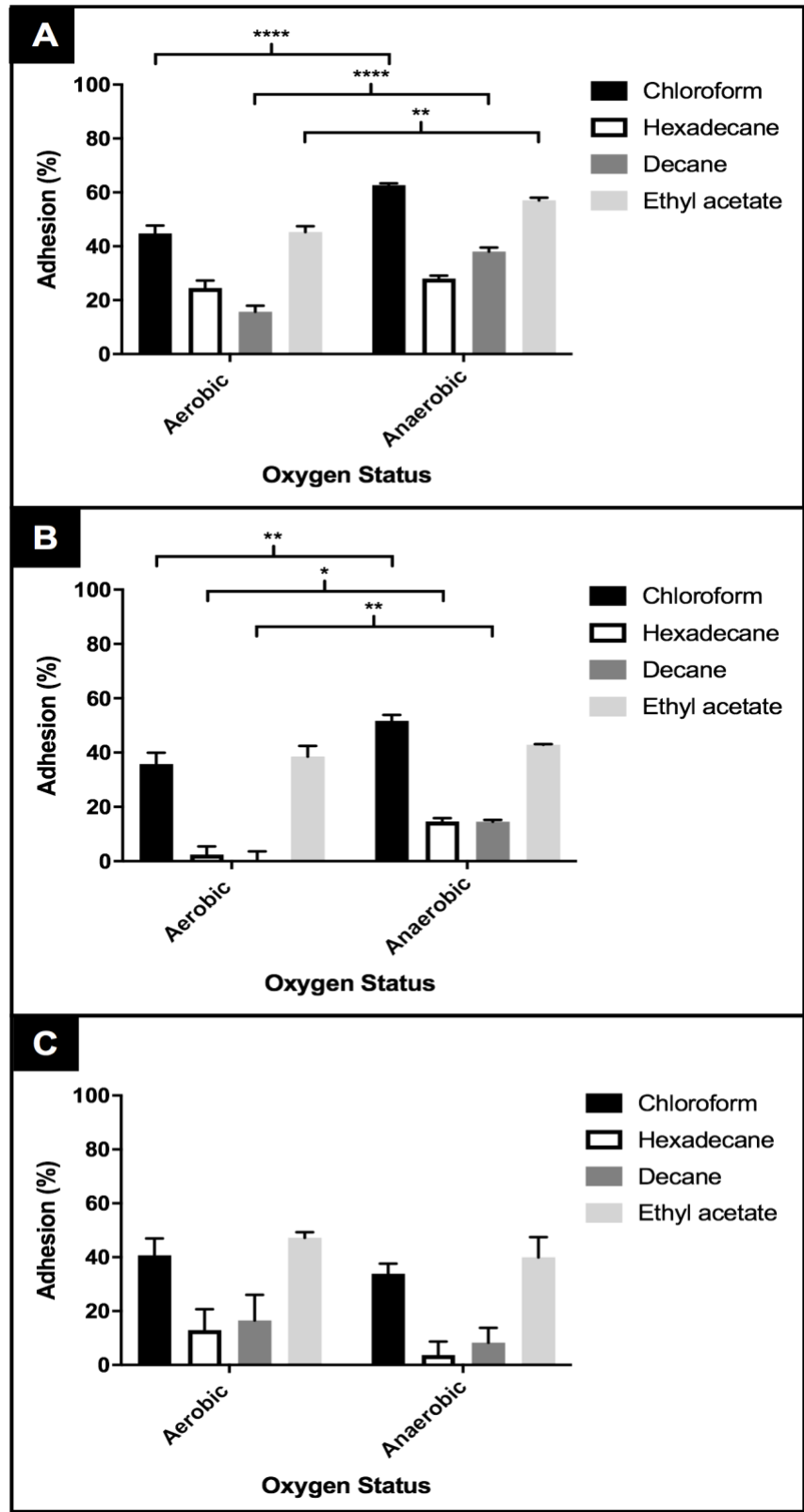


Figure 4.11. MATH Assay of aerobic and anaerobic *P. aeruginosa* strain PAO1 demonstrated adhesion to polar (chloroform and ethyl acetate) and non-polar solvents (hexadecane and decane) following, A) 24 h, B) 72 h and C) 120 h incubation (37 °C; static) ( $n = 3$ ). Asterisks denote significance,  $*P \leq 0.05$ ,  $**P \leq 0.01$  and  $****P \leq 0.0001$ .

Table 4.3. Statistical analysis (two-way ANOVAs) comparing the *P. aeruginosa* strain PAO1, aerobic and anaerobic MATH assay results, over the different time-points. Asterisks denote significance, \* $P \leq 0.05$ , \*\*\* $P \leq 0.001$  and \*\*\*\* $P \leq 0.0001$ .

Hydrocarbons	Time-points tested (h)	P value	Significance
<b>Aerobic – <i>P. aeruginosa</i> strain PAO1</b>			
Chloroform	24 vs. 72	0.9213	Non-significant
	24 vs. 120	>0.9999	Non-significant
	72 vs. 120	0.9995	Non-significant
Hexadecane	24 vs. 72	0.0366	*
	24 vs. 120	0.7088	Non-significant
	72 vs. 120	0.8141	Non-significant
Decane	24 vs. 72	0.3216	Non-significant
	24 vs. 120	>0.9999	Non-significant
	72 vs. 120	0.2534	Non-significant
Ethyl acetate	24 vs. 72	0.9908	Non-significant
	24 vs. 120	>0.9999	Non-significant
	72 vs. 120	0.9399	Non-significant
<b>Anaerobic - <i>P. aeruginosa</i> strain PAO1</b>			
Chloroform	24 vs. 72	0.3106	Non-significant
	24 vs. 120	<0.0001	****
	72 vs. 120	0.0129	*
Hexadecane	24 vs. 72	0.1127	Non-significant
	24 vs. 120	0.0004	***
	72 vs. 120	0.3184	Non-significant
Decane	24 vs. 72	0.0006	***
	24 vs. 120	<0.0001	****
	72 vs. 120	0.9407	Non-significant
Ethyl acetate	24 vs. 72	0.0800	Non-significant
	24 vs. 120	0.0189	*
	72 vs. 120	>0.9999	Non-significant

### **4.3.2 *Pseudomonas aeruginosa* strain ATCC 9027 Optimisation**

For optimisation purposes, the growth of *P. aeruginosa* strain ATCC 9027 was determined against two media sources, namely glucose-based and LB broth. These media were selected to determine the effect of alternative biochemical pathways on *P. aeruginosa* growth and pyocyanin production. Growth kinetics were compared *via* optical density and viability. To compare pyocyanin production, LC-MS analysis was conducted.

#### **4.3.2.1 Bacterial Growth Dynamics**

##### **4.3.2.1.1 Optical Density**

Growth dynamics were determined using a spectrophotometer (Figure 4.12). In the case of the LB medium with aerobic-to-anaerobic starting cultures of *P. aeruginosa* strain ATCC 9027, a correlation between incubation time and turbidity was observed. In the presence of LB medium, aerobic-to-anaerobic starting cultures of *P. aeruginosa* strain ATCC 9027 produced a maximum turbidity of 0.40 (OD<sub>540 nm</sub>) after 120 h. Aerobic-to-anaerobic starting cultures of *P. aeruginosa* strain ATCC 9027 produced a maximum turbidity of 0.20 (at OD<sub>540 nm</sub>) in glucose-based medium. However, for *P. aeruginosa* in LB broth (under complete anaerobic conditions), turbidity increased to a maximum of 0.27 after 72 h, which was followed by a reduction in turbidity. When incubated in glucose-based medium under complete anaerobic conditions, *P. aeruginosa* showed minimal turbidity changes over the incubation periods sampled and the highest turbidity observed was 0.044 (at OD<sub>540 nm</sub>) after 120 h incubation. Overall, when *P. aeruginosa* was incubated with LB medium, a marked increase in turbidity was observed when compared against the glucose-based medium (Figure 4.12).

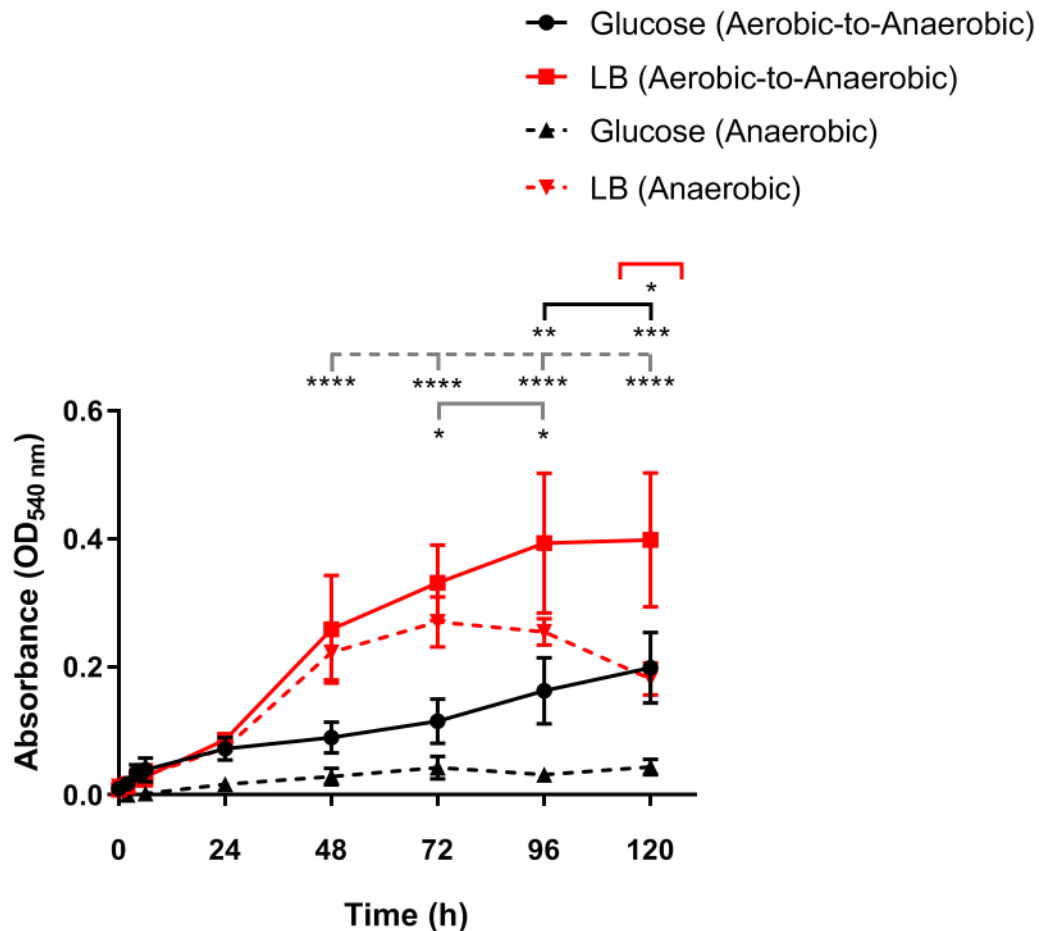


Figure 4.12. Optical density recorded by sampling *P. aeruginosa* strain ATCC 9027 over 120 h, two media types, glucose-based and LB broth were used (incubation conditions; 37 °C; static). Starting cultures were either aerobic-to-anaerobic or fully anaerobic prior to inoculation ( $n = 3$ ). Where error bars are not visible they are of similar or smaller size compared to the symbol. For the significance testing, the red line indicated LB media in different starting conditions, the black line denoted glucose-based medium in different starting conditions, whilst, the grey dotted line indicated glucose-based against LB medium (anaerobic) and the grey solid line compared glucose-based broth against LB broth (aerobic-to-anaerobic). Asterisks denote significance,  $*P \leq 0.05$ ,  $**P \leq 0.01$ ,  $***P \leq 0.001$  and  $****P \leq 0.0001$ .

#### 4.3.2.1.2 Bacterial Viability

Bacterial viability was calculated in colony forming units per mL (CFU mL<sup>-1</sup>). In order to quantify the amount of bacteria present at set time-points when grown in the different

growth media, namely, glucose-based and LB broth and when *P. aeruginosa* strain ATCC 9027 was preconditioned in different oxygen conditions, namely anaerobic and aerobic-to-anaerobic starting cultures (Figure 4.13). All four conditions tested, resulted in traditional growth phase models, including the presence of lag phase, exponential growth (log phase), stationary phase and death phase. Maximum bacterial viability ( $5.5 \times 10^7$  CFU mL<sup>-1</sup>) was recorded when bacteria were grown for 72 h in glucose-based medium from an aerobic-to-anaerobic starting culture of *P. aeruginosa*. In the presence of LB medium, *P. aeruginosa* grew to a maximum of  $3.00 \times 10^7$  CFU mL<sup>-1</sup> and  $2.94 \times 10^7$  CFU mL<sup>-1</sup>, from aerobic-to-anaerobic and fully anaerobic starting cultures respectively. The highest recorded viability for an anaerobic *P. aeruginosa* culture in glucose-based medium was  $1.3 \times 10^7$  CFU mL<sup>-1</sup>. When comparing the viability of *P. aeruginosa* under anaerobic conditions at 72 h in both LB ( $2.94 \times 10^7$  CFU mL<sup>-1</sup>) and glucose-based media ( $9.17 \times 10^6$  CFU mL<sup>-1</sup>), significance was observed ( $P \leq 0.05$ ) which indicated better anaerobic *P. aeruginosa* growth in LB broth (Figure 4.13).

In summary, the highest recorded bacterial viability was observed when *P. aeruginosa* was incubated in glucose-based medium for 72 h, from an aerobic-to-anaerobic starting culture. However, overall there was little significant difference between bacterial viability in both different media types and pre-conditioning stages.

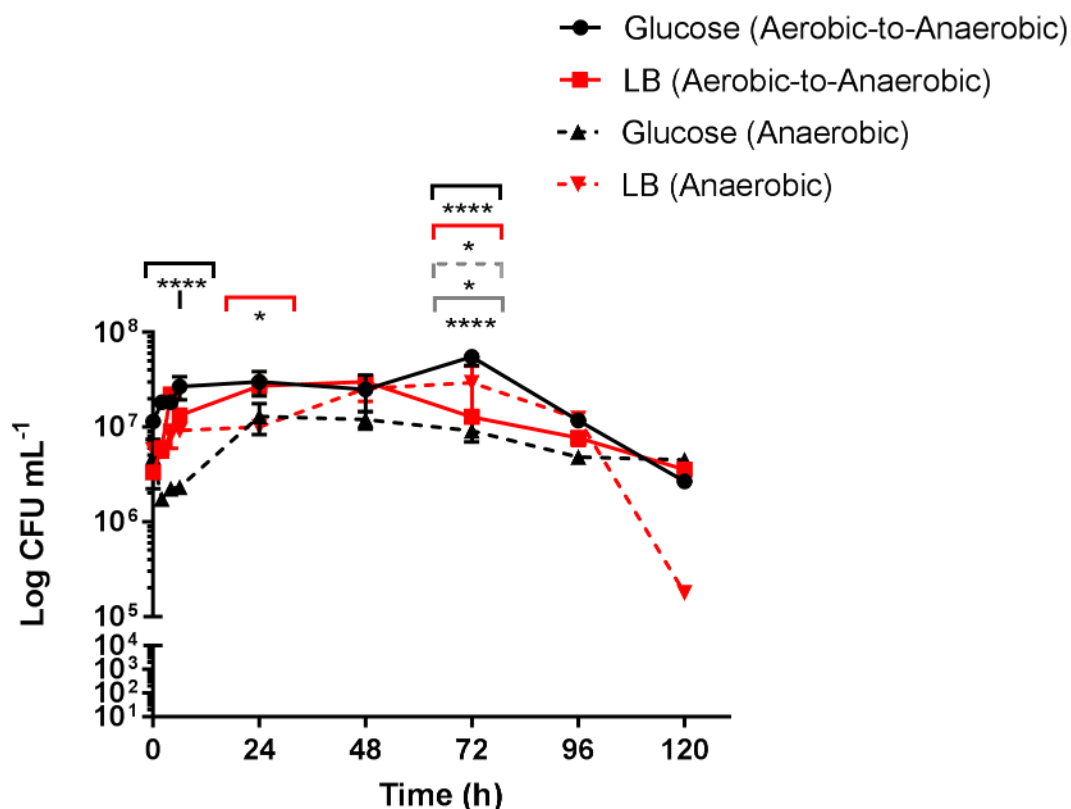


Figure 4.13. Growth kinetics were recorded by sampling *P. aeruginosa* strain ATCC 9027 over 120 h and conducting bacterial viability calculations, using two media types, glucose-based and LB broth (incubation conditions; 37 °C; static). Starting cultures were preconditioned as either aerobic-to-anaerobic or anaerobic prior to inoculation ( $n = 3$ ). Where error bars are not visible they are of similar or smaller size compared to the symbol. For the significance analysis, the red line denoted LB medium in different starting conditions, the black line denoted glucose-based medium in different starting conditions, whilst, the grey dotted line indicated glucose-based broth against LB broth (anaerobic) and the grey solid line compared glucose-based broth against LB broth (aerobic-to-anaerobic). Asterisks denote significance,  $*P \leq 0.05$  and  $****P \leq 0.0001$ .

#### 4.3.2.1.3 Pyocyanin Quantification – LC-MS

Pyocyanin production was quantified in parallel with the bacterial growth kinetics experiment, and samples were prepared after each time-point for LC-MS analysis (Figure 4.14). Overall, the results demonstrated little difference in the quantity of pyocyanin present when the bacteria were grown in different growth media, namely, glucose-based

and LB broth and when preconditioning the *P. aeruginosa* strain ATCC 9027 in different oxygen conditions. However, after 24 h incubation, *P. aeruginosa* strain ATCC 9027 cultured from aerobic-to-anaerobic starting conditions in LB medium produced a maximum concentration of 117.78 ppb pyocyanin (Figure 4.14, solid red line). This was significantly different when compared to the concentration of pyocyanin produced by the fully anaerobic *P. aeruginosa* culture after 24 h incubation in LB broth (Figure 4.14, dotted red line) and against the same preconditioning step in glucose-based medium (Figure 4.14, solid black line).

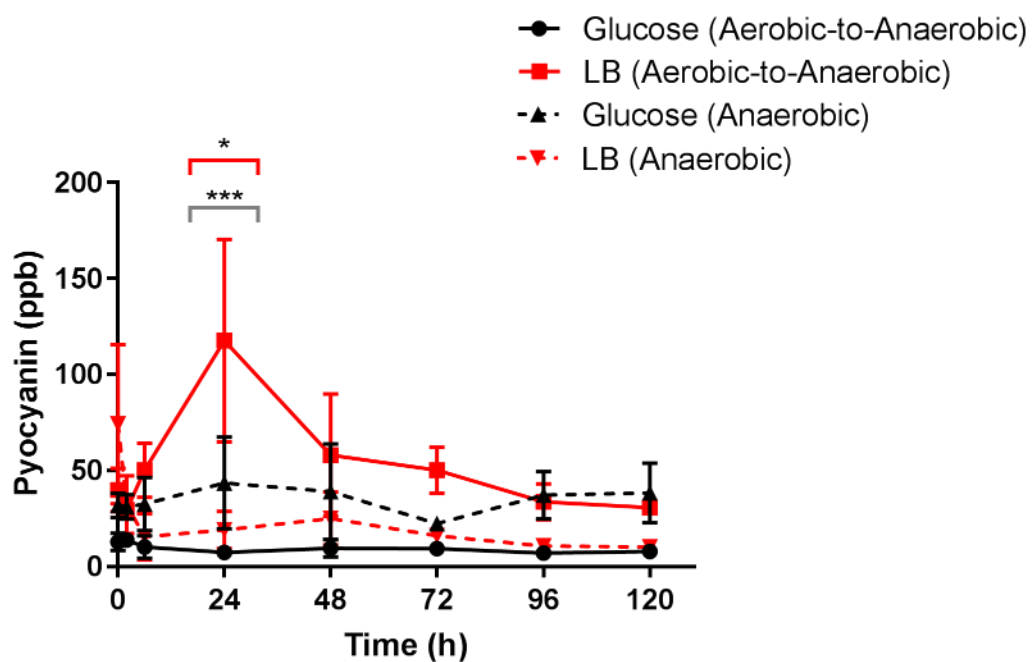


Figure 4.14. Pyocyanin quantification *via* LC-MS from *P. aeruginosa* strain ATCC 9027 over 120 h; utilising two media types, glucose-based and LB broth (incubation conditions; 37 °C; static). Starting cultures were either aerobic-to-anaerobic or anaerobic prior to inoculation ( $n = 3$ ). Where error bars are not visible they are of similar or smaller size compared to the symbol. For significance analysis, a red line represents LB medium in different starting conditions, whilst, a solid grey line compares glucose-based broth against LB broth (aerobic-to-anaerobic). Asterisks denote significance,  $*P \leq 0.05$  and  $***P \leq 0.001$ .

### 4.3.2.2 Biofilm Quantification – Crystal Violet Biofilm Assay in MFC Conditions

Crystal Violet Biofilm Assays were used to determine *P. aeruginosa* strain ATCC 9027 biofilm formation and growth on the 3D-Printed electrodes under MFC conditions. Both the 3D-Printed BM and PLA (control) electrodes were evaluated after the following time-points, 0 h, 1 h, 24 h, 48 h, 72 h, 96 h and 120 h. At each time-point, greater bacterial biomass was observed on the 3D-Printed BM electrodes, which was significant at 24 h ( $P \leq 0.0001$ ), 48 h ( $P \leq 0.0001$ ), 96 h ( $P \leq 0.001$ ) and 120 h ( $P \leq 0.01$ ) compared with the PLA control electrodes. A maximum biomass was recorded on the 3D-Printed BM electrodes at 48 h. After 48 h, a decrease in biomass was observed on both the 3D-Printed BM and PLA electrodes respectively (Figure 4.15).

In summary, the presence of graphene on the 3D-Printed BM electrodes enhanced *P. aeruginosa* biofilm formation when cultured in LB broth under anaerobic conditions. A reduction in biofilm formation was observed following 48 h bacterial incubation on both the 3D-Printed BM and PLA electrodes.

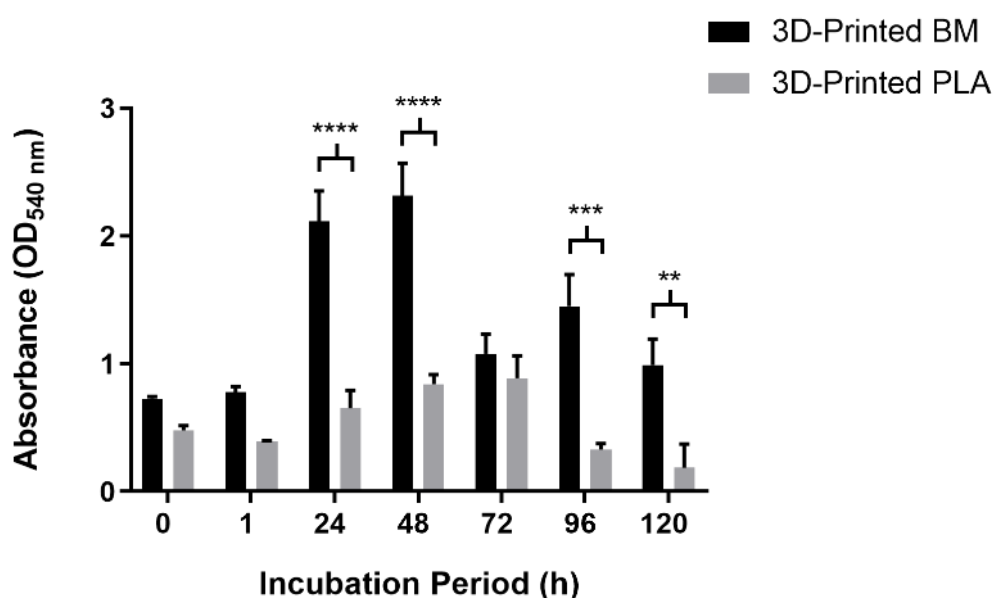


Figure 4.15. Biofilm quantification was determined using CVBA following *P. aeruginosa* strain ATCC 9027 incubation over 120 h in LB broth (deducting the sterile broth controls). Conditions replicated those selected for MFC experimentation (incubation conditions: static, LB broth, 37 °C, anaerobic) ( $n = 3$ ). Asterisks denote significance,  $**P \leq 0.01$ ,  $***P \leq 0.001$  and  $****P \leq 0.0001$ .

### 4.3.2.3 Nitrogen Biolog® Assay

*Pseudomonas aeruginosa* strain ATCC 9027 was incubated for 24 h in a range of amino acid sources in order to evaluate growth in both aerobic and anaerobic conditions.

In aerobic conditions, after 24 h of *P. aeruginosa* incubation with Pro-Gln (proline-glutamine) the maximum absorbance was observed (0.253 at OD<sub>590 nm</sub>) (An increase in absorbance is indicative of enhanced growth), followed by Gln-Gln (glutamine-glutamine) with 0.244 at OD<sub>590 nm</sub> and then Met-Met (methionine-methionine) with 0.232 at OD<sub>590 nm</sub> (Figure 4.16). In the presence of L-proline, *P. aeruginosa* produced the fourth greatest absorbance with 0.222 at OD<sub>590 nm</sub>.

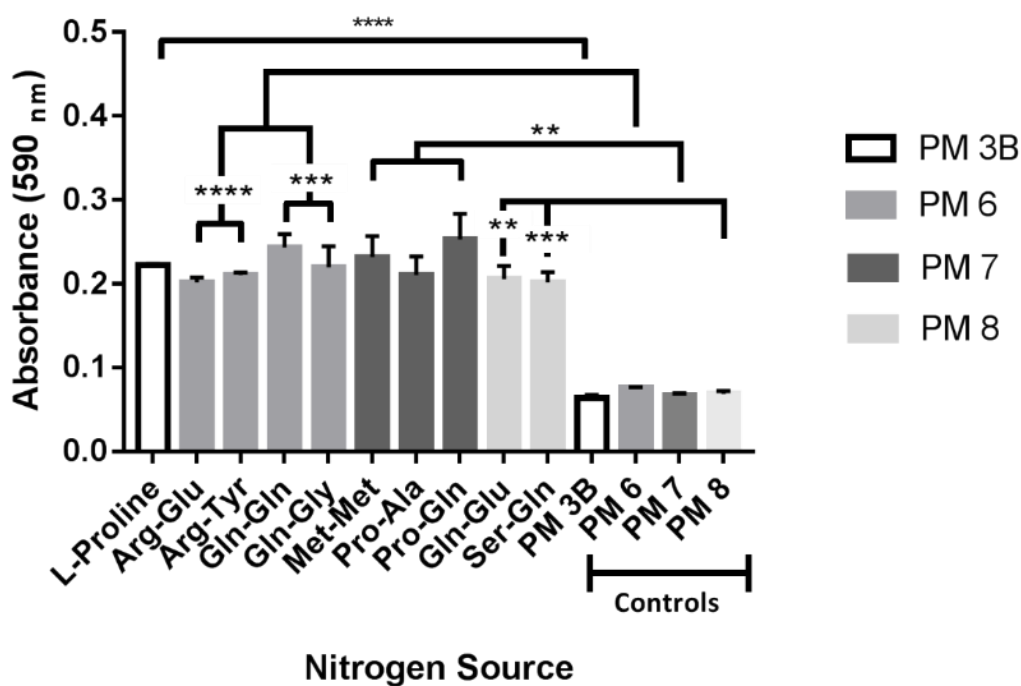


Figure 4.16. *Pseudomonas aeruginosa* strain ATCC 9027 growth after incubation for 24 h (37 °C, aerobic conditions) in the presence of varying nitrogen sources (standardised carbon source, sodium succinate) ( $n = 3$ ). Where error bars are not visible they are of similar or smaller size of the symbol. Asterisks denote significance, \*\* $P \leq 0.01$ , \*\*\* $P \leq 0.001$  and \*\*\*\* $P \leq 0.0001$ .

In anaerobic conditions, the nitrogen sources which achieved the greatest *P. aeruginosa* absorbance were thymine (0.199 at OD<sub>590 nm</sub>), Trp-Trp (tryptophan-tryptophan) (0.171 at OD<sub>590 nm</sub>) and Gly-Phe-Phe (glycine-phenylalanine-phenylalanine) (0.165 at OD<sub>590 nm</sub>) (Figure 4.17). This indicated that under varying oxygen conditions, *P. aeruginosa* can alter the biochemical pathway used to survive and proliferate. In aerobic conditions, proline-glutamine was the optimum nitrogen source, whilst in anaerobic conditions thymine was the optimum nitrogen source after 24 h incubation.

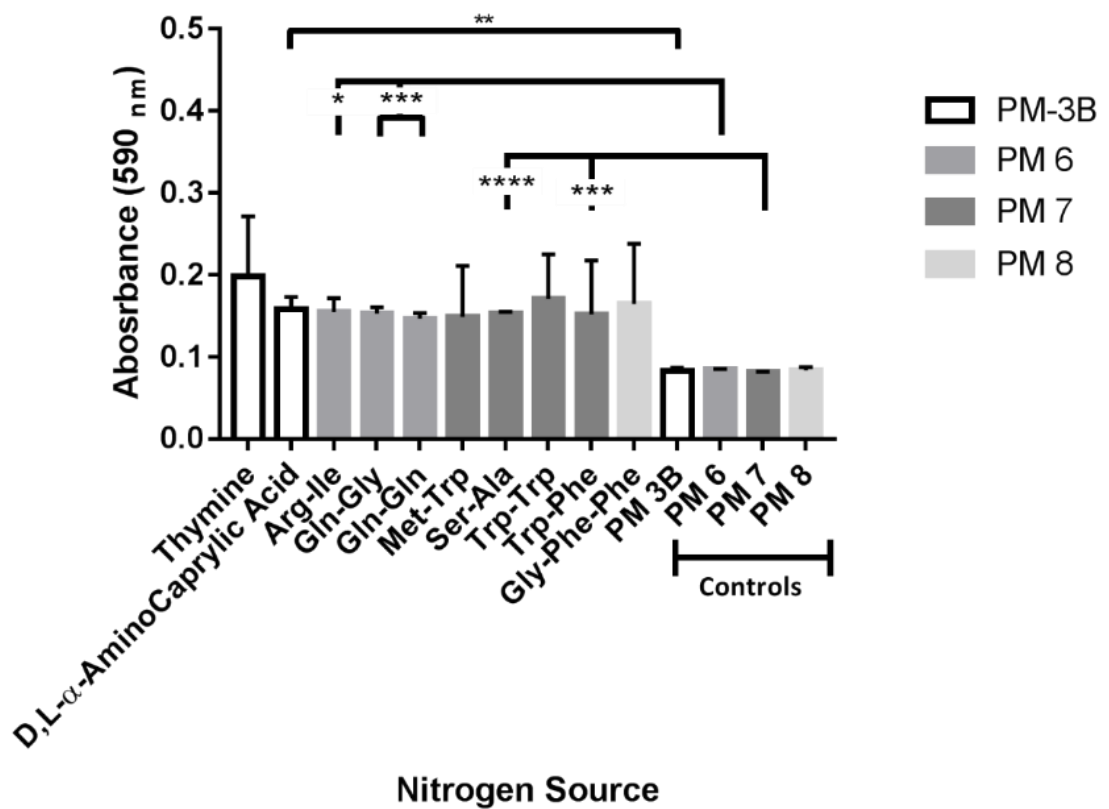


Figure 4.17. *Pseudomonas aeruginosa* strain ATCC 9027 growth after incubation for 24 h (37 °C, anaerobic conditions) in the presence of varying nitrogen sources (standardised carbon source, sodium succinate) ( $n = 3$ ). Asterisks denote significance,  $*P \leq 0.05$ ,  $**P \leq 0.01$ ,  $***P \leq 0.001$  and  $****P \leq 0.0001$ .

## 4.4 Discussion

### 4.4.1 Preliminary Strain Selection

Prior to MFC experimentation, it was essential that a highly exoelectrogenic *P. aeruginosa* strain was selected. The selection criteria for *P. aeruginosa* strains capable of high power outputs from MFC configurations were: (1) high pyocyanin production, (2) good biofilm-forming attributes when incubated with the 3D-Printed graphene electrodes and (3) high degree of cell motility. Several *P. aeruginosa* strains from different sources were selected to identify those which displayed a greater characteristic phenotypical (green) appearance, which was indicative of higher levels of pyocyanin production (Gellatly and Hancock, 2013).

*Pseudomonas aeruginosa* is a known exoelectrogen, due to its production of pyocyanin (Rabaey *et al.*, 2005). This secondary metabolite acts as an electron shuttle which confers electron transfer in MFC configurations (Rashid and Andleeb, 2018). The concentration of pyocyanin in the anode of MFCs has a direct correlation with power generation efficiency, due to its function of shuttling electrons through the cell membrane (Yong *et al.*, 2011). Thus, five *P. aeruginosa* strains were incubated over a range of time-points, namely, 24 h, 48 h, 7 d and 14 d. The results showed that *P. aeruginosa* strain ATCC 9027 and other clinical strains PAO1 and MRI produced the highest quantities of pyocyanin. The highest pyocyanin concentration of 6.34 µg/mL was observed after 14 d incubation of *P. aeruginosa* strain ATCC 9027. The difference in pyocyanin production over the respective incubation periods was negligible, which could be indicative of pyocyanin degradation. Pyocyanin has been shown to exist in either an oxidised or reduced form, with the latter being an unstable free radical (Hassett *et al.*, 1992). The three strains which produced the greatest amount of pyocyanin were then tested for their biofilm forming capabilities.

In order to determine biomass (and therefore biofilm quantification) of the highest pyocyanin producing strains, namely *P. aeruginosa* strains ATCC 9027, PAO1 and MRI, the bacterial strains were subjected to CVBAs over a set period of time (0 h – 14 d). Both polished and unpolished 3D-Printed electrodes were tested to determine any effects on biofilm formation. *Pseudomonas aeruginosa* strain ATCC 9027 exhibited a linear correlation between 0 h and 7 d producing a maximum biomass on the polished 3D-Printed BM electrodes after 5 days. Polishing the electrodes enhanced biofilm formation, which could

be due to alterations in surface topography, such as exacerbating features with microbial dimensions (whilst removing macro-level features), therefore promoting bacterial adhesion (Verran *et al.*, 2010). Strain PAO1 exhibited a peak in biomass between 5 d – 7 d in the presence of all electrode types, and the maximum biomass was identified after 7 d on the unpolished 3D-Printed BM electrodes. *Pseudomonas aeruginosa* strain MRI demonstrated a correlation between incubation period and biomass production. However, between 0 h – 5 d (MFC configuration, Chapter 5), the maximum biomass reported between this timeframe was found on the polished 3D-Printed PLA electrode after 5 d. A monolayer of planktonic cells attached to a surface of an electrode is restricted by the total surface area, this results in low power outputs due to the amount of nanowires able to adhere and contribute to direct electron transfer (Friman *et al.*, 2013). Therefore, biofilms which have been shown to be conductive, have the ability to produce much higher power and current densities, due to multiple layers of bacteria contributing to the overall net energy generation (Friman *et al.*, 2013). A study conducted by Sun *et al.* (2015) revealed that when *Geobacter anodireducens* was used in a MFC configuration, a two-layered biofilm developed over time, this biofilm consisted of an inner dead core and an outer layer of live viable cells. Results suggested that the outer layer was responsible for current generation whilst the inner-layer continued to serve as an electrically conductive matrix (Sun *et al.*, 2015). Therefore, it can be hypothesised that bacterial strains with greater biofilm forming capabilities could produce larger power outputs. *Pseudomonas aeruginosa* strain ATCC 9027 demonstrated the greatest biomass production on the 3D-Printed electrodes.

Flagella are known as nanowires in MFC configurations and contribute to direct electron mediated transfer (Gorby *et al.*, 2006). Traditionally, the major role of the bacterial flagellum is to mediate cell motility (Conrad *et al.*, 2011). Thus, motility assays were performed against the three *P. aeruginosa* strains shown to produce the highest quantity of pyocyanin. Under aerobic conditions, no difference in motility was observed. However, under anaerobic conditions, *P. aeruginosa* ATCC 9027 exhibited the greatest zone of motility, followed by *P. aeruginosa* strains MRI and PAO1 respectively.

Cell surface hydrophobicity is known to play a crucial role in the attachment of bacteria to surfaces (Giaouris *et al.*, 2009; Kochkodan *et al.*, 2008; Krasowska and Sigler, 2014). However, the physicochemical interactions that occur between bacteria and

surfaces has yet to be elucidated. In order to determine the cell hydrophobicity (and compare this with the surface hydrophobicity of the 3D-Printed electrodes), MATH assays were conducted with *P. aeruginosa* strains ATCC 9027 and PAO1 which were selected and incubated for 24 h, 72 h and 120 h under aerobic and anaerobic conditions. *Pseudomonas aeruginosa* ATCC 9027 cells were hydrophilic following 24 h, 72 h and 120 h of aerobic incubation. At 24 h and 72 h incubation a slight preference to electron accepting was observed. However, at 120 h a slight preference to electron donation was observed. *Pseudomonas aeruginosa* strain ATCC 9027 was hydrophilic following 24 h, 72 h and 120 h of anaerobic incubation, this strain also revealed moderate (adhesion value between 10 % and 55 %) electron accepting and donating abilities, with a slight preference to donating electrons (due to increased adhesion to the acidic polar hydrocarbon (chloroform)). Under aerobic conditions, PAO1 exhibited hydrophilic properties and a slight preference of accepting electrons. After anaerobic conditions, strain PAO1 exhibited hydrophilic properties at all incubation times and in contrast to the aerobic conditions, a slight preference to donating electrons was observed after 24 h. However, after 72 h and 120 h moderate electron donating and accepting properties, with a slight preference to accepting electrons was observed. Previously, *P. aeruginosa* strains were thought to possess both hydrophilic and hydrophobic surface properties (Deptula *et al.*, 2004). Microorganisms can switch between hydrophobic and hydrophilic phenotypes in response to changes in both environmental conditions (*i.e.* nutrient composition, temperature) and growth phase (Borecka-Melkusova and Bujdakova, 2008; Bujdaková *et al.*, 2013). The surface hydrophobicity of the 3D-Printed BM electrodes was previously determined (Chapter 3), which revealed that the electrode had a hydrophilic topside and a hydrophobic underside, this phenomenon is possibly due to the manufacturing process. Thus, it could be hypothesised that the topside of the electrodes promoted greater bacterial biofilm growth, due to the hydrophilic nature of both counterparts increasing bacterial attachment. The electron donation preference of *P. aeruginosa* strain ATCC 9027 further suggested that this strain was optimal for future MFC applications, as more electrons would be released into the anodic compartment.

This preliminary strain selection determined that *P. aeruginosa* ATCC 9027 was the optimal bacterial strain for future MFC studies due to the results exhibited against the predetermined criteria: (1) high pyocyanin production (2) good biofilm-forming attributes

and (3) high levels of cell motility. Thus *P. aeruginosa* strain ATCC 9027 was selected for further optimisation.

## **4.4.2 *Pseudomonas aeruginosa* strain ATCC 9027 Optimisation**

### **4.4.2.1 Growth Dynamics**

Growth dynamics of *P. aeruginosa* strain ATCC 9027 were evaluated using two media sources, LB and glucose-based media, with two preconditioning steps (aerobic starting cultures placed into anaerobic conditions or complete anaerobic conditions). The media and preconditioning steps were selected to determine the effect of two alternative biochemical pathways on *P. aeruginosa* growth and pyocyanin production. Aerobic starting cultures (into anaerobic conditions), were explored as this technique has previously been shown to improve electron shuttle production and promote biofilm formation in *P. aeruginosa* MFCs (Yong *et al.*, 2017). In the presence of carbon (*i.e.* glucose) *P. aeruginosa* generates adenosine triphosphate (ATP) by catabolism *via* the citric acid (TCA) cycle, which is also known as the Krebs cycle (Krebs and Eggleston, 1945; Krebs and Johnson, 1937; Krebs *et al.*, 1938). Although LB broth provides a relatively low source of carbon it provides a high concentration of tryptone, which is an assortment of peptides formed by the digestion of casein. This provides a source of amino acids that can be fermented or the nitrogen present from the amine groups of the amino acids could be utilised by bacteria capable of denitrification. Under anaerobic conditions *P. aeruginosa* can utilise nitrogen as an energy source due to denitrification (Schobert and Jahn, 2010; Schreiber *et al.*, 2006; Zumft, 1997). Both glucose-based and LB media have previously been used as the sole anolyte in *P. aeruginosa* MFC configurations (Ali *et al.*, 2017; Choi *et al.*, 2015; Rabaey *et al.*, 2004). In the present study, bacterial growth kinetics were measured over 120 h, and included recording optical density and bacterial cell viability; pyocyanin production was also quantified at each time-point *via* LC-MS analysis. Due to the electron accepting properties of oxygen, most MFCs are maintained under anaerobic conditions (Song *et al.*, 2015). For this reason, bacterial growth dynamic experiments were performed using anaerobic growth conditions. A duration of 120 h was selected as this was representative of the MFC experiments carried out in the sequential study (Chapter Five).

As optical density is non-specific to viable cell growth, it is important to analyse both OD and viable cell quantification simultaneously. A direct correlation between incubation time and an increase in OD (*i.e.* turbidity) was observed in a number of conditions tested. These included *P. aeruginosa* grown in an aerobic-to-anaerobic starting culture in LB medium and both, the aerobic-to-anaerobic and fully anaerobic *P. aeruginosa* starting cultures in glucose-based broth.

Optical density measurements over 120 h revealed that a greater turbidity (at OD<sub>540 nm</sub>) was observed when *P. aeruginosa* was inoculated in LB broth compared to glucose-based medium. As there was no overall significant difference when quantifying viable bacterial growth in the four different conditions, it might be suggested that this difference was not due to enhanced growth and replication of *P. aeruginosa* in LB broth. As OD is non-specific to bacterial growth, this could be indicative of a multitude of factors such as, greater cell turn over (*i.e.* more dead cells present), differences in osmotic pressure, enhanced biofilm formation and therefore greater extracellular polymeric substances (EPS) production and/or enhanced secondary metabolite production (Bernheim, 1963). Furthermore, aerobic-to-anaerobic *P. aeruginosa* starting cultures resulted in a higher OD than their anaerobic counterparts. This could possibly be due to the nutrient limited conditions, for example the presence of residual oxygen, which could induce pyocyanin production due to the inhibition of oxidative phosphorylation by uncouplers (such as carbonyl cyanide *m*-chlorophenyl hydrazone (CCCP)) and therefore turbidity (Qiao *et al.*, 2015; Whooley, 1982). At each incubation period, samples were also taken to calculate the viable cells present. The maximum bacterial viability was observed when using glucose-based medium with an aerobic-to-anaerobic starting culture of *P. aeruginosa* after 72 h. Under complete anaerobic conditions, *P. aeruginosa* exhibited a significantly greater viability when inoculated in LB medium, compared to glucose-based broth.

Under anaerobic conditions, *P. aeruginosa* survival and proliferation is supported by a number of mechanisms including denitrification (with nitrate or nitrite), pyruvate fermentation and arginine fermentation (Schreiber *et al.*, 2006; Vander Wauven *et al.*, 1984). However, in contrast to denitrification, pyruvate fermentation does not sustain anaerobic growth whilst, arginine fermentation can occur independently of pyruvate fermentation and can serve as an energy substrate for anaerobic growth (Eschbach *et al.*, 2004; Schreiber *et al.*, 2006; Vander Wauven *et al.*, 1984). To metabolise glucose, the

Entner-Doudoroff pathway is used, which converts one glucose molecule into two pyruvate molecules, this process is coupled to the synthesis of one ATP molecule and two excess reducing equivalents (Conway, 1992; Glasser *et al.*, 2014). Pyruvate can then be further converted to acetate, producing additional ATP and reducing equivalents (Glasser *et al.*, 2014).

The use of alternative growth media can result in the production of different secondary metabolites at varying concentrations (Hickey *et al.*, 2019). Due to this, pyocyanin production was quantified *via* LC-MS in parallel with each time-point of the growth dynamic experiment. The results showed little variation in the concentration of pyocyanin produced by the bacteria when utilising different growth media with alternative starting culture preconditioning steps (LB and glucose-based media and anaerobic and aerobic-to-anaerobic starting cultures). Interestingly, after 24 h incubation in LB broth, aerobic-to-anaerobic starting cultures of *P. aeruginosa* strain ATCC 9027 produced the maximum concentration of pyocyanin, which could be due to the presence of residual oxygen. Phenazine biosynthesis is positively regulated by the *Pseudomonas* Quinolone Signal (PQS) system (Gallagher *et al.*, 2002). This system requires oxygen and therefore under anaerobic conditions remains largely inactive, ultimately limiting phenazine production (Wang *et al.*, 2013). Therefore, some *P. aeruginosa* MFCs have been trialled under microaerobic conditions but this is normally counterintuitive to traditional MFC operating conditions. Nonetheless, under such operating conditions, an increase by two orders of magnitudes in peak current was observed (Venkataraman *et al.*, 2010; Venkataraman *et al.*, 2011). However, following the chloroform extraction assay, pyocyanin accumulation was not evident over time. This fluctuation in pyocyanin concentration is known to be a consequence of redox cycling, which generates ROS, such as H<sub>2</sub>O<sub>2</sub>, and can oxidatively degrade pyocyanin (Price-Whelan *et al.*, 2006; Reszka *et al.*, 2004).

#### **4.4.2.2 Biofilm Quantification – Crystal Violet Biofilm Assay in MFC Conditions**

Following on from the growth kinetic studies, biofilm quantification was evaluated using predetermined MFC conditions (*P. aeruginosa* ATCC 9027 inoculated into LB broth at 37 °C under static, anaerobic conditions). The 3D-Printed BM (8 wt.% graphene) electrodes

were evaluated for biofilm formation over the MFC duration period of 0 h – 120 h. Over the 120 h duration, greater biofilm formation was consistently evident on the 3D-Printed BM electrodes when compared to the PLA counterparts. This phenomenon could be due to the hydrophilic nature of both the *P. aeruginosa* and the topside of the 3D-Printed BM electrodes. Hydrophilic bacterial cells have been shown to adhere more strongly to hydrophilic surfaces (Giaouris *et al.*, 2009; Kochkodan *et al.*, 2008; Krasowska and Sigler, 2014). A peak in biomass was observed at 48 h and 72 h for the 3D-Printed BM and PLA (control) electrodes respectively. This was followed by a reduction in biomass, and it could be hypothesised that this reduction was due to biofilm detachment mechanisms which can be induced by environmental cues such as nutrients, pH and oxygen availability (Lee and Yoon, 2017). Dispersal mechanisms can be passive such as sloughing and erosion or active, such as seed dispersal, and the latter involves the release of single planktonic cells or microcolonies from the centre of the biofilm, leaving an empty cavity (Kim and Lee, 2016). Therefore, the reduction in biofilm formation on the both types of 3D-Printed electrode observed throughout this thesis could be due to the anaerobic, nutrient limited conditions trialled.

#### **4.4.2.3 Nitrogen Biolog® Assays**

Biolog® plates measure the bacterial cell respiration using a colorimetric redox probe, a dark purple colour is observed when cells proliferate more effectively with a specific nitrogen source, this can be used as an indicator for bacterial cell proliferation. A common characteristic of *Pseudomonas* species are their significant metabolic versatility, being able to break down a large variety of compounds. Under anaerobic conditions, *P. aeruginosa* can utilise nitrogen as an energy source *via* denitrification whilst, amino acids can be fermented as an alternative energy source if alternative terminal electron acceptors (*e.g.* O<sub>2</sub>) are not present (Schobert and Jahn, 2010; Schreiber *et al.*, 2006; Zumft, 1997). It is understood that *P. aeruginosa* utilises organic acids and amino acids preferentially to glucose (Bosire *et al.*, 2016). Under aerobic conditions, Pro-Gln (proline-glutamine) supported the maximum growth of *P. aeruginosa*, followed by, Gln-Gln (glutamine-glutamine), Met-Met (methionine-methionine) and then L-proline. However, under anaerobic conditions, the use of thymine resulted in the greatest growth, followed by Trp-

Trp (tryptophan-tryptophan) and Gly-Phe-Phe (glycine-phenylalanine-phenylalanine). This indicated that under varying oxygen conditions, *P. aeruginosa* could adapt its biochemical pathways in order to survive (Arai, 2011; Arat *et al.*, 2015). The presence of amino acids provides a means for *P. aeruginosa* to generate ATP in the absence of oxygen *via* fermentation. However, the amino acid utilised can have different effects on *P. aeruginosa* phenotypical traits, for example arginine has been shown to enhance biofilm formation whilst, simultaneously repressing bacterial cell motility (Bernier *et al.*, 2011). Amino acid supplements could be used to induce alternative metabolic pathways in *P. aeruginosa*, but phenotypic traits related to specific amino acid fermentation should be carefully considered to effectively enhance MFC power outputs.

## 4.5 Conclusion

A range of *P. aeruginosa* strains were selected based on phenotypic attributes and screened to assess the following parameters, (1) high pyocyanin production, (2) good biofilm-forming attributes and (3) high levels of cell motility. Overall *P. aeruginosa* strain ATCC 9027 exhibited the most exoelectrogenic attributes. This strain was selected for further analysis using growth dynamics experiments which were conducted in LB and glucose media, along with two preconditioning steps (aerobic starting cultures placed into anaerobic conditions or fully anaerobic conditions). Overall, no significant difference was observed between bacterial viability in any conditions tested. However, under anaerobic conditions, *P. aeruginosa* produced the maximum observed cell viability when inoculated in LB medium (when compared to glucose-based medium). Interestingly, pyocyanin accumulation was not evident over the duration of the growth experiments. Biofilm formation on the 3D-Printed BM electrodes showed enhanced biofilm formation when compared to a 3D-Printed PLA electrode. Finally, single nitrogen source Biolog MicroPlates™ assays were conducted and under anaerobic conditions *P. aeruginosa* inoculated in thymine demonstrated the greatest growth following 24 h incubation.

**Chapter 5 – *Pseudomonas aeruginosa* MFC  
Coupled with Additive Manufacturing of  
Graphene-Based Electrodes**

## 5.1. Introduction

### 5.1.1 Additive Manufacturing of MFCs

The application of MFCs at an industrially-relevant scale is yet to be realised, due to issues with scalability (Logan, 2010; Oliveira *et al.*, 2013; Slate *et al.*, 2019b). In order for MFC configurations to reach industrially-relevant levels, it is important to enhance the overall system efficiency. This could be achieved by improving parameters such as, manufacturing and running costs, power outputs, longevity and stability of the MFC configuration (You *et al.*, 2017). The manufacturing and assembly process of MFCs can be significantly improved *via* the design process, for example, neighbouring components could be consolidated which could ultimately lead to the generation of monolithic designs (You *et al.*, 2017). Additive manufacturing, more commonly known as 3D-Printing, provides a unique platform for both the rapid design and fabrication of complex structures with novel materials. Previously, such designs were not possible using more traditional manufacturing routes, such as moulding/casting processes (Farahani *et al.*, 2016; Foster *et al.*, 2017; MacDonald and Wicker, 2016). Therefore, 3D-Printing has the potential to improve MFC architectures, electrodes and ion exchange membranes (Calignano *et al.*, 2015; Ieropoulos *et al.*, 2010; Philamore *et al.*, 2015).

In order for efficient electron transfer to occur, the anode must be conductive (good heterogeneous electron transfer (HET) kinetic properties), whilst also exhibiting good biocompatibility to sustain bacterial growth. A high degree of surface area and surface roughness is also advantageous (Calignano *et al.*, 2015). Highly porous anodes can maximise bacterial adhesion and power generation (Bian *et al.*, 2018). You *et al.* (2017) 3D-Printed the first polymer based anode, where the conductive PLA filament (ProtoPlant, USA) was printed in the shape of a rectangular mesh for greater surface area (You *et al.*, 2017). Although the 3D-printed electrodes produced lower power outputs than the conventional carbon veil electrodes, the results were promising (You *et al.*, 2017). Furthermore, 3D-Printed ion exchange membranes have been trialled, where the polymer-based ion exchange membrane produced power outputs to the same magnitude as a conventional cationic exchange membrane (CEM), whilst being more cost effective (Philamore *et al.*, 2015).

In another study, porous carbon was fabricated *via* 3D-Printing coupled with a controlled carbonation process (Bian *et al.*, 2018). The 3D-Printed anodes (pore size 300  $\mu\text{m}$ ) produced a maximum power density of  $233.5 \pm 11.6 \text{ mW m}^{-2}$  and showed a significant improvement in electrochemical performance when compared to a 2D equivalent, carbon cloth, which produced a maximum power density of  $69.0 \pm 4.7 \text{ mW m}^{-2}$  (Bian *et al.*, 2018). The application of 3D-Printing clearly has unexploited potential and further research should be considered in order to enhance power outputs of MFCs.

### 5.1.2 Graphene

Carbon-based materials are the most widely used electrode type in MFCs, since microbial growth on the surface of metals can accelerate corrosion of the surface whilst, metals submerged in aqueous solutions can produce antimicrobial metal ions (Yu *et al.*, 2016; Zhou *et al.*, 2011; McBrearty *et al.*, 2018; Slate *et al.*, 2019a). Due to the beneficial physical properties of two dimensional nanomaterials, they have been applied in a wide array of energy generation and storage devices (Foster *et al.*, 2017). Graphene, which is defined as a 2D monolayer lattice of  $\text{sp}^2$  hybridised carbon atoms, has attracted intense research interest due to its reported unique properties (Brownson *et al.*, 2014). These properties include high electron mobility/conductivity, a large theoretical surface area and the ability to sustain extremely high densities of current (Mayorov *et al.*, 2011; Moser *et al.*, 2007; Stoller *et al.*, 2008). These properties are ideal for effective electron transfer, therefore graphene is a key target material for use within MFC configurations (Slate *et al.*, 2019b). The highest recorded power density ( $5.61 \text{ W m}^{-2}$ ) in a MFC to date was achieved using a 3D multilayer macroporous graphene scaffold as the anode (Ren *et al.*, 2016). The power density that was recorded with the graphene anode was a 3.3-fold increase compared to single layer, planar control (Ren *et al.*, 2016).

Previously, a graphene-based PLA filament was used to produce a 3D-Printed electrochemical energy storage architecture, *via* additive manufacturing (Foster *et al.*, 2017). This was the first study which demonstrated the fabrication and utilisation of electrochemical energy storage architectures, by using a commercial graphene-based PLA filament (Foster *et al.*, 2017). This filament, known commercially as Black Magic, which is a conductive graphene PLA filament, consisted of a calculated maximum graphene loading

of 8 wt.% (Foster *et al.*, 2017) and was subsequently selected for further study. This filament was 3D-Printed and used as an electrode material, which was then used in a *P. aeruginosa* inoculated MFC, to determine if the application of this 3D-Printed graphene-based electrode enhanced power outputs when compared to conventional electrode materials.

### 5.1.3 *Pseudomonas aeruginosa* MFC configurations

*Pseudomonas aeruginosa* secretes pyocyanin, a phenazine-based, soluble redox metabolite which enables the transfer of electrons between bacteria to a terminal electron acceptor (*i.e.* an electrode) (Liu *et al.*, 2012). Thus, *P. aeruginosa* has been used in a range of MFC configurations (Gomes *et al.*, 2011; Jayapriya and Ramamurthy, 2012; Qiao *et al.*, 2015; Yong *et al.*, 2017; Zhang *et al.*, 2019), including some examples which have employed graphene-based electrodes (He *et al.*, 2012; Liu *et al.*, 2012; Webb *et al.*, 2015; Yong *et al.*, 2017). In one study, Liu *et al.* (2012) electrochemically deposited graphene onto carbon cloth to produce an anode for a *P. aeruginosa* mediator-less MFC (Liu *et al.*, 2012). The introduction of graphene resulted in an increase in power density by 2.7 times, which was attributed to the high biocompatibility of graphene, resulting in enhanced bacterial growth (Liu *et al.*, 2012). The authors also suggested that the presence of graphene resulted in a stimulatory effect, leading to the generation of more mediating molecules (*i.e.* pyocyanin) by *P. aeruginosa* (Liu *et al.*, 2012). *Pseudomonas aeruginosa* has been used as the sole exoelectrogen in MFC configurations and such experiments are often conducted to elucidate and optimise electron transfer mechanisms (Cao *et al.*, 2019; Chong and Li, 2017). It is suggested that the future of MFCs will involve research into sustainable technology and wastewater treatment, once industrially-relevant capabilities are realised (Jiang *et al.*, 2011). However, in such instances pure cultures are not feasible due to the complex microbiome of wastewater (Vilajeliu-Pons *et al.*, 2016). The use of mixed community biofilms, both inter-bacterial and with other microorganisms (*i.e.* fungi, such as yeast) for MFC application has vast potential (Slate *et al.*, 2019b). Studies have previously shown that the phenazines produced by *P. aeruginosa* can be utilised by other bacterial species to transfer electrons to an anode in a MFC configuration (Boon *et al.*, 2008; Rabaey *et al.*, 2005). Although mixed community MFC configurations are out of the scope of this thesis,

they are important to note, as they have considerable implication towards future applications and attainable power outputs.

#### **5.1.3.1 Biofilm Formation and Role in *P. aeruginosa* MFCs**

The formation of bacterial biofilms plays a pivotal role in current generation of MFCs (Angelaalincy *et al.*, 2018; Qiao *et al.*, 2017). The current generated by a monolayer of planktonic cells is limited to the surface area of the electrode used, whilst, in the case of conductive biofilms, multiple layers of bacteria are able to contribute to the overall net energy generation, resulting in higher power and current density generation (Friman *et al.*, 2013). In regards to *P. aeruginosa* inoculated MFCs, the biofilm produced on the anode promotes the interfacial phenazine redox reaction by accumulating the self-generated mediators, such as phenazines (*i.e.* pyocyanin) on the anode, thus resulting in fast interfacial electron transfer (Qiao *et al.*, 2017). This hypothesis was tested by Qiao *et al.* (2017) who produced non-biofilm forming *P. aeruginosa* MFCs *via* the addition of sodium houttuynonate, which inhibited biofilm production of *P. aeruginosa* by alginate biosynthesis repression (Qiao *et al.*, 2017; Wu *et al.*, 2015). The lack of biofilm formation resulted in a marked decline in current generation (Qiao *et al.*, 2017). The authors postulated that surface bound phenazines, rather than phenazines in suspension, determined the performance of the anode (Qiao *et al.*, 2017). Therefore, the MFC experiments in the present study visualised bacterial attachment and subsequent biofilm formation using SEM and confocal microscopy.

#### **5.1.3.2 Varying Medium Sources to Influence Metabolic Pathways**

Glucose-based and Luria-Bertani (LB) media have both previously been used as the sole medium source in *P. aeruginosa* MFC configurations (Ali *et al.*, 2017; Choi *et al.*, 2015; Rabaey *et al.*, 2004). To metabolise glucose under anaerobic conditions, *P. aeruginosa* uses the Entner-Doudoroff pathway; this pathway converts a glucose molecule into two pyruvate molecules, which is coupled to the synthesis of one net ATP molecule and two excess reducing equivalents NAD(P)H, per pyruvate molecule (Glasser *et al.*, 2014). Pyruvate molecules can then be converted to acetate, producing additional ATP and reducing equivalents (Glasser *et al.*, 2014). *Pseudomonas aeruginosa* can effectively utilise

hexose and pentose sugars through anodic respiration. In one study the highest power density was generated from glucose ( $136 \pm 87 \text{ mW m}^{-2}$ ) when compared to both fructose ( $3.6 \pm 1.6 \text{ mW m}^{-2}$ ) and sucrose ( $8.606 \pm \text{ mW m}^{-2}$ ) (Ali *et al.*, 2017). Under anaerobic conditions, pyruvate allows for the long-term anaerobic survival, but not growth of *P. aeruginosa* (Eschbach *et al.*, 2004; Vander Wauven *et al.*, 1984).

Denitrification is one such pathway, which under anaerobic conditions can sustain *P. aeruginosa* growth by using different alternative terminal acceptors in the form of nitrogen oxides (Kuroki *et al.*, 2014; Schreiber *et al.*, 2007). In the absence of oxygen, nitrite and nitrate, the fermentation of amino acids such as arginine is another alternative route for anaerobic survival (Vander Wauven *et al.*, 1984). LB medium provides a high concentration of tryptone, this contains an assortment of peptides, which provides a source of amino acids, these amino acids can then be fermented in the case of arginine or provide a source of nitrogen for denitrification (Eschbach *et al.*, 2004; Vander Wauven *et al.*, 1984). However, as *P. aeruginosa* has no known nitrogen-fixing ability, it is potentially arginine fermentation that is the mechanism responsible for *P. aeruginosa* survival and proliferation in anaerobic LB medium (Yan *et al.*, 2008). Choi *et al.* (2015) developed a paper-based microbial fuel cell array to allow for high throughput screening of electricity producing bacteria and the model microorganism used was *P. aeruginosa* in LB medium (Choi *et al.*, 2015). Both glucose-based and LB media were used in the MFC experimentation, to determine whether different metabolic pathways resulted in enhanced power generation.

### **5.1.4 Aim**

The aim of this chapter was to incorporate the 3D-Printed BM and PLA (control) electrodes into a MFC configuration and test them in conjunction with traditional carbon cloth electrodes with two different media types (anaerobic LB and anaerobic glucose-based media) to determine if a change in media type influenced the metabolic requirements of *P. aeruginosa* and therefore influenced power outputs.

## 5.2 Methods

### 5.2.1 Bacterial Cell Preparation

*Pseudomonas aeruginosa* strain ATCC 9027 was inoculated into 10 mL LB or glucose-based broth, which was previously purged with nitrogen for 30 min to generate an anaerobic environment. The glucose-based medium prepared as per Section 4.2.1.1 (Liu *et al.*, 2012). The culture was incubated at 37 °C, with agitation for 18 h. After incubation, cultures were adjusted to an OD<sub>600 nm</sub> of 1 (± 0.1). This equated to *ca.* 5.0 × 10<sup>8</sup> CFU mL<sup>-1</sup>.

### 5.2.2 MFC Configuration

#### 5.2.2.1 MFC Construction

A classic H-shaped MFC device was developed (Figure 5.1), which consisted of two microbial fuel cell glassware components (Adams & Chittenden Scientific Glass, USA), each with a 120 mL volume. The components were separated by a CEM (CMI-7000 (Membrane International, USA)). All components were sterilised prior to use with 70 % ethanol. The anodic chamber consisted of 120 mL LB or glucose-based broth, which was degassed with nitrogen for 30 min to remove dissolved oxygen prior to inoculation to generate anaerobic conditions. An aliquot of 1 mL of the prepared *P. aeruginosa* culture was added to the anodic compartment, giving a starting OD<sub>540 nm</sub> of 0.01 (this equated to *ca.* 5.0 × 10<sup>6</sup> CFU mL<sup>-1</sup>). The cathodic compartment consisted of 120 mL, 50 mM potassium hexacyanoferrate and 0.1 M potassium chloride (as the supporting electrolyte).

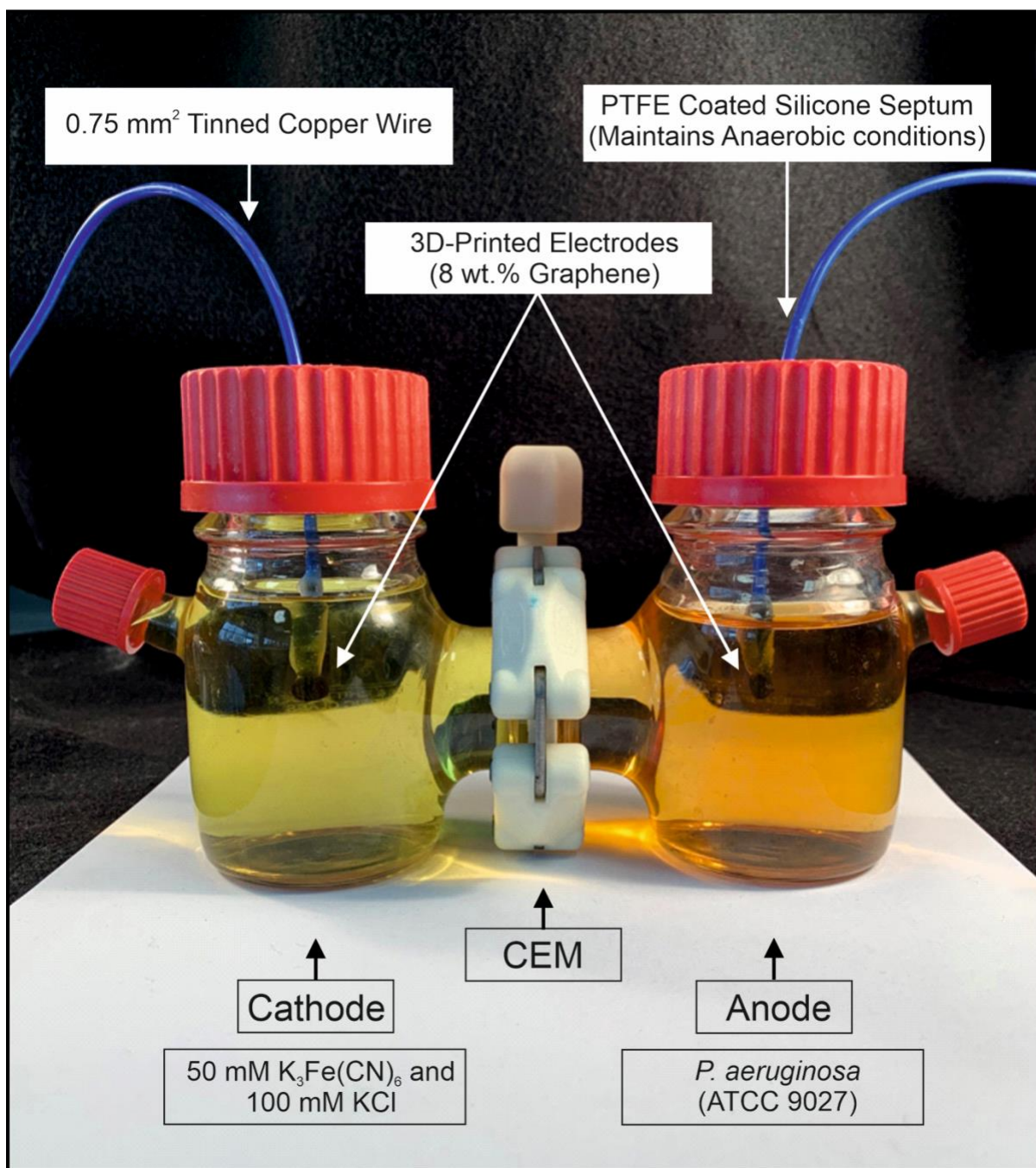


Figure 5.1. The two-chambered, classical H-shaped MFC utilised in this study.  $K_3Fe(CN)_6$ ; Potassium hexacyanoferrate (III), KCl; Potassium chloride; CEM, Cationic Exchange Membrane, Polytetrafluoroethylene; PTFE.

The 3D-Printed BM electrodes (8 wt.% graphene), 3D-Printed PLA electrodes and carbon cloth with a theoretical surface area of  $7.5 \text{ cm}^2$  were used for both the anode and cathode in each study. Electrodes were prepared by attaching the electrodes to  $0.75 \text{ mm}^2$  stranded, tinned copper wire (Farnell, UK) *via* heat shrink tubing. The exposed surface between the electrodes and the heat shrink tubing were covered with electrical tape and

epoxy (Araldite®, Huntsman Advanced Materials, Switzerland) was used to coat the heat shrink tubing and connection points entirely. This ensured the isolation of the wire to prevent direct electron transfer by *P. aeruginosa*. Therefore, only the calculated surface area was available to partake in electron transfer. Each MFC configuration tested was carried out in biological triplicates ( $n = 3$ ).

### 5.2.2.2 Measurement and Analysis

The MFC configuration was connected to a custom-made circuit board (assistance kindly provided from Mr. Daniel Wilson, University of Manchester). This was connected to an Arduino UNO (Arduino, Italy) (Figure 5.2), which was used to switch between open circuit voltage (OCV) and closed circuit voltage (CCV) every 30 min *via* a relay switch and a 10 k $\Omega$  external resistor.

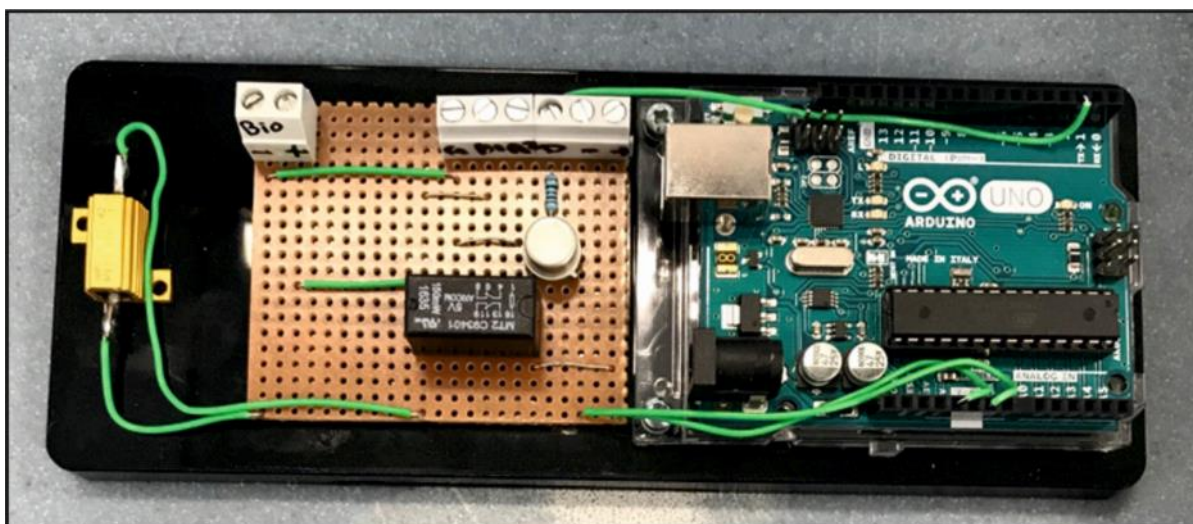


Figure 5.2. Custom made circuit board that was connected to an Arduino UNO board, in order to switch between open and closed (an external 10 k $\Omega$  resistor) circuit voltage every 30 min of the 120 h incubation period.

The MFC was connected to the custom-made circuit board, which was subsequently coupled to a high-resolution ADC-24 (Pico technology, UK) data acquisition system. OCV and CCV was recorded over the 120 h MFC incubation period using Picolog software (version 6.1.10) where data was acquired every 15 min after the OCV/CCV switch. The MFCs were incubated for 120 h and an OCV and CCV reading was recorded every 24 h, which resulted in voltage readings at 0 h, 24 h, 48 h, 72 h, 96 h and 120 h. The CCV recorded at

each time-point was used as the E Cell (cell potential (V)), by using Ohm's law and the following parameters were calculated (Logan *et al.*, 2006) [4.1 – 4.4]:

Current:

$$\text{Current (A)} = \frac{\text{E Cell (V)}}{\text{Resistance } (\Omega)} \quad [4.1]$$

Current density:

$$\text{Current Density (A m}^{-2}\text{)} = \frac{\text{E Cell (V)}}{\text{Resistance } (\Omega) \times \text{Surface Area (m)}} \quad [4.2]$$

Power:

$$\text{Power (W)} = \frac{(\text{E Cell (V)})^2}{\text{Resistance } (\Omega)} \quad [4.3]$$

Power density:

$$\text{Power Density (W m}^{-2}\text{)} = \frac{(\text{E Cell (V)})^2}{\text{Resistance } (\Omega) \times \text{Surface Area (m)}} \quad [4.4]$$

### 5.2.2.3 Arduino Code

The code was written to switch measurements between open and closed circuit potential, using the same voltmeter configuration. The relay switched the MFC between the voltmeter and a voltmeter with a load (an external 10 k $\Omega$  resistor), over a set period of time (every 30 min). The following code was uploaded to the Arduino UNO board in order to record both OCV and CCV:

```
Void setup()
```

```
{pinMode(RELAY, OUTPUT); // tell Arduino RELAY pin is an OUTPUT pin  
pinMode(LED, OUTPUT); // tell the Arduino that the LED is an OUTPUT}
```

```
Void loop(){
```

```
DigitalWrite(RELAY, LOW); // Keep relay off, load is on MFC  
DigitalWrite(LED, HIGH); // LED is on showing load on MFC  
Delay(1800000); // Wait 30 mins, this value is in ms.
```

DigitalWrite(RELAY, HIGH); // switch on relay voltage should now be on other pin of DAC.  
Relay on, load is off.

DigitalWrite(LED, LOW); //LED is off, load is off.

Delay(1800000); // Wait 30 mins, this value is in ms}

#### **5.2.2.4 Bacterial Enumeration**

Bacterial viability was determined by Miles and Misra assays (Miles *et al.*, 1938). At each time-point, 0 h, 24 h, 48 h, 72 h, 96 h and 120 h, 1 mL of inoculated broth were removed from the MFCs. Aliquots of 20  $\mu\text{L}$  of inoculated broth were serially diluted with sterile broth ( $10^{-1}$  to  $10^{-8}$ ). Following vortexing, 20  $\mu\text{L}$  of each diluted sample was inoculated onto either glucose-based agar or LB agar plates (depending on the MFC parameters), followed by incubation at 37 °C for 18 h. Colonies were counted and viability ( $\text{CFU mL}^{-1}$ ) was determined (as per Section 4.3) in order to generate growth curves which could then be compared against the power/current generated. The remaining isolated inoculated broth was stored at -80 °C for future experimentation. Enumeration of bacterial cells was carried out in biological triplicates ( $n = 3$ ).

#### **5.2.3 Scanning Electron Microscopy**

Following the termination of the MFC experiments (after 120 h), the anode, cathode (which were either 3D-Printed BM, 3D-Printed PLA or carbon cloth electrodes) and CEM were isolated, placed into sterile Petri dishes and dried at room temperature in a class 2 biohazard cabinet. Samples were then submerged in 4 % glutaraldehyde for 24 h at 4 °C. Following this fixation step, the glutaraldehyde was discarded and samples were submerged in sterile deionised water and dried at room temperature under aseptic conditions. The samples were then subjected to an ethanol gradient of 10 %, 30 %, 50 %, 70 %, 90 % and 100 %, with the samples submerged in each ethanol concentration for 10 min. This was followed by desiccation for 24 h. The samples were attached to SEM stubs (diameter: 12.5 mm) using carbon tabs (Agar Scientific, UK) and were sputter coated with gold (Polaron, UK) for 30 s (800 V; 5 mA), followed by analysis using SEM.

## 5.2.4 Confocal Microscopy

Following the MFC experiments (120 h), components of the MFC such as the anode, the cathode (which were either 3D-Printed BM, 3D-Printed PLA or carbon cloth electrodes) and the CEM were isolated. These components were placed into sterile Petri dishes and dried at room temperature in a class 2 biohazard cabinet. Samples were submerged in 0.01 M phosphate buffer saline (PBS) to remove unattached cells and debris and stained with 0.1 % w/v acridine orange (Merck, UK) in 2 % v/v glacial acetic acid for 10 min, in the dark (to avoid bleaching of the fluorescent dye) at room temperature. The samples were washed in 0.01 M PBS to remove excess dye, dried at room temperature and fixed in 4 % glutaraldehyde. Prior to microscopy, the glutaraldehyde was removed, samples were rinsed in 0.01 M PBS and secured to a microscope slide. The samples were observed at 63 × under a Leica TSC SPE 1000 confocal microscope (Leica Microsystems, UK) coupled with the Leica Application Suite X (LAS X) software (Leica Microsystems, UK).

## 5.2.5 Statistical Analysis

Datasets were collated and analysed using Microsoft Excel (2016). Graphs were generated using Graphpad Prism (version 8). The standard error of the mean (SEM) was denoted *via* error bars. For statistical analysis, *P* values were calculated at the 95 % confidence level by two-way ANOVAs, this was determined using Graphpad Prism (version 8). In all cases,  $P < 0.05$  was considered statistically significant. Asterisks denote significance,  $*P \leq 0.05$ ,  $**P \leq 0.01$ ,  $***P \leq 0.001$  and  $****P \leq 0.0001$ .

## 5.3 Results

### 5.3.1 MFC Cell Potential

Throughout MFC experimentation, the closed circuit voltage of the three electrode types (3D-Printed BM, 3D-Printed PLA and carbon cloth) was recorded at 0 h, 24 h, 48 h, 72 h, 96 h and 120 h in two media types, anaerobic glucose-based and anaerobic LB (Figure 5.3). The 3D-Printed PLA electrodes were included as a negative control, to confirm that the PLA, which was used as the base material for the 3D-Printed BM (8 wt.% graphene) electrodes, was non-conductive. The insulating nature of PLA was confirmed, given the highest potential recorded from the 3D-Printed PLA electrodes was  $21.00 \pm 5.13$  mV at 120 h in LB broth. Both the 3D-Printed BM and carbon cloth electrodes exhibited conductivity from 0 h to 24 h, which was monitored as an increase in cell potential. This was followed by a stationary period and finally from 72 h to 120 h a decrease in cell potential was observed. Interestingly, this correlated with the kinetics of bacterial viability which were calculated at the same time-points (Figure 5.4). The highest potential recorded was when *P. aeruginosa* was inoculated with carbon cloth in anaerobic glucose-based medium after 96 h ( $324.00 \pm 10.06$  mV). There was no statistical difference between the 3D-Printed BM electrodes in varying media. However, the highest potential recorded from the 3D-Printed BM electrodes was in LB medium after 48 h ( $287.00 \pm 18.52$  mV). Throughout the first 48 h, there was no statistical difference in the potential recorded between the 3D-Printed BM electrodes and the carbon cloth electrodes in either media type. At 72 h, there was a significant difference ( $P \leq 0.01$ ) between the 3D-Printed BM electrode ( $154.67 \pm 12.33$  mV) and carbon cloth ( $314.33 \pm 8.11$  mV) in glucose-based medium. After 96 h and 120 h of *P. aeruginosa* incubation, there was a significant difference between 3D-Printed BM in glucose-based broth ( $155.00 \pm 30.64$  mV and  $118.00 \pm 11.12$  mV, respectively) and carbon cloth in LB broth ( $254.67 \pm 4.98$  mV and  $257.33 \pm 5.21$  mV, respectively) ( $P \leq 0.01$ ). After 120 h of MFC incubation, the carbon cloth in glucose-based medium produced the highest potential,  $319.00 \pm 5.51$  mV, which could be compared to the 3D-Printed BM electrode in glucose-based medium,  $118.00 \pm 1.12$  mV ( $P \leq 0.0001$ ) (Figure 5.3).

In summary, the 3D-Printed PLA electrode demonstrated no conductivity whilst, cell potential of the 3D-Printed BM electrode and carbon cloth demonstrated a similar trend

when compared against the bacterial growth kinetics. Carbon cloth in glucose-based medium produced the highest cell potential after 96 h.

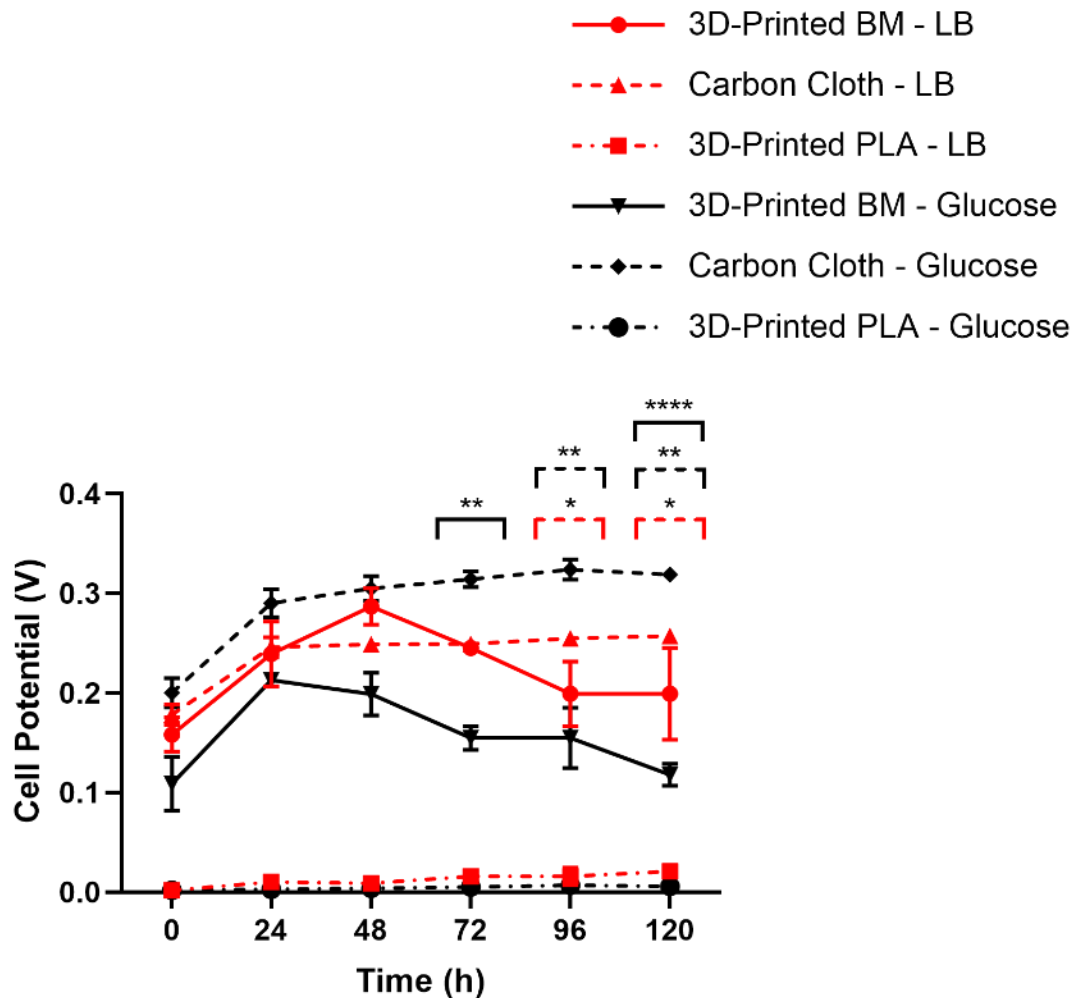


Figure 5.3. Cell potential (V) measured from MFCs, which utilised three electrode types, 3D-Printed BM (8 wt.% graphene content), 3D-Printed PLA and carbon cloth with *P. aeruginosa* strain ATCC 9027 incubated in two types of media, LB and glucose-based broth ( $n = 3$ ). Where error bars are not visible they are of similar or smaller size compared to the symbol. For statistical analysis, only results between the 3D-Printed BM and carbon cloth electrodes were analysed, the black solid line denoted the different electrodes in glucose-based medium, the black dotted line denoted 3D-Printed BM in glucose-based broth against carbon cloth in LB broth, whilst, the red dotted line denoted 3D-Printed BM in LB broth against carbon cloth in glucose-based medium. Asterisks denote significance,  $*P \leq 0.05$ ,  $**P \leq 0.01$  and  $****P \leq 0.0001$ .

### 5.3.2 Bacterial Quantification From MFC – Growth kinetics

Growth kinetic experiments were used to determine the viability of *P. aeruginosa* strain ATCC 9027 from MFCs over defined time-points (0 h, 24 h, 48 h, 72 h, 96 h and 120 h). *Pseudomonas aeruginosa* was incubated in anaerobic glucose-based and anaerobic LB media in the presence of different electrodes, 3D-Printed BM, 3D-Printed PLA and carbon cloth (Figure 5.4). All six conditions resulted in conventional bacterial growth phase models, including the presence of lag phase, exponential growth (log phase), stationary phase and death phase. There was no significant difference ( $P > 0.05$ ) in cell viability when *P. aeruginosa* strain ATCC 9027 was grown in the presence of 3D-Printed BM, 3D-Printed PLA and carbon cloth electrodes in both glucose-based and LB broth, which indicated that there was no significant antimicrobial effect due to the presence of graphene. The maximum viability was observed when *P. aeruginosa* strain ATCC 9027 was inoculated in anaerobic LB medium with carbon cloth electrodes after 72 h ( $6.94 \times 10^7$  CFU mL<sup>-1</sup>), this was followed by 3D-Printed PLA in anaerobic LB broth after 96 h ( $5.94 \times 10^7$  CFU mL<sup>-1</sup>). In the presence of the 3D-Printed BM electrode in anaerobic glucose-based broth, the third highest bacterial viability was observed after 96 h ( $4.50 \times 10^7$  CFU mL<sup>-1</sup>), whilst, in anaerobic LB broth this value was lower after 72 h ( $4.44 \times 10^7$  CFU mL<sup>-1</sup>). The lowest bacterial viability seen throughout the growth dynamic assays when bacteria were exposed to the 3D-Printed BM electrode in glucose-based medium at 0 h ( $4.06 \times 10^6$  CFU mL<sup>-1</sup>), followed by the 3D-Printed BM electrode in LB medium after 120 h ( $4.11 \times 10^6$  CFU mL<sup>-1</sup>).

In summary, there was no significant difference in *P. aeruginosa* viability over 120 h, regardless of the electrode the bacteria were inoculated with. The 3D-Printed BM electrodes which comprised 8 wt.% graphene exhibited no significant antimicrobial activity.

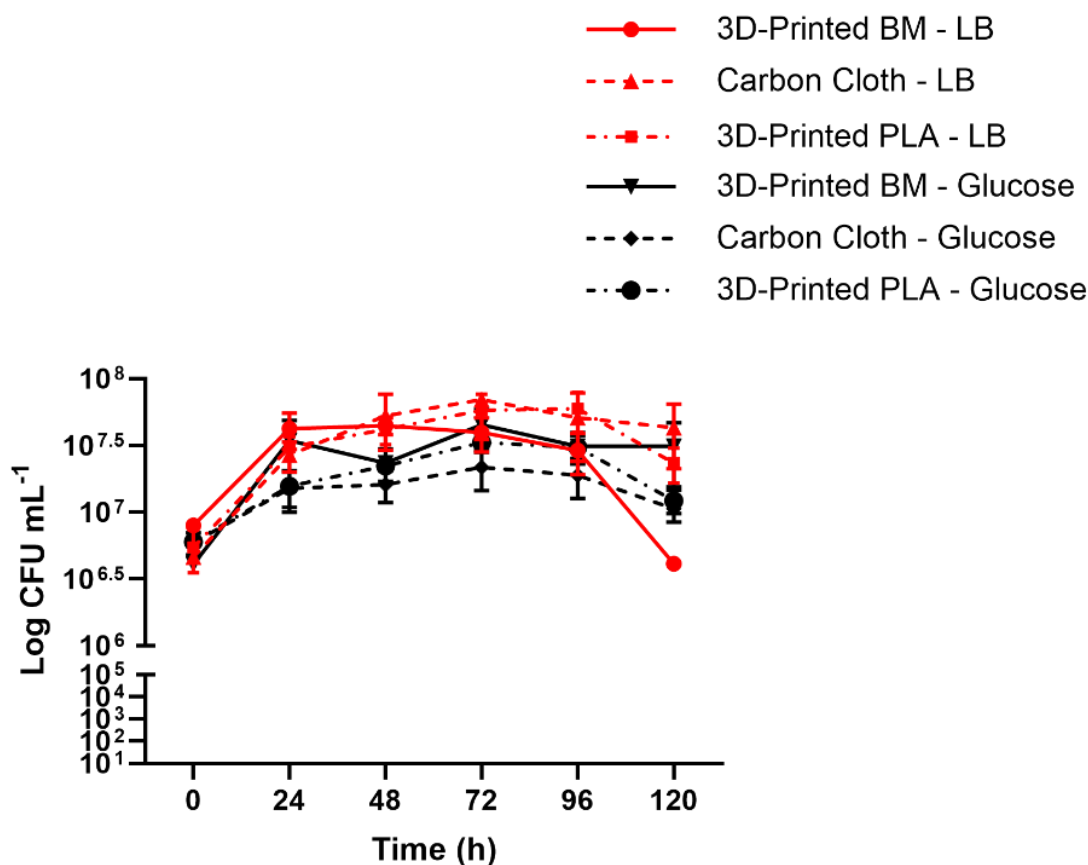


Figure 5.4. Growth kinetics of anaerobic *P. aeruginosa* strain ATCC 9027 during the MFC experiments (120 h) were determined in two media types, LB and glucose-based broth, via bacterial viability calculations. This was conducted in the presence of three electrode types, 3D-Printed BM (8 wt.% graphene content), 3D-Printed PLA and carbon cloth ( $n = 3$ ). Where error bars are not visible they are of similar or smaller size compared to the symbol. No statistical difference ( $*P > 0.05$ ) was observed between the bacterial growth kinetics and the MFC electrode or media type.

### 5.3.3 MFC Current and Current Density

The recorded cell potentials (V) were used to calculate current and current density outputs, from the MFCs at 0 h, 24 h, 48 h, 72 h, 96 h and 120 h from three electrode types (3D-Printed BM, 3D-Printed PLA and carbon cloth) in two types of media, anaerobic LB and anaerobic glucose-based broth (Figure 5.5 and Figure 5.6). The electrode surface area used throughout this study was 7.5 cm<sup>2</sup>. Due to the insulating properties of PLA, the 3D-Printed PLA electrodes (which were included as a negative control for the 3D-Printed BM

electrodes) produced the maximum current of  $2.1 \pm 0.51 \mu\text{A}$  in LB medium after 120 h. The highest current produced from the conductive electrodes in the presence of *P. aeruginosa* strain ATCC 9027 was the 3D-Printed BM electrode in LB broth after 48 h incubation ( $28.70 \pm 1.85 \mu\text{A}$ ). This was followed by the carbon cloth electrode in LB medium after 120 h ( $25.73 \pm 0.52 \mu\text{A}$ ), then the carbon cloth electrode in glucose-based medium after 96 h ( $21.6 \pm 0.67 \mu\text{A}$ ) and finally 3D-Printed BM in glucose-based broth after 24 h ( $21.3 \pm 0.78 \mu\text{A}$ ). The lowest recorded current of the conductive electrodes was recorded against the 3D-Printed BM electrode in glucose-based medium at 0 h ( $10.86 \pm 1.12 \mu\text{A}$ ). A significant result ( $P \leq 0.01$ ) was recorded at 120 h when comparing the carbon cloth electrodes in both glucose-based ( $21.27 \pm 0.37 \mu\text{A}$ ) and LB broth ( $25.73 \pm 0.52 \mu\text{A}$ ).

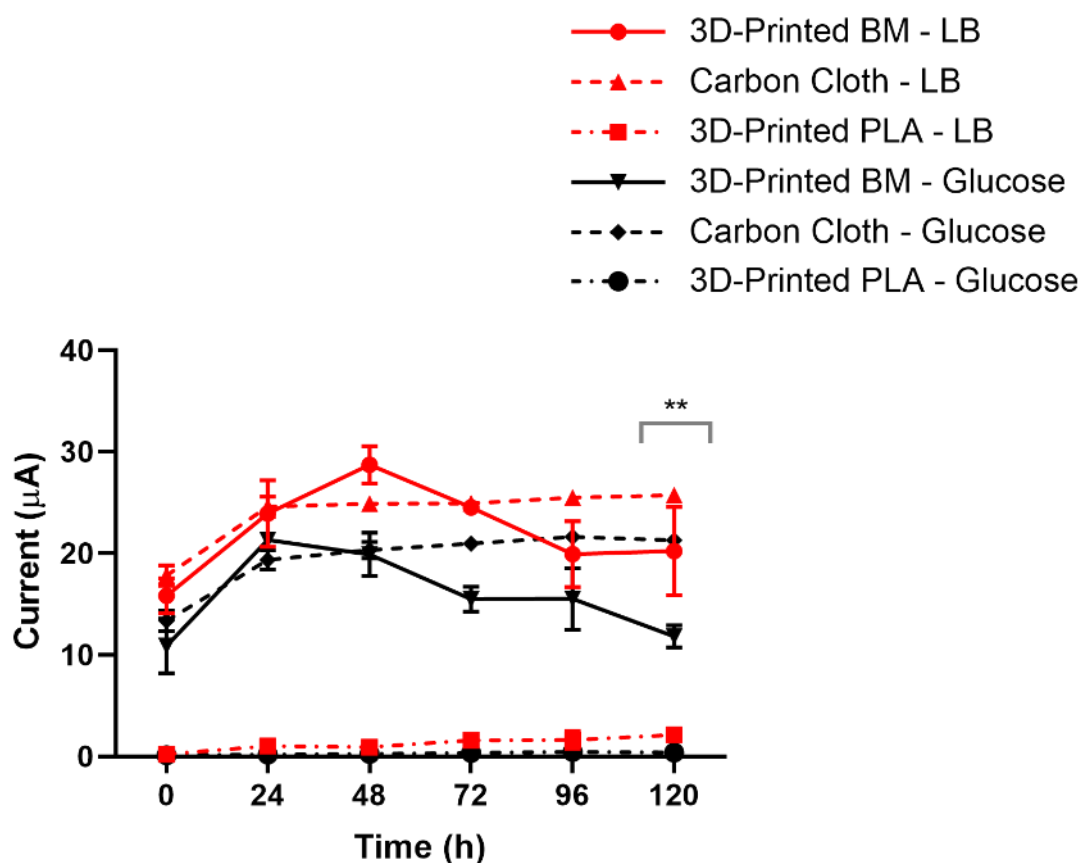


Figure 5.5. Current ( $\mu\text{A}$ ) calculated from the MFCs, which utilised three electrode types, 3D-Printed BM (8 wt.% graphene content), 3D-Printed PLA and carbon cloth utilising two types of media, LB and glucose-based broth ( $n = 3$ ). Where error bars are not visible they are of similar or smaller size compared to the symbol. For statistical analysis, only results between the 3D-Printed BM and carbon cloth electrodes were analysed, the grey solid line denoted the carbon cloth electrode in different media types (glucose-based and LB broth). Asterisks denote significance,  $**P \leq 0.01$ .

Current density was also calculated as this was more comparable to previously published studies, due to the standardised electrode size (Figure 5.6). The highest current density achieved was  $382.67 \pm 24.69 \mu\text{A m}^{-2}$ , which was calculated from the 3D-Printed BM electrode in LB broth after 48 h incubation with *P. aeruginosa* strain ATCC 9027. This was followed by the carbon cloth electrode in LB medium after 120 h ( $343.11 \pm 6.94 \mu\text{A m}^{-2}$ ) and the carbon cloth electrode in glucose-based medium after 96 h incubation with *P. aeruginosa* stain ATCC 9027 ( $288.00 \pm 6.84 \mu\text{A m}^{-2}$ ). Finally, the highest current density

recorded by the last of the conductive electrodes (3D-Printed BM electrode in glucose-based medium) was  $284.00 \pm 10.36 \mu\text{A m}^{-2}$  after 24 h. The 3D-Printed PLA electrodes demonstrated limited current density generation, due to the insulating properties of PLA, and thus the maximum current density recorded from the 3D-Printed PLA electrodes was  $28.00 \pm 6.84 \mu\text{A m}^{-2}$  after 120 h incubation in LB medium. At 120 h, carbon cloth in glucose-based broth produced a current density of  $283.56 \pm 4.90 \mu\text{A m}^{-2}$ , this was significantly different when compared with carbon cloth in LB broth at the same incubation period  $343.11 \pm 6.94 \mu\text{A m}^{-2}$ .

In summary, incubation of *P. aeruginosa* in the presence of the 3D-Printed PLA electrodes demonstrated relatively low current and current density production, due to their non-conductive nature. *Pseudomonas aeruginosa* in the presence of the 3D-Printed BM electrode produced the highest current and current density after 48 h incubation in anaerobic LB medium. No overall difference in current and current density was determined when *P. aeruginosa* was incubated over 120 h, in anaerobic LB broth and anaerobic glucose-based medium, in the presence of the 3D-Printed BM electrodes and carbon cloth electrodes. Therefore, these electrodes showed comparable current and current density generation in a MFC configuration.

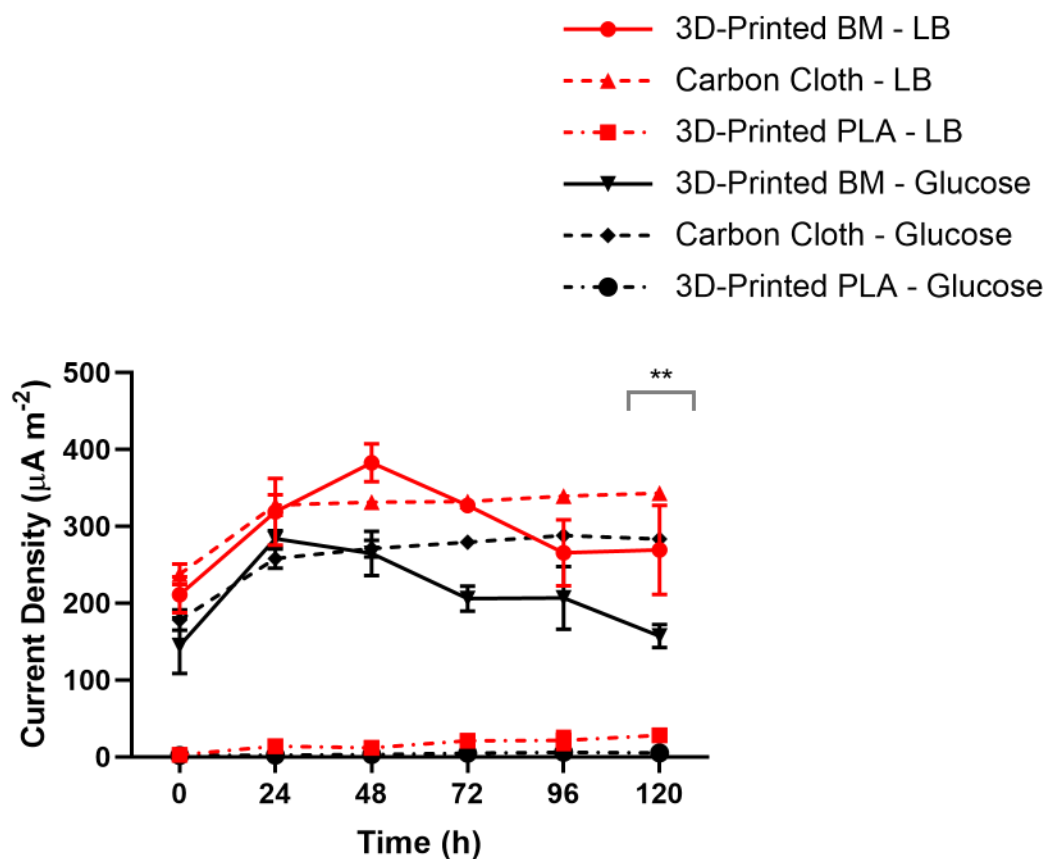


Figure 5.6. Current density ( $\mu\text{A m}^{-2}$ ) calculated from the MFCs, which utilised three electrode types, 3D-Printed BM (8 wt.% graphene content), 3D-Printed PLA and carbon cloth utilising two types of media, LB and glucose-based broth ( $n = 3$ ). Where error bars are not visible they are of similar or smaller size compared to the symbol. For the statistical analysis, only results between the 3D-Printed BM and carbon cloth electrodes were analysed, the grey solid line denoted the carbon cloth electrode in different media types (glucose-based and LB broth). Asterisks denote significance,  $**P \leq 0.01$ .

### 5.3.4 MFC Power and Power Density

The recorded cell potentials (V) were used to calculate power and power density from the MFCs at 0 h, 24 h, 48 h, 72 h, 96 h and 120 h from three electrode types (3D-Printed BM, 3D-Printed PLA and carbon cloth). Two different media types were trialed in the MFC experiments, anaerobic LB and anaerobic glucose-based broth (Figure 5.7 and Figure 5.8). Power was calculated (equation [4.3]) using the surface area of the electrodes ( $7.5 \text{ cm}^2$ ). The highest power generated, in the presence of *P. aeruginosa* strain ATCC 9027,

from the conductive electrodes was the 3D-Printed BM electrodes in LB broth after 48 h ( $8.31 \pm 1.10 \mu\text{W}$ ), followed by carbon cloth in glucose-based medium after 96 h ( $7.01 \pm 0.43 \mu\text{W}$ ), this was followed by carbon cloth in LB broth after 120 h incubation ( $6.63 \pm 0.27 \mu\text{W}$ ). Finally, 3D-Printed BM was  $4.55 \pm 0.34 \mu\text{W}$  and this was recorded after 24 h incubation in glucose-based broth. The 3D-Printed PLA electrodes in the presence of *P. aeruginosa* strain ATCC 9027 produced minimal amounts of power, due to their insulating nature. The maximum power output recorded from the 3D-Printed PLA electrodes was  $0.049 \pm 0.02 \mu\text{W}$  after 96 h incubation in glucose-based medium. The 3D-Printed BM electrode in glucose-based broth at 0 h incubation produced the lowest recorded power output from the conductive electrodes ( $1.33 \pm 0.64 \mu\text{W}$ ). Statistical analysis (two way ANOVA) was performed on the 3D-Printed BM electrodes and carbon cloth in both glucose-based and LB media. There was no statistical difference between the conductive electrodes and media types over the first 24 h, however at 48 h a significant result ( $P \leq 0.05$ ) was obtained, the 3D-Printed BM electrode in LB broth produced a power output of  $8.31 \pm 1.10 \mu\text{W}$  whilst the carbon cloth electrode in LB broth produced a power output of  $6.19 \pm 0.28 \mu\text{W}$ . However, after 72 h ( $P \leq 0.05$ ), 96 h ( $P \leq 0.05$ ) and 120 h ( $P \leq 0.01$ ) incubation, the carbon cloth electrode produced more power than the 3D-Printed BM electrode, when *P. aeruginosa* strain ATCC 9027 was incubated in anaerobic glucose-based broth. The 3D-Printed BM electrodes produced power outputs of  $2.42 \pm 0.36 \mu\text{W}$ ,  $2.59 \pm 0.99 \mu\text{W}$  and  $1.42 \pm 0.27 \mu\text{W}$  during 72 h, 96 h and 120 h incubation, respectively. The carbon cloth electrodes produced power outputs of  $6.60 \pm 0.34 \mu\text{W}$ ,  $7.01 \pm 0.34 \mu\text{W}$  and  $6.79 \pm 0.37 \mu\text{W}$  during 72 h, 96 h and 120 h incubation, respectively. At 120 h the carbon cloth electrode in LB medium produced a power output of  $6.63 \pm 0.28 \mu\text{W}$ , compared to the 3D-Printed BM electrode in glucose-based broth ( $1.42 \pm 0.27 \mu\text{W}$ ), this result was significant ( $P \leq 0.01$ ).

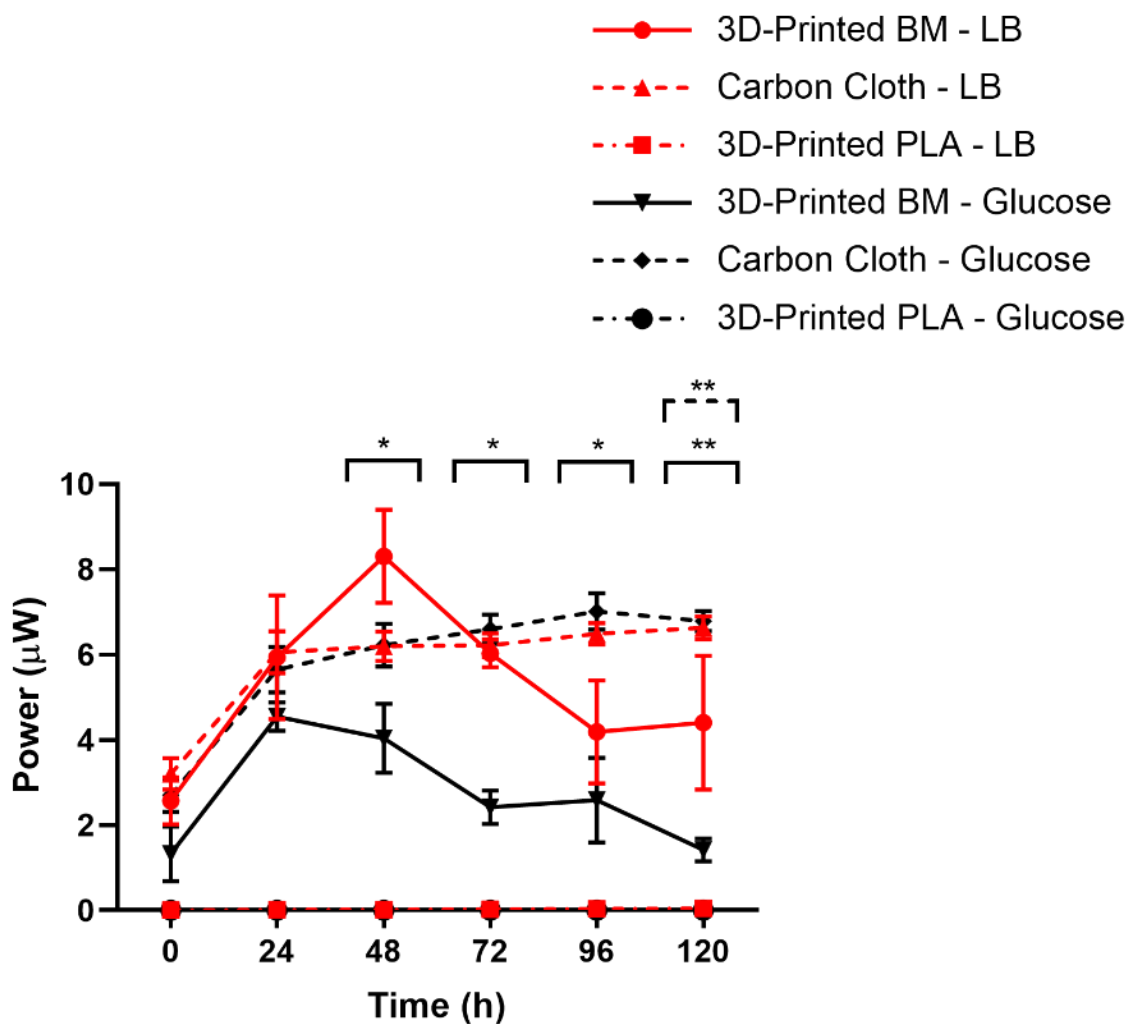


Figure 5.7. Power ( $\mu\text{W}$ ) calculated from the MFCs, which utilised three electrode types, 3D-Printed BM (8 wt.% graphene content), 3D-Printed PLA and carbon cloth utilising two types of media, LB and glucose-based broth ( $n = 3$ ). Where error bars are not visible they are of similar or smaller size compared to the symbol. For statistical analysis, only results between the 3D-Printed BM and carbon cloth electrodes were analysed, the black solid line denoted the different electrodes in glucose-based medium, whilst, the black dotted line denoted 3D-Printed BM in glucose-based against carbon cloth in LB broth. Asterisks denote significance,  $*P \leq 0.05$  and  $**P \leq 0.01$ .

Power density was calculated as this result was more comparable with the literature as the electrode size was standardised (Figure 5.8). In the presence of *P. aeruginosa* strain ATCC 9027, the 3D-Printed PLA electrodes provided low power density ( $< 1 \mu\text{W m}^{-2}$ ). The highest recorded power density from the 3D-Printed PLA electrodes was in anaerobic LB

broth ( $0.44 \pm 0.17 \mu\text{W m}^{-2}$ ) after 120 h. The 3D-Printed BM electrodes and the carbon cloth electrodes recorded an increase in power density until 24 h, this was followed by a stationary period and then a decrease in power density from 96 h. These results followed a similar trend to the bacterial viability that was calculated from bacterial samples taken at each incubation period (Figure 5.4). The highest recorded power density from the electrodes used in this study was  $110.74 \pm 14.63 \mu\text{W m}^{-2}$ , this was obtained from the 3D-Printed BM electrode in LB medium after 48 h incubation. The next highest power density attained was by the carbon cloth electrode in glucose-based medium after 96 h ( $93.49 \pm 5.17 \mu\text{W m}^{-2}$ ), following, the carbon cloth electrode in LB broth after 120 h ( $88.37 \pm 3.57 \mu\text{W m}^{-2}$ ) and finally the 3D-Printed BM electrode in glucose-based broth after 24 h incubation  $60.65 \pm 4.47 \mu\text{W m}^{-2}$ . Statistical analysis revealed at 48 h that the 3D-Printed BM electrode in LB broth ( $110.74 \pm 14.63 \mu\text{W m}^{-2}$ ) outperformed ( $P \leq 0.05$ ) the carbon cloth electrode in glucose-based broth ( $58.86 \pm 10.84 \mu\text{W m}^{-2}$ ). However, after 72 h ( $P \leq 0.05$ ), 96 h ( $P \leq 0.05$ ) and 120 h ( $P \leq 0.01$ ) incubation, the carbon cloth electrode gave a greater current density than the 3D-Printed BM electrode in glucose-based medium. The 3D-Printed BM electrodes produced power outputs of  $32.30 \pm 5.27 \mu\text{W m}^{-2}$ ,  $34.54 \pm 13.25 \mu\text{W m}^{-2}$  and  $18.90 \pm 13.25 \mu\text{W m}^{-2}$  during 72 h, 96 h and 120 h incubation in glucose-based medium, respectively. The carbon cloth electrodes produced power outputs of  $87.94 \pm 4.55 \mu\text{W m}^{-2}$ ,  $93.49 \pm 5.71 \mu\text{W m}^{-2}$  and  $90.51 \pm 3.10 \mu\text{W m}^{-2}$  during 72 h, 96 h and 120 h incubation in glucose-based medium, respectively. This indicated that carbon cloth in glucose-based broth was the more efficient electrode after 72 h incubation in a *P. aeruginosa* strain ATCC 9027 MFC. Interestingly however, the maximum power density obtained was from the 3D-Printed BM electrode in LB broth after 48 h incubation ( $110.74 \pm 14.63 \mu\text{W m}^{-2}$ ) (Figure 5.8, solid red line).

In summary, the non-conductive nature of the 3D-Printed PLA electrodes resulted in relatively low power and power density production following 120 h *P. aeruginosa* incubation in anaerobic LB and anaerobic glucose-based broth. The highest power and power density output obtained from the MFCs was when the 3D-Printed BM electrodes were used in anaerobic LB medium following 48 h *P. aeruginosa* incubation. There was no significant difference in power/power density between the 3D-Printed BM electrodes and carbon cloth electrodes when *P. aeruginosa* was incubated for 120 h in anaerobic LB broth. However, the carbon cloth electrodes outperformed the 3D-Printed BM electrodes,

producing statistically greater power and power densities when used in the presence of *P. aeruginosa* following 48 h, 72 h, 96 h and 120 h incubation in anaerobic glucose-based medium.

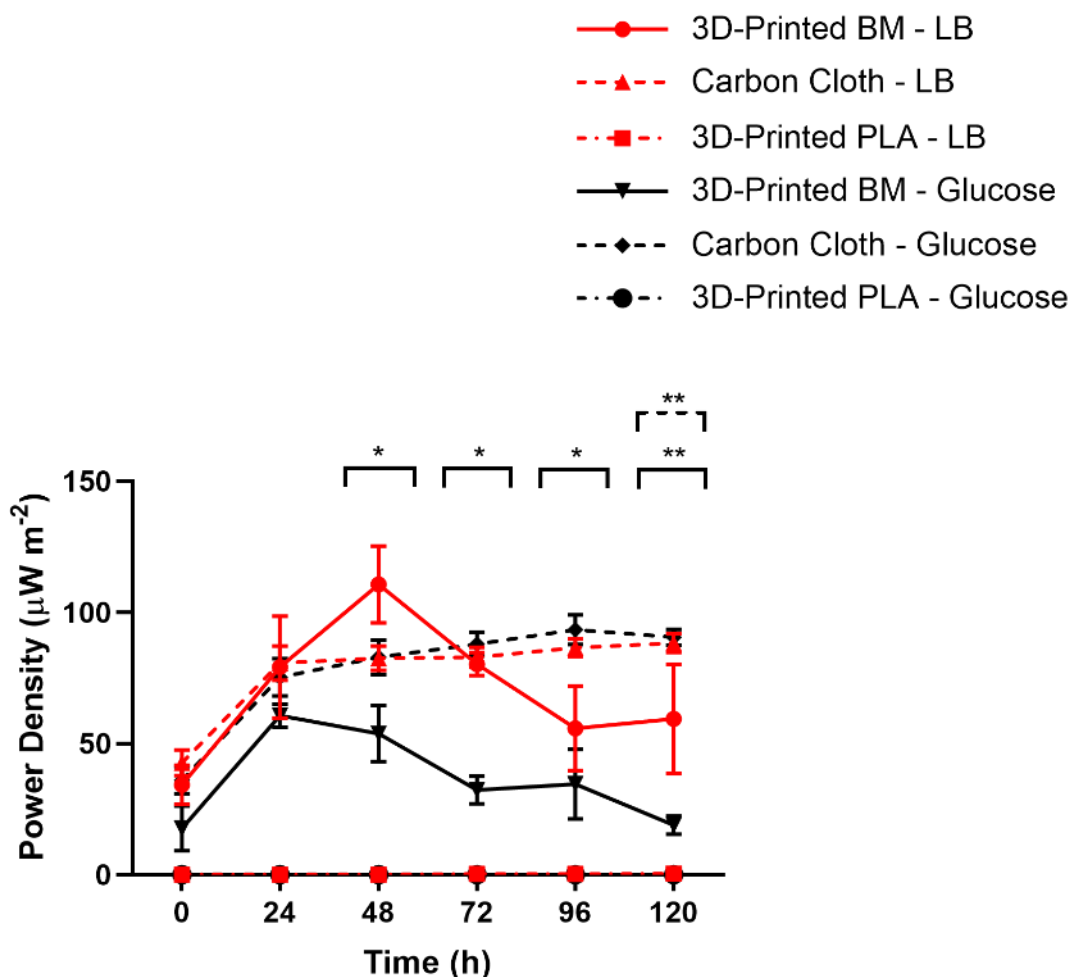


Figure 5.8. Power density ( $\mu\text{W m}^{-2}$ ) calculated from the *P. aeruginosa* strain ATCC 9027 MFCs, which utilised three electrode types, 3D-Printed BM (8 wt.% graphene content), 3D-Printed PLA and carbon cloth utilising two types of media, LB and glucose-based broth ( $n = 3$ ). Where error bars are not visible they are of similar or smaller size compared to the symbol. For statistical analysis, only results between the 3D-Printed BM and carbon cloth electrodes were analysed, the black solid line denoted the different electrodes in glucose-based medium, whilst, the black dotted line denoted 3D-Printed BM in glucose-based broth against carbon cloth in LB broth. Asterisks denote significance,  $*P \leq 0.05$  and  $**P \leq 0.01$ .

### 5.3.5 Bacterial Visualisation *via* Microscopy

Following 120 h incubation, the anode, cathode and the CEM surface, which was in contact the anolyte, were isolated and visualised *via* SEM (Figure 5.9) and confocal microscopy (Figure 5.10). Visualisation of *P. aeruginosa* on the surface of the 3D-Printed BM electrode in LB medium showed a sparsely populated surface (Figure 5.9.A) when compared with the 3D-Printed PLA, which showed denser bacterial attachment (Figure 5.9.D). The cathode (3D-Printed BM) in LB broth showed no bacterial attachment, indicating no bacterial transfer between the two chambers of the MFC (Figure 5.9.B). The surface of the CEM isolated from the anodic chamber showed an abundance of *P. aeruginosa* attachment, which was enhanced around surface defects (Figure 5.9.C). The 3D-Printed BM electrode in glucose-based medium (Figure 5.9.E) demonstrated a thin and evenly distributed bacterial attachment across the surface of the electrode. The 3D-Printed PLA electrode in glucose-based broth (Figure 5.9.F) demonstrated enhanced bacterial attachment around surface defects after 120 h of anaerobic incubation. This variation in bacterial attachment and adhesion may be due to the presence of graphene on the surface of the 3D-Printed BM electrodes and could have influenced the power outputs obtained from the *P. aeruginosa* MFCs.

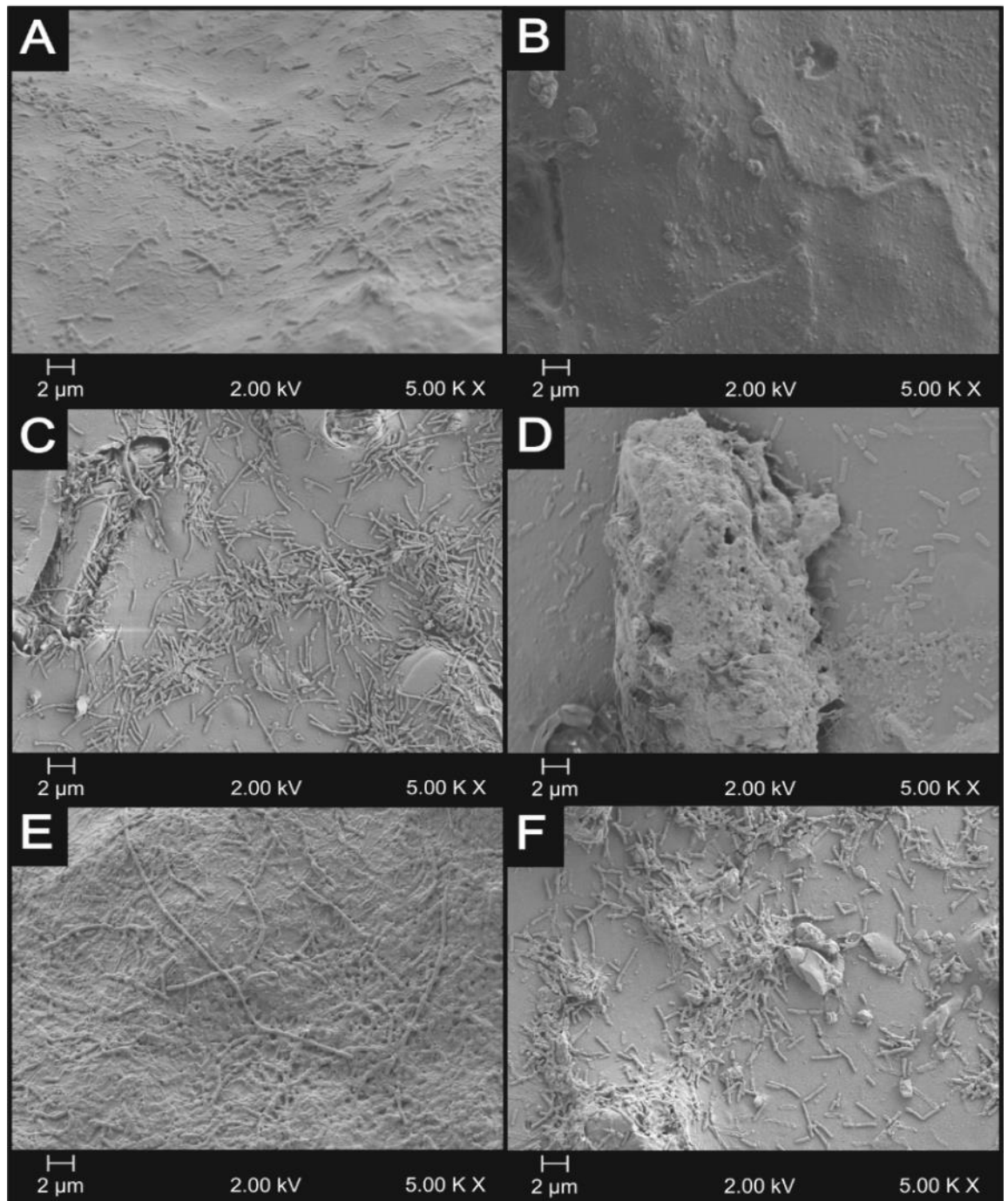


Figure 5.9. Following MFC experiments (120 h incubation), electrodes and CEM were isolated and *P. aeruginosa* strain ATCC 9027 was visualised using SEM (5.00 K × magnification). A) 3D-Printed BM anode incubation in LB broth, B) 3D-Printed BM cathode (no bacteria present), C) CEM in LB broth (surface from the anodic compartment visualised), D) 3D-Printed PLA anode incubation in LB broth, E) 3D-Printed BM anode incubation in glucose-based medium and F) CEM in glucose-based broth (surface from the anodic compartment visualised).

Confocal microscopy was conducted on the 3D-Printed BM electrode after 120 h incubation in LB medium. This sample was selected for confocal microscopy due to *P. aeruginosa* strain ATCC 9027 providing the highest power density when interacting with this electrode (Figure 5.10). Following MFC experimentation, the 3D-Printed BM anode and the surface of the CEM in contact with the anolyte were isolated and stained with acridine orange (as per 5.2.4). The surface of the CEM absorbed the acridine orange fluorescent dye, when visualised with confocal microscopy the sample over fluoresced, subsequently, these images were not included. The *P. aeruginosa* cells on the 3D-Printed BM electrode absorbed the acridine orange and were clearly visible using confocal microscopy (Figure 5.10). Similarly, to the results obtained *via* SEM, *P. aeruginosa* cells were dispersed, evenly across the surface (Figure 5.10.A). A cross sectional image was taken to demonstrate biofilm thickness across the surface (Figure 5.10.B). Results revealed that *P. aeruginosa* strain ATCC 9027 attachment to the 3D-Printed BM electrode was predominantly monolayer.

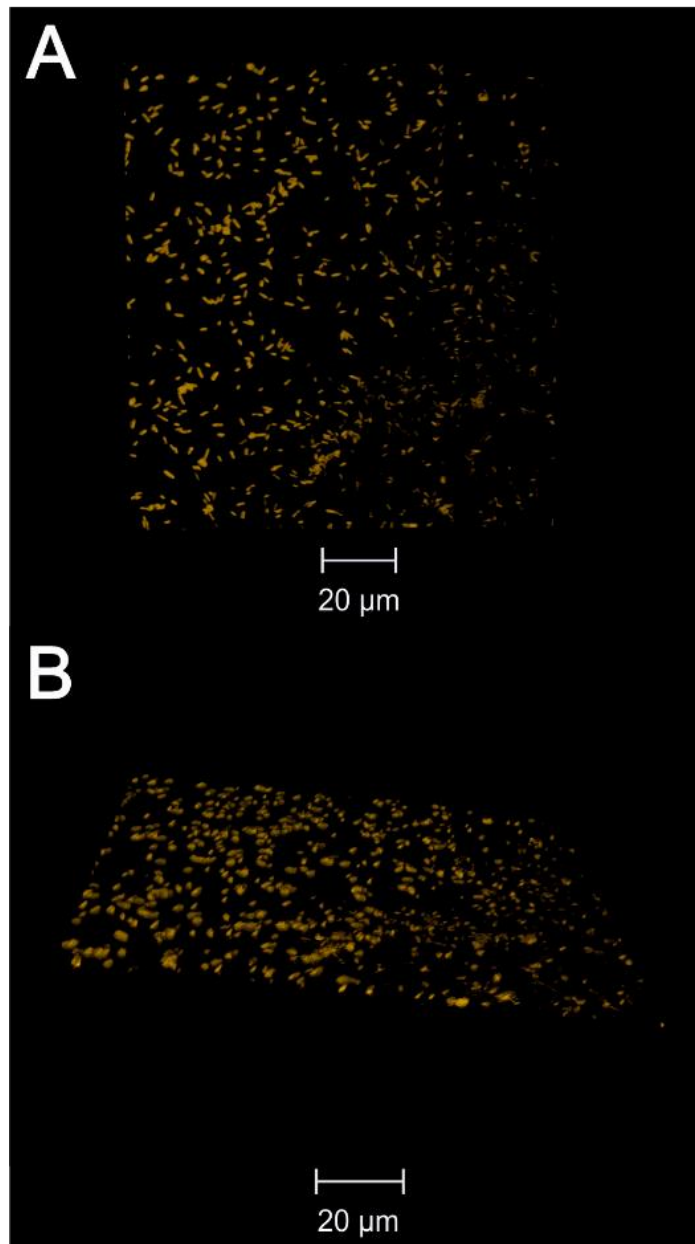


Figure 5.10. Following 120 h of *P. aeruginosa* strain ATCC 9027 incubation in anaerobic LB medium, bacterial attachment to the surface of the 3D-Printed BM anode was visualised using 0.1 % acridine orange (in 2 % v/v glacial acetic acid) *via* confocal microscopy. A) Horizontal view B) Cross sectional view.

## 5.4 Discussion

### 5.4.1 MFC Performance Analysis

In order to assess the performance of the novel 3D-Printed BM electrodes in a MFC, cell potential (CCV) was recorded every 24 h in a 120 h batch configuration. From the recorded cell potential, current, power and power density were calculated *via* Ohm's law. Under anaerobic conditions, two media types (glucose-based and LB broth) were trialled as the anolyte in order to determine if a change in metabolic pathway, resulted in an increase in MFC power outputs, due to an increase in either pyocyanin or electron generation (Glasser *et al.*, 2014; Kuroki *et al.*, 2014; Pierson and Pierson, 2010; Schreiber *et al.*, 2007). Pyocyanin can mediate electron transfer from *P. aeruginosa* to the anode surface in MFC configurations, due to its redox properties, therefore enhancing pyocyanin production by medium optimisation, could improve MFC power outputs (Dantas *et al.*, 2013; Schuster and Greenberg, 2006; Yong *et al.*, 2011; Zhang *et al.*, 2011a).

#### 5.4.1.1 Electrodes used in MFC Configurations

The 3D-Printed BM electrode is a composite of PLA and graphene (*ca.* 8 wt.%), therefore, 3D-Printed PLA (pure) was included as an appropriate control. At temperatures ranging from room temperature to 70 °C, PLA has excellent electrical insulation properties (Dichtl *et al.*, 2017; Oi *et al.*, 2011). However, at higher temperatures the insulation performance deteriorates due to its poor heat resistance (Dichtl *et al.*, 2017; Oi *et al.*, 2011). The 3D-Printed PLA electrodes in this study were unable to efficiently conduct electrons generated by *P. aeruginosa* and therefore it can be theorised that the low potential recorded was due to background noise of the data acquisition system and Arduino board (relay switch) set-up. However, the 3D-Printed BM electrode, which consisted of a PLA base material with 8 wt.% graphene, demonstrated excellent conductivity producing a maximum potential of  $287 \pm 18.52$  mV in LB medium after 48 h incubation. The filament used to fabricate the 3D-Printed BM electrodes, has previously been reported for use in electrochemical energy storage architectures due to its high electrical conductivity (Foster *et al.*, 2017). Carbon cloth is widely used as an electrode material in MFC configurations due to its high conductivity, good biocompatibility, large

surface area and relatively low cost (Choudhury *et al.*, 2017). Due to this, carbon cloth was used as a reference against which the novel 3D-Printed BM electrodes were judged.

#### **5.4.1.2 *Pseudomonas aeruginosa* viability in MFC configurations**

In parallel to the cell potential recording every 24 h, a sample of the anolyte was used to calculate cell viability. In all six parameters (three electrode materials in two types of media) tested, *P. aeruginosa* demonstrated typical growth kinetics, including the presence of a lag phase, exponential growth (log phase), stationary phase and then death phase. There was no significant difference ( $P > 0.05$ ) in bacterial viability between bacteria exposed to the 3D-Printed BM, 3D-Printed PLA, carbon cloth electrodes grown in both media types (LB or glucose-based broth). This indicated that the presence of graphene within the 3D-Printed BM structure did not have a detrimental effect on cell viability. The rather controversial antimicrobial activity of graphene is yet to be fully elucidated (Hegab *et al.*, 2016; Kumar *et al.*, 2019). However, it is believed potential mechanisms of action include membrane perturbation, reactive oxygen species (ROS) generation and cellular wrapping (restriction of membrane transport and growth) (Hegab *et al.*, 2016; Karahan *et al.*, 2018; Slate *et al.*, 2018b). No statistically significant detrimental antimicrobial activity was observed by the presence of 3D-Printed BM electrodes in the MFC.

#### **5.4.1.3 Power and Current Generation**

In order to standardise electrode size and therefore make the results more comparable to the literature, current density and power density were calculated. The MFC power outputs produced in this study were relatively low in relation to those obtained in the literature. This is likely due to a variety of factors including, the data acquisition configuration, such as the resistance value of the resistor (10,000  $\Omega$ ). The MFC physical configuration could also have contributed to this lower power output due to the application of a pure bacterial culture, the single source growth medium and potentially high internal resistance (Permana *et al.*, 2015). The internal resistance of a MFC is a function of the bacteria, electrolyte, electrode and membrane used and it is typically within the range of 100  $\Omega$  - 10 K  $\Omega$  (Zhang *et al.*, 2014). A high external resistance results in high cell voltages but low current, whilst a low external resistance produces low cell voltages but higher

currents (Aelterman *et al.*, 2008). Theoretically, the optimal external resistance for maximum power generation of a MFC should be similar to that of the internal resistance (Logan *et al.*, 2006).

Jayapriya and Ramamurthy (2014), reported a two-chambered MFC configuration where the anodic chamber was inoculated with *P. aeruginosa* in a glucose-based medium (20 g peptone, 13.3 g glucose, 10 g potassium sulphate, 1.4 g magnesium chloride, per litre (pH 7.0)) and potassium ferricyanide was used as the catholyte. When carbon cloth was applied as both the anode and cathode in this configuration, a power density of  $132.9 \mu\text{W m}^{-2}$  was recorded (Jayapriya and Ramamurthy, 2014). To obtain this output, the external resistor was fixed in the ohmic polarisation region, where the voltage decreased almost linearly with the current (Benziger *et al.*, 2006). The resistance in this region was due to electron transfer in the electrolytes, therefore, this resistance value was similar to that of the overall internal resistance of MFC the configuration (Benziger *et al.*, 2006). Another study used bacteria which were isolated from the rumen of a cow, and the culture was inoculated into the anodic chamber and a fungal species (*Nannochloropsis salina*) was used as a biocatalyst (Girme *et al.*, 2014). The resultant microbial desalination cell configuration had a salt removal efficiency of 100 % and produced a maximum power ( $35.73 \mu\text{W m}^{-2}$ ) and current ( $573 \mu\text{A m}^{-2}$ ) density using a fixed external resistor of  $2,500 \Omega$  (Girme *et al.*, 2014). Furthermore, You *et al.* (2017) fabricated a 3D-Printed anode which was incorporated into a MFC, where sewage sludge was used in the anodic chamber. This configuration produced a maximum power of  $43.00 \mu\text{W}$  (power density:  $511.91 \mu\text{W m}^{-2}$ ) with a fixed external resistor of  $3,000 \Omega$  (You *et al.*, 2017). The highest current and power densities generated in the current study were  $382.67 \pm 24.69 \mu\text{A m}^{-2}$  and  $110.74 \pm 14.63 \mu\text{W m}^{-2}$ , respectively. These values were calculated from *P. aeruginosa* strain ATCC 9027 in the presence of 3D-Printed BM electrodes after 48 h anaerobic incubation in LB medium, under a fixed external resistor of  $10,000 \Omega$ . The main restriction of MFCs for socio-economic applications is their low power densities. However, these results demonstrated that the novel utilisation of 3D-Printed electrodes coupled with the addition of graphene could enhance power outputs of MFC technologies (Lyon *et al.*, 2010). The application of 3D-Printing has many advantages over traditional manufacturing process as it can use a wide range of raw base materials including metals, ceramics and polymers and allows for the fabrication of almost infinitely

complex structures, with a high surface area to volume ration and a high level of sustainability (Foster *et al.*, 2017; Guo *et al.*, 2019).

#### 5.4.1.4 Varying Media Sources to Influence Metabolic Pathways

Electron transfer from exoelectrogens to the anode is a vital step in electricity generation in MFCs. This can be influenced by the type of the electron donors used and may result in differences in composition, structure and metabolism of exoelectrogens (He, 2012; Schroder, 2007; Vasylyv *et al.*, 2013). Lou *et al.* (2016) demonstrated the importance of microbial metabolism. In this instance, the MFC was inoculated with *S. oneidensis* (strain MR-1), and the electron donor used was isotopically-labelled formate and lactate (Luo *et al.*, 2016). Using <sup>13</sup>C tracer analysis, a synergistic effect from formate and lactate was observed (Luo *et al.*, 2016). Decoupled cell growth and electricity generation was revealed, lactate was mainly metabolised to support bacterial growth, whilst, formate was oxidised to produce higher levels of electricity generation (Luo *et al.*, 2016). Therefore, the utilisation of varying media sources can have an influence on the metabolic pathway used, if used in a MFC by exoelectrogenic bacteria this could potentially alter generated power outputs.

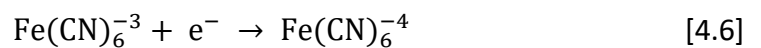
When glucose is used as the sole electron donor in a MFC configuration, the following anodic reaction takes place (Dalvi *et al.*, 2011) [4.5]:



Due to the complex nature of LB medium, it is difficult to assess the metabolic breakdown stages of this medium in a MFC configuration. Luria-Bertani medium is known to provide a high concentration of tryptone (an assortment of peptides formed by the digestion of casein). This provides both an amino acid source (*i.e.* arginine fermentation) and nitrogen which can both be used as energy substrates, under anaerobic conditions (Vander Wauven *et al.*, 1984; Schobert and Jahn, 2010; Schreiber *et al.*, 2006; Zumft, 1997). However, as *P. aeruginosa* has no known nitrogen fixing ability, denitrification was not feasible due to the lack of nitrate/nitrite available and therefore arginine fermentation was the more likely mechanism of anaerobic survival and proliferation (Yan *et al.*, 2008).

Growth in LB broth is also likely to be carbon limited due to its composition whilst, arginine deamination and decarboxylation of amino acids may potentially inhibit *P. aeruginosa* growth over time due to increased alkalinity (Murray *et al.*, 1965; Valli, 2018). However, the glucose-based medium utilised had an excess of carbon, which is likely to be fermented to the organic acids lactate and acetate, with the concomitant formation of ATP. Production of lactate and acetate could result in lowering of the pH, however, the medium was well buffered to compensate for this phenomenon (Glasser, Kern and Newman, 2014).

The catholyte used throughout this study consisted of potassium hexacyanoferrate, the following reaction takes place in the cathodic chamber (Tardast *et al.*, 2014) [4.6]:



Despite the utilisation of different growth media, glucose-based and LB broth as the anolyte in the MFC configuration, there was no significant difference in power density between *P. aeruginosa* grown in each media type. However, after 120 h incubation the current density calculated from carbon cloth in LB broth was significantly greater ( $P \leq 0.01$ ) than the carbon cloth in glucose-based broth over the same incubation period. The greatest power and current density was demonstrated with the 3D-Printed BM electrodes after 48 h incubation in LB broth. This highlighted the importance of careful consideration of the anolyte (with possible addition of supplements) and its effect on the bacterial metabolic pathway used could lead to enhanced power outputs from MFCs. The glucose-based medium demonstrated enhanced *P. aeruginosa* survival at 120 h, when compared to LB medium, when inoculated with the 3D-Printed BM electrodes. It could be hypothesised that the glucose-based medium had a greater reservoir of electrons available and is much better buffered and this could enhance *P. aeruginosa* viability when compared to LB broth. This resulted in an enhanced cell potential when the glucose-based medium was inoculated with *P. aeruginosa* and the carbon cloth (Figure 5.3). Although *P. aeruginosa* strain ATCC 9027 grown in anaerobic LB broth provided the maximum current and power density, the utilisation of the arginine fermentation resulted in a subtle improvement. This could be due to the batch configuration utilised throughout this study, as the nutrient source was limited over 120 h. In a continuous mode over a longer period of time, where the anolyte can be constantly replenished the difference in metabolic pathways may be more distinct. As

glucose metabolism and the formation of pyruvate (*via* the Entner-Doudoroff) promotes *P. aeruginosa* survival, but does not sustain growth, prolonged conditions would potentially exacerbate this phenomenon and enhance differences in MFC power outputs due to alternative metabolic pathways used by *P. aeruginosa* (Conway, 1992).

#### **5.4.2 *Pseudomonas aeruginosa* Visualisation**

Enhanced biofilm formation on the anode of a MFC promotes the generation of current (Qiao *et al.*, 2017). In regards to *P. aeruginosa* biofilms, this is due to the accumulation of phenazines on the electrode surface, which enhances electron transfer (Qiao *et al.*, 2017). *P. aeruginosa* strain ATCC 9027 attachment to the electrodes during MFC experimentation was visualised. Further research into the role of biofilms is required whilst some studies suggested that a thicker biofilm enhances power outputs in MFC configurations (Reguera *et al.*, 2006b), other studies proposed that thicker biofilms can be detrimental to power outputs, due to the production of non-conductive debris (Islam *et al.*, 2016). Biofilms produced under current generating conditions (*i.e.* closed circuit in a MFC) have been shown to be less thick than their non-MFC counterparts (Read *et al.*, 2010). In one MFC study, *P. aeruginosa* biofilms produced on the closed circuit anode and open circuit anode (control) were analysed after 72 h incubation and thickness values of  $30 \pm 3 \mu\text{m}$  and  $42 \pm 3 \mu\text{m}$ , respectively, were obtained (Read *et al.*, 2010). The authors suggested that the thinner biofilms produced under current generating conditions were likely due to a higher energetic gain of the soluble electron acceptors (Read *et al.*, 2010).

The anode, cathode and CEM were isolated after 120 h incubation and prepared for SEM in order to visualise *P. aeruginosa* attachment to the MFC components. When the 3D-Printed BM electrodes were utilised as the anode, in both LB and glucose-based broth, cell attachment observed was sparsely populated. The 3D-Printed PLA electrodes promoted *P. aeruginosa* attachment. The difference in cell viability between the 3D-Printed BM electrodes and the 3D-Printed PLA electrodes was insignificant. This indicated that there was no overall antimicrobial effect due to the presence of graphene. However, the graphene may have resulted in a reduction in bacterial attachment and therefore biofilm formation, due to modifications in surface energy and electrostatic interactions (Zurob *et al.*, 2019). The CEM surface that was isolated from the anodic chamber (in both LB and

glucose-based broth) revealed an abundance of *P. aeruginosa* cells, with greater cell attachment observed around surface defects.

Confocal microscopy was performed on the 3D-Printed BM electrode following 120 h incubation in a MFC configuration with LB medium. Acridine orange is a membrane permanent nucleic acid stain, it intercalates dsDNA and can also bind to both ssDNA and ssRNA *via* dye-base stacking (Harrison *et al.*, 2006). This results in a broad spectrum fluorescence when excited at 476 nm, due to the staining of all cells both live and dead (Bernas *et al.*, 2005; Harrison *et al.*, 2006). In regards to the 3D-Printed BM electrode in LB broth, the *P. aeruginosa* strain ATCC 9027 cells were clearly visible and largely consistent with the SEM images, as the attached cells were sparsely distributed. In order to visualise the thickness of the biofilm on the 3D-Printed BM electrodes a cross sectional image was obtained. After 120 h anaerobic incubation, the biofilm formed on the electrode surface was predominantly monolayer.

The reduction in bacterial attachment observed on the 3D-Printed BM electrodes could be due to the decline in cell viability observed after 120 h in LB medium. The production of non-conductive debris, such as certain polymeric substances and dead cells can isolate the electrochemically active biofilm from the surface of the anode, whilst in the case of 3D structures, this debris can potentially become entrapped resulting in a reduction of the total surface area available to facilitate electron transfer (Islam *et al.*, 2016). The reduction in available surface area results in an increase in internal resistance and a reduction in power generation (Blanchet *et al.*, 2016; Islam *et al.*, 2016; Sun *et al.*, 2016b). Biofilm dispersion can be induced by the depletion of nutrients in growth media, therefore it is possible that the biofilm was actively sloughed off due to the nutrient-limited conditions produced over time (120 h incubation) (Sauer *et al.*, 2004). In order to maximise the performance of MFCs, further, more intensive research into bacterial attachment and subsequent biofilm formation, the effect of the surface properties, biofilm maturation strategies and biofilm thickness control is required (Pasternak *et al.*, 2018).

Although multi-species biofilms for MFC application were not studied in this thesis, it is important to note that this approach has the potential to dramatically enhance MFC energy generation. In one study, *P. aeruginosa* was inoculated in co-culture with *Klebsiella variicola* (Islam *et al.*, 2018). When palm oil mill effluent was used as the anolyte in this MFC, the co-culture showed around three times higher current density than either

bacterium alone (Islam *et al.*, 2018). Analysis revealed that the fermentative metabolite (1,3-propanediol), which was produced by *K. variicola*, stimulated greater pyocyanin production from *P. aeruginosa* (Islam *et al.*, 2018).

## 5.5 Conclusion

The 3D-Printed BM electrodes (comprising 8 wt.% graphene) were utilised in a *P. aeruginosa* strain ATCC 9027 inoculated two-chambered MFC configuration, in order to assess power outputs. Batch mode MFCs were used and were incubated for 120 h in anaerobic LB or anaerobic glucose-based broth. The results demonstrated that the addition of graphene to the 3D-Printed PLA made this electrode conductive, whilst the low graphene percentage present (8 wt.%) did not have a statistical detrimental effect on cell viability. The 3D-Printed BM electrode produced the maximum power and current density after 48 h incubation in LB medium. There was no significant difference between the 3D-Printed BM electrode and the carbon cloth electrode (most widely utilised electrode material in MFC technologies) when used in the same medium over 120 h. Despite the utilisation of different growth media, glucose-based and LB broth, as the anolytes in the MFC configurations, there was no significant difference in power density. A difference in bacterial attachment was revealed as bacterial visualisation on the 3D-Printed BM electrodes showed *P. aeruginosa* cells were sparsely populated and predominantly monolayer, whilst, the 3D-Printed PLA electrodes showed much denser cell attachment which was more pronounced around surface defects. The results of this chapter suggest that the 3D-Printing of electrode materials for MFC application has promising potential to enhance power outputs. This could be one viable option to scale up power outputs to achieve the required industrial levels needed for applications, such as wastewater treatment.

## **Chapter 6 - Conclusion and Future Work**

## 6.1 Conclusion

In conclusion, this thesis highlighted the importance of optimising microbial fuel cells (MFCs) to maximise power outputs. This was achieved using both an electrochemical (*via* additive manufacturing and the addition of graphene to electrodes) and a microbiological perspective (by selection of a *P. aeruginosa* strain, which demonstrated enhanced exoelectrogenic properties).

Chapter One provided an overview of the current developments in MFC technology including, the fundamental basics of bioelectricity generation, limiting factors and optimisation techniques. Other research areas explored included the types of electrode materials used for MFC applications, with a particular focus on carbon-based electrodes (more specifically, graphene) and surface topography. Current known mechanisms of electron transfer were also discussed.

The electrochemical activity of graphite and graphene electrodes were optimised by varying individual lateral flake size of carbon paste electrodes. In the graphite-based electrodes a reduction in lateral flake size resulted in an improvement in electrochemical activity, due to an enhanced number of edge planes present on the electrode surface. Interestingly, for the graphene-based electrodes, which comprised the smallest range of lateral flake sizes, an improvement in electrochemical activity was observed until a distinct size (*ca.* 2  $\mu\text{m}$ ). No further improvement in electrochemical activity was seen beyond this size. This study demonstrated that graphene-based electrodes should comprise a reduced individual lateral flake size in order to enhance electrochemical activity, which could be applied to a plethora of applications in addition to MFCs.

The 3D-Printed BM electrodes (comprising PLA with 8 wt.% graphene; Black Magic), were then produced *via* additive manufacturing. These electrodes were topographically modified (by polishing) and were characterised using cyclic voltammetry, scanning electron microscopy (SEM) and Raman spectroscopy. Electrochemical analysis *via* cyclic voltammetry revealed little difference in electrode response, when comparing polished and non-polished electrodes, therefore the 3D-Printed BM electrodes were used without any post-modification techniques. The electrodeposition of  $\text{MoO}_2$  nanowires was applied to determine the electro-active sites of the 3D-Printed electrodes. The deposition of  $\text{MoO}_2$  was investigated using multifractal analysis (MFA), this novel method was conducted in

order to accurately quantify electro-active sites on the 3D-Printed electrodes. Finally, surface analysis was investigated using optical profilometry to determine surface topography. This revealed that each side of the 3D-Printed BM electrode consisted of varying topographies which was due to the fabrication processes. Physicochemistry measurements revealed that the underside of the 3D-Printed BM electrode was hydrophobic whilst the topside was hydrophilic *i.e.* the most polar, which could be beneficial for bacterial attachment, due to the presence of functional groups. When compared with the control 3D-Printed PLA electrodes, the 3D-Printed BM electrodes demonstrated an increased surface roughness, which correlated with the enhanced electron donating and accepting properties of these electrodes. Such properties could be beneficial for assisting with bacterial attachment, and therefore these electrodes were selected for use within the MFC configuration during this study.

Throughout Chapter Four, attention was directed to the selection and optimisation of *P. aeruginosa* for use within a MFC configuration. Several *P. aeruginosa* strains were selected and evaluated for the following phenotypic attributes, (1) high pyocyanin production, (2) good biofilm-forming attributes (*i.e.* attachment, growth and cell viability) and (3) high levels of cell motility. These parameters have previously been shown to enhance power outputs in *P. aeruginosa* MFCs. The results demonstrated that *P. aeruginosa* strain ATCC 9027 exhibited the most beneficial attributes to the parameters selected and subsequently, this strain was selected for further analysis. Growth kinetics of *P. aeruginosa* strain ATCC 9027 were evaluated using both LB and glucose-based media, combined with two preconditioning steps consisting of either aerobic starting cultures placed into anaerobic MFC conditions or cultures grown in fully anaerobic conditions. The choice of media and preconditioning steps were selected in order to evaluate the effect of different metabolic pathways on *P. aeruginosa* growth and pyocyanin production. Bacterial growth during incubation in these different conditions was determined by optical density measurements and bacterial viability quantification at defined incubation points of 0 h, 2 h, 4 h, 6 h, 24 h, 48 h, 72 h, 96 h and 120 h. Pyocyanin production was also quantified by LC-MS at each time-point. Interestingly, there was no correlation between pyocyanin accumulation within the culture and duration of bacterial growth. Overall, there was no significant difference between bacterial growth in any of the conditions tested. However, the most favourable conditions in terms of greatest bacterial cell viability was observed

when *P. aeruginosa* was cultured in LB broth in anaerobic conditions. *Pseudomonas aeruginosa* biofilm formation was then evaluated on the 3D-Printed BM electrodes, this was quantified using parameters which were representative of the MFC conditions utilised in chapter Five (anaerobic, LB broth, static, 37 °C, 120 h). Biofilm formation was significantly greater on the surface of the 3D-Printed BM electrodes when compared with the surface of 3D-Printed PLA electrode controls. Metabolic pathways such as amino acid fermentation and denitrification of *P. aeruginosa* were further explored using single nitrogen source Biolog MicroPlates™ assays in order to determine which amino acid(s) promoted bacterial growth under anaerobic conditions. Thymine resulted in the highest *P. aeruginosa* strain ATCC 9027 absorbance (this can be used as an indicator for bacterial growth), under anaerobic conditions, the addition of Thymine to a *P. aeruginosa* inoculated MFC could enhance bacterial proliferation.

Finally, the most electrochemically active 3D-Printed BM electrodes were used in a MFC configuration with *P. aeruginosa* strain ATCC 9027 to assess power outputs. The closed circuit voltage measurement (under 10,000  $\Omega$  external resistance) was used as the cell potential and was recorded at 0 h, 24 h, 48 h, 72 h, 96 h and 120 h. From the cell potential, power ( $\mu\text{W}$ ), power density ( $\mu\text{W m}^{-2}$ ), current ( $\mu\text{A}$ ) and current density ( $\mu\text{A m}^{-2}$ ) was determined using Ohms' law. Bacterial cell viability was determined at each time-point during the incubation period and biofilm formation on the anode was visualised after 120 h to determine biofilm thickness and morphology. The results confirmed that the 3D-Printed PLA electrodes were non-conductive. However, upon the addition of 8 wt.% graphene in the 3D-Printed BM electrodes, conductivity was significantly enhanced. Interestingly, the low graphene content did not have a significant detrimental effect on cell viability, in contrast to current research, which indicates that in certain circumstances graphene may possess antimicrobial properties. In this study, the 3D-Printed BM electrode recorded the maximum power and current density values of  $110.74 \pm 14.63 \mu\text{W m}^{-2}$  and  $382.67 \pm 24.69 \mu\text{A m}^{-2}$  respectively, after 48 h incubation in LB medium. There was no significant difference in recorded output between MFCs which used the 3D-Printed BM electrode, compared with the more widely used carbon cloth electrode type, when used in the same medium over 120 h. No significant difference in power density output from the MFC was observed when *P. aeruginosa* was grown in two different media types, LB and glucose-based broth. Following MFC experimentation, bacterial attachment to the

electrodes and the cationic exchange membrane (CEM) was visualised using SEM and confocal microscopy. *Pseudomonas aeruginosa* strain ATCC 9027 incubation over 120 h on the 3D-Printed BM electrodes resulted in sparsely populated, predominantly monolayer bacterial attachment, whilst, the 3D-Printed PLA electrodes showed much denser cell attachment, and biofilm formation around surface defects.

This thesis demonstrated the importance of bacterial selection for use within MFCs to ensure maximum power generation. In this study, 3D-Printing was applied to produce electrode materials, coupled with the addition of graphene to enhance conductivity. This could potentially play an integral role in enhancing power outputs of MFC configurations to the required industrial levels needed for potential applications, such as, for use in wastewater treatment systems. Ultimately, this could have a wider impact on society, leading to the future development of a greener, cost-effective, renewable energy source.

## 6.2 Key Findings

To summarise, the key results of this thesis were:

- In graphite and graphene paste electrodes, a reduction in the individual lateral flake sizes resulted in an improvement in electrochemical activity, until a limiting size (*ca.* 2  $\mu\text{m}$ ), beyond which no further improvement in electrochemical performance was observed.
- Additive manufacturing was used to fabricate 3D-Printed BM electrodes (comprising 8 wt.% graphene), which were sufficient to promote electrical conductivity. Electrodes were characterised to determine electrochemical activity, surface properties and biocompatibility. A novel technique was developed, which involved the electrodeposition of  $\text{MoO}_2$  nanowires, coupled with MFA analysis, to evaluate the electrochemical surface area of the electrodes.
- Of the strains evaluated, *P. aeruginosa* strain ATCC 9027 exhibited the most exoelectrogenic properties for MFC application.
- The presence of graphene in the 3D-Printed BM electrodes, enhanced biofilm formation without having a statistical detrimental effect on the *P. aeruginosa* viability.
- There was no significant difference in power outputs between the 3D-Printed BM electrodes and carbon cloth in two different media types (LB and glucose-based broth) over 120 h anaerobic *P. aeruginosa* strain ATCC 9027 incubation.
- The presence of *P. aeruginosa* strain ATCC 9027, 3D-Printed BM electrodes produced the maximum power and current densities of  $110.74 \pm 14.63 \mu\text{W m}^{-2}$  and  $382.67 \pm 24.69 \mu\text{A m}^{-2}$ , respectively, after 48 h incubation in LB medium.

## 6.3 Future Work

### 6.3.1 Electrode Characterisation and Optimisation

Alterations in lateral flake sizes of graphite and graphene electrodes could be further investigated. For example, a wider variety of carbonaceous flakes with a greater range in average lateral flake size could be evaluated, both, with the same probes utilised in this study and against other redox probes. This study could also be progressed by using the graphite and graphene paste electrodes as biosensors, *e.g.* to electrochemically sense for catecholamines such as dopamine (Sheng *et al.*, 2012; Vicentini *et al.*, 2015; Wang *et al.*, 2009). In theory, the results obtained from the proposed electrochemical sensing study should correlate with the results obtained in this study, *i.e.* a reduction in lateral flake size leads to an improvement in intensity/response of the analyte.

The novel electroactive quantification technique, which incorporated the electrodeposition of MoO<sub>2</sub> nanowires with MFA (Chapter Three) could be applied to a range of high surface carbonaceous electrodes in order to effectively quantify and determine the electroactive regions of other electrodes. This technique could also be potentially employed as a quality control method during the fabrication of 3D/porous electrodes. In order to promote bacterial attachment to the 3D-Printed electrodes, post fabrication techniques could be applied in order to enhance surface roughness. One issue with the electrodes utilised in this study was the topological variation between electrodes, even between those printed in the same batch. This issue could be resolved by flattening the electrodes using high pressure. However, this could remove topographical features, which may be detrimental to bacterial attachment.

### 6.3.2 Bacterial Strain Selection and Optimisation

Throughout Chapter Four, *P. aeruginosa* strain ATCC 9027 was evaluated and selected for MFC experimentation. In order to further this work, a wider range of *P. aeruginosa* strains could be screened for enhanced activity in MFC configurations. Furthermore, results from the sole nitrogen source Biolog MicroPlates™ assay could be taken further and the amino acids, which resulted in the greatest *P. aeruginosa* growth, could be supplemented into a growth medium. One such example would be the addition

of thymine to LB broth. Growth kinetics of *P. aeruginosa* under anaerobic conditions could then be studied alongside the quantification of pyocyanin, in order to determine if this supplemented medium enhanced growth, increased biofilm formation, increased cell motility and increased pyocyanin production. Optimisation of the aforementioned parameters could enhance power outputs of MFCs.

### 6.3.3 MFC Configuration Optimisation

Throughout Chapter Five, *P. aeruginosa* strain ATCC 9027 inoculated MFC configurations were developed and three electrode types, 3D-Printed BM (8 wt.% graphene content), 3D-Printed PLA and carbon cloth were trialled, to assess power outputs. This is the first instance 3D-Printing has been combined with the addition of graphene in a MFC configuration. Different media types, namely LB and glucose-based broth, were also trialled as the anolyte in order to determine if a change in nutrient source resulted in a change in metabolic pathway, leading to a difference in power outputs. A fixed external resistance of 10,000  $\Omega$  was used throughout the MFC experimentation. This study could be improved by calculating the internal resistance (*via* polarization curves) and using an external resistor that is similar to the internal resistance of the MFC (Fan *et al.*, 2012; Logan *et al.*, 2006). Other *P. aeruginosa* species could also be screened for parameters beneficial for MFC application and included in future studies.

In order to further this work, the 3D-Printed electrodes could be optimised further by increasing the graphene content, in order to enhance electrochemical activity (Lee and Oh, 2013). Another potential option to enhance the 3D-Printed electrodes electrochemical activity in a MFC configuration would be to reduce the lateral flake size of the comprising graphene present (as demonstrated in Chapter Two) (Slate *et al.*, 2018a).

As wastewater treatment is the most suitable industrial application of MFCs, wastewater effluent could be collected, sterilised and used as the anolyte in a *P. aeruginosa* based MFC in order to assess the efficacy of 3D-Printed BM electrodes in a nutrient-excessive medium (Jiang *et al.*, 2011). Furthermore, instead of using batch-mode MFC configurations (120 h incubation period), continuous flow culture conditions could be employed in order to assess power output of a MFC by growing *P. aeruginosa* over an extended period of time.

### 6.3.4 RNA Sequencing of MFC Samples

During MFC experimentation (Chapter Five), samples were collected from the anode at 24 h intervals and stored at – 80 °C. The amount of pyocyanin present in each sample could be quantified *via* LC-MS (as per Chapter Four). Molecular techniques such as RNA sequencing could be performed using these samples in order to characterise genome-wide transcriptional changes over the 120 h incubation period (Engelmann *et al.*, 2011). The changes in specific genes involved in *P. aeruginosa* attachment (*pilSR*), biofilm formation (*rhlR*), cell motility (*fliC*) and pyocyanin production (*phzM*) over time could be assessed (Brimer and Montie, 1998; Kilmury and Burrows, 2018; Mavrodi *et al.*, 2001; O’Loughlin *et al.*, 2013).

## 6.4 Publications

During this PhD programme the author successfully published the following articles:

**Slate, A. J.**, Shalamanova, L., Akhidime, I.D. and Whitehead, K.A. (2019). Rhenium and yttrium ions as antimicrobial agents against multidrug resistant *Klebsiella pneumoniae* and *Acinetobacter baumannii* biofilms. *Letters in Applied Microbiology*, 69, 168-174.

**Slate, A. J.**, Whitehead, K. A., Brownson, D. A. C. & Banks, C. E. (2019). Microbial fuel cells: An overview of current technology. *Renewable and Sustainable Energy Reviews*, 101, 60-81.

**Slate, A. J.**, Wickens, D., Wilson-Nieuwenhuis, J., Dempsey-Hibbert, N., West, G., Kelly, P., Verran, J., Banks, C. E. & Whitehead, K. A. (2018). The effects of blood conditioning films on the antimicrobial and retention properties of zirconium-nitride silver surfaces. *Colloids and Surfaces B: Biointerfaces*. 173, 303-311.

**Slate, A. J.**, Brownson, D. A. C., Dena, A. S. A., Smith, G. C., Whitehead, K. A. & Banks, C. E. (2018). Exploring the electrochemical performance of graphite and graphene paste electrodes composed of varying lateral flake sizes. *Physical Chemistry Chemical Physics*, 20, 20010-20022.

Mcbrearty, J., Barker, D., Damavandi, M., Wilson-Nieuwenhuis, J., Pilkington, L. I., Dempsey-Hibbert, N., **Slate, A. J.** & Whitehead, K. A. (2018). Antimicrobial synergy of cationic grafted poly(para-phenylene ethynylene) and poly(para-phenylene vinylene) compounds with UV or metal ions against *Enterococcus faecium*. *RSC Advances*, 8, 23433-23441.

**Slate, A. J.**, Karky, N. & Whitehead, K. A. (2018). Antimicrobial properties of Modified Graphene and other advanced 2D Material Coated Surfaces. *2D Materials*. CRC Press, 86-105.

**Slate, A. J.**, Wickens, D. J., El Mohtadi, M., Dempsey-Hibbert, N., Banks, C. E. & Whitehead, K. A. (2018). Antimicrobial activity of Ti-ZrN/Ag coatings for use in biomaterial applications. *Scientific Reports*, 8, 1497.

## Chapter 7 – References

- Aelterman, P., Rabaey, K., Pham, H. T., Boon, N. & Verstraete, W. (2006) 'Continuous Electricity Generation at High Voltages and Currents Using Stacked Microbial Fuel Cells', *Environmental Science & Technology*, 40(10), pp. 3388-94.
- Aelterman, P., Versichele, M., Marzorati, M., Boon, N. & Verstraete, W. (2008) 'Loading rate and external resistance control the electricity generation of microbial fuel cells with different three-dimensional anodes', *Bioresource Technology*, 99(18), pp. 8895-902.
- Ahn, Y., Hatzell, M. C., Zhang, F. & Logan, B. E. (2014) 'Different electrode configurations to optimize performance of multi-electrode microbial fuel cells for generating power or treating domestic wastewater', *Journal of Power Sources*, 249, pp. 440-5.
- Akande, S. O. (2015) 'Dimensional Accuracy and Surface Finish Optimization of Fused Deposition Modelling Parts using Desirability Function Analysis', *International Journal of Engineering Research & Technology*, 4(4), pp. 196-202.
- Ali, N., Anam, M., Yousaf, S., Maleeha, S. & Bangash, Z. (2017) 'Characterization of the Electric Current Generation Potential of the *Pseudomonas aeruginosa* Using Glucose, Fructose, and Sucrose in Double Chamber Microbial Fuel Cell', *Iranian Journal of Biotechnology*, 15(4), pp. 216-23.
- Allen, L., Dockrell, D. H., Pattery, T., Lee, D. G., Cornelis, P., Hellewell, P. G. & Whyte, M. K. (2005) 'Pyocyanin production by *Pseudomonas aeruginosa* induces neutrophil apoptosis and impairs neutrophil-mediated host defenses in vivo', *The Journal of Immunology*, 174(6), pp. 3643-9.
- Angelaalincy, M. J., Navanietha Krishnaraj, R., Shakambari, G., Kathiresan, S., Ashokkumar, B. & Varalakshmi, P. (2018) 'Biofilm Engineering Approaches for Improving the Performance of Microbial Fuel Cells and Bioelectrochemical systems', *Frontiers in Energy Research*, 6, pp. 63.
- Antonio, F. D. O. (2010) 'Wave energy utilization: A review of the technologies', *Renewable and Sustainable Energy Reviews*, 14(3), pp. 899-918.
- Anvarinejad, M., Japoni, A., Razaatpour, N., Mardaneh, J., Abbasi, P., Shahidi, M. A., Dehyadegari, M. A. & Alipour, E. (2014) 'Burn patients infected with metallo-beta-lactamase-producing *Pseudomonas aeruginosa*: Multidrug-resistant strains', *Archives of Trauma Research*, 3(2), pp. e18182
- Arai, H. (2011) 'Regulation and Function of Versatile Aerobic and Anaerobic Respiratory Metabolism in *Pseudomonas aeruginosa*', *Frontiers in Microbiology*, 2(103), pp. 1-13.
- Arai, H., Igarashi, Y. & Kodama, T. (1995) 'Expression of the nir and nor genes for denitrification of *Pseudomonas aeruginosa* requires a novel CRP/FNR-related transcriptional regulator, DNR, in addition to ANR', *FEBS letters*, 371(1), pp. 73-6.
- Arai, H., Kodama, T. & Igarashi, Y. (1997) 'Cascade regulation of the two CRP/FNR-related transcriptional regulators (ANR and DNR) and the denitrification enzymes in *Pseudomonas aeruginosa*', *Molecular Microbiology*, 25(6), pp. 1141-8.
- Arat, S., Bullerjahn, G. S. & Laubenbacher, R. (2015) 'A network biology approach to denitrification in *Pseudomonas aeruginosa*', *PLoS One*, 10(2), pp. e0118235.
- Araújo, E. A., Bernardes, P. C., Andrade, N. J., Fernandes, P. E. & Sá, J. P. N. (2009) 'Gibbs free energy of adhesion of *Bacillus cereus* isolated from dairy plants on different food processing surfaces evaluated by the hydrophobicity', *International journal of Food Science & Technology*, 44(12), pp. 2519-25.
- Baev, M. V., Baev, D., Radek, A. J. & Campbell, J. W. (2006) 'Growth of *Escherichia coli* MG1655 on LB medium: Monitoring utilization of amino acids, peptides, and

- nucleotides with transcriptional microarrays', *Applied Microbiology and Biotechnology*, 71(3), pp. 317–322.
- Badalamenti, J. P., Krajmalnik-Brown, R. & Torres, C. I. (2013) 'Generation of high current densities by pure cultures of anode-respiring *Geoalkalibacter* spp. under alkaline and saline conditions in microbial electrochemical cells', *MBio*, 4(3), pp. e00144-13.
- Balat, M. (2009) 'Microbial Fuel Cells as an Alternative Energy Option', *Energy Sources, Part A: Recovery, Utilization, and Environmental Effects*, 32(1), pp. 26-35.
- Banks, C. E., Compton, R. G., Fisher, A. C. & Henley, I. E. (2004) 'The transport limited currents at insonated electrodes', *Physical Chemistry Chemical Physics*, 6(12), pp. 3147-52.
- Banks, C. E., Davies, T. J., Wildgoose, G. G. & Compton, R. G. (2005) 'Electrocatalysis at graphite and carbon nanotube modified electrodes: edge-plane sites and tube ends are the reactive sites', *Chemical Communications*, (7), pp. 829-41.
- Banks, C. E., Foster, C. W. & Kadara, R. O. (2015). *Screen-Printing Electrochemical Architectures*: Springer.
- Baran, E. H. & Erbil, H. Y. (2019) 'Surface Modification of 3D Printed PLA Objects by Fused Deposition Modeling: A Review', *Colloids and Interfaces*, 3(2), pp. 43.
- Baranov, A., Bekhterev, A., Bobovich, Y. S. & Petrov, V. (1987) 'Interpretation of certain characteristics in Raman spectra of graphite and glassy carbon', *Optics and Spectroscopy*, 62(5), pp. 612-16.
- Baron, S. S. & Rowe, J. J. (1981) 'Antibiotic action of pyocyanin', *Antimicrobial Agents and Chemotherapy*, 20(6), pp. 814-20.
- Bédard, E., Prévost, M. & Déziel, E. (2016) '*Pseudomonas aeruginosa* in premise plumbing of large buildings', *MicrobiologyOpen*, 5(6), pp. 937-56.
- Bennetto, H. P., Stirling, J. L., Tanaka, K. & Vega, C. A. (1983) 'Anodic reactions in microbial fuel cells', *Biotechnology and Bioengineering*, 25(2), pp. 559-68.
- Benziger, J. B., Satterfield, M. B., Hogarth, W. H., Nehlsen, J. P. & Kevrekidis, I. G. (2006) 'The power performance curve for engineering analysis of fuel cells', *Journal of Power Sources*, 155(2), pp. 272-85.
- Bernas, T., Asem, E. K., Robinson, J. P., Cook, P. R. & Dobrucki, J. W. (2005) 'Confocal Fluorescence Imaging of Photosensitized DNA Denaturation in Cell Nuclei', *Photochemistry and Photobiology*, 81(4), pp. 960-9.
- Berndes, G., Hoogwijk, M. & van den Broek, R. (2003) 'The contribution of biomass in the future global energy supply: a review of 17 studies', *Biomass and Bioenergy*, 25(1), pp. 1-28.
- Bernheim, F. (1963) 'Factors which affect the size of the organisms and the optical density of suspensions of *Pseudomonas aeruginosa* and *Escherichia coli*', *Microbiology*, 30(1), pp. 53-8.
- Bernier, S. P., Ha, D-G., Khan, W., Merritt, J. H. & O'Toole, G. A. (2011) 'Modulation of *Pseudomonas aeruginosa* surface-associated group behaviors by individual amino acids through c-di-GMP signaling', *Research in Microbiology*, 162(7), pp. 680-8.
- Bian, B., Shi, D., Cai, X., Hu, M., Guo, Q., Zhang, C., Wang, Q., Sun, A. X. & Yang, J. (2018) '3D printed porous carbon anode for enhanced power generation in microbial fuel cell', *Nano Energy*, 44, pp. 174-80.
- Biffinger, J. C., Pietron, J., Ray, R., Little, B. & Ringeisen, B. R. (2007) 'A biofilm enhanced miniature microbial fuel cell using *Shewanella oneidensis* DSP10 and oxygen reduction cathodes', *Biosensors and Bioelectronics*, 22(8), pp. 1672-9.

- Binnerup, S. J. & Sørensen, J. (1993) 'Long-term oxidant deficiency in *Pseudomonas aeruginosa* PAO303 results in cells which are non-culturable under aerobic conditions', *FEMS Microbiology Ecology*, 13(1), pp. 79–84.
- Blanchet, E., Erable, B., De Solan, M-L. & Bergel, A. (2016) 'Two-dimensional carbon cloth and three-dimensional carbon felt perform similarly to form bioanode fed with food waste', *Electrochemistry Communications*, 66, pp. 38-41.
- Blanco, E., Foster, C. W., Cumba, L. R., do Carmo, D. R. & Banks, C. E. (2016) 'Can solvent induced surface modifications applied to screen-printed platforms enhance their electroanalytical performance?', *Analyst*, 141(9), pp. 2783-90.
- Bo, Y., Wang, W., Qi, J. & Huang, S. (2011) 'A DNA biosensor based on graphene paste electrode modified with Prussian blue and chitosan', *Analyst*, 136(9), pp. 1946-51.
- Boon, N., Aelterman, P., Clauwaert, P., De Schampelaire, L., Vanhaecke, L., De Maeyer, K., Höfte, M., Verstraete, W. & Rabaey, K. (2008) 'Metabolites produced by *Pseudomonas* sp. enable a Gram-positive bacterium to achieve extracellular electron transfer', *Applied Microbiology and Biotechnology*, 77(5), pp. 1119-29.
- Borecka-Melkusova, S. & Bujdakova, H. (2008) 'Variation of cell surface hydrophobicity and biofilm formation among genotypes of *Candida albicans* and *Candida dubliniensis* under antifungal treatment', *Canadian Journal of Microbiology*, 54(9), pp. 718-24.
- Bosire, E. M. & Rosenbaum, M. A. (2017) 'Electrochemical potential influences phenazine production, electron transfer and consequently electric current generation by *Pseudomonas aeruginosa*', *Frontiers in Microbiology*, 8, pp. 892.
- Bosire, E. M., Blank, L. M. & Rosenbaum, M. A. (2016) 'Strain-and substrate-dependent redox mediator and electricity production by *Pseudomonas aeruginosa*', *Applied and Environmental Microbiology*, 82(16), pp. 5026-38.
- Bracci, R., Maccaroni, E. & Cascinu, S. (2013) 'Bioresorbable airway splint created with a three-dimensional printer', *New England Journal of Medicine*, 368(21), pp. 2043-5.
- Brimer, C. D. & Montie, T. (1998) 'Cloning and Comparison of fliC Genes and Identification of Glycosylation in the Flagellin of *Pseudomonas aeruginosa* a-Type Strains', *Journal of Bacteriology*, 180(12), pp. 3209-17.
- Brint, J. M. & Ohman, D. E. (1995) 'Synthesis of multiple exoproducts in *Pseudomonas aeruginosa* is under the control of RhIR-RhII, another set of regulators in strain PAO1 with homology to the autoinducer-responsive LuxR-LuxI family', *Journal of Bacteriology*, 177(24), pp. 7155-63.
- Brownson, D. A. C. & Banks, C. E. (2014). *The handbook of graphene electrochemistry*: Springer.
- Brownson, D. A. C., Figueiredo-Filho, L. C. S., Ji, X., Gomez-Mingot, M., Iniesta, J., Fatibello-Filho, O., Kampouris, D. K. & Banks, C. E. (2013) 'Freestanding three-dimensional graphene foam gives rise to beneficial electrochemical signatures within non-aqueous media', *Journal of Materials Chemistry A*, 1(19), pp. 5962-72.
- Brownson, D. A. C., Gorbachev, R. V., Haigh, S. J. & Banks, C. E. (2012a) 'CVD graphene vs. highly ordered pyrolytic graphite for use in electroanalytical sensing', *Analyst*, 137(4), pp. 833-9.
- Brownson, D. A. C., Kampouris, D. K. & Banks, C. E. (2012b) 'Graphene electrochemistry: fundamental concepts through to prominent applications', *Chemical Society Reviews*, 41(21), pp. 6944-76.

- Brownson, D. A. C., Kelly, P. J. & Banks, C. E. (2015) 'In situ electrochemical characterisation of graphene and various carbon-based electrode materials: an internal standard approach', *RSC Advances*, 5(47), pp. 37281-6.
- Brownson, D. A. C., Munro, L. J., Kampouris, D. K. & Banks, C. E. (2011) 'Electrochemistry of graphene: not such a beneficial electrode material?', *RSC Advances*, 1(6), pp. 978-88.
- Brownson, D. A. C., Varey, S. A., Hussain, F., Haigh, S. J. & Banks, C. E. (2014) 'Electrochemical properties of CVD grown pristine graphene: monolayer-vs. quasi-graphene', *Nanoscale*, 6(3), pp. 1607-21.
- Bujdáková, H., Didiášová, M., Drahovská, H. & Černáková, L. (2013) 'Role of cell surface hydrophobicity in *Candida albicans* biofilm', *Open Life Sciences*, 8(3), pp. 259-62.
- Butscher, A., Bohner, M., Hofmann, S., Gauckler, L. & Müller, R. (2011) 'Structural and material approaches to bone tissue engineering in powder-based three-dimensional printing', *Acta Biomaterialia*, 7(3), pp. 907-20.
- Calignano, F., Tommasi, T., Manfredi, D. & Chiolerio, A. (2015) 'Additive manufacturing of a microbial fuel cell—a detailed study', *Scientific Reports*, 5, pp. 17373.
- Campbell, J. J. & Stokes, F. N. (1951) 'Tricarboxylic acid cycle in *Pseudomonas aeruginosa*', *Journal of Biological Chemistry*, 190(2), pp. 853-8.
- Canfield, J., Goldner, B. & Lutwack, R. (1963) 'NASA Technical report', *Magna Corporation, Anaheim, California*, pp. 63.
- Cao, Y., Mu, H., Liu, W., Zhang, R., Guo, J., Xian, M. & Liu, H. (2019) 'Electricigens in the anode of microbial fuel cells: pure cultures versus mixed communities', *Microbial Cell Factories*, 18(39), pp. 1-14.
- Capodaglio, A. G., Molognoni, D., Dallago, E., Liberale, A., Cella, R., Longoni, P. & Pantaleoni, L. (2013) 'Microbial Fuel Cells for Direct Electrical Energy Recovery from Urban Wastewaters', *The Scientific World Journal*, 2013, pp. 634738-46.
- Casiraghi, C., Hartschuh, A., Qian, H., Piskanec, S., Georgi, C., Fasoli, A., Novoselov, K., Basko, D. & Ferrari, A. (2009) 'Raman spectroscopy of graphene edges', *Nano letters*, 9(4), pp. 1433-41.
- Chae, K-J., Choi, M-J., Lee, J-W., Kim, K-Y. & Kim, I. S. (2009) 'Effect of different substrates on the performance, bacterial diversity, and bacterial viability in microbial fuel cells', *Bioresource Technology*, 100(14), pp. 3518-25.
- Chambers, M. C., Maclean, B., Burke, R., Amodei, D., Ruderman, D. L., Neumann, S., Gatto, L., Fischer, B., Pratt, B., Egertson, J., Hoff, K., Kessner, D., Tasman, N., Shulman, N., Frewen, B., Baker, T. A., Brusniak, M-Y., Paulse, C., Creasy, D., Flashner, L., Kani, K., Moulding, C., Seymour, S. L., Nuwaysir, L. M., Lefebvre, B., Kuhlmann, F., Roark, J., Rainer, P., Detlev, S., Hemenway, T., Huhmer, A., Langridge, J., Connolly, B., Chadick, T., Holly, K., Eckels, J., Deutsch, E. W., Moritz, R. L., Katz, J. E., Agus, D. B., MacCoss, M., Tabb, D. L. & Mallick, P. (2012) 'A cross-platform toolkit for mass spectrometry and proteomics', *Nature Biotechnology*, 30(10), pp. 918-20.
- Chang, S-H., Liou, J-S., Liu, J-L., Chiu, Y-F., Xu, C-H., Chen, B-Y. & Chen, J-Z. (2016) 'Feasibility study of surface-modified carbon cloth electrodes using atmospheric pressure plasma jets for microbial fuel cells', *Journal of Power Sources*, 336, pp. 99-106.
- Chaudhuri, S. K. & Lovley, D. R. (2003) 'Electricity generation by direct oxidation of glucose in mediatorless microbial fuel cells', *Nature Biotechnology*, 21(10), pp. 1229-32.
- Chavant, P., Martinie, B., Meylheuc, T., Bellon-Fontaine, M-N. & Hebraud, M. (2002) '*Listeria monocytogenes* LO28: surface physicochemical properties and ability to

- form biofilms at different temperatures and growth phases', *Applied and Environmental Microbiology*, 68(2), pp. 728-37.
- Cheng, H-Y., Liang, B., Mu, Y., Cui, M-H., Li, K., Wu, W-M. & Wang, A-J. (2015) 'Stimulation of oxygen to bioanode for energy recovery from recalcitrant organic matter aniline in microbial fuel cells (MFCs)', *Water Research*, 81, pp. 72-83.
- Cheng, Y., Feng, G. & Moraru, C. I. (2019) 'Micro-and Nanotopography Sensitive Bacterial Attachment Mechanisms: A Review', *Frontiers in microbiology*, 10, pp. 191.
- Childers, S. E., Ciuffo, S. & Lovley, D. R. (2002) '*Geobacter metallireducens* accesses insoluble Fe(III) oxide by chemotaxis', *Nature*, 416(6882), pp. 767-9.
- Choi, G., Hassett, D. J. & Choi, S. (2015) 'A paper-based microbial fuel cell array for rapid and high-throughput screening of electricity-producing bacteria', *Analyst*, 140(12), pp. 4277-83.
- Choi, S. & Chae, J. (2012) 'An array of microliter-sized microbial fuel cells generating 100  $\mu$ W of power', *Sensors and Actuators A: Physical*, 177, pp. 10-5.
- Chong, H. & Li, Q. (2017) 'Microbial production of rhamnolipids: opportunities, challenges and strategies', *Microbial Cell Factories*, 16(137), pp. 1-12.
- Choudhury, P., Prasad Uday, U. S., Bandyopadhyay, T. K., Ray, R. N. & Bhunia, B. (2017) 'Performance improvement of microbial fuel cell (MFC) using suitable electrode and Bioengineered organisms: A review', *Bioengineered*, 8(5), pp. 471-87.
- Cohen, B. (1931) 'The bacterial culture as an electrical half-cell', *Journal of Bacteriology*, 21(1), pp. 18-9.
- Conrad, J. C., Gibiansky, M. L., Jin, F., Gordon, V. D., Motto, D. A., Mathewson, M. A., Stopka, W. G., Zelasko, D. C., Shrout, J. D. & Wong, G. C. L. (2011) 'Flagella and Pili-Mediated Near-Surface Single-Cell Motility Mechanisms in *P. aeruginosa*', *Biophysical Journal*, 100(7), pp. 1608-16.
- Conway, T. (1992) 'The Entner-Doudoroff pathway: history, physiology and molecular biology', *FEMS Microbiology Reviews*, 9(1), pp. 1-27.
- Crawford, R. J., Webb, H. K., Truong, V. K., Hasan, J. & Ivanova, E. P. (2012) 'Surface topographical factors influencing bacterial attachment', *Advances in Colloid and Interface Science*, 179-182, pp. 142-9.
- Cumba, L. R., Foster, C. W., Brownson, D. A. C., Smith, J. P., Iniesta, J., Thakur, B., do Carmo, D. R. & Banks, C. E. (2016) 'Can the mechanical activation (polishing) of screen-printed electrodes enhance their electroanalytical response?', *Analyst*, 141(9), pp. 2791-9.
- Daeschel, M. A. & McGuire, J. (1998) 'Interrelationships between protein surface adsorption and bacterial adhesion', *Biotechnology and Genetic Engineering Reviews*, 15(1), pp. 413-38.
- Dalvi, A. D., Mohandas, N., Shinde, O. A. & Kininge, P. T. (2011) 'Microbial fuel cell for production of bioelectricity from whey and biological waste treatment', *International journal of Advanced Biotechnology and Research*, 2(2), pp. 263-8.
- Dantas, L. C. D. M., Silva-Neto, J. P. D., Dantas, T. S., Naves, L. Z., das Neves, F. D. & Da Mota, A. S. (2016) 'Bacterial adhesion and surface roughness for different clinical techniques for acrylic polymethyl methacrylate', *International Journal of Dentistry*, 2016, pp. 1-6.
- Dantas, P., Peres, S., Campos-Takaki, G. & La Rotta, C. (2013) 'Utilization of raw glycerol for pyocyanin production from *Pseudomonas aeruginosa* in half-microbial fuel cells:

- evaluation of two electrochemical approaches', *Journal of the Electrochemical Society*, 160(10), pp. 142-8.
- Dashty, M. (2013) 'A quick look at biochemistry: Carbohydrate metabolism', *Clinical Biochemistry*, 46(15), pp. 1339-52.
- Davies, T. J., Hyde, M. E. & Compton, R. G. (2005) 'Nanotrench arrays reveal insight into graphite electrochemistry', *Angewandte Chemie*, 117(32), pp. 5251-6.
- Dena, A. S. A. & Hassan, W. M. (2016) 'Experimental and quantum mechanical studies on the ion-pair of levocetirizine and bromocresol green in aqueous solutions', *Spectrochimica Acta Part A: Molecular and Biomolecular Spectroscopy*, 163, pp. 108-14.
- Deng, L., Li, F., Zhou, S., Huang, D. & Ni, J. (2010a) 'A study of electron-shuttle mechanism in *Klebsiella pneumoniae* based-microbial fuel cells', *Chinese Science Bulletin*, 55(1), pp. 99-104.
- Deng, Q., Li, X., Zuo, J., Ling, A. & Logan, B. E. (2010b) 'Power generation using an activated carbon fiber felt cathode in an upflow microbial fuel cell', *Journal of Power Sources*, 195(4), pp. 1130-5.
- Dennington, R., Keith, T. & Millam, J. (2009). *GaussView Version 05*. Semichem Inc., Shawnee Mission.
- Deptula, A., Mikucka, A. & Gospodarek, E. (2004) 'Effect of growth conditions on cell surface hydrophobicity of multiresistant *Pseudomonas aeruginosa* strains', *Medycyna Doświadczalna i Mikrobiologia*, 56(4), pp. 359-64.
- Dichtl, C., Sippel, P. & Krohns, S. (2017) 'Dielectric properties of 3D printed polylactic acid', *Advances in Materials Science and Engineering*, 2017, pp. 1-10.
- Dietrich, L. E., Price-Whelan, A., Petersen, A., Whiteley, M. & Newman, D. K. (2006) 'The phenazine pyocyanin is a terminal signalling factor in the quorum sensing network of *Pseudomonas aeruginosa*', *Molecular Microbiology*, 61(5), pp. 1308-21.
- Diggle, S. P., Winzer, K., Chhabra, S. R., Worrall, K. E., Cámara, M. & Williams, P. (2003) 'The *Pseudomonas aeruginosa* quinolone signal molecule overcomes the cell density-dependency of the quorum sensing hierarchy, regulates rhl-dependent genes at the onset of stationary phase and can be produced in the absence of LasR', *Molecular Microbiology*, 50(1), pp. 29-43.
- Diggle, S. P., Winzer, K., Lazdunski, A., Williams, P. & Cámara, M. (2002) 'Advancing the quorum in *Pseudomonas aeruginosa*: MvaT and the regulation of N-acylhomoserine lactone production and virulence gene expression', *Journal of Bacteriology*, 184(10), pp. 2576-86.
- Ditchfield, R. H. (1974) 'Self-consistent perturbation theory of diamagnetism: I. A gauge-invariant LCAO method for NMR chemical shifts', *Molecular Physics*, 27(4), pp. 789-807.
- Ditchfield, R. H., W. J. Pople, J. A. (1971) 'Self-Consistent Molecular-Orbital Methods. IX. An Extended Gaussian-Type Basis for Molecular-Orbital Studies of Organic Molecules', *The Journal of Chemical Physics*, 54(2), pp. 724-28.
- Dobbs, K. D. & Hehre, W. (1986) 'Molecular orbital theory of the properties of inorganic and organometallic compounds 4. Extended basis sets for third-and fourth-row, main-group elements', *Journal of Computational Chemistry*, 7(3), pp. 359-78.
- Dobbs, K. D. & Hehre, W. (1987a) 'Molecular orbital theory of the properties of inorganic and organometallic compounds 5. Extended basis sets for first-row transition metals', *Journal of Computational Chemistry*, 8(6), pp. 861-79.

- Dobbs, K. D. & Hehre, W. (1987b) 'Molecular orbital theory of the properties of inorganic and organometallic compounds. 6. Extended basis sets for second-row transition metals', *Journal of Computational Chemistry*, 8(6), pp. 880-93.
- Dong, Y., Feng, Y., Qu, Y., Du, Y., Zhou, X. & Liu, J. (2015) 'A combined system of microbial fuel cell and intermittently aerated biological filter for energy self-sufficient wastewater treatment', *Scientific Reports*, 5, pp. 18070.
- Dotto, G., Pinto, L., Hachicha, M. & Knani, S. (2015) 'New physicochemical interpretations for the adsorption of food dyes on chitosan films using statistical physics treatment', *Food Chemistry*, 171, pp. 1-7.
- Du, Z., Li, H. & Gu, T. (2007) 'A state of the art review on microbial fuel cells: A promising technology for wastewater treatment and bioenergy', *Biotechnology Advances*, 25(5), pp. 464-82.
- Dumas, C., Mollica, A., Féron, D., Basséguy, R., Etcheverry, L. & Bergel, A. (2007) 'Marine microbial fuel cell: use of stainless steel electrodes as anode and cathode materials', *Electrochimica Acta*, 53(2), pp. 468-73.
- Dunne, W. M., Jr. (2002) 'Bacterial adhesion: seen any good biofilms lately?', *Clinical Microbiology Reviews*, 15(2), pp. 155-66.
- Eatemadi, A., Daraee, H., Karimkhanloo, H., Kouhi, M., Zarghami, N., Akbarzadeh, A., Abasi, M., Hanifehpour, Y. & Joo, S. W. (2014) 'Carbon nanotubes: properties, synthesis, purification, and medical applications', *Nanoscale Research Letters*, 9(393), pp. 1-13.
- El-Fouly, M. Z., Sharaf, A. M., Shahin, A. A. M., El-Bialy, H. A. & Omara, A. M. A. (2015) 'Biosynthesis of pyocyanin pigment by *Pseudomonas aeruginosa*', *Journal of Radiation Research and Applied Sciences*, 8(1), pp. 36-48.
- Elgrishi, N., Rountree, K. J., McCarthy, B. D., Rountree, E. S., Eisenhart, T. T. & Dempsey, J. L. (2018) 'A Practical Beginner's Guide to Cyclic Voltammetry', *Journal of Chemical Education*, 95(2), pp. 197-206.
- ElMekawy, A., Hegab, H., Pant, D. & Saint, C. (2018) 'Bio-analytical applications of microbial fuel cell-based biosensors for onsite water quality monitoring', *Journal of Applied Microbiology*, 124(1), pp. 302-13.
- Engelmann, I., Griffon, A., Tichit, L., Montanana-Sanchis, F., Wang, G., Reinke, V., Waterston, R. H., Hillier, L. W. & Ewbank, J. J. (2011) 'A comprehensive analysis of gene expression changes provoked by bacterial and fungal infection in *C. elegans*', *PLoS One*, 6(5), pp. e19055.
- Erable, B., Feron, D. & Bergel, A. (2012) 'Microbial catalysis of the oxygen reduction reaction for microbial fuel cells: a review', *ChemSusChem*, 5(6), pp. 975-87.
- Eschbach, M., Schreiber, K., Trunk, K., Buer, J., Jahn, D. & Schobert, M. (2004) 'Long-term anaerobic survival of the opportunistic pathogen *Pseudomonas aeruginosa* via pyruvate fermentation', *Journal of Bacteriology*, 186(14), pp. 4596-604.
- Essar, D. W., Eberly, L., Hadero, A. & Crawford, I. P. (1990) 'Identification and characterization of genes for a second anthranilate synthase in *Pseudomonas aeruginosa*: interchangeability of the two anthranilate synthases and evolutionary implications', *Journal of Bacteriology*, 172(2), pp. 884-900.
- Ewing, T., Ha, P. T., Babauta, J. T., Tang, N. T., Heo, D. & Beyenal, H. (2014) 'Scale-up of sediment microbial fuel cells', *Journal of Power Sources*, 272, pp. 311-19.
- Fan, Y., Han, S-K. & Liu, H. (2012) 'Improved performance of CEA microbial fuel cells with increased reactor size', *Energy & Environmental Science*, 5(8), pp. 8273-80.

- Farahani, R. D., Dubé, M. & Therriault, D. (2016) 'Three-dimensional printing of multifunctional nanocomposites: manufacturing techniques and applications', *Advanced Materials*, 28(28), pp. 5794-821.
- Ferrari, A. C. & Robertson, J. (2000) 'Interpretation of Raman spectra of disordered and amorphous carbon', *Physical Review B*, 61(20), pp. 14095.
- Ferrari, A. C. (2007) 'Raman spectroscopy of graphene and graphite: Disorder, electron-phonon coupling, doping and nonadiabatic effects', *Solid State Communications*, 143(1-2), pp. 47-57.
- Ferrari, A. C., Meyer, J., Scardaci, V., Casiraghi, C., Lazzeri, M., Mauri, F., Piscanec, S., Jiang, D., Novoselov, K. & Roth, S. (2006) 'Raman spectrum of graphene and graphene layers', *Physical Review Letters*, 97(18), pp. 187401.
- Figueiredo-Filho, L. C. S., Brownson, D. A. C., Gomez-Mingot, M., Iniesta, J., Fatibello-Filho, O. & Banks, C. E. (2013b) 'Exploring the electrochemical performance of graphitic paste electrodes: graphene vs. graphite', *Analyst*, 138(21), pp. 6354-64.
- Figueiredo-Filho, L. C., Brownson, D. A. C., Fatibello-Filho, O. & Banks, C. E. (2013a) 'Exploring the origins of the apparent "electrocatalytic" oxidation of kojic acid at graphene modified electrodes', *Analyst*, 138(16), pp. 4436-42.
- Flemming, H.-C., Wingender, J., Szewzyk, U., Steinberg, P., Rice, S. A. & Kjelleberg, S. (2016) 'Biofilms: an emergent form of bacterial life', *Nature Reviews Microbiology*, 14(9), pp. 563-75.
- Foo, C. Y., Lim, H. N., Mahdi, M. A., Wahid, M. H. & Huang, N. M. (2018) 'Three-Dimensional Printed Electrode and Its Novel Applications in Electronic Devices', *Scientific Reports*, 8(1), pp. 7399.
- Forkner, C. E. (1961) '*Pseudomonas aeruginosa* infections', *The American Journal of the Medical Sciences*, 242(2), pp. 268.
- Foster, C. W., Brownson, D. A. C., Ruas de Souza, A. P., Bernalte, E., Iniesta, J., Bertotti, M. & Banks, C. E. (2016) 'Pencil it in: pencil drawn electrochemical sensing platforms', *Analyst*, 141(13), pp. 4055-64.
- Foster, C. W., Down, M. P., Zhang, Y., Ji, X., Rowley-Neale, S. J., Smith, G. C., Kelly, P. J. & Banks, C. E. (2017) '3D Printed Graphene Based Energy Storage Devices', *Scientific Reports*, 7, pp. 42233.
- Franks, A. E. & Nevin, K. P. (2010) 'Microbial fuel cells, a current review', *Energies*, 3(5), pp. 899-919.
- Friedheim, E. & Michaelis, L. (1931) 'Potentiometric study of pyocyanine', *Journal of Biological Chemistry*, 91(1), pp. 355-68.
- Friman, H., Schechter, A., Ioffe, Y., Nitzan, Y. & Cahan, R. (2013) 'Current production in a microbial fuel cell using a pure culture of *Cupriavidus basilensis* growing in acetate or phenol as a carbon source', *Microbial Biotechnology*, 6(4), pp. 425-34.
- Galdino, F. E., Foster, C. W., Bonacin, J. A. & Banks, C. E. (2015) 'Exploring the electrical wiring of screen-printed configurations utilised in electroanalysis', *Analytical Methods*, 7(3), pp. 1208-14.
- Gallagher, L. A., McKnight, S. L., Kuznetsova, M. S., Pesci, E. C. & Manoil, C. (2002) 'Functions required for extracellular quinolone signaling by *Pseudomonas aeruginosa*', *Journal of Bacteriology*, 184(23), pp. 6472-80.
- Galushko, A. S. & Schink, B. (2000) 'Oxidation of acetate through reactions of the citric acid cycle by *Geobacter sulfurreducens* in pure culture and in syntrophic coculture', *Archives of Microbiology*, 174(5), pp. 314-21.

- García-Miranda Ferrari, A., Foster, C., Kelly, P., Brownson, D. A. C. & Banks, C. E. (2018) 'Determination of the Electrochemical Area of Screen-Printed Electrochemical Sensing Platforms', *Biosensors*, 8(2), pp. 53.
- Gasnier, A., Pedano, M. L., Rubianes, M. D. & Rivas, G. A. (2013) 'Graphene paste electrode: electrochemical behavior and analytical applications for the quantification of NADH', *Sensors and Actuators B: Chemical*, 176, pp. 921-26.
- Gellatly, S. L. & Hancock, R. E. W. (2013) '*Pseudomonas aeruginosa*: new insights into pathogenesis and host defenses', *Pathogens and Disease*, 67(3), pp. 159-73.
- Georgakilas, V., Perman, J. A., Tucek, J. & Zboril, R. (2015) 'Broad family of carbon nanoallotropes: classification, chemistry, and applications of fullerenes, carbon dots, nanotubes, graphene, nanodiamonds, and combined superstructures', *Chemical Reviews*, 115(11), pp. 4744-822.
- Ghasemi, M., Shahgaldi, S., Ismail, M., Kim, B. H., Yaakob, Z. & Daud, W. R. W. (2011) 'Activated carbon nanofibers as an alternative cathode catalyst to platinum in a two-chamber microbial fuel cell', *International Journal of Hydrogen Energy*, 36(21), pp. 13746-52.
- Giaouris, E., Chapot-Chartier, M-P. & Briandet, R. (2009) 'Surface physicochemical analysis of natural *Lactococcus lactis* strains reveals the existence of hydrophobic and low charged strains with altered adhesive properties', *International Journal of Food Microbiology*, 131(1), pp. 2-9.
- Girme, G. M., Faze, N. R., Bower, T. A., & Christy, A. D. (2014). Algae Powered Microbial Desalination Cells. In: 2014 Montreal, Quebec Canada July 13–July 16, 2014. *American Society of Agricultural and Biological Engineers*, 1.
- Glasser, N. R., Kern, S. E. & Newman, D. K. (2014) 'Phenazine redox cycling enhances anaerobic survival in *Pseudomonas aeruginosa* by facilitating generation of ATP and a proton-motive force', *Molecular Microbiology*, 92(2), pp. 399-412.
- Glasser, N. R., Wang, B. X., Hoy, J. A. & Newman, D. K. (2017) 'The pyruvate and  $\alpha$ -ketoglutarate dehydrogenase complexes of *Pseudomonas aeruginosa* catalyze pyocyanin and phenazine-1-carboxylic acid reduction via the subunit dihydrolipoamide dehydrogenase', *Journal of Biological Chemistry*, 292(13), pp. 5593-607.
- Gomes, A. S., La Rotta, C. E., Nitschke, M. & González, E. R. (2011) 'Evaluation of current output in *Pseudomonas aeruginosa* microbial fuel cells using glycerol as substrate and Nafion 117 as proton exchange membrane', *ECS Transactions*, 41(1), pp. 2011-17.
- Gorby, Y. A., Yanina, S., McLean, J. S., Rosso, K. M., Moyles, D., Dohnalkova, A., Beveridge, T. J., Chang, I. S., Kim, B. H. & Kim, K. S. (2006) 'Electrically conductive bacterial nanowires produced by *Shewanella oneidensis* strain MR-1 and other microorganisms', *Proceedings of the National Academy of Sciences*, 103(30), pp. 11358-63.
- Graf, D., Molitor, F., Ensslin, K., Stampfer, C., Jungen, A., Hierold, C. & Wirtz, L. (2007) 'Spatially resolved Raman spectroscopy of single-and few-layer graphene', *Nano Letters*, 7(2), pp. 238-42.
- Granqvist, C. G. (2007) 'Transparent conductors as solar energy materials: A panoramic review', *Solar energy materials and solar cells*, 91(17), pp. 1529-98.
- Graphene Supermarket. (2016). Available at: <https://graphene-supermarket.com/home.php> [Accessed on: 3/10/2017].

- Grewal, Y. S., Shiddiky, M. J. A., Gray, S. A., Weigel, K. M., Cangelosi, G. A. & Trau, M. (2013) 'Label-free electrochemical detection of an *Entamoeba histolytica* antigen using cell-free yeast-scFv probes', *Chemical Communications*, 49(15), pp. 1551-53.
- Guidelli, R., Compton, R. G., Feliu, J. M., Gileadi, E., Lipkowski, J., Schmickler, W. & Trasatti, S. (2014) 'Defining the transfer coefficient in electrochemistry: An assessment (IUPAC Technical Report)', *Pure and Applied Chemistry*, 86(2), pp. 245-58.
- Guo, H., Lv, R. & Bai, S. (2019) 'Recent advances on 3D printing graphene-based composites', *Nano Materials Science*, 1(2), pp. 101-15.
- Guo, K., Freguia, S., Dennis, P. G., Chen, X., Donose, B. C., Keller, J., Gooding, J. J. & Rabaey, K. (2013) 'Effects of surface charge and hydrophobicity on anodic biofilm formation, community composition, and current generation in bioelectrochemical systems', *Environmental Science & Technology*, 47(13), pp. 7563-70.
- Guo, K., Hassett, D. J. & Gu, T. (2012) 'Microbial Fuel Cells: Electricity Generation from Organic Wastes by Microbes', *Microbial Biotechnology: Energy and Environment*, 9, pp. 162 - 89.
- Gutfraind, R., Sheintuch, M. & Avnir, D. (1991) 'Fractal and multifractal analysis of the sensitivity of catalytic reactions to catalyst structure', *The Journal of Chemical Physics*, 95(8), pp. 6100-11.
- Habermann, W. & Pommer, E. (1991) 'Biological fuel cells with sulphide storage capacity', *Applied Microbiology and Biotechnology*, 35(1), pp. 128-33.
- Haque, F., Alfatah, M., Ganesan, K. & Bhattacharyya, M. S. (2016) 'Inhibitory Effect of Sophorolipid on *Candida albicans* Biofilm Formation and Hyphal Growth', *Scientific Reports*, 6, pp. 23575.
- Harnisch, F., Wirth, S. & Schröder, U. (2009) 'Effects of substrate and metabolite crossover on the cathodic oxygen reduction reaction in microbial fuel cells: platinum vs. iron (II) phthalocyanine based electrodes', *Electrochemistry Communications*, 11(11), pp. 2253-56.
- Harrison, J. J., Ceri, H., Yerly, J., Stremick, C. A., Hu, Y., Martinuzzi, R. & Turner, R. J. (2006) 'The use of microscopy and three-dimensional visualization to evaluate the structure of microbial biofilms cultivated in the Calgary Biofilm Device', *Biological Procedures Online*, 8(1), pp. 194-215.
- Hassan, W. M. & Abo Dena, A. S. (2014) 'Unraveling the Nature of Interaction between Substituted Phenol and Amiodarone', *Analytical chemistry*, 86(3), pp. 1881-86.
- Hassett, D. J., Cuppoletti, J., Trapnell, B., Lyman, S. V., Rowe, J. J., Yoon, S. S., Hilliard, G. M., Parvatiyar, K., Kamani, M. C. & Wozniak, D. J. (2002) 'Anaerobic metabolism and quorum sensing by *Pseudomonas aeruginosa* biofilms in chronically infected cystic fibrosis airways: rethinking antibiotic treatment strategies and drug targets', *Advanced Drug Delivery Reviews*, 54(11), pp. 1425-43.
- Hassett, D. J., Korfhagen, T. R., Irvin, R. T., Schurr, M. J., Sauer, K., Lau, G. W., Sutton, M. D., Yu, H. & Hoiby, N. (2010) '*Pseudomonas aeruginosa* biofilm infections in cystic fibrosis: insights into pathogenic processes and treatment strategies', *Expert Opinion on Therapeutic Targets*, 14(2), pp. 117-30.
- Hassett, D., Charniga, L., Bean, K., Ohman, D. & Cohen, M. (1992) 'Response of *Pseudomonas aeruginosa* to pyocyanin: mechanisms of resistance, antioxidant defenses, and demonstration of a manganese-cofactored superoxide dismutase', *Infection and Immunity*, 60(2), pp. 328-36.

- Hays, S., Zhang, F. & Logan, B. E. (2011) 'Performance of two different types of anodes in membrane electrode assembly microbial fuel cells for power generation from domestic wastewater', *Journal of Power Sources*, 196(20), pp. 8293-300.
- He, Z. & Angenent, L. T. (2006) 'Application of bacterial biocathodes in microbial fuel cells', *Electroanalysis*, 18(19-20), pp. 2009-15.
- He, Z. (2012). 'Microbial fuel cells: now let us talk about energy', *Environmental Science & Technology*, 47(1), pp. 332-3.
- He, Z., Liu, J., Qiao, Y., Li, C. M. & Tan, T. T. Y. (2012) 'Architecture Engineering of Hierarchically Porous Chitosan/Vacuum-Stripped Graphene Scaffold as Bioanode for High Performance Microbial Fuel Cell', *Nano Letters*, 12(9), pp. 4738-41.
- He, Z., Minter, S. D. & Angenent, L. T. (2005) 'Electricity generation from artificial wastewater using an upflow microbial fuel cell', *Environmental Science & Technology*, 39(14), pp. 5262-67.
- Hegab, H. M., ElMekawy, A., Zou, L., Mulcahy, D., Saint, C. P. & Ginic-Markovic, M. (2016) 'The controversial antibacterial activity of graphene-based materials', *Carbon*, 105, pp. 362-76.
- Heijne, A. T., Liu, F., Weijden, R. v. d., Weijma, J., Buisman, C. J. & Hamelers, H. V. (2010) 'Copper recovery combined with electricity production in a microbial fuel cell', *Environmental Science & Technology*, 44(11), pp. 4376-81.
- Herbert, G. J., Iniyar, S., Sreevalsan, E. & Rajapandian, S. (2007) 'A review of wind energy technologies', *Renewable and Sustainable Energy Reviews*, 11(6), pp. 1117-45.
- Hernandez, M. E., Kappler, A. & Newman, D. K. (2004) 'Phenazines and other redox-active antibiotics promote microbial mineral reduction', *Applied and Environmental Microbiology*, 70(2), pp. 921-28.
- Hickey, N. A., Whitehead, K. A., Shalamanova, L., Butler, J. A. & Taylor, R. L. (2019) 'A novel microbiological medium for the growth of periodontitis associated pathogens', *Journal of Microbiological Methods*, 163, pp. 105647.
- Ho Sui, S. J., Lo, R., Fernandes, A. R., Caulfield, M. D. G., Lerman, J. A., Xie, L., Bourne, P. E., Baillie, D. L. & Brinkman, F. S. L. (2012) 'Raloxifene attenuates *Pseudomonas aeruginosa* pyocyanin production and virulence', *International Journal of Antimicrobial Agents*, 40(3), pp. 246-51.
- Hobot, J. A. (2015) 'Bacterial ultrastructure', *Molecular medical microbiology*: Elsevier, pp. 7-32.
- Hou, J., Shao, Y., Ellis, M. W., Moore, R. B. & Yi, B. (2011) 'Graphene-based electrochemical energy conversion and storage: fuel cells, supercapacitors and lithium ion batteries', *Physical Chemistry Chemical Physics*, 13(34), pp. 15384-402.
- Hsu, L. C., Fang, J., Borca-Tasciuc, D. A., Worobo, R. W. & Moraru, C. I. (2013) 'Effect of Micro- and Nanoscale Topography on the Adhesion of Bacterial Cells to Solid Surfaces', *Applied and Environmental Microbiology*, 79(8), pp. 2703-12
- Hu, L., Peng, X., Huo, K., Chen, R., Fu, J., Li, Y., Lee, L. Y. S., Wong, K-Y. & Chu, P. K. (2016) 'Dominant Factors Governing the Electron Transfer Kinetics and Electrochemical Biosensing Properties of Carbon Nanofiber Arrays', *ACS Applied Materials & Interfaces*, 8(42), pp. 28872-79.
- Huang, K-J., Li, J., Liu, Y-M., Cao, X., Yu, S. & Yu, M. (2012) 'Disposable immunoassay for hepatitis B surface antigen based on a graphene paste electrode functionalized with gold nanoparticles and a Nafion-cysteine conjugate', *Microchimica Acta*, 177(3-4), pp. 419-26.

- Huang, L., Regan, J. M. & Quan, X. (2011) 'Electron transfer mechanisms, new applications, and performance of biocathode microbial fuel cells', *Bioresource Technology*, 102(1), pp. 316-23.
- Ieropoulos, I. A., Ledezma, P., Stinchcombe, A., Papaharalabos, G., Melhuish, C. & Greenman, J. (2013) 'Waste to real energy: the first MFC powered mobile phone', *Physical Chemistry Chemical Physics*, 15(37), pp. 15312-16.
- Ieropoulos, I. A., Winfield, J., Greenman, J. & Melhuish, C. (2010) 'Small scale microbial fuel cells and different ways of reporting output', *ECS Transactions*, 28(9), pp. 1-9.
- Islam, M. A., Ethiraj, B., Cheng, C. K., Yousuf, A. & Khan, M. M. R. (2018) 'An insight of synergy between *Pseudomonas aeruginosa* and *Klebsiella variicola* in a microbial fuel cell', *ACS Sustainable Chemistry & Engineering*, 6(3), pp. 4130-37.
- Islam, M. A., Woon, C. W., Ethiraj, B., Cheng, C. K., Yousuf, A. & Khan, M. M. R. (2016) 'Ultrasound driven biofilm removal for stable power generation in microbial fuel cell', *Energy & Fuels*, 31(1), pp. 968-76.
- Jakus, A. E., Secor, E. B., Rutz, A. L., Jordan, S. W., Hersam, M. C. & Shah, R. N. (2015) 'Three-dimensional printing of high-content graphene scaffolds for electronic and biomedical applications', *ACS Nano*, 9(4), pp. 4636-48.
- Jana, P. S., Behera, M. & Ghangrekar, M. (2010) 'Performance comparison of up-flow microbial fuel cells fabricated using proton exchange membrane and earthen cylinder', *International Journal of Hydrogen Energy*, 35(11), pp. 5681-86.
- Janicek, A., Fan, Y. & Liu, H. (2014) 'Design of microbial fuel cells for practical application: a review and analysis of scale-up studies', *Biofuels*, 5(1), pp. 79-92.
- Jariwala, D., Sangwan, V. K., Lauhon, L. J., Marks, T. J. & Hersam, M. C. (2013) 'Carbon nanomaterials for electronics, optoelectronics, photovoltaics, and sensing', *Chemical Society Reviews*, 42(7), pp. 2824-60.
- Javey, A., Nam, S., Friedman, R. S., Yan, H. & Lieber, C. M. (2007) 'Layer-by-layer assembly of nanowires for three-dimensional, multifunctional electronics', *Nano Letters*, 7(3), pp. 773-77.
- Jayapriya, J. & Ramamurthy, V. (2012) 'Use of non-native phenazines to improve the performance of *Pseudomonas aeruginosa* MTCC 2474 catalysed fuel cells', *Bioresource Technology*, 124, pp. 23-28.
- Jayapriya, J. & Ramamurthy, V. (2014) 'The role of electrode material in capturing power generated in *Pseudomonas* catalysed fuel cells', *The Canadian Journal of Chemical Engineering*, 92(4), pp. 610-14.
- Jayaseelan, S., Ramaswamy, D. & Dharmaraj, S. (2014) 'Pyocyanin: production, applications, challenges and new insights', *World Journal of Microbiology and Biotechnology*, 30(4), pp. 1159-68.
- Jayashree, C., Tamilarasan, K., Rajkumar, M., Arulazhagan, P., Yogalakshmi, K., Srikanth, M. & Banu, J. R. (2016) 'Treatment of seafood processing wastewater using upflow microbial fuel cell for power generation and identification of bacterial community in anodic biofilm', *Journal of Environmental Management*, 180, pp. 351-58.
- Ji, X., Banks, C. E., Crossley, A. & Compton, R. G. (2006) 'Oxygenated Edge Plane Sites Slow the Electron Transfer of the Ferro-/Ferricyanide Redox Couple at Graphite Electrodes', *ChemPhysChem*, 7(6), pp. 1337-44.
- Jia, R., Yang, D., Xu, D. & Gu, T. (2017) 'Electron transfer mediators accelerated the microbiologically influence corrosion against carbon steel by nitrate reducing *Pseudomonas aeruginosa* biofilm', *Bioelectrochemistry*, 118, pp. 38-46.

- Jiang, D., Curtis, M., Troop, E., Scheible, K., McGrath, J., Hu, B., Suib, S., Raymond, D. & Li, B. (2011) 'A pilot-scale study on utilizing multi-anode/cathode microbial fuel cells (MAC MFCs) to enhance the power production in wastewater treatment', *International Journal of Hydrogen Energy*, 36(1), pp. 876-84.
- Kampouris, D. K. & Banks, C. E. (2010) 'Exploring the physicoelectrochemical properties of graphene', *Chemical Communications*, 46(47), pp. 8986-88.
- Karahan, H. E., Wiraja, C., Xu, C., Wei, J., Wang, Y., Wang, L., Liu, F. & Chen, Y. (2018) 'Graphene materials in antimicrobial nanomedicine: current status and future perspectives', *Advanced healthcare materials*, 7(13), pp. e1701406.
- Kargar, M., Chang, Y.-R., Khalili Hoseinabad, H., Pruden, A. & Ducker, W. A. (2016) 'Colloidal crystals delay formation of early stage bacterial biofilms', *ACS Biomaterials Science & Engineering*, 2(6), pp. 1039-48.
- Katsikogianni, M. & Missirlis, Y. (2004) 'Concise review of mechanisms of bacterial adhesion to biomaterials and of techniques used in estimating bacteria-material interactions', *European Cells & Materials*, 8(3), pp. 37-57.
- Kazemi, S., Fatih, K. & Mohseni, M. (2015) 'Improved performance of a passive air breathing flat-plate microbial fuel cell', *The Canadian Journal of Chemical Engineering*, 93(3), pp. 479-85.
- Kelleher, S. M., Habimana, O., Lawler, J., O'reilly, B., Daniels, S., Casey, E. & Cowley, A. (2015) 'Cicada wing surface topography: an investigation into the bactericidal properties of nanostructural features', *ACS Applied Materials & Interfaces*, 8(24), pp. 14966-74.
- Kerr, J., Taylor, G., Rutman, A., Høiby, N., Cole, P. & Wilson, R. (1999) '*Pseudomonas aeruginosa* pyocyanin and 1-hydroxyphenazine inhibit fungal growth', *Journal of Clinical Pathology*, 52(5), pp. 385-87.
- Khare, V., Nema, S. & Baredar, P. (2016) 'Solar–wind hybrid renewable energy system: A review', *Renewable and Sustainable Energy Reviews*, 58, pp. 23-33.
- Kilmury, S. L. & Burrows, L. L. (2018) 'The *Pseudomonas aeruginosa* PilSR two-component system regulates both twitching and swimming motilities', *MBio*, 9(4), pp. e01310-18.
- Kim, B. H., Chang, I. S. & Gadd, G. M. (2007a) 'Challenges in microbial fuel cell development and operation', *Applied Microbiology and Biotechnology*, 76(3), pp. 485-94.
- Kim, B. H., Park, D. H., Shin, P. K., Chang, I. S. & Kim, H. J. (1999a). Mediator-less biofuel cell. Google Patents. Patent no. US5976719A.
- Kim, H. J., Hyun, M. S., Chang, I. S. & Kim, B. H. (1999b) 'A microbial fuel cell type lactate biosensor using a metal-reducing bacterium, *Shewanella putrefaciens*', *Journal of Microbiology and Biotechnology*, 9(3), pp. 365-67.
- Kim, H. J., Park, H. S., Hyun, M. S., Chang, I. S., Kim, M. & Kim, B. H. (2002) 'A mediator-less microbial fuel cell using a metal reducing bacterium, *Shewanella putrefaciens*', *Enzyme and Microbial Technology*, 30(2), pp. 145-52.
- Kim, J. R., Cheng, S., Oh, S. E. & Logan, B. E. (2007b) 'Power generation using different cation, anion, and ultrafiltration membranes in microbial fuel cells', *Environmental Science & Technology*, 41(3), pp. 1004-09.
- Kim, K., Coh, S., Tan, L. Z., Regan, W., Yuk, J. M., Chatterjee, E., Crommie, M., Cohen, M. L., Louie, S. G. & Zettl, A. (2012) 'Raman spectroscopy study of rotated double-layer graphene: misorientation-angle dependence of electronic structure', *Physical Review Letters*, 108(24), pp. 246103-8

- Kim, N., Choi, Y., Jung, S. & Kim, S. (2000) 'Effect of initial carbon sources on the performance of microbial fuel cells containing *Proteus vulgaris*', *Biotechnology and Bioengineering*, 70(1), pp. 109-14.
- Kim, S-K. & Lee, J-H. (2016) 'Biofilm dispersion in *Pseudomonas aeruginosa*', *Journal of Microbiology*, 54(2), pp. 71-85.
- Kinnari, T., Esteban, J., Zamora, N., Fernandez, R., López-Santos, C., Yubero, F., Mariscal, D., Puertolas, J. & Gomez-Barrena, E. (2010) 'Effect of surface roughness and sterilization on bacterial adherence to ultra-high molecular weight polyethylene', *Clinical Microbiology and Infection*, 16(7), pp. 1036-41.
- Kochkodan, V., Tsarenko, S., Potapchenko, N., Kosinova, V. & Goncharuk, V. (2008) 'Adhesion of microorganisms to polymer membranes: a photobactericidal effect of surface treatment with TiO<sub>2</sub>', *Desalination*, 220(1), pp. 380-85.
- Kondratowicz, I., Żelechowska, K., Majdecka, D. & Bilewicz, R. (2015) 'Synthesis and modification of reduced graphene oxide aerogels for biofuel cell applications', *Materials Science-Poland*, 33(2), pp. 292-300.
- Kouzuma, A., Meng, X-Y., Kimura, N., Hashimoto, K. & Watanabe, K. (2010) 'Disruption of the putative cell surface polysaccharide biosynthesis gene SO3177 in *Shewanella oneidensis* MR-1 enhances adhesion to electrodes and current generation in microbial fuel cells', *Applied and Environmental Microbiology*, 76(13), pp. 4151-57.
- Krasowska, A. & Sigler, K. (2014) 'How microorganisms use hydrophobicity and what does this mean for human needs?', *Frontiers in Cellular and Infection Microbiology*, 4(112), pp. 1-7.
- Krebs, H. A. & Eggleston, L. V. (1945) 'Metabolism of acetoacetate in animal tissues. 1', *Biochemical Journal*, 39(5), pp. 408-19.
- Krebs, H. A. & Johnson, W. A. (1937) 'Acetopyruvic acid (alpha-gamma-diketovaleric acid) as an intermediate metabolite in animal tissues', *Biochemical Journal*, 31(5), pp. 772-9.
- Krebs, H. A., Salvin, E. & Johnson, W. A. (1938) 'The formation of citric and alpha-ketoglutaric acids in the mammalian body', *Biochemical Journal*, 32(1), pp. 113-7.
- Kumar, A., Katuri, K., Lens, P. & Leech, D. (2012) 'Does bioelectrochemical cell configuration and anode potential affect biofilm response?', *Biochemical Society Transactions*, 40(6), pp. 1308-14.
- Kumar, P., Huo, P., Zhang, R. & Liu, B. (2019) 'Antibacterial Properties of Graphene-Based Nanomaterials', *Nanomaterials*, 9(5), pp. 737.
- Kumar, R., Singh, L. & Zularisam, A. W. (2016) 'Exoelectrogens: Recent advances in molecular drivers involved in extracellular electron transfer and strategies used to improve it for microbial fuel cell applications', *Renewable and Sustainable Energy Reviews*, 56, pp. 1322-36.
- Kurachi, M. (1958) 'Studies on the Biosynthesis of Pyocyanine.(II): Isolation and determination of pyocyanine' *Bulletin of the Institute for Chemical Research, Kyoto University*, 36(6), pp. 174-87.
- Kuroki, M., Igarashi, Y., Ishii, M. & Arai, H. (2014) 'Fine-tuned regulation of the dissimilatory nitrite reductase gene by oxygen and nitric oxide in *Pseudomonas aeruginosa*', *Environmental Microbiology Reports*, 6(6), pp. 792-801.
- Kushwaha, M., Jain, S. K., Sharma, N., Abrol, V., Jaglan, S. & Vishwakarma, R. A. (2018) 'Establishment of LCMS Based Platform for Discovery of Quorum Sensing Inhibitors:

- Signal Detection in *Pseudomonas aeruginosa* PAO1', *ACS Chemical Biology*, 13(3), pp. 657-65.
- Latifi, A., Foglino, M., Tanaka, K., Williams, P. & Lazdunski, A. (1996) 'A hierarchical quorum-sensing cascade in *Pseudomonas aeruginosa* links the transcriptional activators LasR and RhIR (VsmR) to expression of the stationary-phase sigma factor RpoS', *Molecular Microbiology*, 21(6), pp. 1137-46.
- Latifi, A., Winson, M. K., Foglino, M., Bycroft, B. W., Stewart, G. S., Lazdunski, A. & Williams, P. (1995) 'Multiple homologues of LuxR and LuxI control expression of virulence determinants and secondary metabolites through quorum sensing in *Pseudomonas aeruginosa* PAO1', *Molecular Microbiology*, 17(2), pp. 333-43.
- Lau, G. W., Hassett, D. J., Ran, H. & Kong, F. (2004) 'The role of pyocyanin in *Pseudomonas aeruginosa* infection', *Trends in Molecular Medicine*, 10(12), pp. 599-606.
- Lavagnini, I., Antiochia, R. & Magno, F. (2004) 'An Extended Method for the Practical Evaluation of the Standard Rate Constant from Cyclic Voltammetric Data', *Electroanalysis*, 16(6), pp. 505-06.
- Leang, C., Coppi, M. V. & Lovley, D. R. (2003) 'OmcB, a c-type polyheme cytochrome, involved in Fe(III) reduction in *Geobacter sulfurreducens*', *Journal of Bacteriology*, 185(7), pp. 2096-103.
- Ledezma, P., Stinchcombe, A., Greenman, J. & Ieropoulos, I. (2013) 'The first self-sustainable microbial fuel cell stack', *Physical Chemistry Chemical Physics*, 15(7), pp. 2278-81.
- Lee, C., Wei, X., Kysar, J. W. & Hone, J. (2008) 'Measurement of the elastic properties and intrinsic strength of monolayer graphene', *Science*, 321(5887), pp. 385-8.
- Lee, C., Yang, W. & Parr, R. G. (1988) 'Development of the Colle-Salvetti correlation-energy formula into a functional of the electron density', *Physical Review B*, 37(2), pp. 785.
- Lee, K. & Yoon, S. S. (2017) '*Pseudomonas aeruginosa* biofilm, a programmed bacterial life for fitness', *Journal of Microbiology and Biotechnology*, 27(6), pp. 1053-64.
- Lee, S. & Oh, E. S. (2013) 'Performance enhancement of a lithium ion battery by incorporation of a graphene/polyvinylidene fluoride conductive adhesive layer between the current collector and the active material layer', *Journal of Power Sources*, 244, pp. 721-25.
- Lee, Y., Bae, S., Moon, C. & Lee, W. (2015) 'Flavin mononucleotide mediated microbial fuel cell in the presence of *Shewanella putrefaciens* CN32 and iron-bearing mineral', *Biotechnology and Bioprocess Engineering*, 20(5), pp. 894-900.
- Lefebvre, O., Tan, Z., Kharkwal, S. & Ng, H. Y. (2012) 'Effect of increasing anodic NaCl concentration on microbial fuel cell performance', *Bioresource Technology*, 112, pp. 336-40.
- Li, C. & Shi, G. (2012) 'Three-dimensional graphene architectures', *Nanoscale*, 4(18), pp. 5549-63.
- Li, C., Lesnik, K. L., Fan, Y. & Liu, H. (2016) 'Redox Conductivity of Current-Producing Mixed Species Biofilms', *PLoS One*, 11(5), pp. e0155247.
- Li, F., Li, J., Feng, Y., Yang, L. & Du, Z. (2011a) 'Electrochemical behavior of graphene doped carbon paste electrode and its application for sensitive determination of ascorbic acid', *Sensors and Actuators B: Chemical*, 157(1), pp. 110-14.
- Li, W., Tan, C., Lowe, M. A., Abruña, H. D. & Ralph, D. C. (2011b) 'Electrochemistry of Individual Monolayer Graphene Sheets', *ACS Nano*, 5(3), pp. 2264-70.

- Li, Y., Wu, Y., Liu, B., Luan, H., Vadas, T., Guo, W., Ding, J. & Li, B. (2015) 'Self-sustained reduction of multiple metals in a microbial fuel cell–microbial electrolysis cell hybrid system', *Bioresource Technology*, 192, pp. 238-46.
- Lin, Z., Ye, X., Han, J., Chen, Q., Fan, P., Zhang, H., Xie, D., Zhu, H. & Zhong, M. (2015) 'Precise control of the number of layers of graphene by picosecond laser thinning', *Scientific Reports*, 5, pp. 11662.
- Liu, H. & Logan, B. E. (2004) 'Electricity Generation Using an Air-Cathode Single Chamber Microbial Fuel Cell in the Presence and Absence of a Proton Exchange Membrane', *Environmental Science & Technology*, 38(14), pp. 4040-46.
- Liu, H., Cheng, S. & Logan, B. E. (2005) 'Production of Electricity from Acetate or Butyrate Using a Single-Chamber Microbial Fuel Cell', *Environmental Science & Technology*, 39(2), pp. 658-62.
- Liu, H., Ramnarayanan, R. & Logan, B. E. (2004) 'Production of electricity during wastewater treatment using a single chamber microbial fuel cell', *Environmental Science & Technology*, 38(7), pp. 2281-85.
- Liu, J., Liu, Y., Feng, C., Wang, Z., Jia, T., Gong, L. & Xu, L. (2017) 'Enhanced performance of microbial fuel cell using carbon microspheres modified graphite anode', *Energy Science & Engineering*, 5(4), pp. 217-25.
- Liu, J., Qiao, Y., Guo, C. X., Lim, S., Song, H. & Li, C. M. (2012) 'Graphene/carbon cloth anode for high-performance mediatorless microbial fuel cells', *Bioresource Technology*, 114, pp. 275-80.
- Liu, Z., Zhou, L., Chen, Q., Zhou, W. & Liu, Y. (2016) 'Advances in Graphene/Graphene Composite Based Microbial Fuel/Electrolysis Cells', *Electroanalysis*, 29(3), pp. 652-61.
- Logan, B. E. & Regan, J. M. (2006) 'Electricity-producing bacterial communities in microbial fuel cells', *Trends in Microbiology*, 14(12), pp. 512-18.
- Logan, B. E. (2004). 'Extracting hydrogen and electricity from renewable resources', *Environmental Science and Technology*, 38(9), pp. 160-7.
- Logan, B. E. (2009) 'Exoelectrogenic bacteria that power microbial fuel cells', *Nature Reviews Microbiology*, 7(5), pp. 375-81.
- Logan, B. E. (2010) 'Scaling up microbial fuel cells and other bioelectrochemical systems', *Applied Microbiology and Biotechnology*, 85(6), pp. 1665-71.
- Logan, B. E., Hamelers, B., Rozendal, R., Schroder, U., Keller, J., Freguia, S., Aelterman, P., Verstraete, W. & Rabaey, K. (2006) 'Microbial fuel cells: methodology and technology', *Environmental Science and Technology*, 40(17), pp. 5181-92.
- Lopes, R. & Betrouni, N. (2009) 'Fractal and multifractal analysis: a review', *Medical Image Analysis*, 13(4), pp. 634-49.
- López, D., Vlamakis, H. & Kolter, R. (2010) 'Biofilms', *Cold Spring Harbor perspectives in Biology*, 2(7), pp. a000398-a98.
- Lovley, D. R. & Phillips, E. J. (1988) 'Novel mode of microbial energy metabolism: organic carbon oxidation coupled to dissimilatory reduction of iron or manganese', *Applied and Environmental Microbiology*, 54(6), pp. 1472-80.
- Lovley, D. R. (2006a) 'Bug juice: harvesting electricity with microorganisms', *Nature Reviews Microbiology*, 4(7), pp. 497-508.
- Lovley, D. R. (2006b) 'Microbial energizers: fuel cells that keep on going', *Microbe-American Society for Microbiology*, 1(7), pp. 323-9.

- Lovley, D. R. (2011) 'Powering microbes with electricity: direct electron transfer from electrodes to microbes', *Environmental Microbiology Reports*, 3(1), pp. 27-35.
- Lovley, D. R. (2012) 'Electromicrobiology', *Annual Review of Microbiology*, 66, pp. 391-409.
- Lu, Y. & Chen, S. (2004) 'Micro and nano-fabrication of biodegradable polymers for drug delivery', *Advanced Drug Delivery Reviews*, 56(11), pp. 1621-33.
- Lund, J. W., Freeston, D. H. & Boyd, T. L. (2011) 'Direct utilization of geothermal energy 2010 worldwide review', *Geothermics*, 40(3), pp. 159-80.
- Lundqvist, B., Andersson, Y., Shao, H., Chan, S. & Langreth, D. (1995) 'Density functional theory including van der Waals forces', *International Journal of Quantum Chemistry*, 56(4), pp. 247-55.
- Luo, J., Jang, H. D., Sun, T., Xiao, L., He, Z., Katsoulidis, A. P., Kanatzidis, M. G., Gibson, J. M. & Huang, J. (2011) 'Compression and Aggregation-Resistant Particles of Crumpled Soft Sheets', *ACS Nano*, 5(11), pp. 8943-49.
- Luo, S., Guo, W., Nealon, K. H., Feng, X. & He, Z. (2016) '13 C Pathway Analysis for the Role of Formate in Electricity Generation by *Shewanella Oneidensis* MR-1 Using Lactate in Microbial Fuel Cells', *Scientific Reports*, 6, pp. 20941.
- Lyon, D. Y., Buret, F., Vogel, T. M. & Monier, J-M. (2010) 'Is resistance futile? Changing external resistance does not improve microbial fuel cell performance', *Bioelectrochemistry*, 78(1), pp. 2-7.
- MacDonald, E. & Wicker, R. (2016) 'Multiprocess 3D printing for increasing component functionality', *Science*, 353(6307), pp. aaf2093-8.
- Macia, M. D., Rojo-Molinero, E. & Oliver, A. (2014) 'Antimicrobial susceptibility testing in biofilm-growing bacteria', *Clinical Microbiology and Infection*, 20(10), pp. 981-90.
- Mahajan-Miklos, S., Tan, M-W., Rahme, L. G. & Ausubel, F. M. (1999) 'Molecular mechanisms of bacterial virulence elucidated using a *Pseudomonas aeruginosa*-*Caenorhabditis elegans* pathogenesis model', *Cell*, 96(1), pp. 47-56.
- Malvankar, N. S. & Lovley, D. R. (2014) 'Microbial nanowires for bioenergy applications', *Current Opinion in Biotechnology*, 27, pp. 88-95.
- Malvankar, N. S., Tuominen, M. T. & Lovley, D. R. (2012) 'Biofilm conductivity is a decisive variable for high-current-density *Geobacter sulfurreducens* microbial fuel cells', *Energy & Environmental Science*, 5(2), pp. 5790-97.
- Manish, S. & Banerjee, R. (2008) 'Comparison of biohydrogen production processes', *International Journal of Hydrogen Energy*, 33(1), pp. 279-86.
- Mansour, A. M., Hassaneen, H. M., Mohammed, Y. S. & Ghani, N. T. A. (2013) 'Single crystal, spectral, computational studies and in vitro cytotoxicity of 2-chloro-3-formylpyrido [2, 1-a] isoquinoline-1-carbonitrile derivative', *Journal of Molecular Structure*, 1045, pp. 180-90.
- Manzanares Palenzuela, C. L., Novotný, F., Krupička, P., Sofer, Z. & Pumera, M. (2018) '3D-Printed Graphene/Poly(lactic Acid) Electrodes Promise High Sensitivity in Electroanalysis', *Analytical Chemistry*, 90(9), pp. 5753-57.
- Marsili, E., Baron, D. B., Shikhare, I. D., Coursolle, D., Gralnick, J. A. & Bond, D. R. (2008) '*Shewanella* secretes flavins that mediate extracellular electron transfer', *Proceedings of the National Academy of Sciences*, 105(10), pp. 3968-73.
- Maruthupandy, M., Anand, M., Maduraiveeran, G., Beevi, A. S. H. & Priya, R. J. (2015) 'Electrical conductivity measurements of bacterial nanowires from *Pseudomonas aeruginosa*', *Advances in Natural Sciences: Nanoscience and Nanotechnology*, 6(4), pp. 045007.

- Mavrodi, D. V., Bonsall, R. F., Delaney, S. M., Soule, M. J., Phillips, G. & Thomashow, L. S. (2001) 'Functional analysis of genes for biosynthesis of pyocyanin and phenazine-1-carboxamide from *Pseudomonas aeruginosa* PAO1', *Journal of Bacteriology*, 183(21), pp. 6454-65.
- Mayorov, A. S., Gorbachev, R. V., Morozov, S. V., Britnell, L., Jalil, R., Ponomarenko, L. A., Blake, P., Novoselov, K. S., Watanabe, K., Taniguchi, T. & Geim, A. K. (2011) 'Micrometer-scale ballistic transport in encapsulated graphene at room temperature', *Nano Letters*, 11(6), pp. 2396-9.
- McBrearty, J., Barker, D., Damavandi, M., Wilson-Nieuwenhuis, J., Pilkington, L. I., Dempsey-Hibbert, N., Slate, A. J. & Whitehead, K. A. (2018) 'Antimicrobial synergy of cationic grafted poly (para-phenylene ethynylene) and poly (para-phenylene vinylene) compounds with UV or metal ions against *Enterococcus faecium*' *RSC advances*, 8(41), pp. 23433-23441.
- McCreery, R. L. (2008) 'Advanced carbon electrode materials for molecular electrochemistry', *Chemical Reviews*, 108(7), pp. 2646-87.
- Mehta, T., Coppi, M. V., Childers, S. E. & Lovley, D. R. (2005) 'Outer Membrane c-Type Cytochromes Required for Fe(III) and Mn(IV) Oxide Reduction in *Geobacter sulfurreducens*', *Applied and Environmental Microbiology*, 71(12), pp. 8634-41.
- Melhuish, C., Ieropoulos, I., Greenman, J. & Horsfield, I. (2006) 'Energetically autonomous robots: Food for thought', *Autonomous Robots*, 21(3), pp. 187-98.
- Méthé, B. A., Nelson, K. E., Eisen, J. A., Paulsen, I. T., Nelson, W., Heidelberg, J. F., Wu, D., Wu, M., Ward, N., Beanan, M. J., Dodson, R. J., Madupu, R., Brinkac, L. M., Daugherty, S. C., DeBoy, R. T., Durkin, A. S., Gwinn, M., Kolonay, J. F., Sullivan, S. A., Haft, D. H., Selengut, J., Davidsen, T. M., Zafar, N., White, O., Tran, B., Romero, C., Forberger, H. A., Weidman, J., Khouri, H., Feldblyum, T. V., Utterback, T. R., Van Aken, S. E., Lovley, D. R. & Fraser, C. M. (2003) 'Genome of *Geobacter sulfurreducens*: metal reduction in subsurface environments', *Science*, 302(5652), pp. 1967-69.
- Metters, J. P., Houssein, S. M., Kampouris, D. K. & Banks, C. E. (2013) 'Paper-based electroanalytical sensing platforms', *Analytical Methods*, 5(1), pp. 103-10.
- Miles, A. A., Misra, S. & Irwin, J. (1938) 'The estimation of the bactericidal power of the blood', *Epidemiology & Infection*, 38(6), pp. 732-49.
- Min, B. & Logan, B. E. (2004) 'Continuous Electricity Generation from Domestic Wastewater and Organic Substrates in a Flat Plate Microbial Fuel Cell', *Environmental Science & Technology*, 38(21), pp. 5809-14.
- Min, B., Cheng, S. & Logan, B. E. (2005) 'Electricity generation using membrane and salt bridge microbial fuel cells', *Water Research*, 39(9), pp. 1675-86.
- Mink, J. E., Qaisi, R. M., Logan, B. E. & Hussain, M. M. (2014) 'Energy harvesting from organic liquids in micro-sized microbial fuel cells', *NPG Asia Materials*, 6(3), pp. e89.
- Mohanakrishna, G., Abu-Reesh, I. M., Al-Raoush, R. I. & He, Z. (2018) 'Cylindrical graphite based microbial fuel cell for the treatment of industrial wastewaters and bioenergy generation', *Bioresour Technol*, 247, pp. 753-58.
- Moon, H., Chang, I. S., Kang, K. H., Jang, J. K. & Kim, B. H. (2004) 'Improving the dynamic response of a mediator-less microbial fuel cell as a biochemical oxygen demand (BOD) sensor', *Biotechnology Letters*, 26(22), pp. 1717-21.

- Moorcroft, M. J., Lawrence, N. S., Coles, B. A., Compton, R. G. & Trevani, L. N. (2001) 'High temperature electrochemical studies using a channel flow cell heated by radio frequency radiation', *Journal of Electroanalytical Chemistry*, 506(1), pp. 28-33.
- Moreira, J., Gomes, L., Whitehead, K., Lynch, S., Tetlow, L. & Mergulhão, F. (2017) 'Effect of surface conditioning with cellular extracts on *Escherichia coli* adhesion and initial biofilm formation', *Food and Bioproducts Processing*, 104, pp. 1-12.
- Moser, J., Barreiro, A. & Bachtold, A. (2007) 'Current-induced cleaning of graphene', *Applied Physics Letters*, 91(16), pp. 163513.
- Mukherjee, S., Su, S., Panmanee, W., Irvin, R. T., Hassett, D. J. & Choi, S. (2013) 'A microliter-scale microbial fuel cell array for bacterial electrogenic screening', *Sensors and Actuators A: Physical*, 201, pp. 532-37.
- Murray, K., Rasmussen, P. S., Neustaedter, J. & Luck, J. M. (1965) 'The Hydrolysis of Arginine', *The Journal of biological chemistry*, 240(2), pp. 705-9.
- Mustakeem (2015) 'Electrode materials for microbial fuel cells: nanomaterial approach', *Materials for Renewable and Sustainable Energy*, 4(4), pp. 22-32.
- Myung, J., Yang, W., Saikaly, P. & Logan, B. E. (2018) 'Copper current collectors reduce long-term fouling of air cathodes in microbial fuel cells', *Environmental Science: Water Research & Technology*, 4, pp. 513-9.
- Nader, M., Wan, R., Rahimnejad, M. & Najafpour, G. (2012) 'Bioelectricity generation in biological fuel cell with and without mediators', *World Applied Sciences Journal*, 18(4), pp. 559-67.
- Nanchaiah, Y., Mohan, S. V. & Lens, P. (2015) 'Metals removal and recovery in bioelectrochemical systems: a review', *Bioresource Technology*, 195, pp. 102-14.
- Nathwani, D., Raman, G., Sulham, K., Gavaghan, M. & Menon, V. (2014) 'Clinical and economic consequences of hospital-acquired resistant and multidrug-resistant *Pseudomonas aeruginosa* infections: a systematic review and meta-analysis', *Antimicrobial Resistance and Infection Control*, 3(32), pp. 1-16.
- Neumann, C., Batchelor-McAuley, C., Downing, C. & Compton, R. G. (2011) 'Anthraquinone monosulfonate adsorbed on graphite shows two very different rates of electron transfer: surface heterogeneity due to basal and edge plane sites', *Chemistry-A European Journal*, 17(26), pp. 7320-26.
- Nevin, K. P., Kim, B-C., Glaven, R. H., Johnson, J. P., Woodard, T. L., Methé, B. A., DiDonato, R. J., Jr., Covalla, S. F., Franks, A. E., Liu, A. & Lovley, D. R. (2009) 'Anode Biofilm Transcriptomics Reveals Outer Surface Components Essential for High Density Current Production in *Geobacter sulfurreducens* Fuel Cells', *PLoS One*, 4(5), pp. e5628.
- Newman, D. K. & Kolter, R. (2000) 'A role for excreted quinones in extracellular electron transfer', *Nature*, 405(6782), pp. 94-97.
- Nicholson, R. S. (1965) 'Theory and Application of Cyclic Voltammetry for Measurement of Electrode Reaction Kinetics', *Analytical Chemistry*, 37(11), pp. 1351-55.
- Niessen, J., Schröder, U., Rosenbaum, M. & Scholz, F. (2004) 'Fluorinated polyanilines as superior materials for electrocatalytic anodes in bacterial fuel cells', *Electrochemistry Communications*, 6(6), pp. 571-75.
- Novoselov, K. S., Fal, V., Colombo, L., Gellert, P., Schwab, M. & Kim, K. (2012) 'A roadmap for graphene', *Nature*, 490(7419), pp. 192-200.

- Novoselov, K. S., Geim, A. K., Morozov, S. V., Jiang, D., Zhang, Y., Dubonos, S. V., Grigorieva, I. V. & Firsov, A. A. (2004) 'Electric field effect in atomically thin carbon films', *Science*, 306(5696), pp. 666-69.
- Ntagia, E., Rodenas, P., Ter Heijne, A., Buisman, C. & Sleutels, T. (2016) 'Hydrogen as electron donor for copper removal in bioelectrochemical systems', *International Journal of Hydrogen Energy*, 41(13), pp. 5758-64.
- O'Loughlin, C. T., Miller, L. C., Siryaporn, A., Drescher, K., Semmelhack, M. F. & Bassler, B. L. (2013) 'A quorum-sensing inhibitor blocks *Pseudomonas aeruginosa* virulence and biofilm formation', *Proceedings of the National Academy of Sciences*, 110(44), pp. 17981-86.
- Ochsner, U. A., Koch, A. K., Fiechter, A. & Reiser, J. (1994) 'Isolation and characterization of a regulatory gene affecting rhamnolipid biosurfactant synthesis in *Pseudomonas aeruginosa*', *Journal of Bacteriology*, 176(7), pp. 2044-54.
- Oh, S. E. & Logan, B. E. (2006) 'Proton exchange membrane and electrode surface areas as factors that affect power generation in microbial fuel cells', *Applied Microbiology and Biotechnology*, 70(2), pp. 162-69.
- Oh, S. E. & Logan, B. E. (2007) 'Voltage reversal during microbial fuel cell stack operation', *Journal of Power Sources*, 167(1), pp. 11-17.
- Oi, T., Shinyama, K. & Fujita, S. (2011) 'Electrical properties of heat-treated poly-lactic acid', *IEEJ Transactions on Fundamentals and Materials*, 131(1), pp. 395-400.
- Oliveira, V., Simões, M., Melo, L. & Pinto, A. (2013) 'Overview on the developments of microbial fuel cells', *Biochemical Engineering Journal*, 73, pp. 53-64.
- Ortiz, J., Cioslowski, J. & Fox, D. (2009) 'Gaussian 09, revision B. 01', *Wallingford CT*.
- Ortiz-Martínez, V. M., Gajda, I., Salar-García, M. J., Greenman, J., Hernández-Fernández, F. J. & Ieropoulos, I. (2016) 'Study of the effects of ionic liquid-modified cathodes and ceramic separators on MFC performance', *Chemical Engineering Journal*, 291, pp. 317-24.
- O'toole, G. A. & Kolter, R. (1998) 'Flagellar and twitching motility are necessary for *Pseudomonas aeruginosa* biofilm development', *Molecular Microbiology*, 30(2), pp. 295-304.
- Ow, Y. P., Green, D. R., Hao, Z. & Mak, T. W. (2008) 'Cytochrome c: functions beyond respiration', *Nature Reviews Molecular Cell Biology*, 9(7), pp. 532-42.
- Pant, D., Van Bogaert, G., De Smet, M., Diels, L. & Vanbroekhoven, K. (2010a) 'Use of novel permeable membrane and air cathodes in acetate microbial fuel cells', *Electrochimica Acta*, 55(26), pp. 7710-16.
- Pant, D., Van Bogaert, G., Diels, L. & Vanbroekhoven, K. (2010b) 'A review of the substrates used in microbial fuel cells (MFCs) for sustainable energy production', *Bioresource Technology*, 101(6), pp. 1533-43.
- Panwar, N., Kaushik, S. & Kothari, S. (2011) 'Role of renewable energy sources in environmental protection: a review', *Renewable and Sustainable Energy Reviews*, 15(3), pp. 1513-24.
- Papaharalabos, G., Greenman, J., Melhuish, C., Santoro, C., Cristiani, P., Li, B. & Ieropoulos, I. (2013) 'Increased power output from micro porous layer (MPL) cathode microbial fuel cells (MFC)', *International Journal of Hydrogen Energy*, 38(26), pp. 11552-58.
- Park, D. H. & Zeikus, J. G. (2003) 'Improved fuel cell and electrode designs for producing electricity from microbial degradation', *Biotechnology and Bioengineering*, 81(3), pp. 348-55.

- Parkash, A. (2016) 'Microbial fuel cells: a source of bioenergy', *Journal of Microbial and Biochemical Technology*, 8(3), pp. 247-55.
- Parkash, A., Aziz, S. & Soomro, S. A. (2015) 'Utilization of sewage sludge for production of electricity using mediated salt bridge based dual chamber microbial fuel cell', *Journal of Bioprocessing & Biotechniques*, 5(8), pp. 1000251.
- Parvin, M. H. (2011) 'Graphene paste electrode for detection of chlorpromazine', *Electrochemistry Communications*, 13(4), pp. 366-69.
- Pasternak, G., Greenman, J. & Ieropoulos, I. (2018) 'Dynamic evolution of anodic biofilm when maturing under different external resistive loads in microbial fuel cells. Electrochemical perspective', *Journal of Power Sources*, 400, pp. 392-401.
- Pearson, J. P., Passador, L., Iglewski, B. H. & Greenberg, E. (1995) 'A second N-acylhomoserine lactone signal produced by *Pseudomonas aeruginosa*', *Proceedings of the National Academy of Sciences*, 92(5), pp. 1490-94.
- Peltola, S. M., Melchels, F. P., Grijpma, D. W. & Kellomäki, M. (2008) 'A review of rapid prototyping techniques for tissue engineering purposes', *Annals of Medicine*, 40(4), pp. 268-80.
- Perera-Costa, D., Bruque, J. M., González-Martín, M. L., Gómez-García, A. C. & Vadillo-Rodríguez, V. (2014) 'Studying the influence of surface topography on bacterial adhesion using spatially organized microtopographic surface patterns', *Langmuir*, 30(16), pp. 4633-41.
- Permana, D., Rosdianti, D., Ishmayana, S., Rachman, S. D., Putra, H. E., Rahayuningwulan, D. & Hariyadi, H. R. (2015) 'Preliminary investigation of electricity production using dual chamber microbial fuel cell (dcMFC) with *Saccharomyces cerevisiae* as biocatalyst and methylene blue as an electron mediator', *Procedia Chemistry*, 17, pp. 36-43.
- Pham, V. T., Truong, V. K., Quinn, M. D., Notley, S. M., Guo, Y., Baulin, V. A., Al Kobaisi, M., Crawford, R. J. & Ivanova, E. P. (2015) 'Graphene induces formation of pores that kill spherical and rod-shaped bacteria', *ACS Nano*, 9(8), pp. 8458-67.
- Philamore, H., Rossiter, J., Walters, P., Winfield, J. & Ieropoulos, I. (2015) 'Cast and 3D printed ion exchange membranes for monolithic microbial fuel cell fabrication', *Journal of Power Sources*, 289, pp. 91-9.
- Phiri, J., Gane, P. & Maloney, T. C. (2019) 'Multidimensional Co-Exfoliated Activated Graphene-Based Carbon Hybrid for Supercapacitor Electrode', *Energy Technology*, 7(10), pp. 1900578-87
- Pierson, L. S. & Pierson, E. A. (2010) 'Metabolism and function of phenazines in bacteria: impacts on the behavior of bacteria in the environment and biotechnological processes', *Applied Microbiology and Biotechnology*, 86(6), pp. 1659-70.
- Ploux, L., Ponche, A. & Anselme, K. (2010) 'Bacteria/material interfaces: role of the material and cell wall properties', *Journal of Adhesion Science and Technology*, 24(13-14), pp. 2165-201.
- Pluskal, T., Castillo, S., Villar-Briones, A. & Oresic, M. (2010) 'MZmine 2: modular framework for processing, visualizing, and analyzing mass spectrometry-based molecular profile data', *BMC Bioinformatics*, 11(1), pp. 395-95.
- Potter, M. C. (1911) 'Electrical Effects Accompanying the Decomposition of Organic Compounds', *Proceedings of the Royal Society of London. Series B, Containing Papers of a Biological Character*, 84(571), pp. 260-76.

- Price-Whelan, A., Dietrich, L. E. & Newman, D. K. (2006) 'Rethinking'secondary'metabolism: physiological roles for phenazine antibiotics', *Nature Chemical Biology*, 2(2), pp. 71-8.
- Price-Whelan, A., Dietrich, L. E. & Newman, D. K. (2007) 'Pyocyanin alters redox homeostasis and carbon flux through central metabolic pathways in *Pseudomonas aeruginosa* PA14', *Journal of Bacteriology*, 189(17), pp. 6372-81.
- Prickett, M. H., Hauser, A. R., McColley, S. A., Cullina, J., Potter, E., Powers, C. & Jain, M. (2016) 'Aminoglycoside resistance of *Pseudomonas aeruginosa* in cystic fibrosis results from convergent evolution in the mexZ gene', *Thorax*, 72(1), pp. 40-7.
- Qian, F. & Morse, D. E. (2011) 'Miniaturizing microbial fuel cells', *Trends in Biotechnology*, 29(2), pp. 62-9.
- Qian, X., Reguera, G., Mester, T. & Lovley, D. R. (2007) 'Evidence that OmcB and OmpB of *Geobacter sulfurreducens* are outer membrane surface proteins', *FEMS Microbiology Letters*, 277(1), pp. 21-7.
- Qiao, Y., Li, C. M., Bao, S-J., Lu, Z. & Hong, Y. (2008) 'Direct electrochemistry and electrocatalytic mechanism of evolved *Escherichia coli* cells in microbial fuel cells', *Chemical Communications*, 11, pp. 1290-2.
- Qiao, Y., Qiao, Y. J., Zou, L., Ma, C. X. & Liu, J. H. (2015) 'Real-time monitoring of phenazines excretion in *Pseudomonas aeruginosa* microbial fuel cell anode using cavity microelectrodes', *Bioresource Technology*, 198, pp. 1-6.
- Qiao, Y-J., Qiao, Y., Zou, L., Wu, X-S. & Liu, J-H. (2017) 'Biofilm promoted current generation of *Pseudomonas aeruginosa* microbial fuel cell via improving the interfacial redox reaction of phenazines', *Bioelectrochemistry*, 117, pp. 34-9.
- Rabaey, K. & Verstraete, W. (2005) 'Microbial fuel cells: novel biotechnology for energy generation', *Trends in Biotechnology*, 23(6), pp. 291-8.
- Rabaey, K., Boon, N., Höfte, M. & Verstraete, W. (2005) 'Microbial phenazine production enhances electron transfer in biofuel cells', *Environmental Science & Technology*, 39(9), pp. 3401-8.
- Rabaey, K., Boon, N., Siciliano, S. D., Verhaege, M. & Verstraete, W. (2004) 'Biofuel Cells Select for Microbial Consortia That Self-Mediate Electron Transfer', *Applied and Environmental Microbiology*, 70(9), pp. 5373-82.
- Rabin, N., Zheng, Y., Opoku-Temeng, C., Du, Y., Bonsu, E. & Sintim, H. O. (2015) 'Biofilm formation mechanisms and targets for developing antibiofilm agents', *Future Medicinal Chemistry*, 7(4), pp. 493-512.
- Rahimnejad, M., Adhami, A., Darvari, S., Zirepour, A. & Oh, S-E. (2015) 'Microbial fuel cell as new technology for bioelectricity generation: A review', *Alexandria Engineering Journal*, 54(3), pp. 745-56.
- Rahimnejad, M., Jafary, T., Haghparast, F., Najafpour, G. & Ghoreyshi, A. A. (2011) 'Nafion as a nanoproton conductor in microbial fuel cells', *Turkish Journal of Engineering and Environmental Sciences*, 34(4), pp. 289-92.
- Randviir, E. P., Brownson, D. A. C., Metters, J. P., Kadara, R. O. & Banks, C. E. (2014) 'The fabrication, characterisation and electrochemical investigation of screen-printed graphene electrodes', *Physical Chemistry Chemical Physics*, 16(10), pp. 4598-611.
- Rashid, M. I. & Andleeb, S. (2018). Pyocyanin yield improvement for enhancement of *Pseudomonas aeruginosa* inoculated Microbial Fuel Cell efficiency. In: *2018 International Conference on Power Generation Systems and Renewable Energy Technologies (PGSRET)*, pp. 1-6.

- Read, S. T., Dutta, P., Bond, P. L., Keller, J. & Rabaey, K. (2010) 'Initial development and structure of biofilms on microbial fuel cell anodes', *BMC Microbiology*, 10(1), pp. 98.
- Regan, J. M., Yan, H., Beyenal, H. & Babauta, J. (2015) 'Microbial Community Characterization on Polarized Electrode Surfaces', *Biofilms in Bioelectrochemical Systems: From Laboratory Practice to Data Interpretation*, Wiley, pp. 61-82.
- Reguera, G., McCarthy, K. D., Mehta, T., Nicoll, J. S., Tuominen, M. T. & Lovley, D. R. (2005) 'Extracellular electron transfer *via* microbial nanowires', *Nature*, 435(7045), pp. 1098-101.
- Reguera, G., Nevin, K. P., Nicoll, J. S., Covalla, S. F., Woodard, T. L. & Lovley, D. R. (2006) 'Biofilm and nanowire production leads to increased current in *Geobacter sulfurreducens* fuel cells', *Applied and Environmental Microbiology*, 72(11), pp. 7345-8.
- Reich, S. & Thomsen, C. (2004) 'Raman spectroscopy of graphite', *Philosophical Transactions of the Royal Society of London A: Mathematical, Physical and Engineering Sciences*, 362(1824), pp. 2271-88.
- Ren, H., Pyo, S., Lee, J. I., Park, T.-J., Gittleson, F. S., Leung, F. C., Kim, J., Taylor, A. D., Lee, H.-S. & Chae, J. (2015) 'A high power density miniaturized microbial fuel cell having carbon nanotube anodes', *Journal of Power Sources*, 273, pp. 823-30.
- Ren, H., Tian, H., Gardner, C. L., Ren, T. L. & Chae, J. (2016) 'A miniaturized microbial fuel cell with three-dimensional graphene macroporous scaffold anode demonstrating a record power density of over 10,000 W m<sup>-3</sup>', *Nanoscale*, 8(6), pp. 3539-47.
- Reszka, K. J., O'Malley, Y., McCormick, M. L., Denning, G. M. & Britigan, B. E. (2004) 'Oxidation of pyocyanin, a cytotoxic product from *Pseudomonas aeruginosa*, by microperoxidase 11 and hydrogen peroxide', *Free Radical Biology and Medicine*, 36(11), pp. 1448-59.
- Rinaldi, A., Mecheri, B., Garavaglia, V., Licocchia, S., Di Nardo, P. & Traversa, E. (2008) 'Engineering materials and biology to boost performance of microbial fuel cells: a critical review', *Energy & Environmental Science*, 1(4), pp. 417-29.
- Rismani-Yazdi, H., Carver, S. M., Christy, A. D. & Tuovinen, O. H. (2008) 'Cathodic limitations in microbial fuel cells: an overview', *Journal of Power Sources*, 180(2), pp. 683-94.
- Rajo, F. (2010) 'Carbon catabolite repression in *Pseudomonas*: optimizing metabolic versatility and interactions with the environment', *FEMS Microbiology Reviews*, 34(5), pp. 658-84.
- Roller, S. D. (1984) 'Electron-transfer coupling in microbial fuel cells: 1. comparison of redox-mediator reduction rates and respiratory rates of bacteria', *Journal of Chemical Technology and Biotechnology. Biotechnology*, 34(1), pp. 3-12.
- Romano, S., Schulz-Vogt, H. N., González, J. M. & Bondarev, V. (2015) 'Phosphate limitation induces drastic physiological changes, virulence-related gene expression, and secondary metabolite production in *Pseudovibrio* sp. strain FO-BEG1', *Applied and Environmental Microbiology*, 81(10), pp. 3518-28.
- Rosenberg, B., Van Camp, L. & Krigas, T. (1965) 'Inhibition of cell division in *Escherichia coli* by electrolysis products from a platinum electrode', *Nature*, 205(4972), pp. 698-99.
- Rosenberg, M. & Kjelleberg, S. (1986) 'Hydrophobic interactions: role in bacterial adhesion', *In: Marshall K.C. (eds) Advances in Microbial Ecology*, Springer, Boston, MA, 9, pp. 353-93.

- Rosenberg, M., Judes, H. & Weiss, E. (1983) 'Cell surface hydrophobicity of dental plaque microorganisms in situ', *Infection and Immunity*, 42(2), pp. 831-34.
- Rowley-Neale, S. J., Brownson, D. A. C. & Banks, C. E. (2016a) 'Defining the origins of electron transfer at screen-printed graphene-like and graphite electrodes: MoO<sub>2</sub> nanowire fabrication on edge plane sites reveals electrochemical insights', *Nanoscale*, 8(33), pp. 15241-51.
- Rowley-Neale, S. J., Brownson, D. A. C., Smith, G. C., Sawtell, D. A. G., Kelly, P. J. & Banks, C. E. (2015) '2D nanosheet molybdenum disulphide (MoS<sub>2</sub>) modified electrodes explored towards the hydrogen evolution reaction', *Nanoscale*, 7(43), pp. 18152-68.
- Rowley-Neale, S. J., Fearn, J. M., Brownson, D. A., Smith, G. C., Ji, X. & Banks, C. E. (2016b) '2D molybdenum disulphide (2D-MoS<sub>2</sub>) modified electrodes explored towards the oxygen reduction reaction', *Nanoscale*, 8(31), pp. 14767-77.
- Rowley-Neale, S. J., Foster, C. W., Smith, G. C., Brownson, D. A. C. & Banks, C. E. (2017) 'Mass-producible 2D-MoSe<sub>2</sub> bulk modified screen-printed electrodes provide significant electrocatalytic performances towards the hydrogen evolution reaction', *Sustainable Energy & Fuels*, 1(1), pp. 74-83.
- Santoro, C., Arbizzani, C., Erable, B. & Ieropoulos, I. (2017) 'Microbial fuel cells: From fundamentals to applications. A review', *Journal of Power Sources*, 356, pp. 225-44.
- Santoro, C., Babanova, S., Artyushkova, K., Cornejo, J. A., Ista, L., Bretschger, O., Marsili, E., Atanassov, P. & Schuler, A. J. (2015) 'Surface Chemistry Enhanced Microbial Bioelectrocatalysis', *Bioelectrochemistry*, 106(Pt A), pp. 141-9.
- Sauer, K., Cullen, M., Rickard, A., Zeef, L., Davies, D. G. & Gilbert, P. (2004) 'Characterization of nutrient-induced dispersion in *Pseudomonas aeruginosa* PAO1 biofilm', *Journal of Bacteriology*, 186(21), pp. 7312-26.
- Schneider, C. A., Rasband, W. S. & Eliceiri, K. W. (2012) 'NIH Image to ImageJ: 25 years of image analysis', *Nature Methods*, 9(7), pp. 671-5.
- Schobert, M. & Jahn, D. (2010) 'Anaerobic physiology of *Pseudomonas aeruginosa* in the cystic fibrosis lung', *International Journal of Medical Microbiology*, 300(8), pp. 549-56.
- Schreiber, K., Boes, N., Eschbach, M., Jaensch, L., Wehland, J., Bjarnsholt, T., Givskov, M., Hentzer, M. & Schobert, M. (2006) 'Anaerobic Survival of *Pseudomonas aeruginosa* by Pyruvate Fermentation Requires an Usp-Type Stress Protein', *Journal of Bacteriology*, 188(2), pp. 659-68.
- Schreiber, K., Krieger, R., Benkert, B., Eschbach, M., Arai, H., Schobert, M. & Jahn, D. (2007) 'The anaerobic regulatory network required for *Pseudomonas aeruginosa* nitrate respiration', *Journal of Bacteriology*, 189(11), pp. 4310-14.
- Schröder, U. (2007) 'Anodic electron transfer mechanisms in microbial fuel cells and their energy efficiency', *Physical Chemistry Chemical Physics*, 9(21), pp. 2619-29.
- Schröder, U. (2011) 'Discover the possibilities: microbial bioelectrochemical systems and the revival of a 100-year-old discovery', *Journal of Solid State Electrochemistry*, 15(7-8), pp. 1481-86.
- Schuster, M. & Greenberg, E. P. (2006) 'A network of networks: quorum-sensing gene regulation in *Pseudomonas aeruginosa*', *International Journal of Medical Microbiology*, 296(2-3), pp. 73-81.
- Schwarzer, C., Fischer, H., Kim, E.-J., Barber, K. J., Mills, A. D., Kurth, M. J., Gruenert, D. C., Suh, J. H., Machen, T. E. & Illek, B. (2008) 'Oxidative stress caused by pyocyanin

- impairs CFTR Cl<sup>-</sup> transport in human bronchial epithelial cells', *Free Radical Biology and Medicine*, 45(12), pp. 1653-62.
- Serra, T., Ortiz-Hernandez, M., Engel, E., Planell, J. A. & Navarro, M. (2014) 'Relevance of PEG in PLA-based blends for tissue engineering 3D-printed scaffolds', *Materials Science and Engineering: C*, 38, pp. 55-62.
- Service, R. F. (2009) 'Materials science. Carbon sheets an atom thick give rise to graphene dreams', *Science*, 324(5929), pp. 875-7.
- Sezonov, G., Joseleau-Petit, D. & D'Ari., R. (2007) *Escherichia coli* physiology in Luria-Bertani broth', *Journal of Bacteriology*, 189(23), pp. 8746-9.
- Shao, Y., Wang, J., Wu, H., Liu, J., Aksay, I. A. & Lin, Y. (2010) 'Graphene Based Electrochemical Sensors and Biosensors: A Review', *Electroanalysis*, 22(10), pp. 1027-36.
- Sharaf, O. Z. & Orhan, M. F. (2014) 'An overview of fuel cell technology: Fundamentals and applications', *Renewable and Sustainable Energy Reviews*, 32, pp. 810-53.
- Sharma, Y. & Li, B. (2010) 'The variation of power generation with organic substrates in single-chamber microbial fuel cells (SCMFCs)', *Bioresource Technology*, 101(6), pp. 1844-50.
- Shen, H-B., Yong, X-Y., Chen, Y-L., Liao, Z-H., Si, R-W., Zhou, J., Wang, S-Y., Yong, Y-C., OuYang, P-K. & Zheng, T. (2014) 'Enhanced bioelectricity generation by improving pyocyanin production and membrane permeability through sophorolipid addition in *Pseudomonas aeruginosa*-inoculated microbial fuel cells', *Bioresource Technology*, 167, pp. 490-4.
- Sheng, Z-H., Zheng, X-Q., Xu, J-Y., Bao, W-J., Wang, F-B. & Xia, X-H. (2012) 'Electrochemical sensor based on nitrogen doped graphene: simultaneous determination of ascorbic acid, dopamine and uric acid', *Biosensors and Bioelectronics*, 34(1), pp. 125-31.
- Shi, W. & Sun, H. (2002) 'Type IV Pilus-Dependent Motility and Its Possible Role in Bacterial Pathogenesis', *Infection and Immunity*, 70(1), pp. 1-4.
- Shin, S., Jin, Z., Kwon, D. H., Bose, R. & Min, Y-S. (2015) 'High Turnover Frequency of Hydrogen Evolution Reaction on Amorphous MoS<sub>2</sub> Thin Film Directly Grown by Atomic Layer Deposition', *Langmuir*, 31(3), pp. 1196-202.
- Shoener, B., Bradley, I., Cusick, R. & Guest, J. (2014) 'Energy positive domestic wastewater treatment: the roles of anaerobic and phototrophic technologies', *Environmental Science: Processes & Impacts*, 16(6), pp. 1204-22.
- Shreeram, D. D., Hassett, D. J. & Schaefer, D. W. (2016) 'Urine-powered microbial fuel cell using a hyperpiliated pilT mutant of *Pseudomonas aeruginosa*', *Journal of industrial Microbiology & Biotechnology*, 43(1), pp. 103-7.
- Slate, A. J., Brownson, D. A. C., Dena, A. S. A., Smith, G. C., Whitehead, K. A. & Banks, C. E. (2018a) 'Exploring the electrochemical performance of graphite and graphene paste electrodes composed of varying lateral flake sizes', *Physical Chemistry Chemical Physics*, 20(30), pp. 20010-22.
- Slate, A. J., Karaky, N. & Whitehead, K. A. (2018b) 'Antimicrobial properties of Modified Graphene and other advanced 2D Material Coated Surfaces', *2D Materials: CRC Press*, pp. 86-104.
- Slate, A. J., Shalamanova, L., Akhidime, I. D. and Whitehead, K. A. (2019a) 'Rhenium and yttrium ions as antimicrobial agents against multidrug resistant *Klebsiella pneumoniae* and *Acinetobacter baumannii* biofilms', *Letters in Applied Microbiology*, 69(3), pp. 168-174.

- Slate, A. J., Whitehead, K. A., Brownson, D. A. & Banks, C. E. (2019b) 'Microbial fuel cells: An overview of current technology', *Renewable and Sustainable Energy Reviews*, 101, pp. 60-81.
- Slate, A. J., Wickens, D. J., El Mohtadi, M., Dempsey-Hibbert, N., Banks, C. E. & Whitehead, K. A. (2018c) 'Antimicrobial activity of Ti-ZrN/Ag coatings for use in biomaterial applications', *Scientific Reports*, 8, pp. 1497.
- Slate, A. J., Wickens, D. J., Wilson-Nieuwenhuis, J., Dempsey-Hibbert, N., West, G., Kelly, P., Verran, J., Banks, C. E. & Whitehead, K. A. (2019c) 'The effects of blood conditioning films on the antimicrobial and retention properties of zirconium-nitride silver surfaces', *Colloids and Surfaces B: Biointerfaces*, 173, pp. 303-11.
- Smith, J. A., Tremblay, P. L., Shrestha, P. M., Snoeyenbos-West, O. L., Franks, A. E., Nevin, K. P. & Lovley, D. R. (2014) 'Going wireless: Fe(III) oxide reduction without pili by *Geobacter sulfurreducens* strain JS-1', *Applied and Environmental Microbiology*, 80(14), pp. 4331-40.
- Smith, R. E. G., Davies, T. J., Baynes, N. d. B. & Nichols, R. J. (2015) 'The electrochemical characterisation of graphite felts', *Journal of Electroanalytical Chemistry*, 747, pp. 29-38.
- Song, H-L., Zhu, Y. & Li, J. (2015) 'Electron transfer mechanisms, characteristics and applications of biological cathode microbial fuel cells—A mini review', *Arabian Journal of Chemistry*, pp. 1-8.
- Stoller, M. D., Park, S., Zhu, Y., An, J. & Ruoff, R. S. (2008) 'Graphene-based ultracapacitors', *Nano Letters*, 8(10), pp. 3498-502.
- Strycharz-Glaven, S. M., Snider, R. M., Guiseppi-Elie, A. & Tender, L. M. (2011) 'On the electrical conductivity of microbial nanowires and biofilms', *Energy & Environmental Science*, 4(11), pp. 4366-79.
- Sun, D., Chen, J., Huang, H., Liu, W., Ye, Y. & Cheng, S. (2016a) 'The effect of biofilm thickness on electrochemical activity of *Geobacter sulfurreducens*', *International Journal of Hydrogen Energy*, 41(37), pp. 16523-8.
- Sun, D., Cheng, S., Wang, A., Li, F., Logan, B. E. & Cen, K. (2015) 'Temporal-spatial changes in viabilities and electrochemical properties of anode biofilms', *Environmental Science & Technology*, 49(8), pp. 5227-35.
- Sun, M., Zhai, L-F., Li, W-W. & Yu, H-Q. (2016b) 'Harvest and utilization of chemical energy in wastes by microbial fuel cells', *Chemical Society Reviews*, 45(10), pp. 2847-70.
- Sund, C. J., McMasters, S., Crittenden, S. R., Harrell, L. E. & Sumner, J. J. (2007) 'Effect of electron mediators on current generation and fermentation in a microbial fuel cell', *Applied Microbiology and Biotechnology*, 76(3), pp. 561-8.
- Sure, S., Ackland, M. L., Torriero, A. A., Adholeya, A. & Kochar, M. (2016) 'Microbial nanowires: an electrifying tale', *Microbiology*, 162(12), pp. 2017-28.
- Țălu, S. t., Stach, S., Ghodselahi, T., Ghaderi, A., Solaymani, S., Boochani, A. & Garczyk, Z. a. (2015) 'Topographic characterization of Cu-Ni NPs@ aC: H films by AFM and multifractal analysis', *The Journal of Physical Chemistry B*, 119(17), pp. 5662-70.
- Tan, Y., Adhikari, R. Y., Malvankar, N. S., Ward, J. E., Nevin, K. P., Woodard, T. L., Smith, J. A., Snoeyenbos-West, O. L., Franks, A. E., Tuominen, M. T. & Lovley, D. R. (2016) 'The Low Conductivity of *Geobacter uraniireducens* Pili Suggests a Diversity of Extracellular Electron Transfer Mechanisms in the Genus *Geobacter*', *Frontiers in Microbiology*, 7, pp. 980.

- Tanimoto, S. & Ichimura, A. (2013) 'Discrimination of Inner- and Outer-Sphere Electrode Reactions by Cyclic Voltammetry Experiments', *Journal of Chemical Education*, 90(6), pp. 778-81.
- Tardast, A., Rahimnejad, M., Najafpour, G., Ghoreyshi, A., Premier, G. C., Bakeri, G. & Oh, S-E. (2014) 'Use of artificial neural network for the prediction of bioelectricity production in a membrane less microbial fuel cell', *Fuel*, 117(Pt. A), pp. 697-703.
- Tautenhahn, R., Boettcher, C. & Neumann, S. (2008) 'Highly sensitive feature detection for high resolution LC/MS', *BMC Bioinformatics*, 9(1), pp. 504.
- Tellefsen, G., Linder, L., Liljeborg, A. & Johannsen, G. (2016) 'The Influence of Surface Roughness of Titanium on Bacterial Accumulation/Adhesion', *Dentistry*, 6(361), pp. 1000361.
- Tender, L. M. (2011) 'From mud to microbial electrode catalysts and conductive nanomaterials', *MRS bulletin*, 36(10), pp. 800-5.
- Ter Heijne, A., Liu, F., van Rijnsoever, L. S., Saakes, M., Hamelers, H. V. M. & Buisman, C. J. N. (2011) 'Performance of a scaled-up Microbial Fuel Cell with iron reduction as the cathode reaction', *Journal of Power Sources*, 196(18), pp. 7572-7.
- Tetlow, L. A., Lynch, S. & Whitehead, K. A. (2017) 'The effect of surface properties on bacterial retention: A study utilising stainless steel and TiN/25.65 at.% Ag substrata', *Food and Bioproducts Processing*, 102, pp. 332-9.
- Teughels, W., Van Assche, N., Sliepen, I. & Quirynen, M. (2006) 'Effect of material characteristics and/or surface topography on biofilm development', *Clinical oral Implants Research*, 17(S2), pp. 68-81.
- Tortora, G. J., Funke, B. R., Case, C. L. & Johnson, T. R. (2004). *Microbiology: an introduction* (Vol. 9): Benjamin Cummings, San Francisco, CA.
- Toyofuku, M., Nomura, N., Fujii, T., Takaya, N., Maseda, H., Sawada, I., Nakajima, T. & Uchiyama, H. (2007) 'Quorum sensing regulates denitrification in *Pseudomonas aeruginosa* PAO1', *Journal of Bacteriology*, 189(13), pp. 4969-72.
- Toyofuku, M., Nomura, N., Kuno, E., Tashiro, Y., Nakajima, T. & Uchiyama, H. (2008) 'Influence of the *Pseudomonas* quinolone signal on denitrification in *Pseudomonas aeruginosa*', *Journal of Bacteriology*, 190(24), pp. 7947-56.
- Valli, K. (2018) 'A Comparative Study Between Rapid And Conventional Moeller Decarboxylase And Dihydrolase Medium For Identification Of Enterobacteriaceae And Nonfermentative Bacteria', *University Journal of Pre and Paraclinical Sciences*, 4(1).
- Valota, A. T., Kinloch, I. A., Novoselov, K. S., Casiraghi, C., Eckmann, A., Hill, E. W. & Dryfe, R. A. W. (2011) 'Electrochemical Behavior of Monolayer and Bilayer Graphene', *ACS Nano*, 5(11), pp. 8809-15.
- Van Loosdrecht, M. C., Lyklema, J., Norde, W. & Zehnder, A. J. (1989) 'Bacterial adhesion: a physicochemical approach', *Microbial Ecology*, 17(1), pp. 1-15.
- Van Oss, C. J. (1989) 'Energetics of cell-cell and cell-biopolymer interactions', *Cell Biophysics*, 14(1), pp. 1-16.
- Van Oss, C. J., Chaudhury, M. K. & Good, R. J. (1988) 'Interfacial Lifshitz-van der Waals and polar interactions in macroscopic systems', *Chemical Reviews*, 88(6), pp. 927-41.
- Vander Wauven, C., Pierard, A., Kley-Raymann, M. & Haas, D. (1984) '*Pseudomonas aeruginosa* mutants affected in anaerobic growth on arginine: evidence for a four-gene cluster encoding the arginine deiminase pathway', *Journal of Bacteriology*, 160(3), pp. 928-34.

- Vasylyv, O. M., Bilyy, O. I., Ferensovych, Y. P. & Hnatush, S. O. (2013). Application of acetate, lactate, and fumarate as electron donors in microbial fuel cell. *In: Reliability of Photovoltaic Cells, Modules, Components, and Systems VI*, 8825, International Society for Optics and Photonics, pp. 88250Q.
- Velasquez-Orta, S. B., Head, I. M., Curtis, T. P., Scott, K., Lloyd, J. R. & von Canstein, H. (2010) 'The effect of flavin electron shuttles in microbial fuel cells current production', *Applied Microbiology and Biotechnology*, 85(5), pp. 1373-81.
- Venkataraman, A., Rosenbaum, M. A., Perkins, S. D., Werner, J. J. & Angenent, L. T. (2011) 'Metabolite-based mutualism between *Pseudomonas aeruginosa* PA14 and *Enterobacter aerogenes* enhances current generation in bioelectrochemical systems', *Energy & Environmental Science*, 4(11), pp. 4550-9.
- Venkataraman, A., Rosenbaum, M., Arends, J. B., Halitschke, R. & Angenent, L. T. (2010) 'Quorum sensing regulates electric current generation of *Pseudomonas aeruginosa* PA14 in bioelectrochemical systems', *Electrochemistry Communications*, 12(3), pp. 459-62.
- Verran, J. & Whitehead, K. A. (2005) 'Factors affecting microbial adhesion to stainless steel and other materials used in medical devices', *The International Journal of Artificial Organs*, 28(11), pp. 1138-45.
- Verran, J., Packer, A., Kelly, P. & Whitehead, K. A. (2010) 'The retention of bacteria on hygienic surfaces presenting scratches of microbial dimensions', *Letters in Applied Microbiology*, 50(3), pp. 258-63.
- Vicentini, F. C., Ravanini, A. E., Figueiredo-Filho, L. C. S., Iniesta, J., Banks, C. E. & Fatibello-Filho, O. (2015) 'Imparting improvements in electrochemical sensors: evaluation of different carbon blacks that give rise to significant improvement in the performance of electroanalytical sensing platforms', *Electrochimica Acta*, 157, pp. 125-33.
- Vilajeliu-Pons, A., Baneras, L., Puig, S., Molognoni, D., Vila-Rovira, A., Hernandez-del Amo, E., Balaguer, M. D. & Colprim, J. (2016) 'External resistances applied to MFC affect core microbiome and swine manure treatment efficiencies', *PLoS one*, 11(10), pp. e0164044.
- Walter, E. C., Zach, M. P., Favier, F., Murray, B. J., Inazu, K., Hemminger, J. C. & Penner, R. M. (2003) 'Metal nanowire arrays by electrodeposition', *ChemPhysChem*, 4(2), pp. 131-8.
- Walter, X. A., Forbes, S., Greenman, J. & Ieropoulos, I. A. (2016) 'From single MFC to cascade configuration: The relationship between size, hydraulic retention time and power density', *Sustainable Energy Technologies and Assessments*, 14, pp. 74-79.
- Wang, H., Luo, H., Fallgren, P. H., Jin, S. & Ren, Z. J. (2015a) 'Bioelectrochemical system platform for sustainable environmental remediation and energy generation', *Biotechnology advances*, 33(3), pp. 317-34.
- Wang, V. B., Chua, S-L., Cao, B., Seviour, T., Nesatyy, V. J., Marsili, E., Kjelleberg, S., Givskov, M., Tolker-Nielsen, T. & Song, H. (2013) 'Engineering PQS biosynthesis pathway for enhancement of bioelectricity production in *Pseudomonas aeruginosa* microbial fuel cells', *PLoS One*, 8(5), pp. e63129.
- Wang, Y. Y., Ni, Z. H., Yu, T., Shen, Z. X., Wang, H. M., Wu, Y. H., Chen, W. & Shen Wee, A. T. (2008) 'Raman studies of monolayer graphene: the substrate effect', *The Journal of Physical Chemistry C*, 112(29), pp. 10637-40.

- Wang, Y., Kern, S. E. & Newman, D. K. (2010) 'Endogenous phenazine antibiotics promote anaerobic survival of *Pseudomonas aeruginosa* via extracellular electron transfer', *Journal of Bacteriology*, 192(1), pp. 365-69.
- Wang, Y., Lee, S. M. & Dykes, G. (2015c) 'The physicochemical process of bacterial attachment to abiotic surfaces: Challenges for mechanistic studies, predictability and the development of control strategies', *Critical reviews in microbiology*, 41(4), pp. 452-64.
- Wang, Y., Li, Y., Tang, L., Lu, J. & Li, J. (2009) 'Application of graphene-modified electrode for selective detection of dopamine', *Electrochemistry Communications*, 11(4), pp. 889-92.
- Wang, Y-Z., Wang, Y-K., He, C-S., Yang, H-Y., Sheng, G-P., Shen, J-Y., Mu, Y. & Yu, H-Q. (2015b) 'Hydrodynamics of an electrochemical membrane bioreactor', *Scientific Reports*, 5, pp. 10387.
- Watanabe, K., Manefield, M., Lee, M. & Kouzuma, A. (2009) 'Electron shuttles in biotechnology', *Current Opinion in Biotechnology*, 20(6), pp. 633-41.
- Webb, H. K., Notley, S. & Evans, D. R. (2015) 'Observation of electron transfer between bacteria and high conductivity graphene-PEDOT composites', *RSC Advances*, 5(57), pp. 45642-5.
- Wei, J., Liang, P. & Huang, X. (2011) 'Recent progress in electrodes for microbial fuel cells', *Bioresource Technology*, 102(20), pp. 9335-44.
- Wei, X., Li, D., Jiang, W., Gu, Z., Wang, X., Zhang, Z. & Sun, Z. (2015) '3D Printable Graphene Composite', *Scientific Reports*, 5, pp. 11181.
- Whitehead, K. A. & Verran, J. (2006) 'The effect of surface topography on the retention of microorganisms', *Food and Bioprocess Processing*, 84(4), pp. 253-9.
- Whitehead, K. A. & Verran, J. (2015) 'Formation, architecture and functionality of microbial biofilms in the food industry', *Current Opinion in Food Science*, 2, pp. 84-91.
- Wickens, D., Lynch, S., West, G., Kelly, P., Verran, J. & Whitehead, K. A. (2014) 'Quantifying the pattern of microbial cell dispersion, density and clustering on surfaces of differing chemistries and topographies using multifractal analysis', *Journal of Microbiological Methods*, 104, pp. 101-8.
- Wilcox, J. (2014) 'Grand Challenges in Advanced Fossil Fuel Technologies', *Frontiers in Energy Research*, 2, pp. 47.
- Williams, P. & Cámara, M. (2009) 'Quorum sensing and environmental adaptation in *Pseudomonas aeruginosa*: a tale of regulatory networks and multifunctional signal molecules', *Current Opinion in Microbiology*, 12(2), pp. 182-91.
- Wilson, C., Lukowicz, R., Merchant, S., Valquier-Flynn, H., Caballero, J., Sandoval, J., Okuom, M., Huber, C., Brooks, T.D., Wilson, E. & Clement, B. (2017) 'Quantitative and qualitative assessment methods for biofilm growth: A mini-review', *Research & reviews. Journal of engineering and technology*, 6(4).
- Wilson, R. & Dowling, R. B. (1998) '*Pseudomonas aeruginosa* and other related species', *Thorax*, 53(3), pp. 213-9.
- Wilson-Nieuwenhuis, J. S., Dempsey-Hibbert, N., Liauw, C. M. & Whitehead, K. A. (2017) 'Surface modification of platelet concentrate bags to reduce biofilm formation and transfusion sepsis', *Colloids and Surfaces B: Biointerfaces*, 160, pp. 126-35.
- Winfield, J., Greenman, J., Huson, D. & Ieropoulos, I. (2013a) 'Comparing terracotta and earthenware for multiple functionalities in microbial fuel cells', *Bioprocess and Biosystems Engineering*, 36(12), pp. 1913-21.

- Winfield, J., Ieropoulos, I., Rossiter, J., Greenman, J. & Patton, D. (2013b) 'Biodegradation and proton exchange using natural rubber in microbial fuel cells', *Biodegradation*, 24(6), pp. 733-9.
- Winson, M. K., Camara, M., Latifi, A., Foglino, M., Chhabra, S. R., Daykin, M., Bally, M., Chapon, V., Salmond, G. & Bycroft, B. W. (1995) 'Multiple N-acyl-L-homoserine lactone signal molecules regulate production of virulence determinants and secondary metabolites in *Pseudomonas aeruginosa*', *Proceedings of the National Academy of Sciences*, 92(20), pp. 9427-31.
- Winzer, K., Falconer, C., Garber, N. C., Diggle, S. P., Camara, M. & Williams, P. (2000) 'The *Pseudomonas aeruginosa* lectins PA-IL and PA-III are controlled by quorum sensing and by RpoS', *Journal of Bacteriology*, 182(22), pp. 6401-11.
- Wu, D. Q., Cheng, H., Duan, Q. & Huang, W. (2015) 'Sodium houthuyfonate inhibits biofilm formation and alginate biosynthesis-associated gene expression in a clinical strain of *Pseudomonas aeruginosa* in vitro', *Experimental and Therapeutic Medicine*, 10(2), pp. 753-8.
- Wu, X., Shi, Z., Zou, L., Li, C. M. & Qiao, Y. (2018) 'Pectin assisted one-pot synthesis of three dimensional porous NiO/graphene composite for enhanced bioelectrocatalysis in microbial fuel cells', *Journal of Power Sources*, 378, pp. 119-24.
- Xiao, L., Damien, J., Luo, J., Jang, H. D., Huang, J. & He, Z. (2012) 'Crumpled graphene particles for microbial fuel cell electrodes', *Journal of Power Sources*, 208, pp. 187-92.
- Xu, B., Ge, Z. & He, Z. (2015) 'Sediment microbial fuel cells for wastewater treatment: challenges and opportunities', *Environmental Science: Water Research & Technology*, 1(3), pp. 279-84.
- Yan, Y., Yang, J., Dou, Y., Chen, M., Ping, S., Peng, J., Lu, W., Zhang, W., Yao, Z., Li, H. & Liu, W., 2008. Nitrogen fixation island and rhizosphere competence traits in the genome of root-associated *Pseudomonas stutzeri* A1501. *Proceedings of the National Academy of Sciences*, 105(21), pp.7564-9.
- Yang, C., Denno, M. E., Pyakurel, P. & Venton, B. J. (2015a) 'Recent trends in carbon nanomaterial-based electrochemical sensors for biomolecules: A review', *Analytica Chimica Acta*, 887, pp. 17-37.
- Yang, C-J. (2009) 'An impending platinum crisis and its implications for the future of the automobile', *Energy Policy*, 37(5), pp. 1805-8.
- Yang, W., Kim, K-Y., Saikaly, P. E. & Logan, B. E. (2017) 'The impact of new cathode materials relative to baseline performance of microbial fuel cells all with the same architecture and solution chemistry', *Energy & Environmental Science*, 10(5), pp.1025-1033.
- Yang, Y., Kumar, A., Zheng, Q. & Yuk, H-G. (2015b) 'Preacclimation alters *Salmonella Enteritidis* surface properties and its initial attachment to food contact surfaces', *Colloids and Surfaces B: Biointerfaces*, 128, pp. 577-85.
- Yang, Z., Chabi, S., Xia, Y. & Zhu, Y. (2015c) 'Preparation of 3D graphene-based architectures and their applications in supercapacitors', *Progress in Natural Science: Materials International*, 25(6), pp. 554-62.
- Ye, T-R., Song, N., Chen, M., Yan, Z-S. & Jiang, H-L. (2016) 'No enhancement of cyanobacterial bloom biomass decomposition by sediment microbial fuel cell (SMFC) at different temperatures', *Environmental Pollution*, 218, pp. 59-65.

- Ye, Z., Hou, J., Ellis, M. W. & Behkam, B. (2012) 'ASME International Mechanical Engineering Congress and Exposition,' *ASME 2012 International Mechanical Engineering Congress and Exposition*, pp. 1409-14.
- Yilanci, A., Dincer, I. & Ozturk, H. K. (2009) 'A review on solar-hydrogen/fuel cell hybrid energy systems for stationary applications', *Progress in Energy and Combustion Science*, 35(3), pp. 231-44.
- Yin, Y., Huang, G., Tong, Y., Liu, Y. & Zhang, L. (2013) 'Electricity production and electrochemical impedance modeling of microbial fuel cells under static magnetic field', *Journal of Power Sources*, 237, pp. 58-63.
- Yoda, I., Koseki, H., Tomita, M., Shida, T., Horiuchi, H., Sakoda, H. & Osaki, M. (2014) 'Effect of surface roughness of biomaterials on *Staphylococcus epidermidis* adhesion', *BMC Microbiology*, 14(1), pp. 234.
- Yong, X-Y., Shi, D-Y., Chen, Y-L., Jiao, F., Lin, X., Zhou, J., Wang, S-Y., Yong, Y-C., Sun, Y-M. & OuYang, P-K. (2014) 'Enhancement of bioelectricity generation by manipulation of the electron shuttles synthesis pathway in microbial fuel cells', *Bioresource Technology*, 152, pp. 220-4.
- Yong, X-Y., Yan, Z-Y., Shen, H-B., Zhou, J., Wu, X-Y., Zhang, L-J., Zheng, T., Jiang, M., Wei, P. & Jia, H-H. (2017) 'An integrated aerobic-anaerobic strategy for performance enhancement of *Pseudomonas aeruginosa*-inoculated microbial fuel cell', *Bioresource Technology*, 241, pp. 1191-6.
- Yong, Y-C., Yu, Y-Y., Li, C-M., Zhong, J-J. & Song, H. (2011) 'Bioelectricity enhancement via overexpression of quorum sensing system in *Pseudomonas aeruginosa*-inoculated microbial fuel cells', *Biosensors and Bioelectronics*, 30(1), pp. 87-92.
- Yoon, D., Moon, H., Cheong, H., Choi, J. S., Choi, J. A. & Park, B. H. (2009) 'Variations in the Raman Spectrum as a Function of the Number of Graphene Layers', *Journal of the Korean Physical Society*, 55(3), pp. 1299-303.
- Yoon, S. S., Hennigan, R. F., Hilliard, G. M., Ochsner, U. A., Parvatiyar, K., Kamani, M. C., Allen, H. L., DeKievit, T. R., Gardner, P. R. & Schwab, U. (2002) '*Pseudomonas aeruginosa* anaerobic respiration in biofilms: relationships to cystic fibrosis pathogenesis', *Developmental Cell*, 3(4), pp. 593-603.
- You, J., Preen, R. J., Bull, L., Greenman, J. & Ieropoulos, I. (2017) '3D printed components of microbial fuel cells: Towards monolithic microbial fuel cell fabrication using additive layer manufacturing', *Sustainable Energy Technologies and Assessments*, 19, pp. 94-101.
- Yu, F., Wang, C. & Ma, J. (2016) 'Applications of Graphene-Modified Electrodes in Microbial Fuel Cells', *Materials*, 9(10), pp. 807.
- Yuan, W., Zhou, Y., Li, Y., Li, C., Peng, H., Zhang, J., Liu, Z., Dai, L. & Shi, G. (2013) 'The edge- and basal-plane-specific electrochemistry of a single-layer graphene sheet', *Scientific Reports*, 3, pp. 2248.
- Yuan, Y., Hays, M. P., Hardwidge, P. R. & Kim, J. (2017) 'Surface characteristics influencing bacterial adhesion to polymeric substrates', *RSC Advances*, 7(23), pp. 14254-61.
- Yue, H., Khoshtariya, D., Waldeck, D. H., Grochol, J., Hildebrandt, P. & Murgida, D. H. (2006) 'On the Electron Transfer Mechanism Between Cytochrome c and Metal Electrodes. Evidence for Dynamic Control at Short Distances', *The Journal of Physical Chemistry B*, 110(40), pp. 19906-13.

- Yuvraj, C. & Aranganathan, V. (2017) 'MFC—An Approach in Enhancing Electricity Generation Using Electroactive Biofilm of Dissimilatory Iron-Reducing (DIR) Bacteria', *Arabian Journal for Science and Engineering*, 42(6), pp. 2341-7.
- Zabihallahpoor, A., Rahimnejad, M. & Talebnia, F. (2015) 'Sediment microbial fuel cells as a new source of renewable and sustainable energy: present status and future prospects', *RSC Advances*, 5(114), pp. 94171-83.
- Zach, M. P., Ng, K. H. & Penner, R. M. (2000) 'Molybdenum nanowires by electrodeposition', *Science*, 290(5499), pp. 2120-3.
- Zhang, B., Zhao, H., Zhou, S., Shi, C., Wang, C. & Ni, J. (2009) 'A novel UASB–MFC–BAF integrated system for high strength molasses wastewater treatment and bioelectricity generation', *Bioresource Technology*, 100(23), pp. 5687-93.
- Zhang, E., Xu, W., Diao, G. & Shuang, C. (2006) 'Electricity generation from acetate and glucose by sedimentary bacterium attached to electrode in microbial-anode fuel cells', *Journal of Power Sources*, 161(2), pp. 820-5.
- Zhang, M., Ma, Z., Zhao, N., Zhang, K. & Song, H. (2019) 'Increased power generation from cylindrical microbial fuel cell inoculated with *P. aeruginosa*', *Biosensors and Bioelectronics*, 141, pp. 111394.
- Zhang, T., Cui, C., Chen, S., Yang, H. & Shen, P. (2008) 'The direct electrocatalysis of *Escherichia coli* through electroactivated excretion in microbial fuel cell', *Electrochemistry Communications*, 10(2), pp. 293-7.
- Zhang, T., Zhang, L., Su, W., Gao, P., Li, D., He, X. & Zhang, Y. (2011a) 'The direct electrocatalysis of phenazine-1-carboxylic acid excreted by *Pseudomonas alcaliphila* under alkaline condition in microbial fuel cells', *Bioresource Technology*, 102(14), pp. 7099-102.
- Zhang, X., Ren, H., Pyo, S., Lee, J.-I., Kim, J. & Chae, J. (2014) 'A high-efficiency DC–DC boost converter for a miniaturized microbial fuel cell', *IEEE Transactions on Power Electronics*, 30(4), pp. 2041-9.
- Zhang, Y., Mo, G., Li, X., Zhang, W., Zhang, J., Ye, J., Huang, X. & Yu, C. (2011b) 'A graphene modified anode to improve the performance of microbial fuel cells', *Journal of Power Sources*, 196(13), pp. 5402-7.
- Zhao, C., Wang, C., Gorkin, R., Beirne, S., Shu, K. & Wallace, G. G. (2014) 'Three dimensional (3D) printed electrodes for interdigitated supercapacitors', *Electrochemistry Communications*, 41, pp. 20-3.
- Zhao, F., Harnisch, F., Schröder, U., Scholz, F., Bogdanoff, P. & Herrmann, I. (2006) 'Challenges and constraints of using oxygen cathodes in microbial fuel cells', *Environmental Science & Technology*, 40(17), pp. 5193-9.
- Zhao, Y. N., Li, X. F., Ren, Y. P. & Wang, X. H. (2016) 'Effect of static magnetic field on the performances of anode biofilms in microbial fuel cells', *RSC Advances*, 6(85), pp. 82301-8.
- Zhou, E., Wang, C., Zhao, Q., Li, Z., Shao, M., Deng, X., Liu, X. & Xu, X. (2016a) 'Facile synthesis of MoO<sub>2</sub> nanoparticles as high performance supercapacitor electrodes and photocatalysts', *Ceramics International*, 42(2,A), pp. 2198-203.
- Zhou, M., Chi, M., Luo, J., He, H. & Jin, T. (2011) 'An overview of electrode materials in microbial fuel cells', *Journal of Power Sources*, 196(10), pp. 4427-35.
- Zhou, S., Huang, S., He, J., Li, H. & Zhang, Y. (2016b) 'Electron transfer of *Pseudomonas aeruginosa* CP1 in electrochemical reduction of nitric oxide', *Bioresource Technology*, 218, pp. 1271-4.

- Zhu, C., Han, T. Y-J., Duoss, E. B., Golobic, A. M., Kuntz, J. D., Spadaccini, C. M. & Worsley, M. A. (2015) 'Highly compressible 3D periodic graphene aerogel microlattices', *Nature Communications*, 6(6962), pp. 1-8.
- Zumft, W. G. (1997) 'Cell biology and molecular basis of denitrification', *Microbiology and Molecular Biology Reviews*, 61(4), pp. 533-616.
- Zurob, E., Dennett, G., Gentil, D., Montero-Silva, F., Gerber, U., Naulín, P., Gómez, A., Fuentes, R., Lascano, S. & Rodrigues da Cunha, T. (2019) 'Inhibition of Wild *Enterobacter cloacae* Biofilm Formation by Nanostructured Graphene-and Hexagonal Boron Nitride-Coated Surfaces', *Nanomaterials*, 9(49), pp. 1-18.